Plasmachemical patterning of polymer surfaces

Woodward, lain Stuart

Plasmachemical Patterning of Polymer Surfaces

Ph. D. Thesis

by

Iain Stuart Woodward

Department of Chemistry

University of Durham

2001

For my Parents and for Jenny

STATEMENT OF COPYRIGHT

DECLARATION

The work described in this thesis was carried out in the Chemistry Department at the University of Durham between October 1998 and September 2001. It is the original work of the author, except where otherwise acknowledged, and has not been submitted previously for a degree at this or any other University.

Raman Mapping and dynamic contact angle analysis (Chapter 2) were performed by Dr Vincent Rococoules (University of Durham). Film thickness measurements (Chapters 2, 3 and 4) were carried out by Dr Wayne Schofield (University of Durham). Film hardness measurement (Chapter 2) was carried out by Dr S. Bull (Newcastle University). Pulsed plasma polymerisation of 2-hydroxyethyl methacrylate, 2-cyanoethyl acrylate, furfuryl methacrylate, and glycidyl methacrylate (Chapter 6) was carried out by Cinzia Tarducci (University of Durham), Pulsed plasma polymerisation of maleic anydride (Chapter 6) was carried out by Dr Declan Tear (University of Durham). Pulsed plasma polymerisation of butyl acrylate (Chapter 6) was carried out by Dr Wayne Schofield (University of Durham). Adhesion measurement and treatment of the

microwave oxygen plasma treated cords (Chapter 6) was performed by Plasma Finish and Pirelli.

PUBLICATIONS

Work carried out in this thesis has been published or will be submitted for publication as follows:-

(1) Super-Hydrophobic Surfaces Produced by Plasma Fluorination of Polybutadiene Films, *in progress..*

(2) Microfluidic Surface Patterning of Metal Salts and Polymer Microspheres, *in progress.*

(3) Super-Hydrophobic Surfaces Produced by Plasma Fluorination of Polybutadiene Films, *Patenting in Progress.*

ACKNOWLEDGEMENTS

I would like to thank my supervisor Professor J.P.S Badyal for his help and guidance over the last three years, and also to Pirelli, for financial support. Thanks also to everyone in lab 98 past and present for guidance, and to Steve and Luke for the occasional pint after work.

Thanks also to George, Kelvin and Barry in the electrical workshops, Neil and Jim in the Mechanical workshops and George, Ray, Malcolm and Peter the glassblowers for all their technical support.

Finally special thanks to Jenny for always being there and for everything.

ABSTRACT

The work in this thesis has been primarily aimed at the production of composite surfaces, comprising regions of differing chemistries. The use of these surfaces as templates for guided self assembly of aqueous species and production of controlled bifunctional surfaces is investigated.

Guided self assembly of aqueous species was achieved through production of surfaces exhibiting areas of high and low water contact angle. These were produced through successive plasma treatments, photo-lithographic patterning, and macromolecular self assembly in polymer films.

Also investigated was the effect of surface charge deposition from an AFM tip on phase segregated polymer films, with components exhibiting differing charging characteristics.

Also investigated was the plasma modification of polymer cords to improve adhesion into a rubber matrix. The aim of this work was to provide a dry plasma process capable of replacing current wet chemical processing techniques.

Contents

Chapter 1

Introduction to Chemically Patterning Surfaces on the Micron Scale and Surface Analysis Techniques 1

Chapter 2

Photolithographic Patterning of Super-Hydrophobic Polymer Films: a means to Ordered Micro-Arrays 25

Chapter 3

Polybutadiene / Polystyrene Phase Segregated Films: a Pathway to Bifunctionalisation 76

Chapter 4

Selective Plasma Functionalisation of a Segregated Block Copolymer 113

Chapter 5

Selective Charge Deposition on Phase Segregated Polymer Surfaces Using the Electric Force Microscope 148

Chapter 6

Plasma Enhanced Adhesion of Polymer Reinforcing Cord for Tyres 185

Appendix A

Chapter 1

Introduction to Chemically Patterning Surfaces on the Micron Scale and Surface Analysis Techniques

1.1 Overview

The aim of this chapter is to provide an introduction to the micron-scale chemical patterning of polymer surfaces, and provide a background to the surface modification techniques used here, as well as to the surface analysis techniques employed.

1.2 Patterning of Surfaces on the Micron Scale

1.2.1 Introduction

Our ability to reduce the dimensions of small structures is a fundamental area of research in modern day science. The strive to fabricate structures of increasingly reduced dimensions has been primarily driven by the microelectronics industry.[4] However application of minaturised devices is also found in optical devices,[16] magnetic storage devices,[1] and lab on a chip technologies.[2] Many methodologies are currently under development, with the aim of reducing the size of fabricated structures, for cheap, rapid and defect-free production. This review covers the well established photolithographic approaches to micro patterning, along with promising strategies involving self assembly, and also the use of scanning probes.

1.2.2 Photolithographic Methods

Photolithography has in many respects been the work horse of microfabrication for the microelectronics industry. The process involves the modification of selected surface regions using incident radiation, commonly UV, DUV (Deep UV), EUV (Extreme UV) or X-rays. The substrate is normally coated in a photoresist, sensitive to the radiation used, which upon exposure undergoes an exploitable change (commonly solubility).[3] Regions of photoresist are

selectively irradiated by the use of a mask, which is either positioned in contact with the substrate (contact mode photolithography), or, as is commonly used in the microelectronics industry, utilized to project an image onto the photoresist, (projection mode photolithography). The differences in the photoresist are then exploited to form a relief structure through etching.

The limitations imposed on the size of structures fabricated in this manner are predominantly wavelength based, as in practice, structures no smaller than wavelength of incident light can be manufactured.[4] Therefore the size of fabrication can in theory be reduced by the use of source of shorter wavelength, e.g. EUV ($\lambda \approx$ 10-91 nm) or X-rays ($\lambda \approx$ 0.01-10 nm),[5,6] however a lack of suitable materials for lenses at these wavelengths introduces some difficulty.[7] With improvements in optics used for lithography the potential still exists for significant reduction in the size of features fabricated in this manner.[8]

Lithography can also be performed in a similar manner using energetic particles / electrons. Typically lithography is performed using a focussed beam, and in the case of electrons can achieve resolutions in excess of 10 nm.[9] However, the time involved for these processes negates their use in mass production.[10] Improvements in production rate through the use of projection systems similar to those used for photons are promising and may yield significantly increased throughput.[11]

1.2.3 Self Assembling Systems

An alternative approach to patterning surfaces is the use of self assembling systems. The concept of self assembly arises from processes in nature, for example the formation of the DNA double helix.[12] Self assembly entails the spontaneous aggregation of sub-units into an organised structure. Assembly of

the units is guided by information inherent in each unit, thus no external interference is necessary.

The most prolific use of self assembling systems in microlithography is almost certainly the application of self assembled monolayers (SAM's). These monolayers are typically formed from linear alkane molecules with functionality at both ends of the chain. Typically one end of the chain has a functional group tailored for reaction to a chosen substrate, for example a thiol group is used for gold substrates. Upon exposure of the thiol terminated chain to a gold substrate chemisorption takes place, with a close packed alignment of the alkane chains, due to the arrangement of the sulfur on the gold.[4] The resultant surface is therefore composed of the chosen functional group at the other end of the alkane chain. The potential for surface functionalisation is obvious, and several methods exist for the lithographic patterning of SAM's.

Lithographic patterning with SAM's is most widely associated with microcontact printing techniques. However, clever application of photolithography has also been used to selectively alter the functionality presented at the surface.[13] Microcontact printing of alkanethiols involves the inking of an elastomeric polydimethylsiloxane (PDMS) stamp with the alkanethiol followed by contact with a gold substrate. This results in SAM formation only in the regions of contact, by the topographically patterned stamp. This technology has been used to pattern large areas of substrate (50 cm^2)[14] with features of less than 100nm in width.[15] After application of a patterned SAM, the remaining unfunctionalised substrate can be functionalised by flooding of the surface using a second SAM of differing functionality.[16] SAM's have been used as masks for wet etching processes[17] and also as templates for selective depositions.[16,18,19,20,21,22]

Another class of self assembling systems are block copolymers. These can exhibit phase segregation of the two composite polymer blocks, into regions rich in only one polymer component. The immiscibility of the components in combination with the constraints imposed by the covalent connection between blocks can produce a range of microphase separated morphologies including spheres, cylinders and lamella structures.[23,24] In some instances control may be exercised over these morphologies by variations in film thickness.[25] Block copolymer films have been used as masks to successfully fabricate 20 nm pillars and pits in silicon nitride, by first selectively etching one polymer component and then exploiting the resultant height differences to etch into the silicon nitride.[26] Exploitation of the chemical differences of the polymer blocks has also facilitated production of arrays of gold particles on the nanoscale.[27]

Self assembled systems provide some advantage over alternative methods of fabrication. Firstly as the structures formed during assembly are normally at or near to equilibrium, defects are generally precluded. [28] Also the propensity of some systems to aggregate is not limited to two dimensions, thus the possibility exists for self assembly of three dimensional structures with relative ease.[29,30]

1.2.4 Patterning Using Scanning Probes

The capacity of scanning probes to modify surfaces at the atomic level[31] suggests great potential for lithographic patterning of surfaces. Numerous applications to lithography have been presented in this fast evolving field, and many of these are summarised in table 1.1

Mode	Action
AFM	Scratching structures into soft materials.[32,33]
AFM	Exposing thin films of resist.[34,35]
AFM	Oxidising Si-H terminated silicon.[36]
AFM	Writing alkane thiols onto gold.[37]
AFM	Electrical charge deposition on polymers.[38]
STM*	Oxidising Si-H terminated silicon.[39,40]
STM	Inducing phase transitions in solid materials.[41]
STM	Manipulating atoms and molecules.[31,42]
NSOM**	Exposing photoresist films.[43,44,45]

* Scanning tunneling microscope
** Near field scanning optical microscope

Table 1.1 Summary of the application of scanning probes to lithography

Although scanning probe lithographies offer exceptional resolution they are blighted by the time taken to pattern a surface. Development of tips with built in actuators multi tip arrays[46] may improve the rate of patterning, but much ingenuity will be required to facilitate the throughput required.

1.3 Plasma Modification of Polymer Surfaces

1.3.1 Introduction

A Plasma is a partially or fully ionised gas, containing electrons, positive and negative ions, neutrals, metastables and electromagnetic radiation.[47,48] These reactive species are all capable of participating in and undergoing reactions.[49] Plasmas are classified as having equal numbers of positive and negative species present; although local perturbations may occur in the charge, overall neutrality is maintained.

1.3.2 Types of Plasma

There are three types of plasma, which are categorised according to the method of ignition and the physical properties they possess. Plasmas in complete thermodynamic equilibrium exits when all the constituent species have the same temperature (such states occur in stars). Local thermodynamic plasmas exist where the temperature of all species, with the exception of radiation, is equal. These plasmas are very dense and are considered 'hot'. Due to their high temperature, they can find application where thermal reactions are needed, such as in metallurgy.[48] The third type of plasma is a non-equilibrium plasma where the temperature of the electrons greatly exceeds that of the gas (10,000 K and 300 - 500 K respectively). This type of plasma is termed a glow discharge and is considered a 'cold' plasma. Glow discharges are commonly used to modify surfaces through etching,[50] polymerisation,[51] and functionalisation by means of chemical reaction of species in the plasma.[52]

1.3.3 Plasma Theory

A glow discharge is achieved in this work by the passage of a radio frequency (R.F.) oscillating electric field around a low pressure gas or vapour. Ignition of the plasma requires energy greater than the ionisation energy of the gas molecules to be applied to the system. This applied energy accelerates randomly occurring free electrons.[53] Inelastic collision of these electrons leads to ionisation and the production of secondary electrons.[48] Once the plasma is ignited, the glow may be sustained by a lower applied power, as the initial ionisation produces many reactive species, which in turn cause further excitations and ionisation via a cascade effect.

To maintain plasma stability a quasi-neutral state is required. This in turn requires the discharge volume to be greater than the Debye length, λ_D, the distance over which a small potential can perturb the plasma,[49] Equation 1.1.

Equation 1.1

$$\lambda_D = \left(\frac{\varepsilon_o k T_e}{n_e e^2} \right)^{1/2}$$

where ε_o is the permittivity of free space, k is Boltzman's constant, T_e is the electron temperature, n_e is the electron density per cm^3 in the plasma and e is the charge of an electron. For our 'cold' plasmas T_e and n_e are typically 1 eV and 10^{10} respectively; this gives a Debye length of 74 μm. Localised charge perturbations within the plasma are confined to λ_D. These electric fields are minimised in the plasma by a redistribution of the charged components. The electrons are fastest to move due to their considerably lower mass than that of ions. This results in Debye shielding, leading in turn to the quasi-neutrality of the system. A consequence of this is the production of a plasma potential, due to the rapid acceleration of the electrons to the reactor walls, thus leaving a net positive charge in the plasma. This results in a potential difference between the reactor walls and the plasma bulk.[49,54]

As ionisation reactions in plasmas are essential for the maintenance of the discharge, it is important to understand the energies of these electrons. In thermal plasmas, where the temperature of the electrons is equal to that of the gas (T_e = T_g), the distribution of electron energies fit to a maxwellian distribution.[49] In non-equilibrium 'cold' plasmas the energy fits to a Druyvesteyan distribution,[49] which is more fitting to the electron temperature being far greater than that of the gas. For both distributions a high energy tail is

evident. These high energy electrons play an important role in the chemistry and physical conditions in the plasma.

The individual components of the plasma treat polymer films to different depths. UV and VUV components will penetrate deep into the polymer altering the bulk as well as the surface. Impact of neutrals, ions and electrons will only affect the surface of the polymer undergoing treatment.[55]

Plasma treatment offers numerous advantages over conventional methods of treatment:

- Economical treatments only need small quantities of gas or vapour, as carried out at low pressure.
- Objects of any shape may be treated, as the treatment medium is gaseous.
- The bulk properties are generally un-affected unless severe treatments are used.
- Reactions are enclosed and waste products are trapped in a cold finger, making the process clean and safe.
- Judicious choice of plasma parameters can yield a wide variety of well adhered, pin hole free, polymer films of tailored functionality on most substrates.

The only disadvantage of plasma treatments is the complexity of the reactions occurring within the plasma.

1.4 Surface Analysis Techniques

1.4.1 X-ray Photoelectron Spectroscopy (XPS)

1.4.1.1 Introduction

X-ray photoelectron spectra are generated by photo-ejection of core level electrons, using soft X-rays.[56] Photoelectrons emitted in the uppermost 1-5 nm[57] of the sample escape from the surface and pass through an electron analyser prior to detection. A spectrum of electron intensity as a function of kinetic energy (K.E.) is produced. According to the conservation of energy the kinetic energy is dependant upon the binding energy of the electrons (B.E.) as shown in equation 1.2:

Equation 1.2 $$KE = hv - BE - \phi$$

Where hv is the energy of the incident photon and ϕ is the work function of the spectrometer.

1.4.1.2 Requirements

The passage of ejected photoelectrons from the sample to the analyser requires ultra-high vacuum so as to prevent collision with gaseous molecules.[58] The X-ray source must produce a line width sufficiently narrow so as to allow resolution of photoelectron peaks, and a characteristic energy high enough to eject a wide range of core level electrons. In this work all studies were performed using a Mg Kα (hv=1253.5 eV; line width = 0.7 eV) source, satisfying these requirements.

1.4.1.3 Theory

As each element's core level electrons have a characteristic binding energy, (although H and He cannot be photoionised by usual X-ray sources), the spectrum provides elemental analysis. With the aid of suitable reference samples, the spectra may be interpreted quantitatively to give elemental abundances. Small changes in binding energy are also evident for changes in the chemical environment. For example attachment of electron withdrawing groups such as fluorine causes an increase in the binding energy of the core level electrons due to reduced nuclear screening, consequently the kinetic energy of photoelectrons is reduced.[59]

The surface sensitivity of XPS is a result of the inelastic mean free path length, λ, of the photoelectrons. Only electrons within the statistical distance λ from the surface will be detected in the spectra, as those electrons emitted deeper in the sample are more likely to have undergone an inelastic collision, thus losing their energy. The inelastic path length is dependant upon the energy of the photoelectron, and thus variation is seen according to element. A further factor on the depth of analysis is the angle at which electrons are detected from the surface. The greatest depth of analysis being for detection normal to the surface, here around 95% of electrons are emitted from a depth of 3λ (the escape depth). If we reduce the angle with respect to the surface normal (the take-off angle θ), the escape depth is now a function of $3\lambda\sin\theta$.[58]

1.4.2 Scanning Probe Microscopy

1.4.2.1 Introduction

Since the advent of contact mode atomic force microscopy (AFM) in 1986,[60] many advances, broadening the range of application, have come about. Scanning probe microscopes can now be used to measure surface mechanical properties,[61] map magnetic and electrical fields,[62] gain localised thermal information,[63] and attain electromagnetic information about surfaces without wavelength limitations.[63] Here we focus on tapping mode AFM (TMAFM), where intermittent contact is used.

1.4.2.2 Basic Principles

The atomic force microscope comprises a very sharp silicon probe tip (typical radius of curvature = 13 nm),[64] mounted at the end of an ultra-light cantilever. This is then held at a fixed position above a piezoelectric scanner, capable of lateral movement (X,Y) and also vertical movement (Z).

Images are produced by rastering a sample under the tip, using the lateral motion of the piezoelectric transducer. Rastering is controlled by the application of slowly ramped voltage to one of the lateral axes (slow scan axis), and a rapidly alternating voltage to the other lateral axis (fast scan axis). The fast scan axis travels from limit to limit 1024 times in the time the slow axis take to travel from one limit to the other. As the surface moves under the stationary tip, surface properties can be measured. For example in contact mode AFM, the deflection in the cantilever caused by interactions between the tip and surface is monitored through a laser beam reflected from the back of the cantilever. This, through a feedback loop, drives the Z motion of the piezoelectric transducer, so as to maintain a constant tip sample interaction force.

The extremely high resolutions achieved by atomic force microscopy arises from the use of very sharp tips on ultra-light cantilevers in combination with a very sensitive optical detection method, allowing high topographical sensitivity and measurement of very low deflection forces (10^{-9} N).[65] High precision, calibrated piezoelectrics are also necessary to facilitate the excellent XY resolution.

1.4.2.3 Tapping Mode Atomic Force Microscopy

The drawback of using contact mode AFM to image soft surfaces such as polymers is the damage to the surface and the tip due to the dragging motion of the tip across the surface.[66] By using tapping mode these lateral forces are reduced due to the intermittent contact of the tip with the surface. This entails oscillating the cantilever and tip arrangement at its resonant frequency (70 KHz – 350 KHz depending on probe type).[67] Thus only during part of the oscillation is the tip in contact with the surface. The force with which the tip 'taps' the surface is controlled by the set point,[68] this is the ratio of the free amplitude of the oscillating cantilever to the amplitude during tapping. Low set point values signify hard tapping whilst high values signify softer tip-sample interactions. These parameters can lead to the generation of height artifacts in softer samples.[69] The degree of interaction between the tip and sample during tapping mode imaging is monitored using a laser bounced from the back of the cantilever onto a split photodiode array. During interaction with the surface the tip loses energy and the resonance peak shifts to a higher frequency,[68] thus the amplitude of the peak at the monitored resonance will change. A feedback loop is used to alter the Z piezoelectric position so as to maintain a constant tip-

sample interaction while scanning, and these adjustments are used to form the height image.

In addition to monitoring the amplitude of the resonance peak, we can also monitor the shift in phase from the drive frequency. This can provide important information when mapping heterogeneous systems.[69] Interpretation of phase images can be difficult however, and shifts have been attributed to: elasticity,[68] hydrophobicity,[70,71] adhesion,[72] and energy dissipation.[69]

1.4.3 Contact Angle Measurement

1.4.3.1 Introduction

Contact angle analysis is an extremely surface sensitive technique, analysing the upper-most 5-10 angstroms.[73] Analysis is performed, by dispensing a known quantity of a chosen probe liquid from a syringe, to form a droplet. This is then placed on the surface. A CCD camera displays the droplet in real time on an interfaced PC. A snap-shot of the image is then captured and through placement of markers around the droplet perimeter, the computer can calculate the tangent to the droplet shape and correspondingly the contact angle.

1.4.3.2 Theory

Liquids are commonly referred to as having a surface tension. This is the force which minimises the surface area of liquid drops, causing them to form the shape with lowest surface area to volume ratio (a sphere). In order to perturb the spherical nature of the liquid droplet, the surface area is increased, necessitating work to be done against the surface tension. This work is termed the surface energy in the case of solid surfaces. Surface energy and tension are represented by the symbol γ and given appropriate subscripts to denote the

interface represented. When a drop of probe liquid is placed onto a polymer surface, the spreading of the drop is a result of the surface energy outweighing the surface tension of the liquid. This energy is calculated as the difference between the surface energy of the solid / vapour and the solid / liquid interfaces γ_{SV} and γ_{SL} respectively.[74]

The surface energy may be evaluated from the contact angle, θ, formed by the drop of probe liquid at the three phase boundary, Figure 1.1.

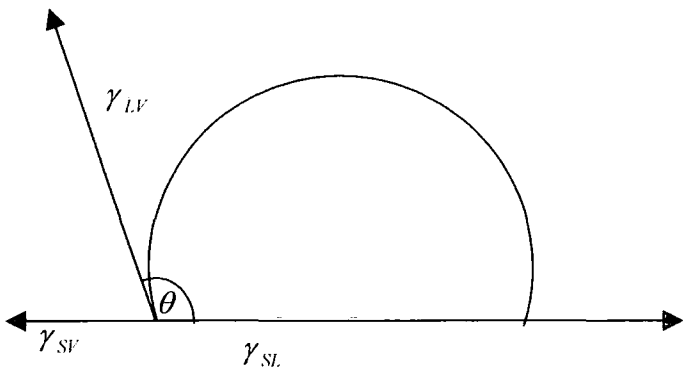

Figure 1.1 Contact angle formed by probe liquid droplet on surface.

In order to calculate the surface energy it is necessary to relate this to the contact angle measured. This is evaluated by considering the wetting phenomenon of a liquid drop placed on the surface,[75] Figure 1.2.

γ_{LV}

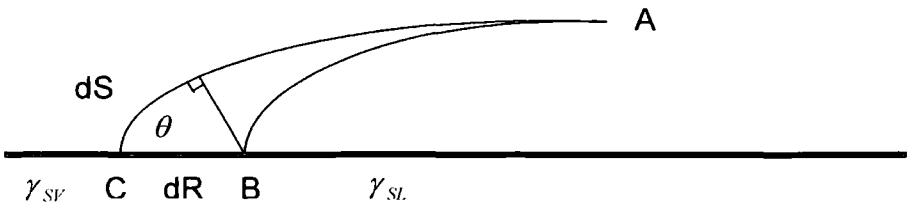

Figure 1.2 Schematic diagram of the probe liquid drop spreading to equilibrium on the surface.

Here we consider the spreading of the drop across the surface from an initial periphery **A-B** to the equilibrium position **A-C**. The change in Gibbs' free energy at constant volume can be related to the change in area, Equations 1.3 to 1.8.

Equation 1.3 $$dG = 2\pi RdR\gamma_{SV} - 2\pi RdR\gamma_{SL} - 2\pi RdS\gamma_{LV}$$

and from trigonometry

Equation 1.4 $$dS = dR\cos\theta$$

so

Equation 1.5 $$dG = 2\pi RdR\gamma_{SV} - 2\pi RdR\gamma_{SL} - 2\pi RdR\cos\theta\gamma_{LV}$$

simplifies to

Equation 1.6 $$dG = 2\pi RdR(\gamma_{SV} - \gamma_{SL} - \gamma_{LV}\cos\theta)$$

At equilibrium dG=0 therefore:

Equation 1.7 $$0 = \gamma_{SV} - \gamma_{SL} - \gamma_{LV}\cos\theta$$

so

Equation 1.8 $$\gamma_{SV} = \gamma_{SL} + \gamma_{LV}\cos\theta$$

Equation 1.8 is known as the Young's equation[76] and relates the contact angel to the individual surface energy components.

The surface energy may be calculated by measurement of contact angle using probe liquids of differing polar and dispersive surface energies. In this work the geometric mean method was used for such calculation.[77] The method derives from the Young's equation and that the surface energy may be split into two separate components (Polar, γ^p, and Dispersive, γ^d). Owens and Wendt proposed that a geometrical averaging existed between the solid and liquid surface energies at the vapour interface, Equation 1.9. In combination with the Young's equation this leads to the geometric mean equation, Equation 1.10

Equation 1.9

$$\gamma_{SL} = \gamma_{Sv} + \gamma_{Lv} - 2(\gamma_{Sv}^d \gamma_{Lv}^d)^{1/2} - 2(\gamma_{Sv}^p \gamma_{Lv}^p)^{1/2}$$

Equation 1.10

$$\gamma_{Lv}(1+\cos\theta) = 2(\gamma_{Sv}^d \gamma_{Lv}^d)^{1/2} + 2(\gamma_{Sv}^p \gamma_{Lv}^p)^{1/2}$$

By measurement of contact angles for the two fully characterised probe liquids equation 1.10 can be solved to give the dispersive and polar components of the surface energy.

1.4.3.3 Contact Angle Hysteresis

Contact angle hysteresis is the difference between the contact angle measured for a probe liquid advancing across a sample from the angle measured for the same probe liquid receding across the same sample. There are two types of hysteresis. Firstly kinetic hysteresis, which arises through modification of the sample by the probe liquid, i.e. swelling, washing, or surface group re-orientation.[78] Secondly thermodynamic hysteresis, which is a factor of surface roughness or surface heterogeneity.[78]

1.4.4 Infrared Spectroscopy

Infrared (IR) spectroscopy allows us to probe changes occurring in the bulk of the polymer films. IR radiation comprises the electromagnetic radiation between 400 and 4000cm^{-1}. Functional groups present in the polymers give rise to characteristic bands in the IR spectrum. When a functional group absorbs electromagnetic radiation of a characteristic wavelength, λ, an accompanying energy increase occurs, according to Equation 1.11:

Equation 1.11 $$\Delta E = \frac{hc}{\lambda}$$

Where h is Planck's constant and c is the speed of light. The energy increase may take the form of either excitation of vibrational or rotational energy levels in the molecule. A change in the dipole moment is necessary for the absorption to be allowed. Absorbance may be calculated using the Beer-Lambert equation, Equation 1.12.

Equation 1.12 $$A = \varepsilon c l$$

Where ε is the permittivity of free space, *c* is the concentration and *l* is the path length. The absorbance spectrum is simply a plot of absorbance as a function of wavelength.

1.4.5 Raman Microscopy

Raman microscopy allows us to spatially probe chemical changes on the surface of materials. Surface sensitivity is limited to a depth of 1 micron by the use of a confocal lens, and the lateral resolution of 1 micron is obtained by

focusing the beam and collecting the signal through microscope optics. A laser of characteristic wavelength is focussed on the surface of the sample and the corresponding scattered light is monitored. The wavelength of the scattered light is dependant upon energy gain or loss of the molecule according to changes in its polarizability, and can be used for molecular identification. Reflected incident light is not permitted to the detector by use of a notch filter. Mapping of a particular band of a spectrum can be performed by the Raman microscope, by stepping across the surface in a predetermined array, acquiring a spectra at each position. A map is then produced according to the intensity of the chosen frequency range in each of the spectra, with pixel brightness reflecting the intensity of the chosen spectral band.

1.4.6 Film Thickness Measurement

Film thickness measurements were evaluated using a reflectometer. The process entails monitoring light reflected and transmitted from and through the sample, as a function of irradiation wavelength. An interfaced computer is then used to mathematically model the curves produced according to a Cauchy material model,[79] for dielectric materials using a modified Levenberg Marqardt method.[80]

1.4.7 Film Hardness Measurement

Material hardness is unusual in that it is not an intrinsic property of a material. Rather, it is a result of a defined measurement procedure. Measurements are taken from indentations made in the sample using an indenter of defined geometry under a specified force for a specified time. The indentation left after removal of the indenter, provides the hardness value. Several methods exist for

such measurement including Brinnel, Rockwell and Vickers. Each method is divided into a range of scales defined by the force used and the geometry of the indenter. Thin polymer films would typically be analysed using a Vickers indentation method, here a square based pyramid with an angle of 136° between opposite faces is pushed into the surface using a prescribed force for a defined time. After removal of the indenter the diagonal lengths of the indentation are measured. The Vickers hardness value is then defined as the test force divided by the sloping area of the indentation.[81] Alternatively a Berkovitch indenter may be used, this is similar to the Vickers indenter but is based around a triangular based pyramidal geometry.

In the case of very thin films it is possible that the substrate may have effect on the indentation forces measured, and in this instance a mathematical model is used to remove substrate interplay.[82]

1.5 References

1 Chou, S.Y., Wei, M. S., Krauss, P. R., Fischer, P. B. *J. Appl. Phys.*, 1994, 76, 6673.

2 Xie, X. S. *Acc. Chem. Res.*, **1996**, 29, 598.

3 Reichmanis, E., Houlihan, E., nalamasu, O., Neenan, T. X. *Adv. Mater. Opt. Electon.* **1994**, 4, 83.

4 Xia, Y., Whitesides, G. M. *Angew. Chem. Int. Ed.*, **1998**, 37, 550.

5 White, D. L., Bjorkholm, J. E., Bokor, J., Eichner, L., Freeman, R. R., Jewell, T. E., Mansfield, W. M., MacDowell, A. A., Szeto, L. H., Taylor, D. W., Tennant, D. M., Wasceiwicz, W. K., Windt, D. L., Wood, O. R. II *Solid State Technol.*, **1991**, 37.

6 Dunn, P. N. *Solid State Technol.*, **1994**, 49.

7 Smith, H. I. *J. Vac. Sci. Technol. B*, **1995**, 13, 2323.

8 Geppert, L. *IEEE Spectrum*, **1996**, 33, 33.

9 Broers, A. N., Molzen, W., Cuomo, J., Wittels, N. *Appl. Phys. Lett.*, **1976**, 29, 596.

10 Chou, S. Y., Krauss, P. R.,Renstrom, P. J. *Science*, **1996**, 272, 85.

11 Gibson, J. M. *Phys. Today*, **1997**, 56.

12 Sanger, W. *Principles of Nucleic Acid Strucutures*, Springer Verlag, New York, **1986**.

13 Liu, J-F., Zhang, L-G., Gu, N., ren, J-Y., Wu, Y-P., Lu, Z-H., Mao, P-S., Chen, D-Y. *Thin Solid Films*, **1998**, 327-329, 176.

14 Xia, Y., Venkateswaren, N., Qin, D., Tien, J., Whitesides, G. M. *Langmuir*, **1998**, 14, 363.

15 Biebuyck, H. A., Larsen, N. B., Delamarche, E., Michael, B. *IBM J. Res. Dev.*, **1997**, 41, 159.

16 Qin, D., Xia, Y., Xu, B., Yang, H., Zhu, C., Whitesides, G. M. *Advanced Materials*, **1999**, 11, 1433.

17 Xia, Y., Zhao, X-M., Kin, E., Whitesides, G. M. *Chem. Mater.*, **1995**, 7, 2332.

18 Jeon, N. L., Clem, P. G., Payne, A. A., Nuzzo, R. G. *Langmuir*, **1996**, 12, 5350.

19 Wang, D., Thomas, S. G., Wang, K. L., Xia, Y., Whitesides, G. M. *Appl. Phys. Lett.*, **1997**, 70, 1593.

20 Jeon, N. L., Finnie, K., Branshaw, K., Nuzzo, R. G. *Langmuir*, **1997**, 13, 3382.

21 Jeon, N. L., Nuzzo, R. G., Xia, Y., Mrksich, M., Whitesides, G. M. *Langmuir*, **1995**, 11, 3024.

22 Hidber, P. C., Helbif, W., Kim, E., Whitesides, G. M. *Langmuir*, **1996**, 12, 1375.

23 Koizumi, S., Hasegawa, H., Hashimoto, T.*Macromolecules*, **1994**, 27, 4371.

24 Chen, J. T., Thomas, E. L., Ober, C. K., Mao, G.-P.*Science*, **1996**, 273, 343.

25 van Dijk, M. A., van den Berg, R. *Macromolecules*, **1995**, 28, 6773.

26 Park, M., Harrison, C., Chaikin, P. M., Register, R. A., Adamson, D. H. *Science*, **1997**, 276, 1401.

27 Moeller, M., Spatz, J. P., Moessmer, P., Eibeck, P., Ziemann, P., Kabius, B. *Polym. Mater. Sci. Eng.*, **1999**, 80, 3.

28 Whitesides, G. M. *Sci. Am.*, **1995**, 273, 146.

29 Francois, B., Pitois, O., Francois, J. *Advanced Materials*, **1995**, 7, 1041.

30 Johnson, S. A., Ollivier, P. J., Mallouk, T. E. *Science*, **1999**, 283, 963.

31 Crommie, M. F., Lutz, C. P., Eigler, D. M. *Science*, **1993**, 262, 218.

32 Kim, Y. Lieber, C. M., *Science*, **1992**, 257, 375.

33 Sheehan, P. E., Lieber, C. M. *Nanotechnology*, **1996**, 7, 1236.

34 Sohn, L. L., Willett, R. L. *Appl. Phys. Lett.*, **1995**, 67, 1552.

35 Wilder, K.,.Quate, C. F., Addreton, D., Bernstein, R. Ellings, V. *Appl. Phys. Lett.*, **1998**, 73, 2527.

36 Snow, E. S., Campbell, P. M. *Science*, **1995**, 1639.

37 Piner, R. D., Zhu, J., Xu, F., Hong, S., Mirkin, C.A. *Science*, **1999**, 283, 661.

38 Ebbens, S. J. Ph.D. Thesis, *Chemical and Electrical Modification of Polypropylene Surfaces*, University of Durham, **2000**.

39 Lyding, J. W., Shen, T. –C., Hubacek, J. S., Tucker, J. R., Abeln, C. *Appl. Phys. Lett.*, **1994**, 64, 2010.

40 Kramer, N., Birk, H., Jorritsma, J., Schoenberger, C. *Appl. Phys. Lett.*, **1995**, 66, 1325.

41 Zhang, J., Liu, J., Huang, J. L., Kim, P., Lieber, C. M. *Science*, **1996**, 274, 757.

42 Meyer, G., Rieder, K. H. *MRS Bull.*, **1998**, 28.

43 Pohl, D. W., Novotny, L. *J. Vac. Sci. Technol. B*, **1994**, 12, 1441.

44 Krausch, G., Mlynek, J. *J. Microelectronic Eng.*, **1996**, 32, 219.

45 Betzig, E., Trautman, K. *Science*, **1992**, 257, 189.

46 Miller, S. A., Turner, S. R., MacDonald, N. C. *Rev. Sci. Instum.*, **1997**, 68, 4155.

47 Coburn, J. W. *IEEE Trans. Plas. Sci.*, **1991**, 19, 1048.

48 Von Engel, A. in *Electric Plasma: Their Nature and Uses,* Taylor and Francis, London, **1983**.

49 Grill, A. in *Cold Plasma in Materials Technology* IEEE press, Piscataway, New Jersey, **1994**.

50 Flamm, D. L., Donnelly, V. M., Ibbotson, D. E. *J. Vac. Sci. Technol., B*, **1983**, 1, 23.

51 Biederman, H, Osada, Y. *Adv. Polym. Sci.*, **1990**, 95, 57.

52 Hopkins, J., Badyal, J. P. S. *J. Phys. Chem.*, **1995**, 99, 4261.

53 Penning, F. M. in *Electrical Discharges in Gasses*, Philips Technical Library, **1957**.

54 Chapman, B. in *Glow Discharge Processes*, John Wiley and Sons, USA, **1980**

55 Clark, D. T., Dilks, A. *J. Polym. Sci., Chem. Ed.*, **1977**, 15, 2321.

56 Sherwood, P. M. A. In *Spectroscopy*, Straughan, B. P., Walker, S. Eds.; Chapman and Hall: London, 1976.

57 Seah, M. P.; Deanch, W. A., *Surf. Interface Anal.* **1979**, *1*, 2.

58 *Practical Surface Analysis*, 2nd Ed., Briggs, D., Seah, M. P. Eds.; Wiley: New York, 1990; Vol. 1.

59 Beamson, G.; Briggs, D. *High Resolution XPS of Organic Polymer. The Scienta ESCA300 Database*; Wiley: New York, 1992.

60 Binnig, G.; Quate, C. F. *Phys. Rev. Lett.* **1986**, *57*, 930.

61 Burnham, N. A.; Colton, R. J. *J. Vac. Sci. Technol. A* **1989**, *7*, 2906.

62 Saurenbach, F.; Terris, B. D. *Appl. Phys. Lett.* **1990**, *56*, 1703.

63 Pylkki, R. J.; Moyer, P. J.; West, P. E. *Jpn. J. Appl. Phys.* **1994**, *33*, 3785.

64 Ramirez-Aguilar, K. A. *Langmuir* **1998**, *14*, 2562.

65 Quate, C. F. *Surf. Sci.* **1994**, *299-300*, 980.

66 Digital Instruments Application Notes. http://www.di.com/Appnote/TapMode/tapmodeMain.html (accessed September 2000).

67 Zhong, Q.; Innis, D.; Kjoller, K. K.; Elings, V. B. *Surf. Sci. Lett.* **1993**, *290*, L688.

68 Brandsch, R.; Bar, G. *Langmuir* **1997**, *13*, 6349.

69 Bar, G.; Thomann, Y.; Brandsch, R.; Cantow, H. J.; Whangbo, M. -H *Langmuir* **1997**, *13*, 3807.

70 Refier, D.; Windeit, R.; Kumpf. R. J.; Karbach, A.; Fuchs, H. *Thin Solid Films* **1995, *264,*** 148.

71 Chen, X.; Davies, M. C.; Roberts, C. J.; Tendler, S. J. B; Williams, P. M.; Davies, J.; Dawkes, A. C.; Edwards, J. C. *Ultramicroscopy* **1998**, *75*, 171.

72 Finot, M. O.; McDermott, M. T. *J. Am. Chem. Soc.* **1997**, *119*, 8564.

73 Domingue, J. *American Laboratory*, **1990**, 22, 50.

74 Cherry, B. W. in *Polymer Surfaces*, Cambridge University, Cambridge, **1981**.

75 Cherry, B. W. in *Aspects of Surface Chemistry and Morphology in Plastics-Surface and Finish*, Eds. Pinner, S. H., Simpson, W. G., Butterworths, London, **1971**.

76 Young, T. *Philos. Trans. R. Soc.*, London, **1805**, 95, 65.

77 Owens, D. K., Wendt, R. C. *J. Appl. Polym. Sci.*, **1969**, 13, 1741.

78 Andrade, J. D., Chen, W. Y. *Surf. Int. Anal.*, **1986**, 9, 418.

79 Tabet, M. F.; McGraham, W. A. *Thin Solid Films*, **2000**, 370, 122.

80 Lovering, D. N.K.D 6000 Technical Manual Aquila Instruments, Cambridge, UK., **1999**.

81 BS EN ISO 6507-1,2&3: **1998**, Metallic materials - Vickers hardness test.

82 Korsunsky, A. M., McGurk, M. R., Bull, S. J., Page, T. F. *Surf. and Coat. Technol.*, **1998**, 99, 171.

Chapter 2

Photolithographic Patterning of Super-Hydrophobic Polymer Films: a Means to Ordered Micro-Arrays

Part A: Super-Hydrophobic Surfaces Produced by Plasma Fluorination of Polybutadiene Films

2.1.1 Introduction

Fluorinated polymer surfaces exhibit many desirable characteristics; these include repellency towards water and oils, chemical inertness, low coefficient of friction, and small dielectric constant values.[1,2] Such attributes find application in protective clothing,[3] stain-proof textiles,[4] medical implants,[5] marine coatings,[6] and microelectronics. Highly fluorinated surfaces can be generated by direct exposure to F_2 gas[7] or fluorine-containing glow discharges,[8] plasma polymerisation of fluoromonomers,[9] VUV assisted fluorination,[10] sputter deposition of fluorocarbon layers using a polytetrafluorethylene (PTFE) target,[11] and chemical derivatisation.[12] Alternatively, small amounts of fluorine containing material can be mixed into a polymer melt,[4,13,14,15] whereupon solidification leads to preferential segregation of the additive towards the air-solid interface as a consequence of its lower surface energy.[16,17,18,19]

In this article, we describe a novel two step method for producing super-repellent fluoropolymer surfaces (i.e. where liquid droplets easily roll off), which is cheap, quick, and adaptable to a variety of substrates. This entails plasma fluorination of polybutadiene thin films followed by curing (crosslinking). X-ray photoelectron spectroscopy (XPS), Tapping Mode atomic force microscopy (AFM), infrared spectroscopy, hardness measurement, and contact angle analysis have been employed to characterise the physicochemical nature of these super-repellent films.

2.1.2 Experimental

Polybutadiene (Aldrich, M_w = 420,000, 36% cis 1,4 addition, 55% trans 1,4 addition, 9% 1,2 addition) dissolved in toluene (BDH, +99.5% purity) was spin coated onto silicon wafers using a spin coater (Cammax Precima) operating at speeds between 1500 rpm - 4500 rpm. These films were subsequently annealed at 90 °C under vacuum for 1 hour (i.e. below the crosslinking temperature of polybutadiene) in order to remove entrapped solvent from the polymer film.

Plasma treatments were carried out in a cylindrical glass reactor (5 cm diameter, 470 cm^3 volume) with a base pressure of 4 x 10^{-3} mbar, and a leak rate of better than 6 x 10^{-9} mol s^{-1}. The system was connected to a two stage rotary pump via a liquid nitrogen cold trap, and the pressure was monitored with a thermocouple pressure gauge. An L-C matching unit was used to minimise the standing wave ratio (SWR) of the power transmitted from a 13.56 MHz R.F. generator to a copper coil wound around the reactor walls. The leak rate of the plasma chamber was calculated to be better than 3 x 10^{-10} Mols S^{-1}. Prior to each plasma treatment, the chamber was scrubbed with detergent, rinsed in propan-2-ol, and further cleaned using a 50 W air plasma for 30 min. A piece of polybutadiene-coated silicon wafer was then placed into the centre of the reactor, followed by pumping down to base pressure. Next, CF_4 gas (99.7% purity, Air Products) was admitted into the system via a needle valve at a pressure of 2 x 10^{-1} mbar, and the electrical discharge ignited. Upon completion of surface modification, the chamber was evacuated, followed by venting to atmosphere. These plasma fluorinated polybutadiene films were then cured (crosslinked) at different temperatures in a vacuum oven.

XPS spectra were recorded on a VG Escalab MkII spectrometer equipped with an unmonochromated Mg K_α X-ray source (1253.6 eV) and a hemispherical analyser. Photoemitted core level electrons were collected at a fixed take-off angle (75° away from the sample surface) with electron detection in constant analyser energy (CAE) mode operating at 20 eV pass energy. Instrument calibration consisted of referencing to the Au($4f_{7/2}$) peak at 83.8 eV with a full-width-at-half-maximum (fwhm) of 1.2 eV. No spectral deterioration due to X-ray radiation damage was observed during the time scale associated with data accumulation. Elemental sensitivity factors were taken as being C(1s) : F(1s) : O(1s) equals 1.00 : 0.35 : 0.45.

Infrared analysis of polybutadiene films coated onto polished KBr disks was carried out on a Perkin Elmer Spectrum One instrument operating in transmission mode at 4 cm^{-1} resolution using a DTGS detector. Spectra were acquired over 128 scans.

AFM micrographs were acquired with a Digital Instruments Nanoscope III. Damage to the tip and sample surface was minimised by using Tapping Mode AFM.[20] RMS roughness values were calculated over 50 μm x 50 μm scan areas.

Sessile drop contact angle measurements were undertaken at 20 °C using a video capture apparatus (A.S.T. Products VCA2500XE). The chosen probe liquids were high purity water (B.S. 3978 Grade 1) and a variety of linear chain alkanes (hexadecane, tetradecane, dodecane, decane, and octane, +99% purity, Aldrich). In the case of super-hydrophobic surfaces, the water droplets were kept stationary by the dispensing syringe. Advancing and receding contact angle measurements entailed increasing or decreasing the liquid drop volume at the surface.[21]

Hardness testing before and after crosslinking was performed by nanoindentation using a Nanoinstruments Nano II machine equipped with a Berkovich indenter.[21]

Film thickness measurements were taken using a reflectometer (NKD 6000). Transmission and reflection curves acquired over a 350-1000 nm range, were fitted to a Cauchy material model for dielectric materials using a modified Levenburg Marqardt method.[22]

2.1.3 Results

2.1.3.1 Polybutadiene Films

XPS analysis of the spin coated polybutadiene surface following annealing at 90 °C gave an elemental composition of 82% carbon and 18% oxygen (compared to only 1% oxygen at the polymer surface prior to annealing), Figure 2.1(a). The absence of oxygenated groups in the FTIR spectra of these films confirmed that oxidation is localised to just the outer surface during annealing at 90 °C, (i.e. limited to the XPS sampling depth of 2-5 nm), Figure 2.2 and Table 2.1. AFM indicated that the polybutadiene films were flat and featureless prior to plasma treatment, Figure 2.3. A water contact angle value of approximately 104° was measured for these films, which is typical of polyolefin surfaces,[23] Figure 2.1(b). No values were obtained for alkane probe liquids, since they dissolve the polybutadiene films.

2.1.3.2 Power and Time Dependency of CF_4 Plasma Treatment

The oxygen previously observed by XPS at the surface of the annealed polybutadiene films was quickly removed during CF_4 plasma exposure, Figure 2.1(a). A corresponding shift in the C(1s) envelope towards higher binding energies was seen due to the formation of $\underline{C}F$ (287.8 eV), $\underline{C}F_2$ (291.2 eV) and $\underline{C}F_3$ (293.3 eV) functionalities[24,25] at the expense of the $\underline{C}_xH_y$ (285.0 eV) hydrocarbon component.

No new infrared absorption bands were identified following CF_4 plasma fluorination, Figure 2.2. This is consistent with only the outermost surface succumbing to plasma fluorination.

However, CF_4 plasma treatment gave rise to two different types of topography discernible by AFM, Figure 2.3. At low powers (up to 30 W), large-scale undulating features appeared at the surface. These diminished at high power levels to be replaced by a finer scale roughness. The two different types of topography were identifiable in the corresponding AFM surface roughness measurements, Figure 2.1(c). Both types of roughness give rise to large RMS roughness values since this is a measure of deviation of height from the mean height of the surface over the complete area of the image.[26] The intermediate drop corresponds to the transition from one type of topography to the other.

Sessile drop water contact angle values exceeded 157° for electrical discharge power settings above 40 W (the actual contact angle value could in fact have been higher, but it was not possible to measure by this technique due to the water droplet rolling off the substrate), Figure 2.1(b).

Similar trends for XPS, FTIR, AFM, and contact angle measurements were observed with increasing plasma exposure times at a fixed power level, Figures 2.4 and 2.5. It is of interest to note that the large-scale roughness features are lost at short plasma exposure times, to be replaced by the finer scale roughness for longer exposures.

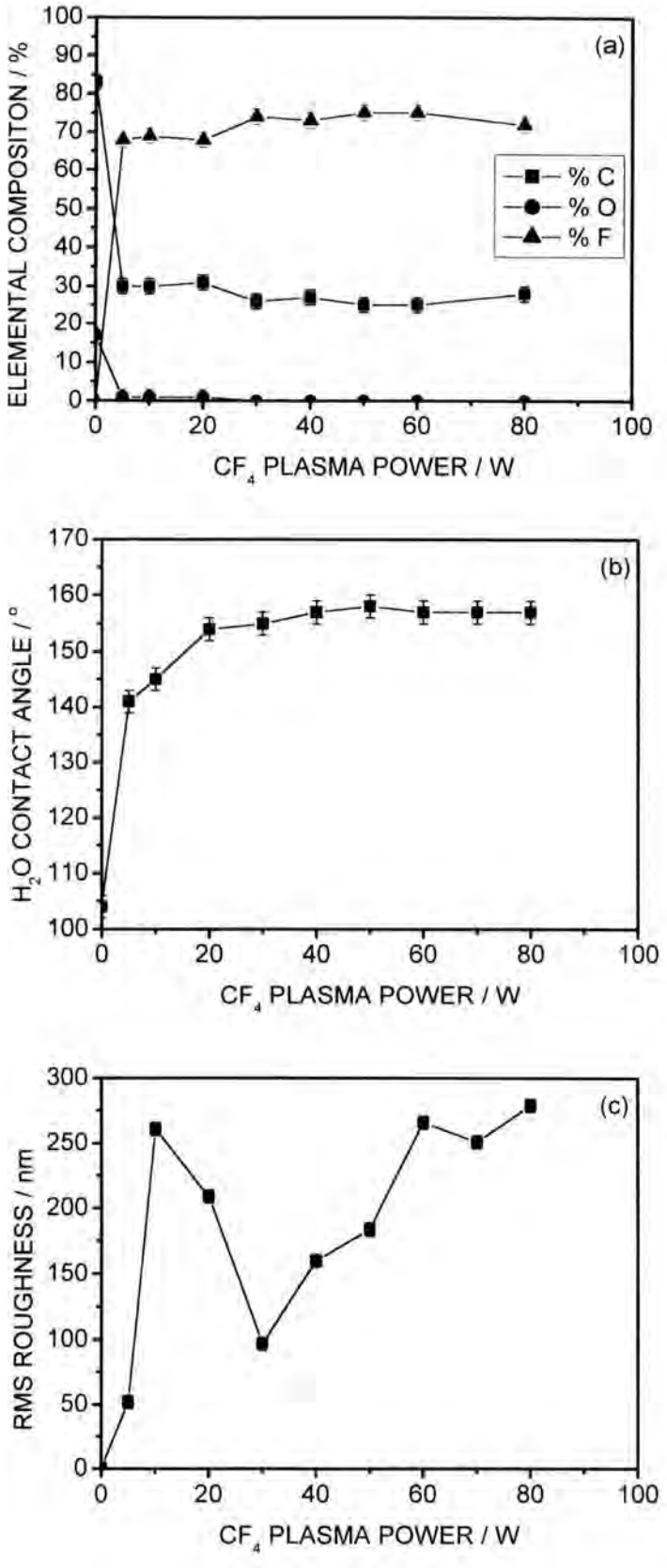

Figure 2.1 5 min CF_4 plasma modification of 4.5 μm thick polybutadiene film as a function of power: (a) XPS elemental composition; (b) H_2O contact angle; and (c) AFM RMS surface roughness.

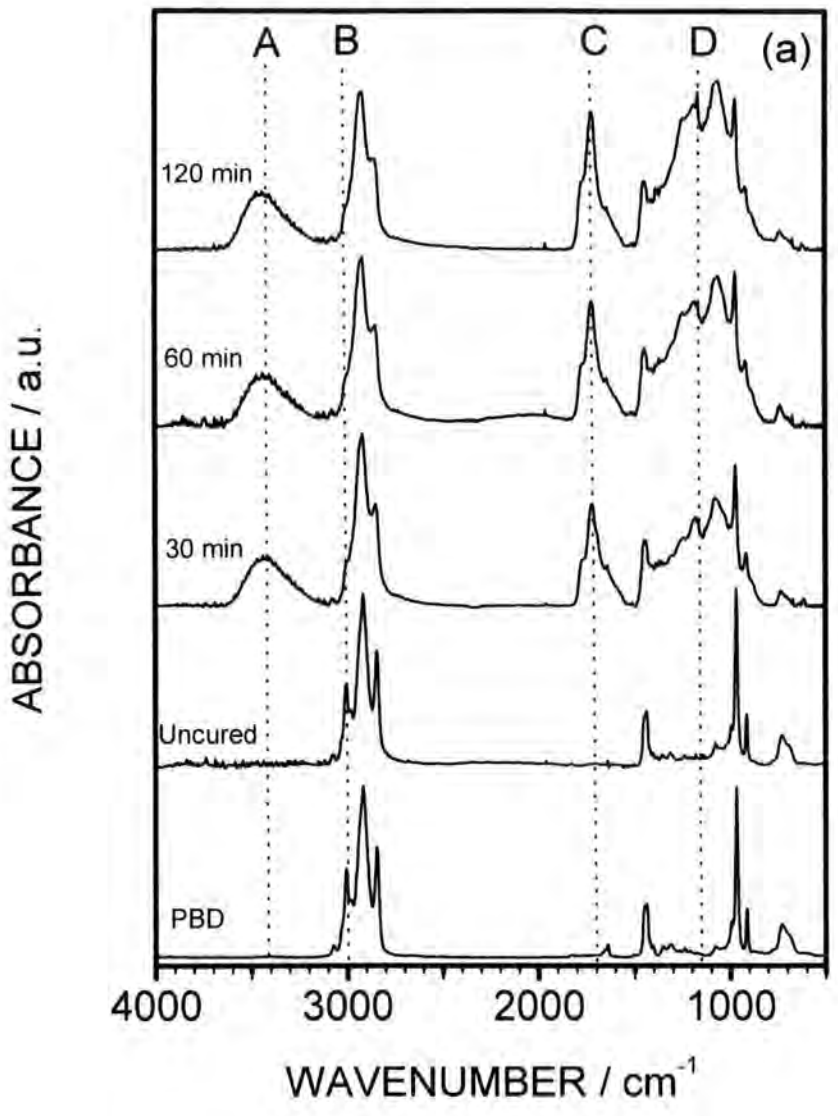

Figure 2.2 IR spectra of CF_4 plasma treated polybutadiene (60 W 5 min) as a function of: (a) curing time (annealing temperature = 155°C); and (b) curing temperature (60 min annealing time).

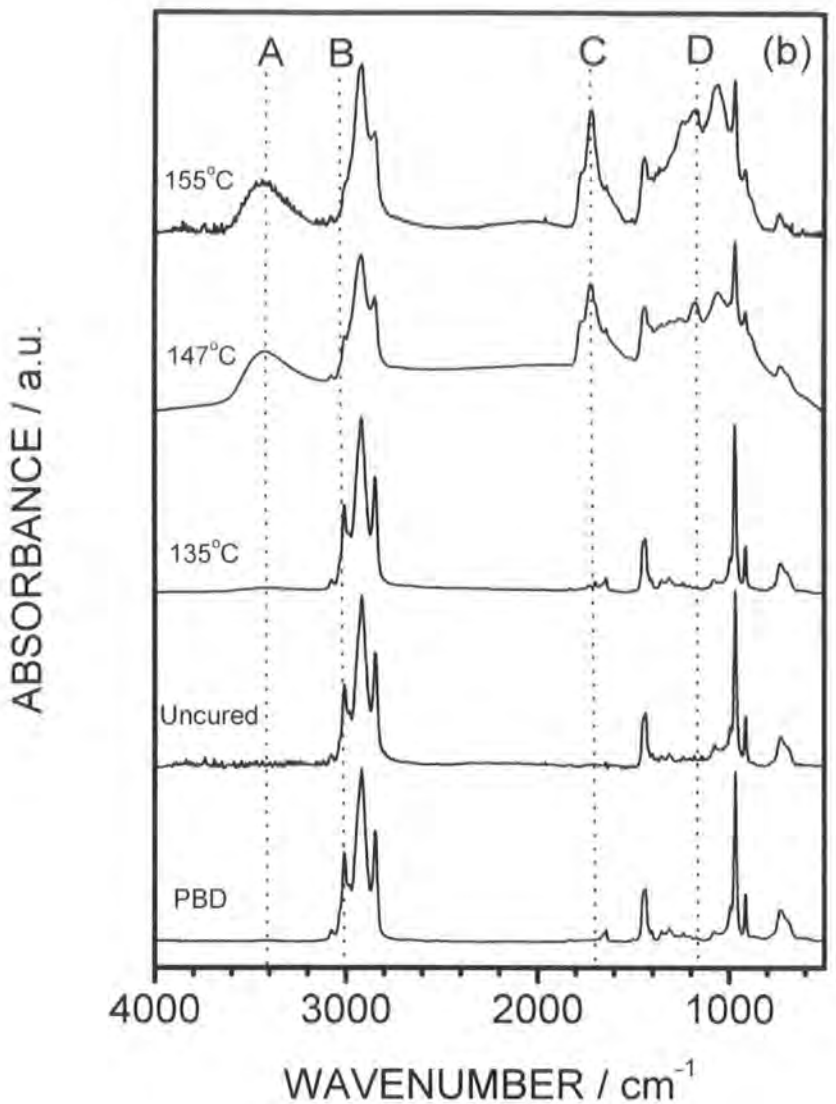
A
B
C
D
(b)
155°C
147°C
135°C
Uncured
PBD
ABSORBANCE / a.u.
4000
3000
2000
1000
WAVENUMBER / cm-1

Frequency cm-1	Intensity*	Assignment
3075	m	CH_2 asymmetric stretch in –CH=CH_2; 1,2-addition
3005	sh	CH stretch in cis-CH=CH-; 1,4-addition
2988	w, sh	CH stretch in –CH=CH_2; 1,2-addition
2975	sh	CH_2 symmetric stretch in –CH-CH_2; 1,2-addition
2917	vs	-CH_2 symmetric stretch plus –CH- stretch
2845	s	-CH_2 symmetric stretch
1652	sh	-C=C- stretch, 1,4-addition
1640	m	-C=C-stretch in –C=CH_2; 1,2 addition
1453	m	-CH_2- deformation; 1,2 addition
1438	sh	-CH_2- deformation; 1,4 addition
1419	m	-CH_2- in plane deformation; 1,2-addition
1406	vw, sh	-CH- in plane deformation in cis-CH=CH-; 1,4-addition
1325-1350	w	-CH_2- wag
1294-1320	w	-CH- in plane rock
1238	vw, br	-CH_2- twist
1080	w, br	-CH_2- in plane rock of –CH=CH_2; 1,2 addition
995	s	CH out of plane bending in –CH=CH_2, 1,2 addition
967	s	CH out of plane bending in trans –CH=CH-; 1,4-addition
911	vs	CH out of plane bending in –CH=CH_2
727	w, br	CH out of plane bending in cis –CH=CH-; 1,4-addition
681	w	unknown; 1,2-addition

* s = strong; m = medium; w = weak; v = very; sh = shoulder; br = broad.

Table 2.1 IR assignments for uncured polybutadiene

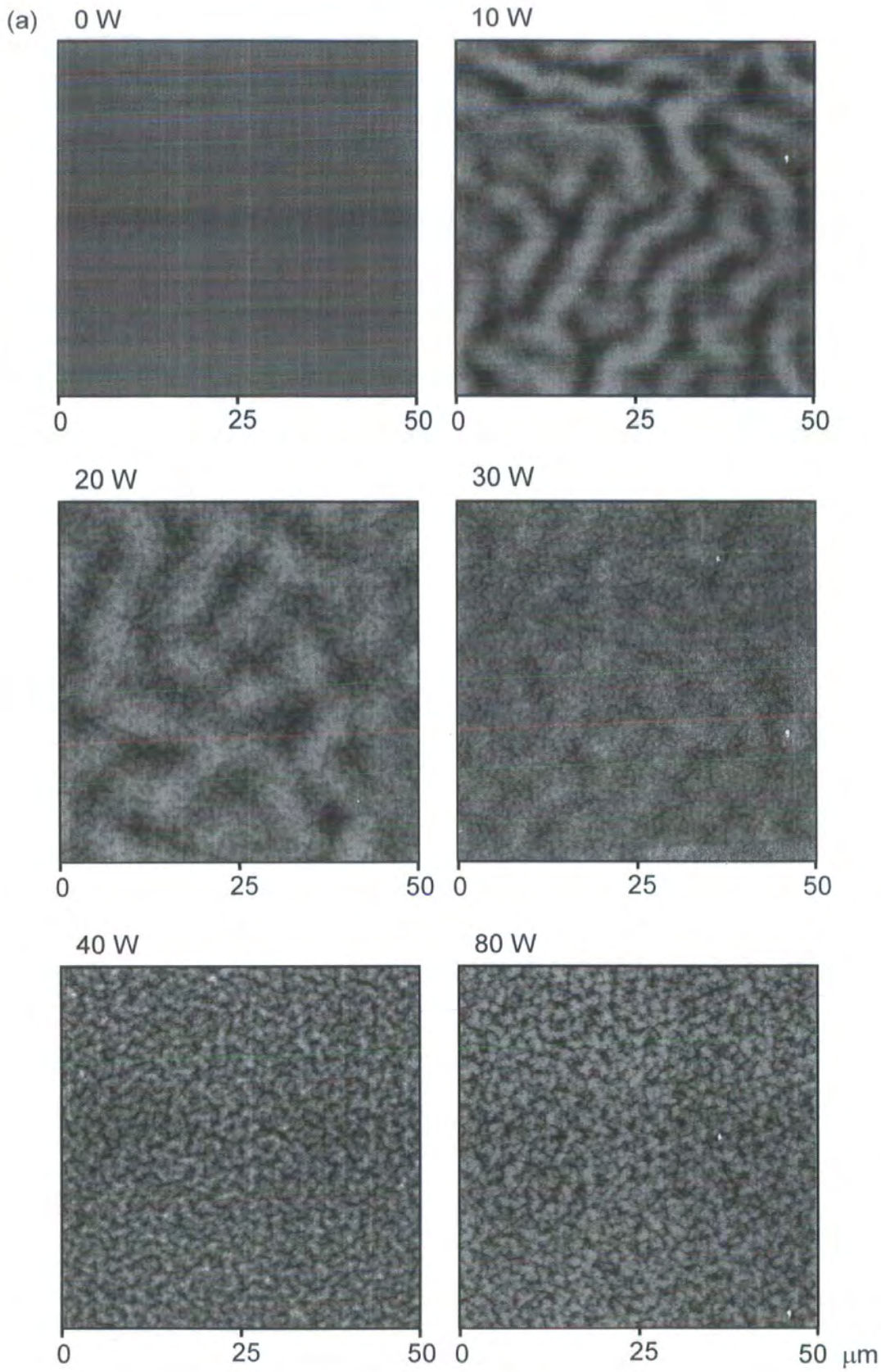

Figure 2.3 AFM height images of polybutadiene as a function of CF_4 plasma power level (time = 5 min): (a) low resolution (x=y=50μm, z = 2μm); and (b) high resolution (x=y=10μm, z = 2μm).

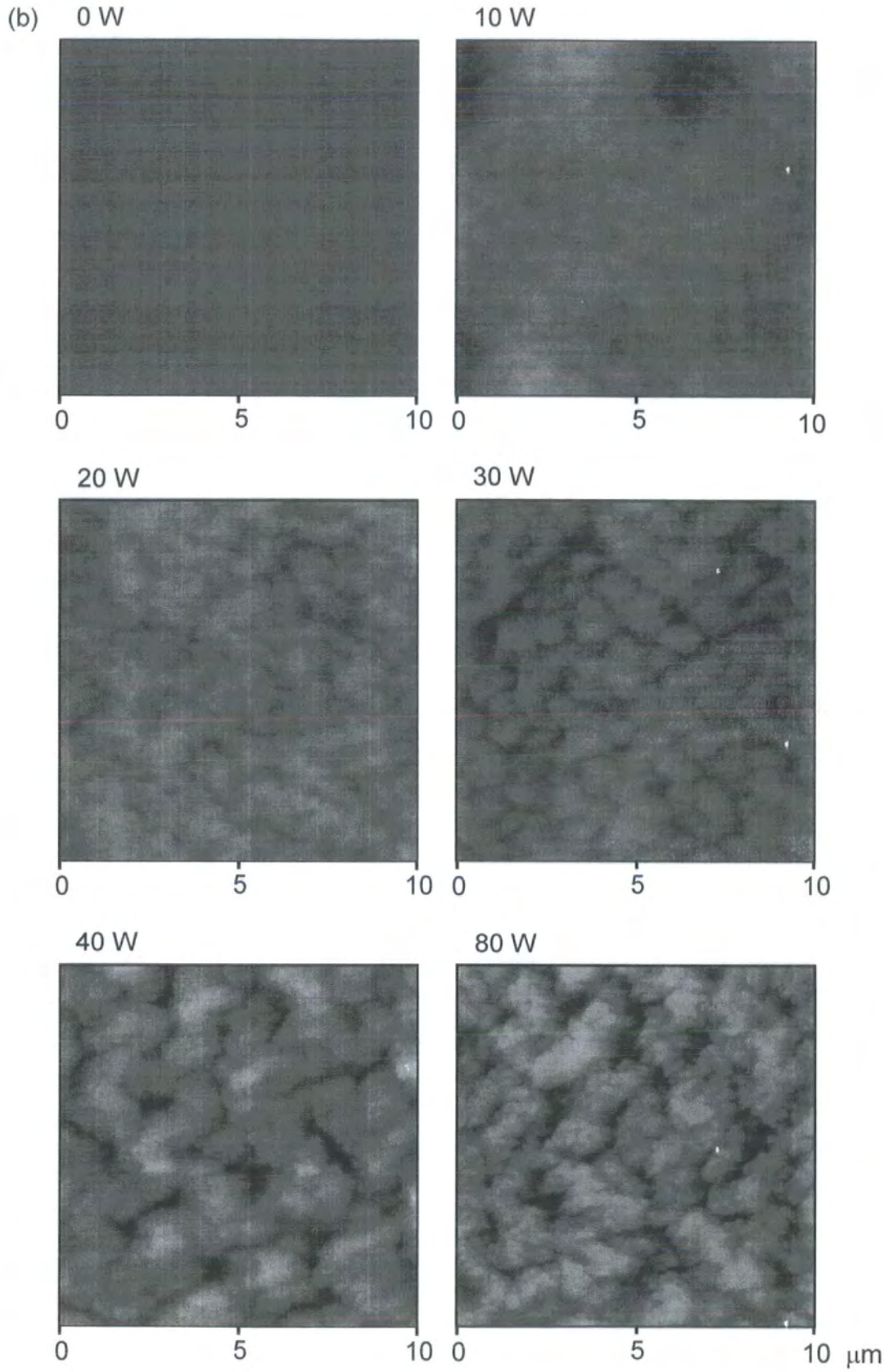
(b)
0 W
10 W
20 W
30 W
40 W
80 W
0
5
10
0
5
10
0
5
10
0
5
10
0
5
10
0
5
10
μm

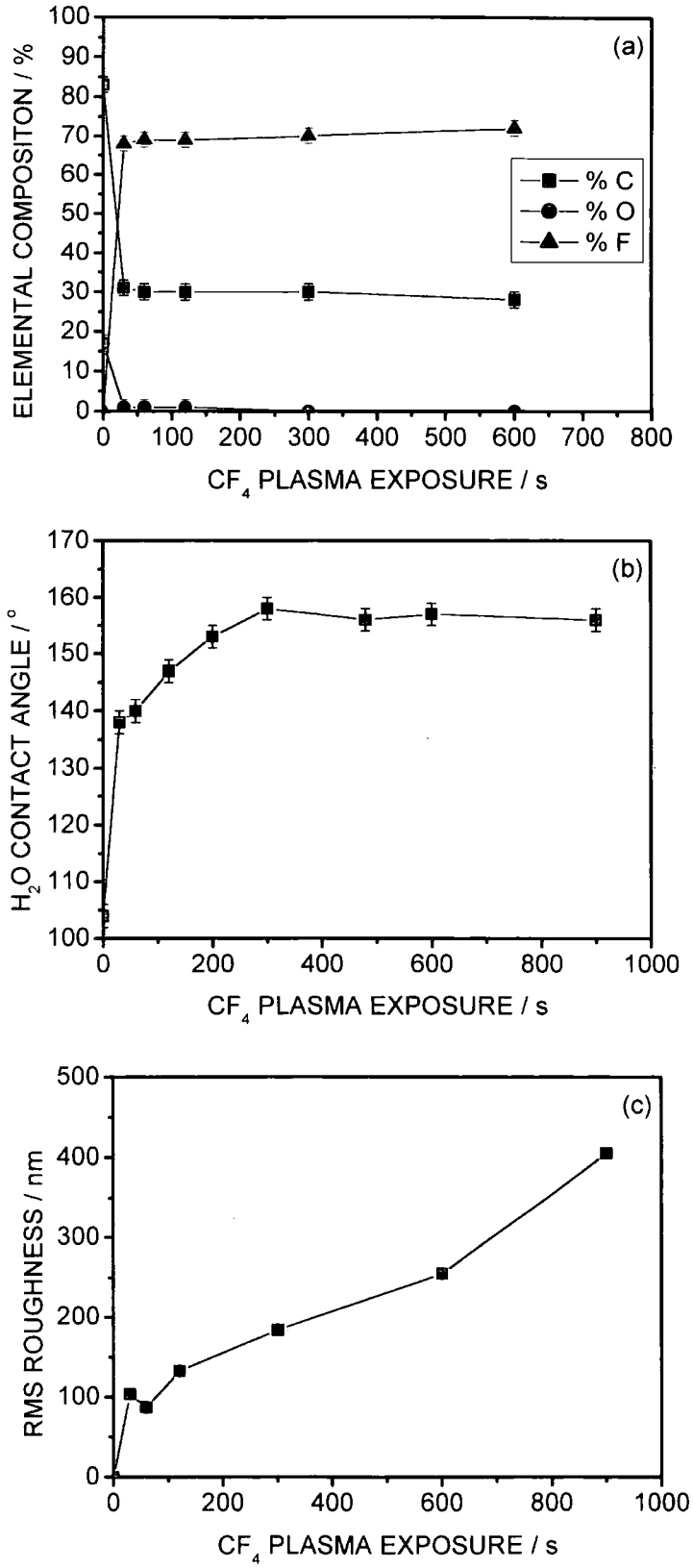

Figure 2.4 50 W CF_4 plasma modification of 4.5 μm thick polybutadiene film as a function of time: (a) XPS elemental compostion; (b) H_2O contact angle; and (c) AFM RMS roughness.

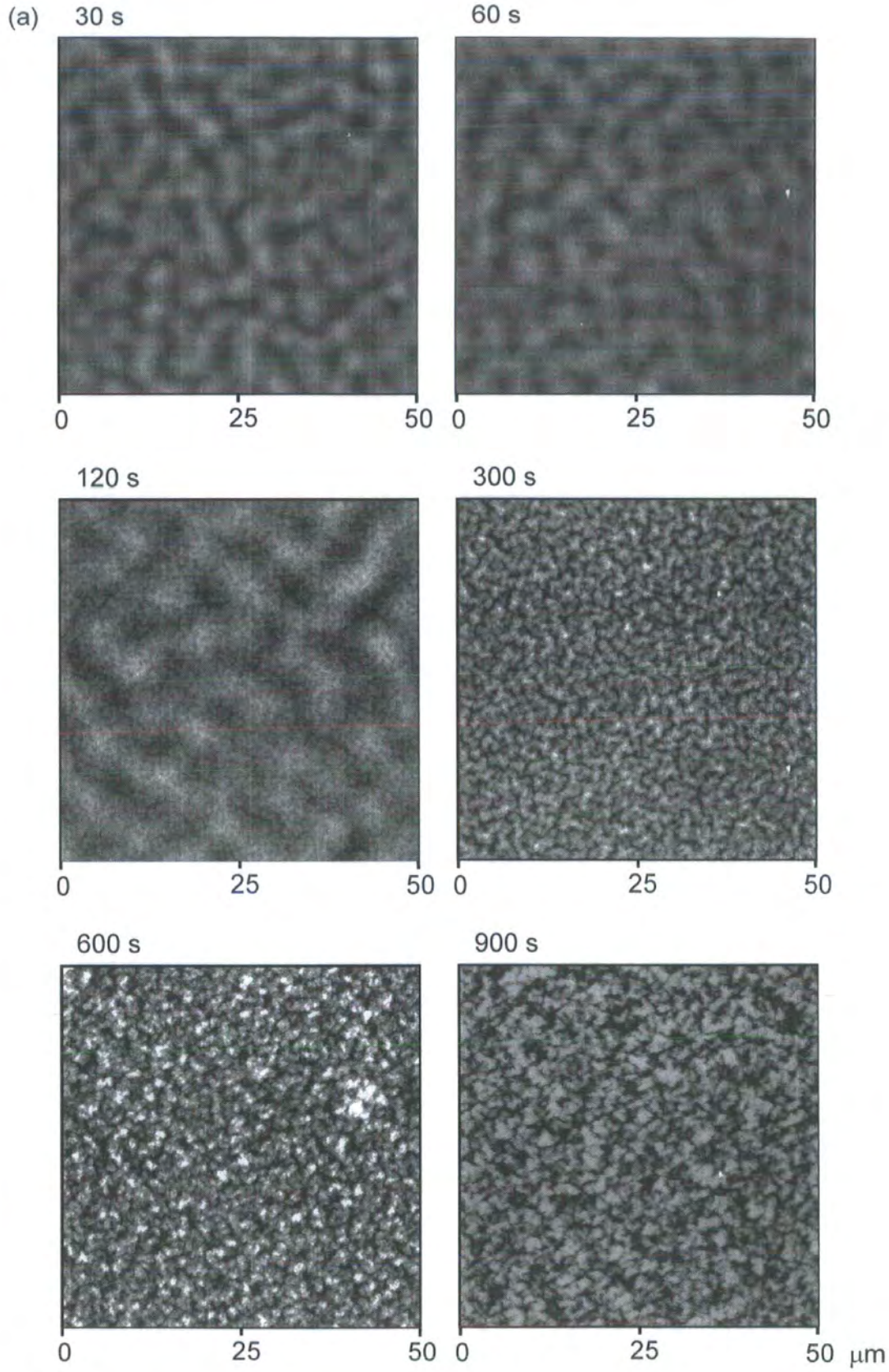

Figure 2.5 AFM height images of polybutadiene as a function of CF_4 plasma exposure time (power = 50 W): (a) low resolution (x=y=50μm, z = 2μm); and (b) high resolution(x=y=10μm, z = 2μm).

(b)

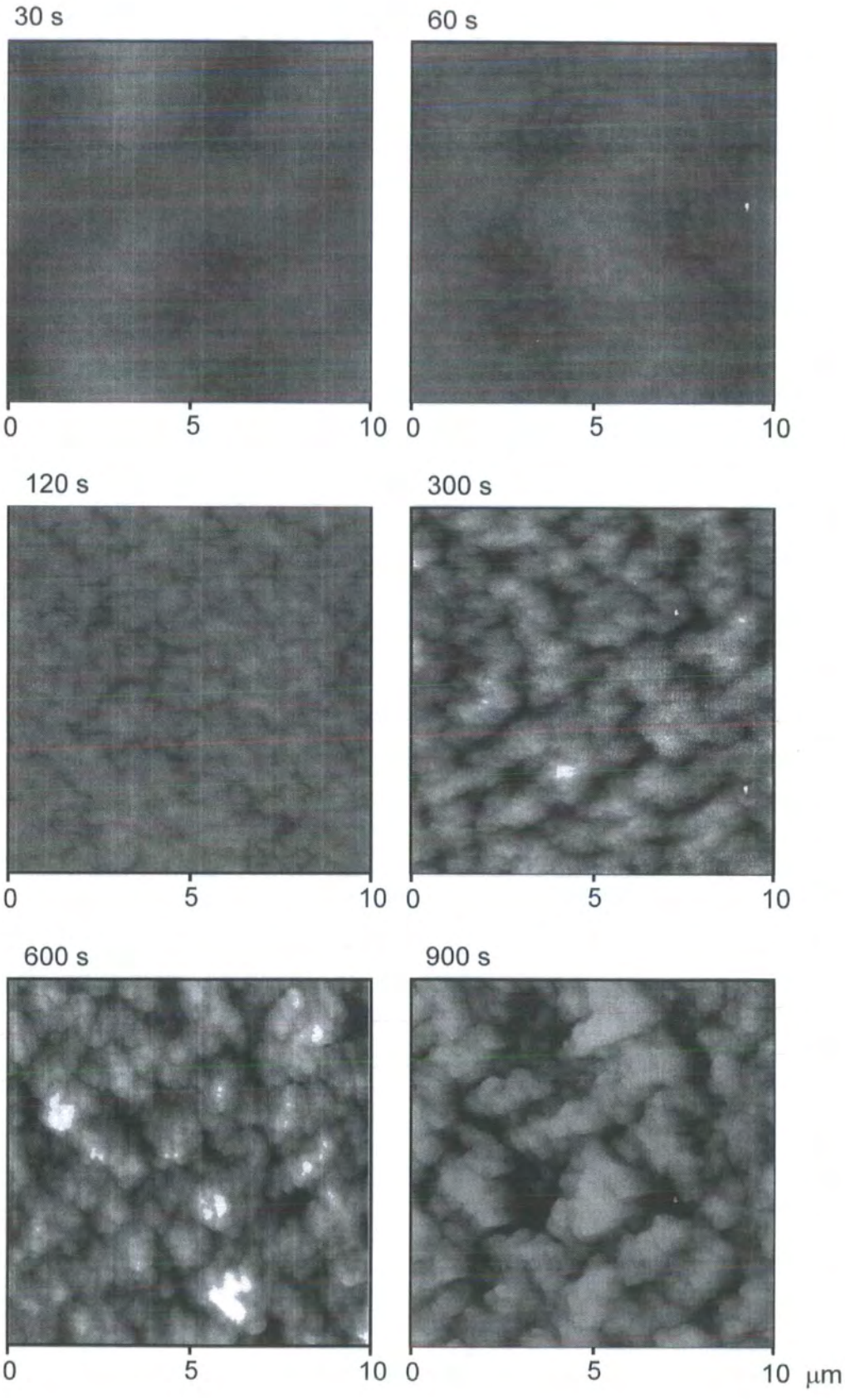

2.1.3.3 Film Thickness Dependency

CF_4 plasma treatment of a series of different thickness spin-coated polybutadiene films revealed that a critical minimum value (approximately 213 nm) was necessary in order to attain the maximum measurable water contact angle of 157°, Figure 2.6(a). Also for a fixed set of CF_4 plasma treatment conditions, the surface roughness was found to increase steadily for up to around 1 μm thick films; thicker films gave no significant further rise in roughness, Figure 2.6(b). It was found that a RMS roughness value in excess of approximately 46 ± 5 nm was required to attain super-hydrophobicity, Figure 6(c).

Advancing and receding contact angle values for liquids with different surface energies placed onto the superhydrophobic substrate are summarised in Table 2.2. Negligible hysteresis was evident for water, whereas a large hysteresis was found for all of the hydrocarbon oils. Furthermore, it is of interest to note that the receding contact angle remained virtually constant for all the alkane probe liquids.

Liquid	Surface Tension mN m^{-1} (20°C)[27]	Equilibrium	Advancing	Receding	Hysteresis
Water	72.8	174.9 ± 0.4	173.1 ± 0.4	172.7 ± 0.5	0.4 ± 0.6
Hexadecane	27.5	118.7 ± 0.8	119.1 ± 1.0	30.1 ± 1.7	89 ± 2.0
Tetradecane	26.6	109.6 ± 0.9	110.8 ± 1.2	29.8 ± 1.3	81 ± 1.8
Dodecane	25.4	98.4 ± 0.9	100.2 ± 1.1	29.5 ± 1.9	70.7 ± 2.2
Decane	23.8	89.8 ± 1.5	92.9 ± 1.1	29.7 ± 1.0	63.2 ± 1.5
Octane	21.6	65.2 ± 0.8	67.4 ± 0.9	28.5 ± 1.0	38.9 ± 1.3

Table 2.2 Contact angle measurements for CF_4 plasma treated 4.5 μm thick polybutadiene (60 W, 10 min)

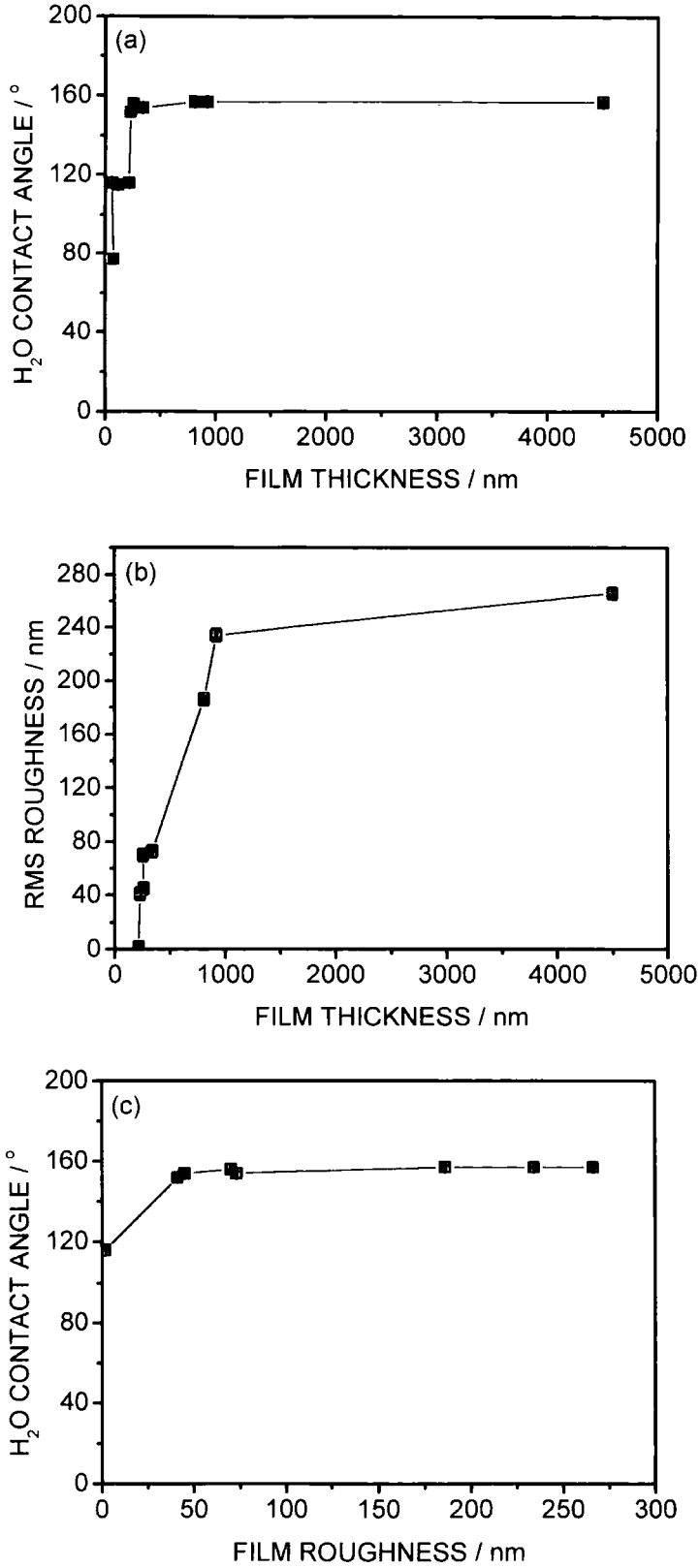

Figure 2.6 CF_4 plasma modification of polybutadiene as a function of film thickness (60 W, 5 min): (a) water contact angle; and (b) AFM RMS roughness; and (c) water contact angle versus RMS roughness.

2.1.3.4 Crosslinking of Super-Repellent Polybutadiene Films

Infrared spectroscopy confirmed that the CF_4 plasma treated films undergo oxidative cross-linking upon heating at elevated temperatures, Figure 2.2 and Table 2.3. AFM analysis of the thermally cured versus uncured films revealed that there was no significant morphological change to the surface, Figure 2.7. A small increase in oxygen content was observed by XPS after curing, which gave rise to a slight reduction in water contact angle value, Table 2.4. Interestingly, curing prior to CF_4 plasma fluorination only gave a water contact angle of 111°.

Frequency cm^{-1}		Intensity*	Assignment
3300-3600	A	m, br	-OH stretch
3005	B	sh	CH stretch in cis-CH=CH-; 1,4-addition
2988	B	w, sh	CH stretch in $-CH=CH_2$; 1,2-addition
1790	C	w, sh	cyclic ester
1730	C	m	aliphatic ester
1180	D	m	O-H bend, principally primary alcohol

* s = strong; m = medium; w = weak; v = very; sh = shoulder; br = broad.

Table 2.3 IR assignments for changes seen after curing of polybutadiene

	Uncured	Cured
Water contact angle	174.9 ± 0.4	173.8 ± 0.5
Decane contact angle	89.8 ± 1.5	76.4 ± 2
XPS % F	70 ± 2	69 ± 2
XPS % C	30 ± 2	29 ± 2
XPS % O	0 ± 0	2 ± 2
AFM roughness (RMS /nm)	193 ± 5	191 ± 5

Table 2.4 Comparison of uncured and cured (1 hour, 155 °C) CF_4 plasma treated polybutadiene (60 W, 10 min, 4.5 μm thickness)

Microindentation testing indicated an eight-fold increase in hardness of the fluorinated film after curing, Table 2.5. This corresponds to a relatively hard polymeric material.

Material	Hardness (Mpa)
Uncured fluorinated polybutadiene	8 ± 1
Cured fluorinated polybutadiene	64 ± 8
Isotactic Polystyrene[28]	129-170

Table 2.5 Microindentation measurements of hardness of cured and uncured fluorinated polybutadiene films (60 W, 10 min, 4.5 μm thickness). Curing for 48 hours at 155 C.

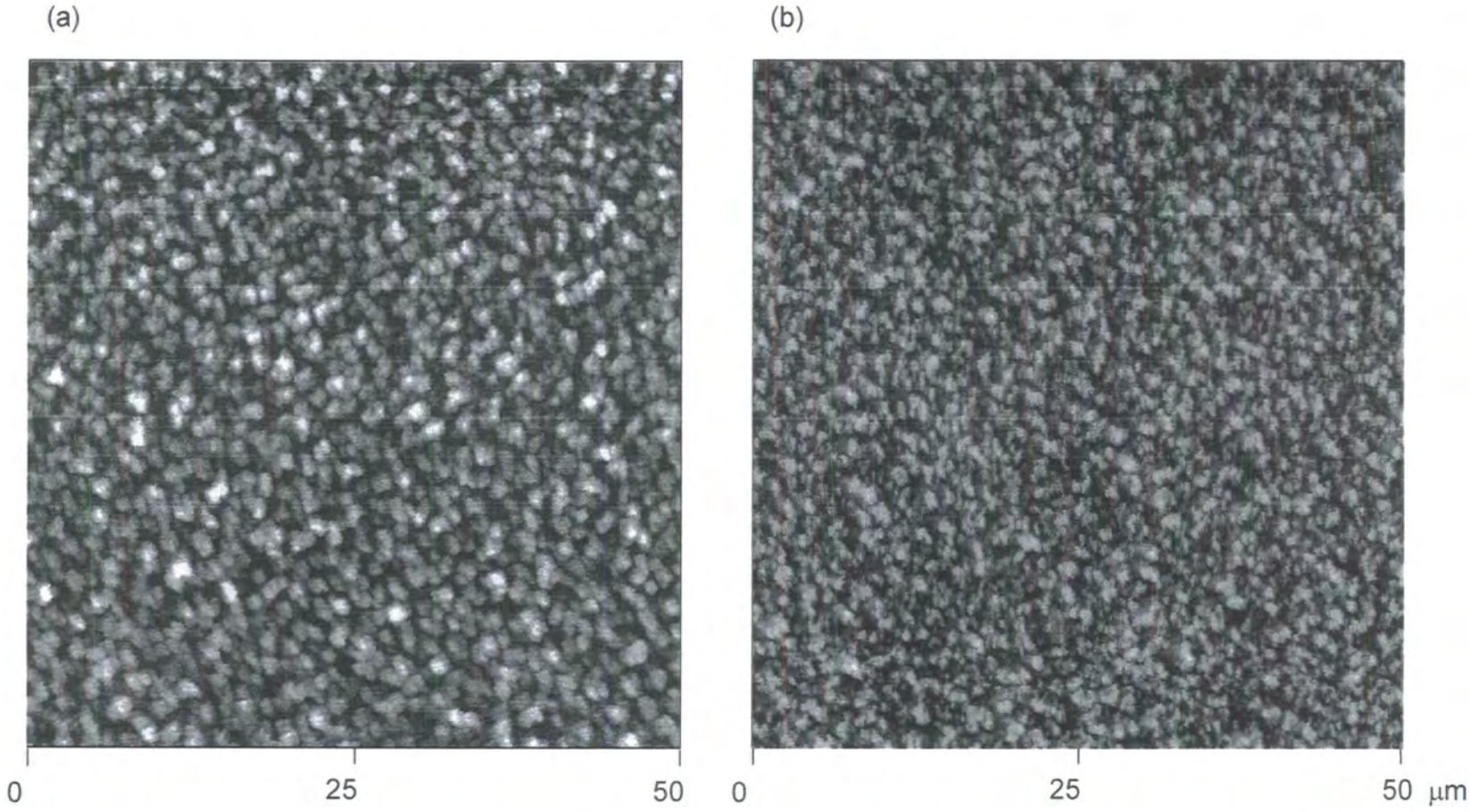

Figure 2.7 AFM height images (x=y=50 μm, z=2 μm) of CF_4 plasma treated polybutadiene (60 W, 10 min) (a) before curing (b) after curing for 1 hour at 155°C

2.1.4 Discussion

The liquid repellency of a surface is principally governed by a combination of its chemical nature (i.e. surface energy) and topographical microstructure (roughness). Although flat low surface energy materials can often exhibit high water contact angle values,[29] this is not normally sufficient to produce super-hydrophobicity (this description is reserved for materials upon which water drops move spontaneously or easily across horizontal or near horizontal surfaces).[30,31] In order for this to occur, the difference between the advancing and the receding contact angles (contact angle hysteresis) must be minimal. Effectively, contact angle hysteresis can be regarded as the force required to move a liquid droplet across the surface; i.e. in the case of little or no hysteresis, very little force is required to move a droplet, hence it easily rolls off.[32,33] Theoretical studies for idealised rough hydrophobic surfaces predict that initially contact angle hysteresis increases with surface roughness,[34] until eventually a maximum value is reached; greater roughness scales lead to a fall due to the formation of a composite interface (where the liquid does not completely penetrate the surface). Therefore, low contact angle hysteresis can be achieved by roughening the substrate.

Various methods have been reported in the literature for producing super-hydrophobic surfaces based on composite interfaces. These include: sublimation of aluminium acetylacetonate from a boehmite, titania or silica coating,[35,36] sol-gel deposition of alumina and silica,[37,38] anodic oxidation of aluminium,[31] and photolithograpically etched surfaces.[39] All of these approaches entail a pre-roughening step followed by functionalization with a fluoroalkyl coupling agent. Other ways have included: embedding PTFE

oligomer particles into nickel electrodes,[40] compressing sub-micrometer particles,[30] and plasma based etching[41] or deposition[42] techniques.

In the present case, plasma fluorination of polymer surfaces using non-depositing flurocarbon precursors (such as CF_4)[43,8,44,45,46,47,48,49] relies on the generation of fluorine atoms and ions, in conjunction with low concentrations of CF_x species.[48,50,51,52] The exceptionally high degree of fluorination (CF, CF_2 and CF_3 functionalities) observed for polybutadiene is consistent with atomic fluorine attacking the unsaturated carbon-carbon double bonds contained in the polymer repeat unit (as well as hydrogen substitution reactions).[8] The accompanying change in surface roughness could be attributed to the CF_4 plasma causing restructuring/cross-linking (by the VUV component) or etching (atomic and reactive ion etching).[53,54] However, the observed dependency of surface roughness upon film thickness (Figure 2.6) makes etching an unlikely cause for this phenomena.[46,47,48,49] These changes in surface chemistry and roughness[55] help to contribute towards the observed liquid repellency behaviour. The fluorinated groups reduce the surface energy due to their chemical inertness,[56] whilst surface roughness leads to the formation of a composite interface as described by the Cassie-Baxter equation where the inherent surface roughness causes air to become trapped in voids (i.e. prevents liquid from penetrating).[57, 58]

In the case of water probe liquid, a high sessile contact angle is observed with little hysteresis between advancing and receding contact angle values as is consistent for a composite surface.[59,60] Furthermore, based on the fact that the polybutadiene film is fluorinated to a similar level above and below the threshold thickness of 213 nm, it can be concluded that surface roughening is critical for the observed superhydrophobicity, since low water contact angle

hysteresis is indicative of a composite interface.[30,42] In the case of alkane liquids, the high hysteresis is consistent with wicking into the surface pores because of their lower surface tension, and is best described by the model proposed by Johnson and Dettre,[34] where the level of roughness is insufficient to form a composite interface (i.e. hysteresis prohibits super-oleophobic behaviour).

The mechanical durability of the plasma fluorinated polybutadiene films was found to improve by cross-linking (e.g. thermal, UV, etc.). However, such bulk cross-linking caused no discernible change to the surface morphology, which would support the viewpoint that the surface region undergoes extensive cross-linking during CF_4 plasma treatment. The incorporation of oxygenated functionalities into the fluorinated polybutadiene as measured by IR and the small increase in oxygen content at the surface as measured by XPS, during curing (Table 2.3, 2.4 and Figure 2.2) is consistent with the oxidative cross linking mechanism reported for thermally cured polybutadiene.[61,62]

Previous reports in the literature related to CF_4 plasma fluorination of polybutadiene membranes observed much lower levels of fluorination (61% F, 34% C, 5% O) as well as the absence of roughening (as seen by SEM) and water contact angles of only 140^{o}.[63] Also, no cross-linking was reported after CF_4 plasma treatment. Other types of cross-linked liquid repellent polymer films[64,65] tend to exhibit lower water contact angle values and are much more complicated to make.

2.1.5 Conclusions

Plasma fluorination of polybutadiene thin films followed by bulk crosslinking (curing) gives rise to hard super-hydrophobic films. This behaviour can be attributed to a combination of atomic fluorine and excited fluorinated species, attacking the polymer surface, and simultaneous cross-linking induced surface roughening in the electrical discharge to form a highly fluorinated composite interface.

Part B: Microfluidic Surface Patterning of Metal Salts and Polymer Microspheres

2.2.1 Introduction

High spatial density arrays are important for electrical, optical, and biotechnological applications.[66] Several methods exist for the fabrication of such structures, these include: molecular beam epitaxy,[67] chemical vapour deposition,[68] Langmuir Blodgett films,[69] electrochemical deposition,[70] and selective wetting of bifunctionalized surfaces.[66,71] The latter technique in particular offers a number of advantages which include low cost and applicability to a variety of systems.[37,66,72,73] For example, the preferential segregation of aqueous species has been shown to occur on patterned self-assembled monolayers prepared by microcontact printing.[66] These comprise a hydrophobic monolayer printed as a grid array on a gold surface with the remaining regions filled in with an hydrophilic group terminated alkanethiol. Another approach entails the selective functionalisation of a polymer brush, where acid groups are produced during UV irradiation[72] through a mask. One of the largest contact angle differences achieved for patterned surfaces has consisted of preparing a super-hydrophobic surface by reacting a perfluoroalkyl silane coupling agent onto a roughened titanium dioxide surface, followed by UV irradiation through a mask in order to cleave localised regions of perfluoroalkyl groups due to the photocatalytic activity of the underlying titanium dioxide layer.[37] This approach yields spatially localised contact angle differences in excess of 150°. All of these methods are complex. In this article we describe a simple two-step method for fabricating spatially ordered arrays of micron size particles and also metal salts by using a combination of patterned

super-repellent surfaces and microfluidic flow obtained from a nebulized mist. This comprises plasmachemical fluorination of polybutadiene surfaces followed by spatially localised UV curing.

2.2.2 Experimental

Polybutadiene (Aldrich, M_w = 420,000, 36% cis 1,4 addition, 55% trans 1,4 addition, 9% 1,2 addition) dissolved in toluene (BDH, +99.5% purity) was spin coated onto silicon wafers or potassium bromide disks using a photoresist spinner (Cammax Precima) operating at speeds between 1500 - 4500 rpm. All films were subsequently annealed, at 90 ^{o}C under vacuum for 1 hour, in order to remove entrapped solvent from the polymer. Thick (4.5 μm) films were deposited using a spin speed of 2000 rpm from a 10% w/v solution, and thin 236 nm thick films were produced by spin coating at 4000 rpm from a 2.5% w/v solution.

CF_4 plasma fluorination of these film surfaces was carried out in a cylindrical glass reactor (5 cm diameter, 470 cm^3 volume) connected to a two stage rotary pump via a liquid nitrogen cold trap (base pressure of 4 x 10^{-3} mbar, and a leak rate of better than 6 x 10^{-9} mol s^{-1}). An L-C matching unit was used to minimise the standing wave ratio (SWR) of the power transmitted from a 13.56 MHz R.F. generator to a copper coil wound around the reactor wall. Prior to each plasma treatment, the chamber was scrubbed with detergent, rinsed in propan-2-ol, and then further cleaned using a 0.2 mbar air plasma operating at 50 W for 30 min. A piece of polybutadiene coated substrate was then placed into the centre of the reactor, followed by pumping down to base pressure. Next CF_4 gas (99.7% purity, Air Products) was admitted into the system via a needle valve at a pressure of 0.2 mbar, and after 5 min of purging,

the electrical discharge was ignited. Upon completion of plasma treatment, the chamber was evacuated, followed by venting to atmosphere.

The fluorinated polybutadiene film surfaces were patterned by exposure to UV radiation (Oriel low pressure Hg-Xe arc lamp operating at 50 W, emitting a strong line spectrum in the 240-600 nm wavelength region). A copper grid (1000 mesh, Agar Scientific) was positioned just above the polymer surface to act as a photo-mask. All irradiation was unless otherwise specified carried out for 1 hour.

Solvent soaking experiments were performed by immersing the fluorinated and UV irradiated films in either toluene or tetrohydrofuran (THF) for 1 hour or 10 minutes, respectively. AFM analysis was performed immediately after removal from these solvents.

These micro-patterned surfaces were then exposed to a nebulized aqueous mist (Inspiron nebulizer operating with a nitrogen gas flow of 3 dm^3 min^{-1}) containing either $CuSO_4$ salt solution (0.00125 molar) or polystyrene beads (1×10^9 beads per ml). Also, gold (III) chloride (Aldrich 99%) was selectively deposited onto these micropatterned substrates by submerging into a 10% (w/v) solution in ethyl acetate (Fisher 99%) for 10 min duration followed by rinsing in methanol to dislodge extraneous $AuCl_3$ species.

XPS analysis was undertaken on a VG ESCALAB MkII spectrometer equipped with an unmonochromatised Mg K_α X-ray source (1253.6 eV) and a hemispherical analyser. Photoemitted core level electrons were collected at a fixed take-off angle (75° away from the sample surface) with electron detection in constant analyser energy (CAE) mode operating at 20 eV pass energy. The instrument was calibrated with respect to the Au($4f_{7/2}$) reference peak at 83.8 eV with a full-width-at-half-maximum (fwhm) value of 1.2 eV. No spectral

deterioration due to X-ray radiation damage was observed during the time scale associated with data accumulation. Elemental sensitivity (multiplication) factors were taken as being C(1s) : F(1s) : O(1s) equals 1.00 : 0.35 : 0.45.

Infrared analysis of polybutadiene films coated onto polished KBr disks was carried out on a Perkin Elmer Spectrum One instrument operating in transmission mode at 4 cm^{-1} resolution in conjunction with a DTGS detector.

Sessile drop contact angle measurements were taken at 20 °C with a video capture apparatus (A.S.T. Products VCA2500XE) using pure water as the probe liquid (B.S. 3978 Grade 1). In the case of super-hydrophobic surfaces, the water droplets were kept stationary by the dispensing syringe. Advancing and receding contact angle measurements comprised increasing or decreasing the liquid drop volume at the surface.[34]

AFM micrographs of the patterned surfaces were acquired using a Digital Instruments Nanoscope III. Damage to the tip and substrate was minimised by operating in Tapping Mode AFM.[20] Corresponding optical images were captured using an Olympus BX40 microscope.

Raman spectroscopy and spatial mapping was performed on a Dilor Labram microscope equipped with a 1800 lines mm^{-1} diffraction grating and a helium-neon laser excitation source (632.8 nm line operating at 11 mW). Raman microscopy entailed plotting the intensity of a characteristic absorbance band associated with $AuCl_3$ species over a 50 μm x 50 μm square area.

2.2.3 Results

2.2.3.1 UV Irradiation of Fluorinated Polybutadiene Films

XPS analysis detected a small amount of oxygen incorporation (2%) at the surface following UV irradiation of fluorinated polymer film, Table 2.6. Infrared

band assignments for polybutadiene are summarised in Table 2.1. No new infrared absorption features were observed following CF_4 plasma fluorination of polybutadiene. This can be explained in terms of the surface sensitivity of this analytical technique being poor in transmission mode of analysis (since only the outermost layer of polybutadiene has undergone plasma fluorination - as exemplified by XPS analysis). Bulk oxidative crosslinking of these films during UV irradiation was evident as seen by the attenuation of the CH stretch associated with the polybutadiene alkene bonds (B) and also the emergence of oxygenated groups, (A, C and D) Figure 2.8 and Table 2.3. Corresponding water sessile drop contact angle measurements confirmed the super-hydrophobic character of plasma fluorinated polybutadiene surface. Better surface wettability observed following UV irradiation is most likely to be attributable to oxygen incorporation at the surface, Table 2.7.

Substrate	% C	% O	% F
Prior to UV	29 ± 2	0	71 ± 2
UV Cured	31 ± 2	2 ± 2	67 ± 2

Table 2.6 XPS analysis of CF_4 plasma modified 236 nm thick polybutadiene film (60 W, 10 min) prior to and following UV exposure.

UV Exposure / mins	Contact Angle / °		
	Equilibrium	Advancing	Receding
0	174.9 ± 0.4	173.1 ± 0.4	172.7 ± 0.5
20	173 ± 1.0	171.6 ± 0.5	170.8 + 0.4
40	172 ± 1.2	171.4 ± 0.5	170.0 ± 1.0
60	170.3 ± 1.0	171.0 ± 0.7	169.0 ± 0.7

Table 2.7 Water contact angle measurements of CF_4 plasma / UV patterned 4.5 μm thick polybutadiene film (60 W, 10 min).

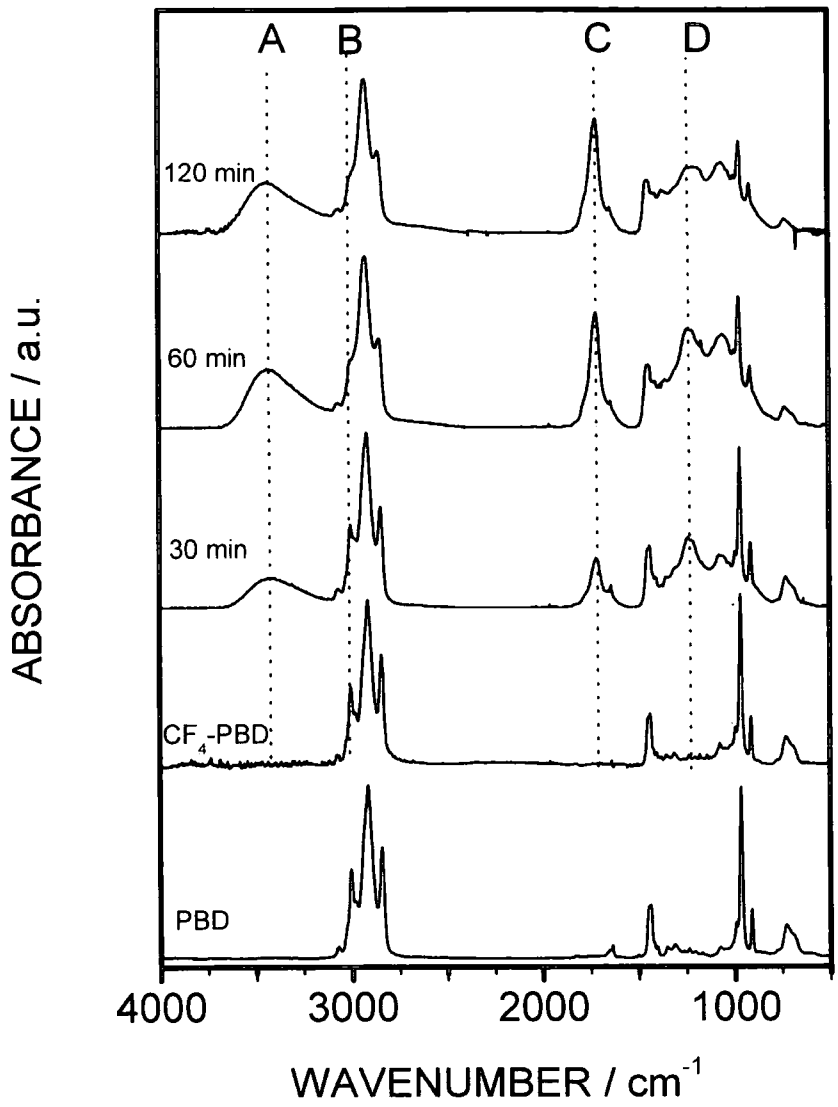

Figure 2.8 IR spectra of CF_4 treated polybutadiene (60 W, 10 min) as a function of UV exposure time.

2.2.3.2 UV Patterning of Fluorinated Polybutadiene Films

In the case of CF_4 plasma fluorinated polybutadiene films, AFM indicated a clear drop in height for the UV irradiated square regions, Figure 2.9. Soaking of the 4.5 μm thick film in toluene results in an exacerbation of the height, but soaking in THF causes a height reversal. However the 236 nm thick film demonstrates exacerbation of the existent morphology with immersion in both toluene and THF.

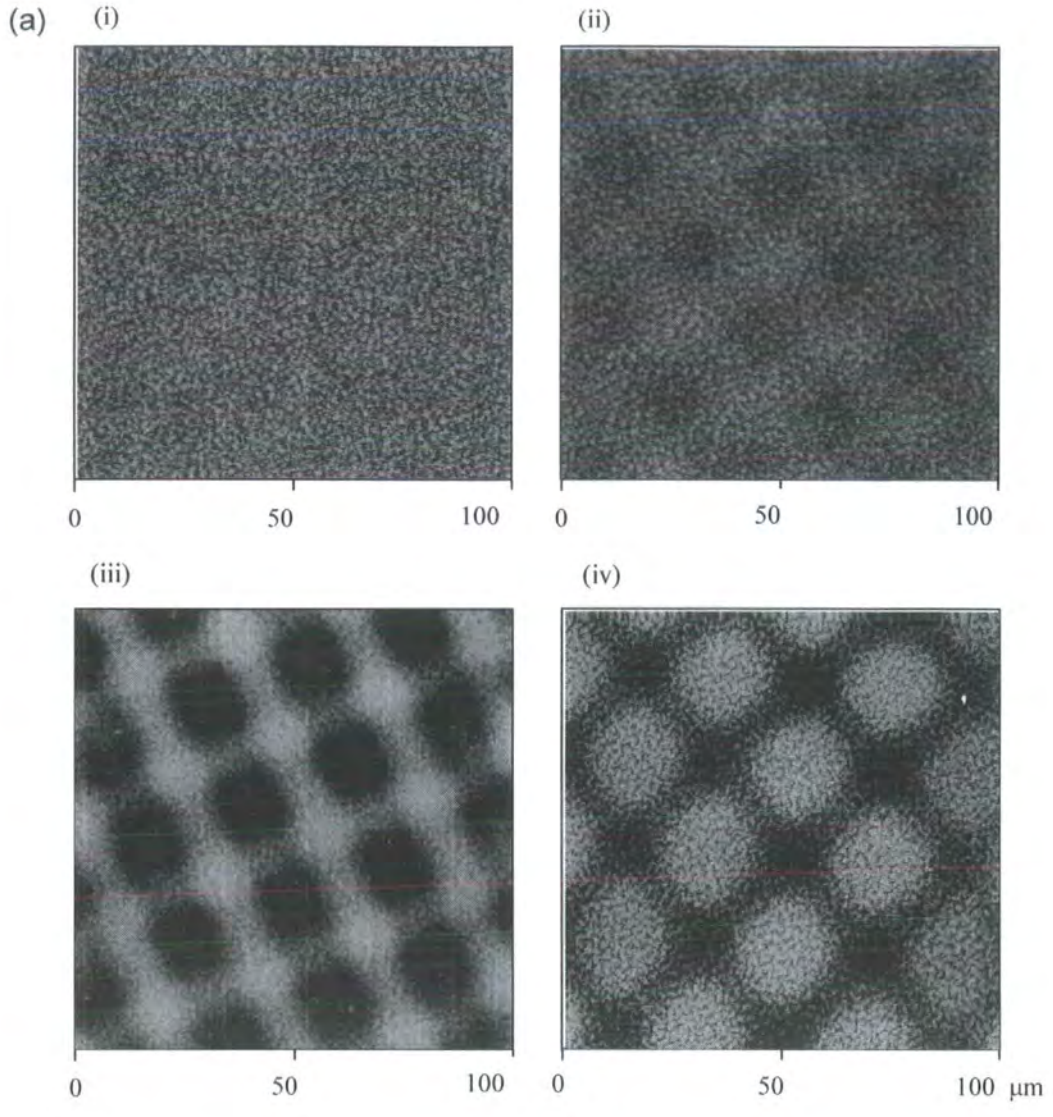

Figure 2.9 AFM height images (z = 2 μm, except for (iii) where z = 4 μm) of CF_4 plasma treated polybutadiene (60 W, 10 min): (a) 4.5 μm thick, (b) 236 nm thick. Where: (i) before UV; (ii) UV exposure (1hr); (iii) toluene soaked (1hr) of (ii) and (iv) THF soaked (10 min) of (ii).

(b)

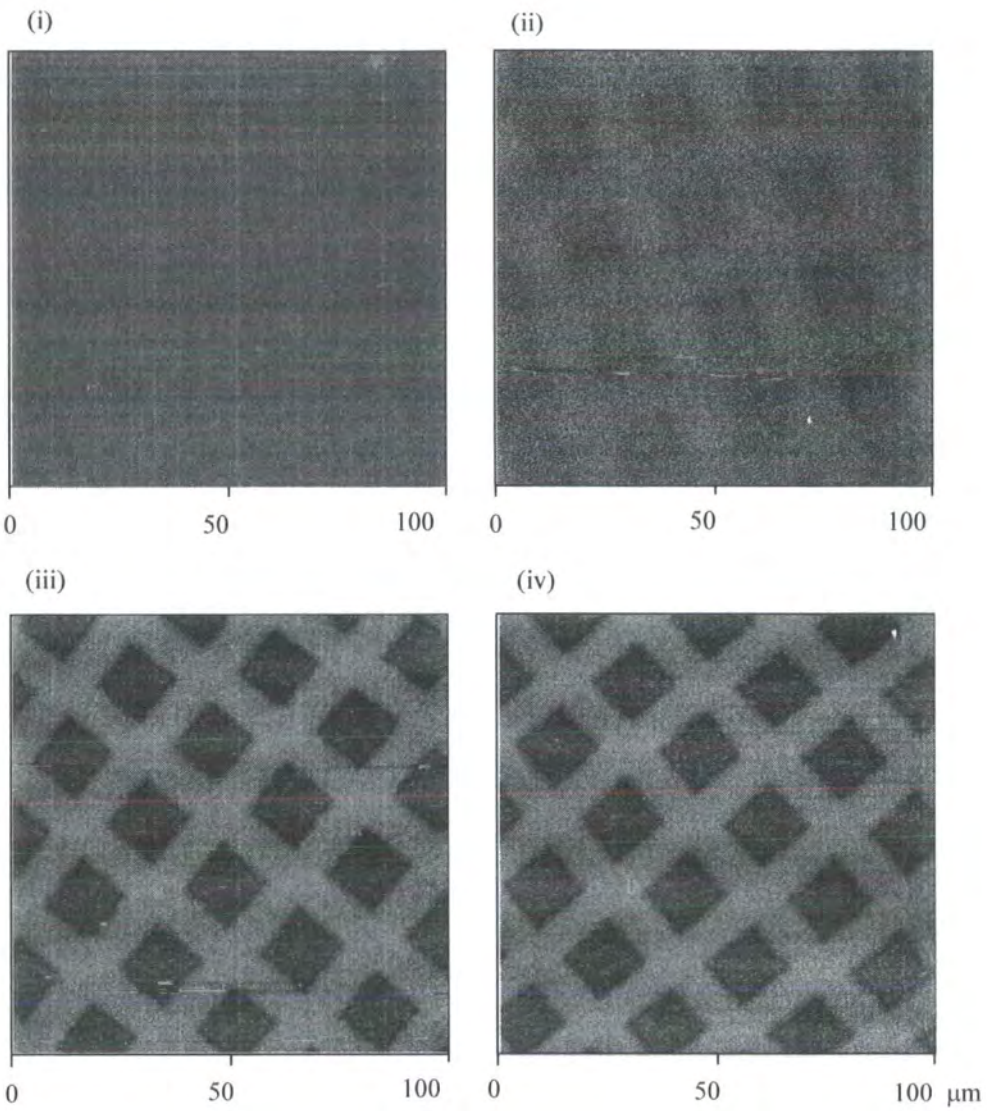

2.2.3.3 Copper Sulfate and Polystyrene Microsphere Patterning

It was found that water droplets undergo selective condensation onto the UV irradiated square areas present on the fluorinated polybutadiene film surface during exposure to a humid environment, (steam from beaker of Ultrapure water (B.S. 3978 Grade 1)) Figure 2.10. Analogous behaviour was also observed in the case of a nebulized mist of aqueous $CuSO_4$ solution, leading to selective growth of salt crystals into the patterned squares, Figure 2.11. It was found that the actual crystal size could be controlled by varying the mist exposure time.

In a similar fashion, exposure to a nebulized aqueous mist containing polystyrene microspheres of either 0.61 μm or 9.1 μm diameter, produced arrays comprising either agglomerations of 0.61 μm beads, or individual 9.1 μm beads in each square (since only one bead can physically occupy an individual square), Figure 2.12.

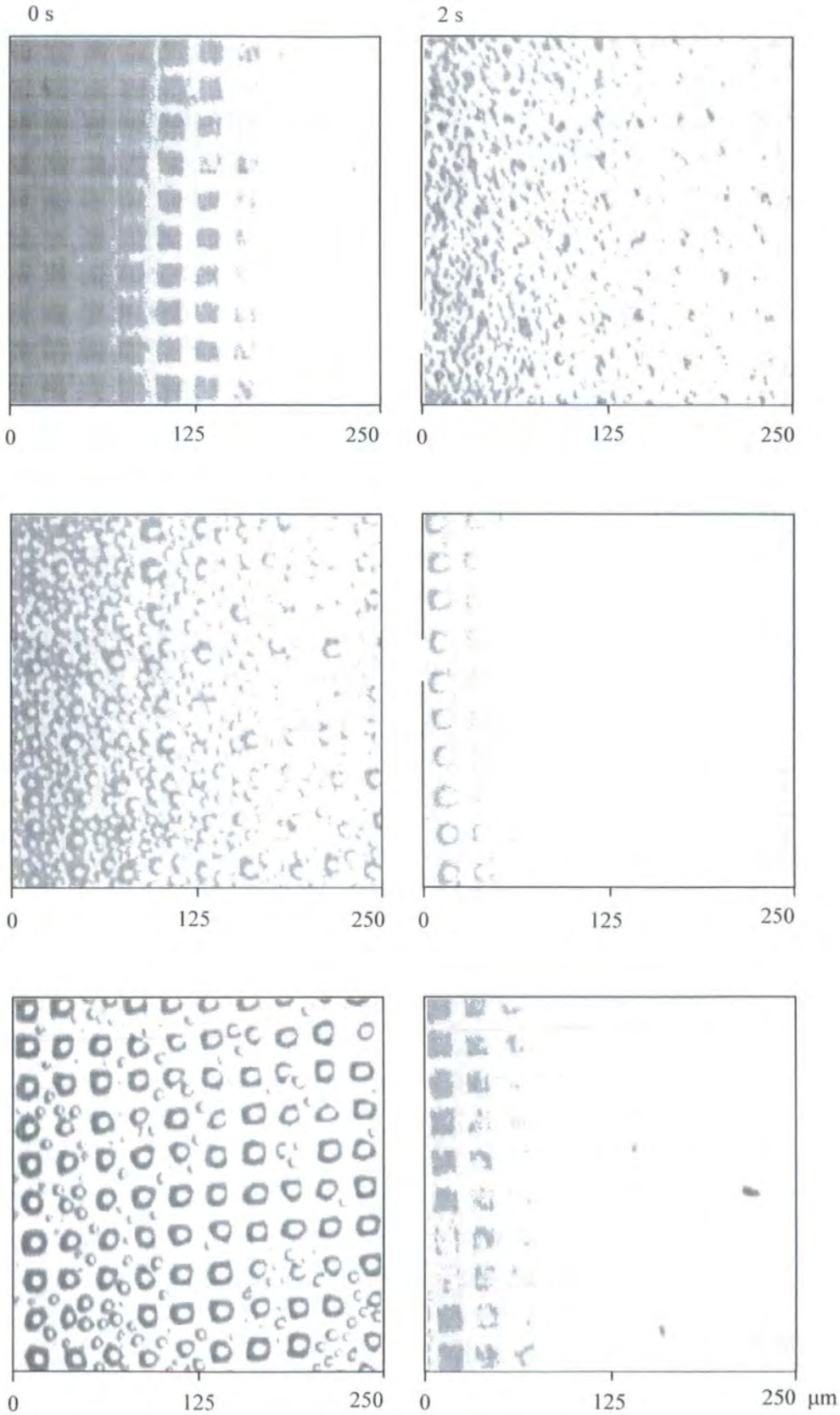

Figure 2.10 Optical microscope images showing microfluidic self-organisation of water droplets on CF_4 plasma treated 236 nm thick polybutadiene film after UV irradiation through a copper grid.

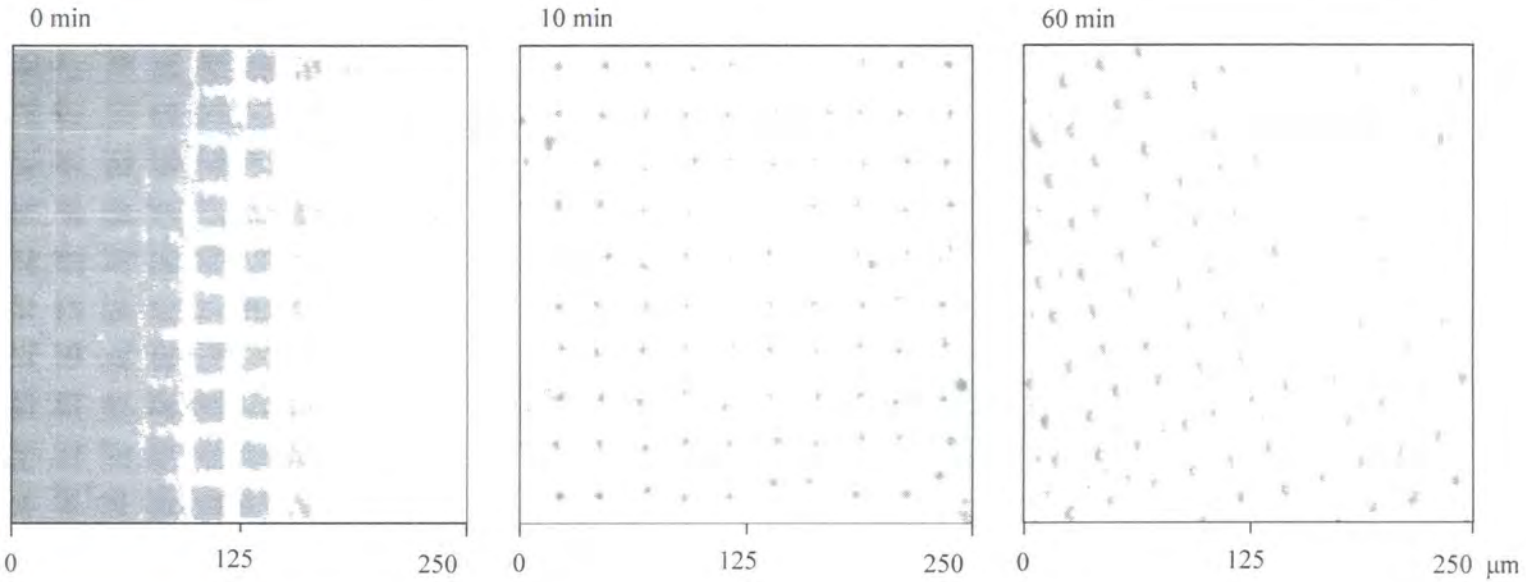

Figure 2.11 Optical microscope images of $CuSO_4$ crystals grown on UV patterned CF_4 plasma treated 236 nm thick polybutadiene film (60 W, 10 min).

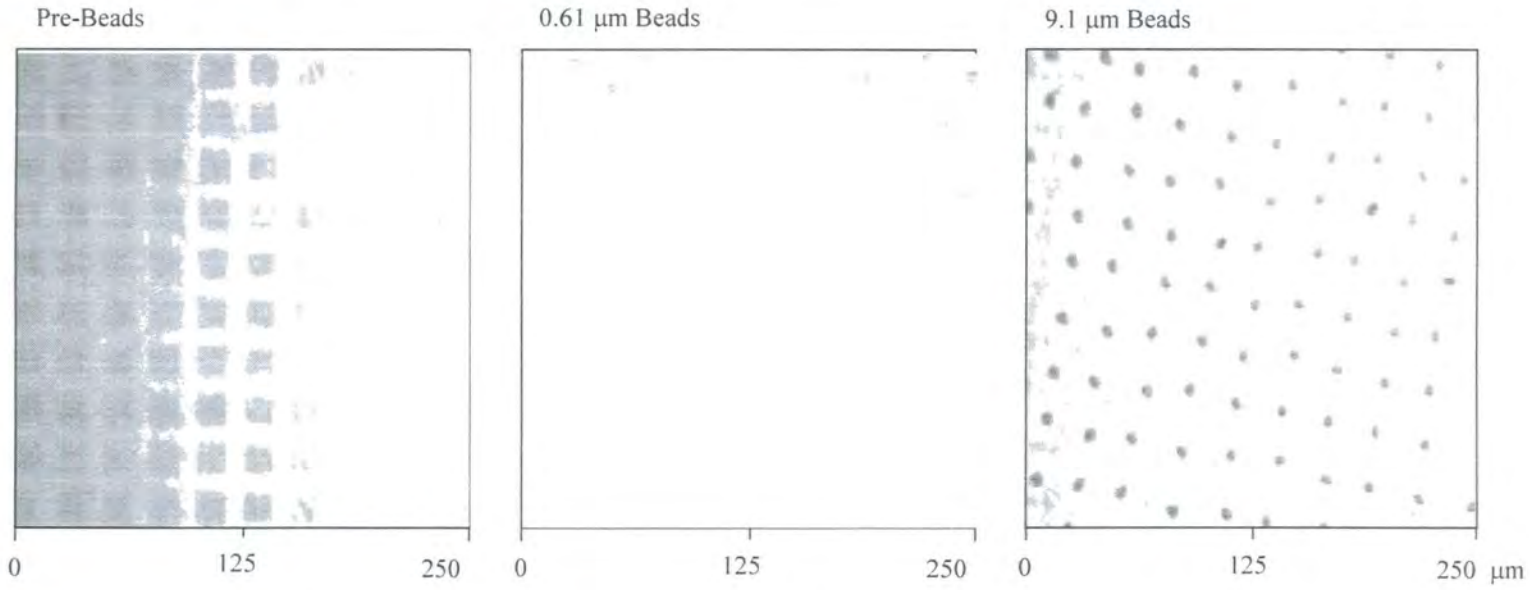

Figure 2.12 Optical microscope images of polystyrene beads deposited onto UV patterned CF_4 plasma treated 236 nm thick polybutadiene (60 W, 10 min).

2.2.3.4 Gold Patterning

No strong Raman absorbances were measured for the polybutadiene film over the frequency ranges measured, which is consistent with findings in the literature.[74] Raman spectroscopy of CF_4 plasma treated and UV cured polybutadiene film followed by soaking in $AuCl_3$ / ethylacetate (10 % w/v) solution and then rinsing in methanol gave a distinct band structure between 246-370 cm^{-1}, attributable to $AuCl_3$ salt species,[75,76] Figure 2.13. Raman spectral mapping using this spectral region confirmed selective deposition of $AuCl_3$ into the UV irradiated squares, Figure 2.13. XPS analysis of $AuCl_3$ soaked films, before and after UV irradiation (no patterning), showed very little gold or chlorine content on either of the films. Raman spectra taken from these films in several locations correlates as no bands associated with $AuCl_3$ are found. Hence it is necessary to have small entrapping domains on the surface to gain any $AuCl_3$ coverage.

(a)

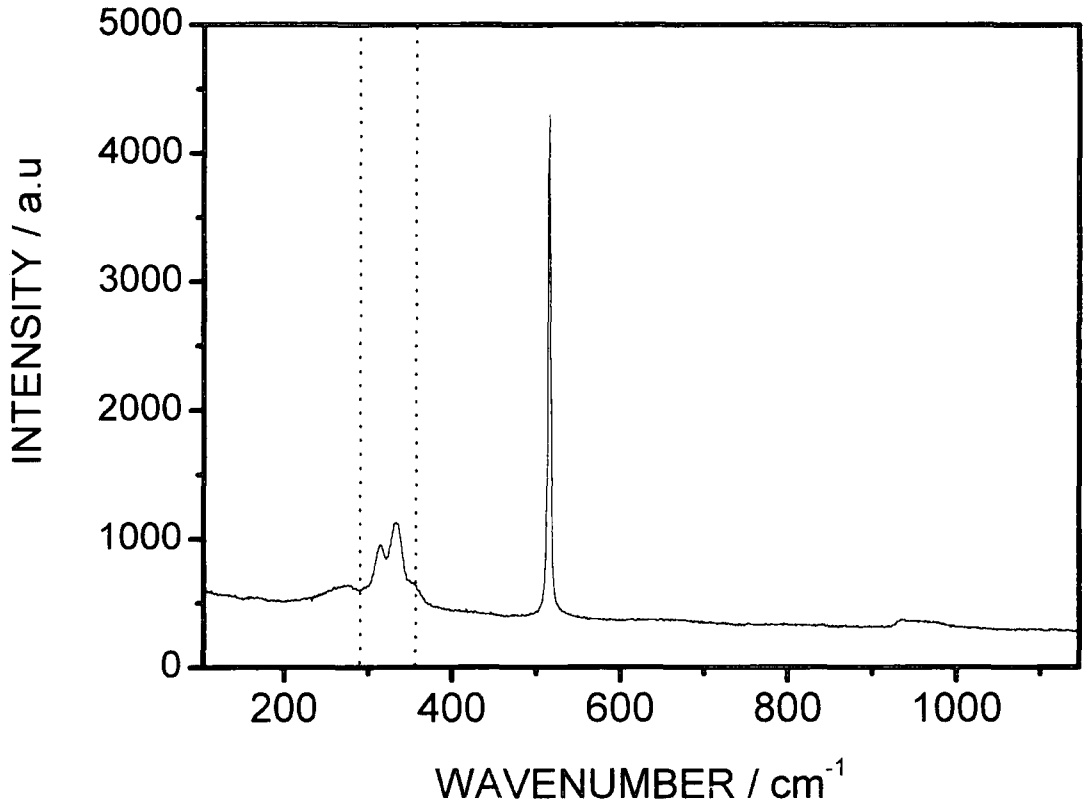

Figure 2.13 Raman analysis of CF_4 plasma treated 4.5μm thick polybutadiene (60W, 10 min) after UV irradiation through a copper grid, and immersion in a $AuCl_3$ / ethyl acetate solution and subsequent MeOH rinsing; (a) Spectrum of $AuCl_3$ rich region, (b) Spectral map of indicated band.

(b)

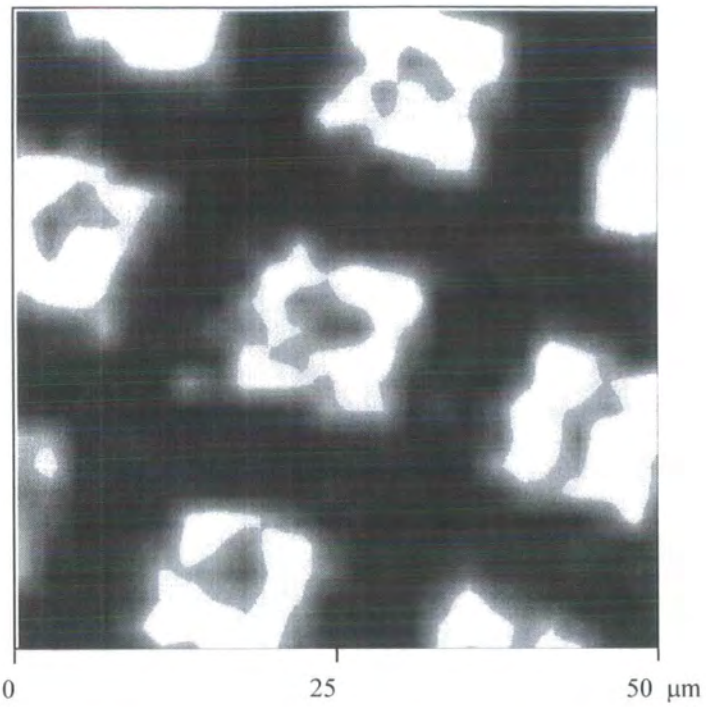

2.2.4 Discussion

CF_4 plasma modification of polybutadiene film leads to a highly fluorinated and cross-linked surface (i.e. the electrical discharge penetration depth) and polybutadiene underneath which can be subsequently cross-linked. Several methods of curing polybutadiene have been reported in the literature, these include heat,[79] UV[77] and γ[78] irradiation. Infrared spectroscopy has shown that the super-hydrophobic CF_4 plasma fluorinated polybutadiene films can also be cured by UV irradiation (thermal and γ irradiation curing would also be expected to work, however these do not lend themselves towards spatially controlled patterning on this scale). Oxygen incorporation into the film during UV exposure is consistent with an oxidative cross-linking mechanism,[79] giving rise to a reduction in water contact angle, Table 2.8. It has been noted in the literature that the UV cross-linking of polybutadiene occurs primarily through the pendant double bonds rather than those in the chain, and also that the rate of cure can be dramatically accelerated by addition of multifunctional acrylate or thiol monomers.[77] The corresponding surface roughness was not found to change markedly upon UV exposure (as previously seen with thermal curing in section A), thereby ruling out any change in water contact angle being exclusively a manifestation of enhanced roughening.[57,58] UV irradiation through a micron-scale copper grid, produced a reduction in height in the exposed regions for both film thicknesses, which is consistent with shrinkage of the sub-surface elastomer during curing.[80] The observed exacerbation of this height by toluene soaking of both films and THF immersion of only the thinner film may be attributed to solvent swelling of predominantly the uncured regions, due to the greater conformational freedom of the un-crosslinked polybutadiene. The height reversal seen after THF immersion of the thicker film is most probably

due to dissolution of the bulk un-cured polybutadiene. This is not observed after toluene immersion due to differences in solvation rate. This dramatic difference is almost certainly due to the difference in hydrogen bonding capability of the two solvents, THF being considered a medium polar solvent and toluene an apolar solvent.[81] Although the polybutadiene is not polar in itself, it would seem likely that some oxygenated groups have been incorporated into the polymer during UV irradiation, thus increasing its polar nature. The reason for no dissolution in the thinner film is something of a mystery, but may be due to the lower rates of diffusion of solvated polybutadiene from under the extensively cross-linked skin (Section A and Chapter III), due to the reduced thickness of the film.

Localised microfluidic deposition of salt crystals has previously been accomplished by using patterned hydrophilic SAM regions and dipping.[66] In the present study, the localised deposition / growth of salt crystals and polystyrene beads into the UV irradiated squares occurs in a similar manner. Condensation of the nebulised mist on the surface is followed by droplet coalescence into regions of lower height and lower surface energy. Subsequent water evaporation leaves behind the solid particulates in these squares. This mechanism is supported by the fact that dilute salt solutions worked best, whereas higher concentrations gave rise to random crystal growth on the surface. The deposited crystal size could easily be controlled by varying mist exposure time. Unlike techniques involving dipping,[66] there appear to be no limitations on the crystal size that can be grown.

In a similar fashion, $AuCl_3$ species can be entrapped from solution into these lower surface energy pockets. Several other methods exist for selective patterning of gold onto polymer surfaces, these include gold island formation on

annealed polystyrene / polymethylmethacrylate and polystyrene / polyvinylylpyridene systems.[71] Also spatially controlled gold domains have been produced by Liu et al[82] using exposed thiol terminated ends of self assembled monolayers on silicon and photolithographic patterning.

2.2.5 Conclusions

Metal salts and polystyrene microspheres can be selectively deposited from a nebulized mist into UV photolithographic patterned regions of greater surface energy and lower height on super-repellent CF_4 plasma fluorinated polybutadiene.

2.3 References

1. Kissa, E. In *Handbook of Fibre Science and Technology*, Vol II, Part B, Lewin, M.; Sello, S. B. Eds.; Marcel Dekker Inc: New York, **1984**
2 Brady, R. F. Jr. In *Encyclopaedia of Polymer Science and Technology*, Mark, H.; Bikales, N. M.; Overberger, C. G.; Menges, G. Eds.; John Wiley & Sons: Chichester, **1986**
3 DeMarco, C. G.; Mc Quade, A. J.; Kennedy, S. J. *Modern Textiles Magazine* **1960,** *Part 2*, 50
4 Sargent, R. R.; Alender, J. R. U.S. Patent 5,560,992, 1996
5 Anderson, M. H.; Lyons, C. S.; Wigness, B. D. U.S. Patent 4,536,179,1985
6 Honeychuck, R. V.; Ho, T.; Wynne, K. J.; Nissan, R. A. *Chem. Mater.***1993**, *5*, 113
7 Clark, D. T., Feast, W. J., Musgrove, W. K. R., Ritchie, I. *J. Polym. Sci., Part A: Polym. Chem.* **1975**, *13*, 857
8 Hopkins, J., Badyal, J. P. S. *J. Phys. Chem.* **1995**, *99*, 4261
9 Coulson, S.R., Woodward, I.S., Brewer, S.A., Willis, C., Badyal, J. P. S. *Chem. Mater.* **2000**, *12,* 2031.
10 Wheale, S. H. Physicochemical Phenomena at the Plasma - Polymer Interface. Ph.D. Thesis, Durham University, 1997
11 Ryan, M. E., Fonseca, J. L. C., Tasker, S., Badyal, J. P. S. *J. Phys. Chem.* **1995**, *99*, 7060.
12 Popat, R. H.; Sutherland, I.; Shang, E. -S. *J. Mater. Chem.* **1995**, *5*, 713
13 Fitzgerald, P. H., Raiford, K. G., Greenwood, E. J. U.S. Patent 5,798,402, 1998.
14 Raiford, K. G., Liss, T. A., Greenwood, E. U.S. Patent 5,898,046,1997.
15 Smith, R. S. U.S. Patent 5,672,651, 1997
16 Kassis, C. M., Steehler, J. K., Betts, D. E., Guan, Z. B., Romack, T. J., Desimone, J.M., Linton, R. W. *Macromolecules* **1996**, *29*, 3247
17 Schaub, T. F., Kellogg, G. J., Mayes, A. M. *Macromolecules* **1996**, *29*, 3982
18 Champagne, F., Li, J. F., Schreiber, H. P., Dipaloa-Baranyi, G. *J. Appl. Polym. Sci.* **1994**, *54*, 743

19. Ebbens, S. J.; Badyal, J. P. S. *Langmuir*, **2001**, 17, 4050.
20 Zhong, Q. Innis, D. Kjoller, K., Elings, V.B. *Surf. Sci.* **1993**, *14*, 3045
21. Korsunsky, A.M., McGurk, M.R., Bull, S.J., Page, T.F. *Surface and Coatings Technology*, **1998**, *99*, 171.
22 Lovering, D. N.K.D 6000 Technical Manual Aquila Instruments, Cambridge, UK., **1999**.
23. Xiao, G. *J. Colloid and Interface Science*, **1995**, 171, 2000.
24 Clark, D. T., Shuttleworth, D., *J. Polym. Sci. Chem. Ed.*, **1980**, 18, 27.
25. Beamson, G., Briggs, D. *High Resolution XPS of Organic Polymers, the Scienta ESCA 300 Database*, John Wiley and Sons, Chichester, **1992**.
26. DI Nanoscope III Command Reference Manual, Update Version 4.10, **1995**.
27 Jasper, J. J. *J. Phys. Chem. Ref Data*, **1972**, 1, 841.
28. *Concise Encyclopedia of polymer science and engineering*. Ed. Jacqueline I. Kroschwitz. John Wiley and Sons., **1990**.
29. Tsibouklis, J., Graham, P., Eaton, P. J., Smith, J. R., Nevell, T. G., Smart, J. D., Ewen, R. J. *Macromolecules,* **2000**, *33*, 8460.
30. Chen, W., Fadeev, A. Y., Hsieh, M. C., Oner, D., Youngblood, J., McCarthy, T. J. *Langmuir,* **1999**, 15, 3395.
31. Shibuichi, S., Yamamoto, T., Onda, T., Tsujii, K. *Journal of Colloid and Interface Science,* **1998**, *208*, 287.
32. Furmidge, C. G. L. *J. Colloid Sci.,* **1962,** 17, 309
33. Miwa, M., Nakajima, A., Fujishima, A., Hashimoto, K., Watanabe, T. *Langmuir,* **2000,** 16, 5754
34. Johnson, R. E., Dettre, R. H. *Adv. Chem. Ser.,* **1964**, 43, 112.
35. Nakajima, A., Hashimoto, K., Watanabe, T., Takai, K., Yamauchi, G., Fujishima, A. *Langmuir,* **2000**, 16, 7044.
36. Nakajima, A., Fujishima, A., Hashimoto, K., Watanabe, T., *Adv. Mater.,* **1999**, 16, 1365.
37. Tadanaga, K., Morinaga, J., Matsuda, A., Minami, T. *Chem. Mat.,* **2000,** 12, 590
38. Hong, B. S., Han, J. H., Kim, S. T., Cho, Y. J., Park, M. S., Dolukhanyan, T., Sung, C. *Thin Solid Films,* **1999,** 351, 274
39. Oner, D., McCarthy, T. J. *Langmuir,* **2000,** 16, 7777

40. Kunugi, Y., Nonaku, T., Chong, Y. B., Watanabe, N. *J. Electroanal. Chem.,* **1993,** 353, 209
41. Busscher, H. J., Stokroos, I., Vandermei, H. C., Rouxhet, P. G., Schakenraad, J. M. *J. Adhes. Sci. Technol.,* **1992,** 6, 347
42. Youngblood, J. P., McCarthy, T. J. *Macromolecules,* **1999,** 32, 6800
43. Strobel, M., Corn, S., Lyons,C. S., Korba, G.A., *J. Polym. Sci: Part A: Polym. Chem.*, **1987**, *25*, 1295
44. Hopkins, J.; Badyal, J. P. S., *Macromolecules*, **1994**, *27*, 5498.
45. Sigurdsson, S., Shishoo, R., *J. Appl. Polym. Sci.*, **1997**, *66*, 1591.
46. Wang J., Feng D., Wang H., Rembold M., Thommen F., *J. Appl. Polym Sci.*, **1993**, *50*, 585.
47. Egitto, F. D., *Pure Appl. Chem.*, **1990**, *62*, *9*, 1699
48. Truesdale, E. A., Smolinksky, G., *J. Appl. Phys.*, **1979**, *50*, *11*, 6594.
49. Klausner, M., Loh, I. H., Baddour, R. F., Cohen, R. E., *Polym. Mater. Sci. Eng.*, **1987**, 56, 227.
50. D'Agostino, r., Cramarossa, F., DeBenedictis, S., *Plasma Chem. Plasma Process*, **1982**, *2*, 213.
51. Egitto, D. F.,Vukanovic, V., Taylor, G. N., *Plasma Depostion Treatment and Etching of Polymers*, d'Agastino R., Ed.; Academic Press Inc., San Diego, **1990**, Chapter 5.
52. Iriyama Y., Yasuda, H., *J. Polym. Sci. Chem. Ed.*, **1992**, *30*, 1731.
53. Inagaki, N., Kobayashi, N., Matsushima, M. J., *Membr. Sci.*, **1988**, *38*, 85.
54. Kerle, T., Yerushalmi-Rozen, R.; Klein, J., *Europhys. Lett.*, **1997**, *38*, 207.
55. Satoshi Shibuichi; Tomohiru Onda, Naoki Satoh and Kaoru Tsujii, *J. Phys. Chem.*, **1996**, *100*, 19512.
56. Smart, B. E., *Chemistry of Organic Fluorine Compounds*, Hudlicky, M., Ed., Pavlath, A. E., ACS, Washington, **1995**.
57. Cassie, A. B. D.; Baxter, S. *Trans. Faraday Soc.*, **1994**, *40*, 546.
58. Cassie, A. B. D.; Baxter, S. *Trans. Faraday Soc.* **1944**, *3*, 16.
59. Garbassi, F.. Morra, M.. Occhiello, E., *Polymer Surfaces: From Physics to Technology*, John Wiley and Sons, Chichester, **1994**.
60. Chen, W., Fadeev, A. Y., Hsieh, M. C., Oner; D., Youngblood, J., McCarthy, T. J. *Langmuir*, **1999**, *5*, 3395.

61. Dickle, R. A., Carter, R. O., Hammond; J. S., Parsons, J. L., Holubka, J. W. *Ind. Eng. Chem. Prod. Res. Dev.*, **1984**, *23*, 297.

62 Raghavan, D., Gu, X., Nguyen, T., Vanlandingham, M., Karim, A. *Macromolecules*, **2000**, *33*, 2583.

63. Liang-Pen, Z., Atsushi, T., Kouji; N., Joshitake, H., Tisato, K. *Sen-i Gakkaishi*, **1991**, *47*, 635.

64. Anton, D. *Advanced Materials*, **1998**, *10*, 1197.

65. Scheirs,.J. *Modern Fluoropolymers*, Wiley, New York **1997**.

66. Quin, D., Xia, Y., Xu, B., Yang, H., Zhu, C., Whitesides, G.M. *Advanced materials*, **1999**, *11*, 1433.

67. Delamarche, E., Schmid, H., Bietsch, A., Larsen, N.B., Rothuizen, H., Michael, B., Biebuyck, H. *J. Phys. Chem. B*, **1998**, *102*, 3324.

68. Xia, Y., Whitesides, G. M. *Angew. Chem. Int. Ed.*, **1998**, *37*, 550.

69. Pompe, T., Fery, A., Herminghaus, S., Kriel, A. Lorenz, H., Knotthaus, J. P. *Langmuir*, **1999**, *15*, 2398.

70. Goetting, L. B., Deng, T., Whitesides, G. M. *Langmuir*, **1999**, *15*, 1182.

71. Morkved, T. L., Wiltzius, P., Jaeger, H. M., Grier, D. G., Witten, T. A. *Appl. Phys. Lett.*, **1994**, *64*, 422.

72. Husemann, M., Morrison, M., Benoit, D., Frommer, J., Mate, C.M., Hinsberg, W.D., Hedrick, J.I., and Hawker, C.J. *J. Am. Chem. Soc.*, **2000**, *122*, 1844.

73. Kumar, A. Whitesides, G.M. *Science*, **1994**, *263*, 61.

74. Guilment, J., Bokobza, L. *Vibrational Spectroscopy*, **2001**, 26, 133.

75. Degan, I.A., Rowlands, A.J. *Spectrochemica Acta*, 1991, 47A, 1263.

76 Murphy R. J., LaGrange, M. S., *Geochemica Cosmochemica Acta*, 62, 3515.

77. Decker, C., Nguyen Thi Viet, T. *Journal of Applied Polymer Science*, **2000**, 77, 1902.

78. Shen, Y., Fei, L., Zhao, X. *Appl. Magn. Reson.* **1995**, 8, 181.

79. Dickle, R.A., Carter, III, R.O., Hammond, J.S., Parsons, J.L., Holubka, J.W. *Ind. Eng. Chem. Prod. Res. Dev.*, **1984**. *23*, 297.

80. Patra, P. K., Das, C. K., Pandey, K. N., Marthur, G. N. *J. Appl. Polym. Sci.*, **1998**. *68*, 597.

81 Polymer handbook fourth edition, Eds, Brandrup, J., Immergut, E. H., Grulke, E. A. John Wiley & sons Inc, New York, **1999**.

82 liu, J-F., Zhang, L-G., Gu, N., Ren, J-Y., Wu, Y-P., Lu, Z-H., Mao, P-S., Chen, D-Y. *Thin Solid Films*, **1998**, 327-329, 176.

Chapter 3

Polybutadiene / Polystyrene Phase Segregated Films: a Pathway to Bifunctionalisation

3.1 Aim

The aim of the work described in this chapter is to create a tailored bifunctional surface utilising a phase segregated polymer thin film as a template. The procedure involves production of a polymer surface containing pores transient to the underlying substrate. The polymer is then to undergo plasma functionalisation and the substrate selectively functionalised by other means. This is outlined in scheme 3.1:

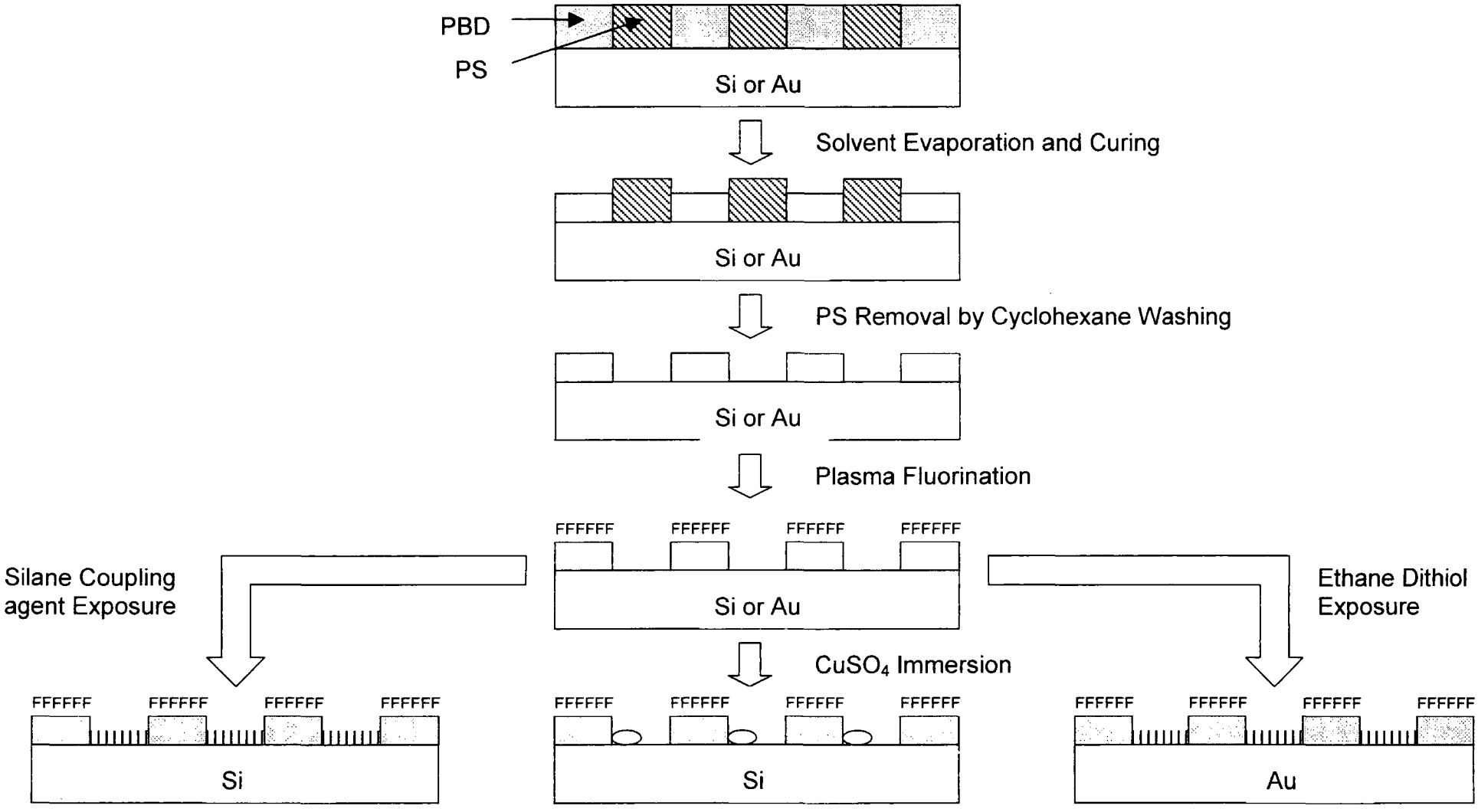

Scheme 3.1 Steps Involved in Production of Bifunctional Surfaces and $CuSO_4$ Arrays

3.2 Polymer Segregation

3.2.1 Introduction

Phase segregation can occur in polymer blends where the components have almost any chemical difference.[1] The immiscibility of two polymers can be predicted in terms of enthalpy and entropy according to the Flory-Huggins theory, Equation 3.1.

Equation 3.1

$$\Delta G^{M} = kT[\{N_A \ln \phi_A + N_B \ln \phi_B\} + \{N_A \phi_B \chi_{AB}\}]$$

Entropic term Entalpy term

where ϕ represents the volume fraction and N represents the statistical chain length. The first term in parenthesis describes the entropy of mixing, in the case of large polymer molecules this is small and so we consider the enthaly contribution. The Flory-Huggins parameter χ_{AB} can be evaluated using solubility parameters, Equation 3.2.

Equation 3.2

$$\chi_{AB} = \frac{V_R}{RT}(\delta_A - \delta_B)^2$$

where δ represents the solubility parameter. In general the more positive the value, the more immiscible the polymers are, however interactions such as hydrogen bonding are not catered for by this theory. Guideline threshold values for $\Delta\delta$ are presented in the polymer handbook[2] according the the degree of polymer / polymer interaction predicted for a given system. In the case of

apolar polymers, values of $\Delta\delta$ greater than 1.0 are predicted to lead to miscibility.

Segregated polymers are of much interest due to their use in paints, adhesives and lubricants, and potential use in optics, microelectronics and for microelectronic patterning.[3,4,11] Phase segregation of multi-component polymer systems has been widely studied in the bulk[5,6,7,8] and also in thin films.[3,4,9,10,11,12,13]

When considering phase separation in thin polymer films we must consider the effects of the air and substrate interfaces as well as the polymer separation dynamics.[3,9]

Many different morphologies have been seen in segregated multi-component polymer thin films. The de-mixing that gives rise to this morphology takes place during the spin coating procedure.[13] Some control may be exercised over pattern formation by judicious choice of film thickness,[10] different affinities of a component for one or both interfaces,[12,14,15,16] the ratio of the polymers in the blend,[11] and also the solvent from which the film is cast.[10]

It has been observed that for thin polymer films annealed to achieve thermodynamic equilibrium, that purely two dimensional spinodal decomposition may occur, leading to polymer domains which extend from the air / polymer interface through to the substrate polymer interface.[4,12] Thus selective removal of one of the components by solvent washing leads to formation of holes between both interfaces.[4]

Tapping Mode AFM is a useful technique in the analysis of polymer blends of differing physical character.[13] This is due to the development of phase imaging technology allowing mapping of heterogeneous surface properties.[17]

Phase differences can be attributed to several factors including: elasticity,[18] hydrophobicity,[19,20] adhesion,[21] and energy dissipation.[17] This facilitates imaging which differentiates between regions of physically different materials as is found in some phase segregated polymer films.[13,22] The degree of phase change measured is also dependant upon the set point to free amplitude ratio used, and shows variance and even reversal according to this ratio.[13,22] The dependence of phase shift on the set point value may be better understood by correlation of phase distance curves for the materials present on the surface.[20] Similarly amplitude distance curves for varying materials may also be correlated to understand height artifacts introduced by the tapping parameters. Such height artifacts typically only alter the height measurement of soft materials by less than 10 nm.[18,20]

3.2.2 Experimental

Varying percentages of polybutadiene (Aldrich, M_w = 420,000, 36 % cis, 55% trans 1,4 addition, 9% 1,2 addition) and polystyrene (Aldrich, M_w = 280,000) dissolved in toluene (BDH, 99.5%) to make a 1% w/v solution were deposited onto silicon wafers, gold substrates and KBr discs using a spin coater (Cammax Precima) operating at a speed of 2000 rpm (including the 100% polybutadiene film). All films were subsequently annealed at 120°C for 1 hour under vacuum, in order to enhance phase separation of the polymer components and remove solvent entrapped in the polymer films.[23] Curing of these films was performed in an oven open to atmosphere at 165°C for 3 hours.

Solvent washing of polymer films was performed by 1 minute submergence in cyclohexane (Prolabo 99%), followed by complete drying under atmospheric conditions, before proceeding to any further step. After washing

the films were stored for 24 hours prior to analysis to reduce solvent swelling effects.

AFM micrographs were acquired with a Digital Instruments Nanoscope III. Damage to the tip and sample surface was minimised by using Tapping Mode AFM.[24]

XPS spectra were recorded on a VG escalab MkII spectrometer equipped with an unmonochromated Mg K_α X-ray source (1253.6 eV) and a hemispherical analyser. Photoemitted core level electrons were collected at a fixed take-off angle (75° away from the sample surface) with electron detection in constant analyser energy (CAE) mode operating at 20 eV pass energy. Instrument calibration was performed using the Au($4f_{7/2}$) reference peak at 83.8 eV with a full-width-at-half-maximum (fwhm) of 1.2 eV. No spectral deterioration due to radiation damage was observed during the time scale required for data accumulation. Elemental sensitivity factors were taken as being C(1s) : F(1s) : O(1s) : N(1s) : Si(2p) : Au($4f_{7/2}$) : S($2p_{3/2}$) Cu ($2p_{3/2}$) equals 1.00 : 0.35 : 0.45 : 0.95 : 0.9 : 0.05 : 0.52 : 0.26.

Infrared analysis of polybutadiene films coated onto polished KBr disks was carried out on a Perkin Elmer Spectrum One instrument operating in transmission mode at 4 cm^{-1} resolution using a DTGS detector.

Film thickness measurements were taken using a reflectometer (NKD 6000). Transmission and reflection curves acquired over a 350-1000 nm range, were fitted to a Cauchy material model, for dielectric materials using a modified Levenberg Marqardt method.[25]

3.2.3 Results

AFM demonstrates the formation of circular domains surrounded by a bulk matrix, following annealing of the 10% polystyrene film. This film was found to be approximately 50nm thick by reflectometry. Increasing the polystyrene content is observed to change the morphology of the film dramatically. It is interesting to note that a height difference is evident between domains of differing polymer composition in all the films, Figure 3.1. A large AFM phase difference is also evident between the circular domains and the bulk polymer after initial annealing under vacuum. Further heating for 3 hours under air (curing) at 165°C reduces the phase difference between the domains, but has little impact on the morphology, Figure 3.2. IR shows that curing of thin (50 nm thick) polybutadiene films at 165°C for 3 hours causes a reduction in the band associated with the CH stretch adjacent to the double bond (B), and an increase in the oxygenated functionalities; alcohol (A and D), and carbonyl (C), Figure 3.3, (full assignments for polybutadiene can be found in Tables 2.1, and 2.3 in chapter 2). The increase in oxygenation is reflected by an increase in surface oxygen content as shown by XPS, Table 3.1.

	Un-Cured	Cured
% C	99 ± 2	85 ± 2
% O	1 ± 2	15 ± 2

Table 3.1 XPS elemental surface composition of 56nm thick polybutadiene films as a function of curing.

Washing of the uncured phase segregated films results in removal of both polymers. However washing of the cured film demonstrates removal of the polystyrene only, Figure 3.4. The depth of the holes formed in the 10% PS film with respect to the bulk material is on average 52 ± 10 nm, as measured by

AFM image analysis. A clear phase difference is seen between the remaining polymer and the regions once occupied by the removed polystyrene, Figure 3.2.

Interestingly the height difference between the pits and the cured polybutadiene after washing is seen to reduce, with increased polystyrene content, Figure 3.5. Film thickness measurements also demonstrated a consistent reduction in film thickness with increased polystyrene content.

We have shown that the phase segregation is independent of substrate for gold and silicon and that in both cases the underlying substrates are visible to XPS after cyclohexane washing, Tables 3.5 and 3.6.

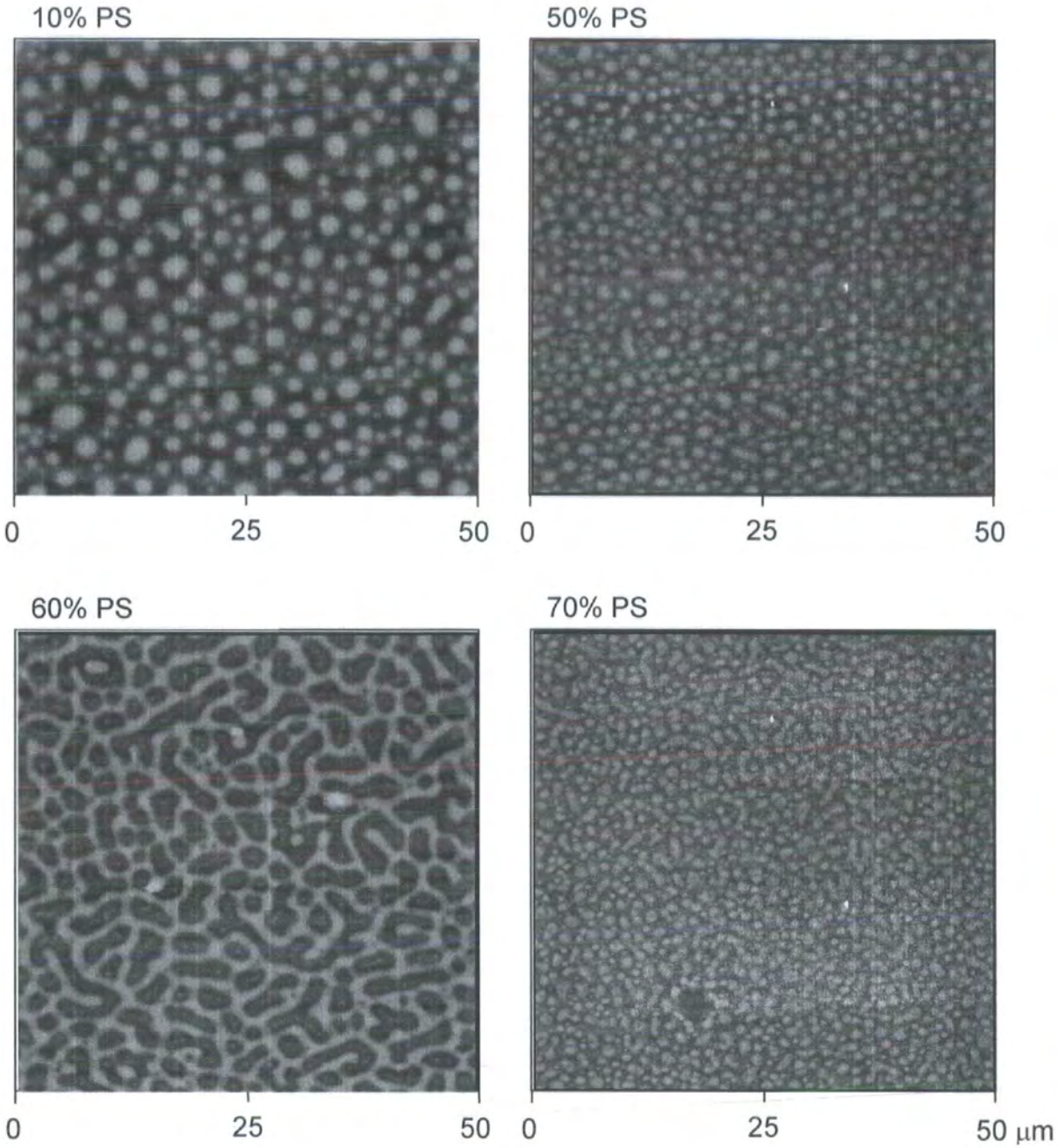

Figure 3.1 AFM height images (x=y=50μm, z=600nm) of PS/PBD blend as a function of PS percentage.

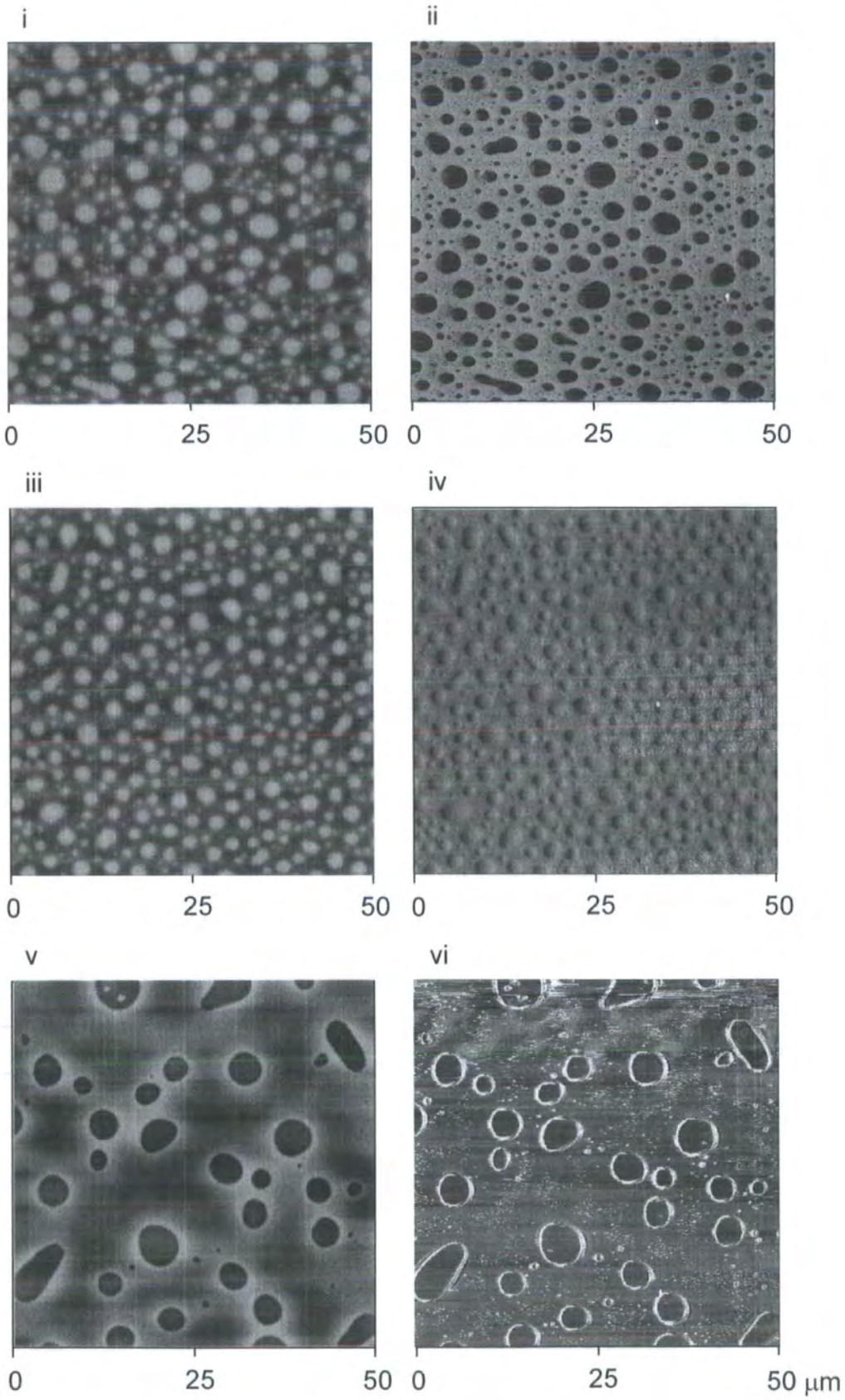

Figure 3.2 AFM height and phase images (x=y=50μm, z=300nm) of 10% PS/PBD films as a function of curing (165°C, 3 hours): (i) uncured height; (ii) uncured phase; (iii) cured height; (iv) cured phase; (v) cured and cyclohexane washed height; (vi) cured and cyclohexane washed phase.

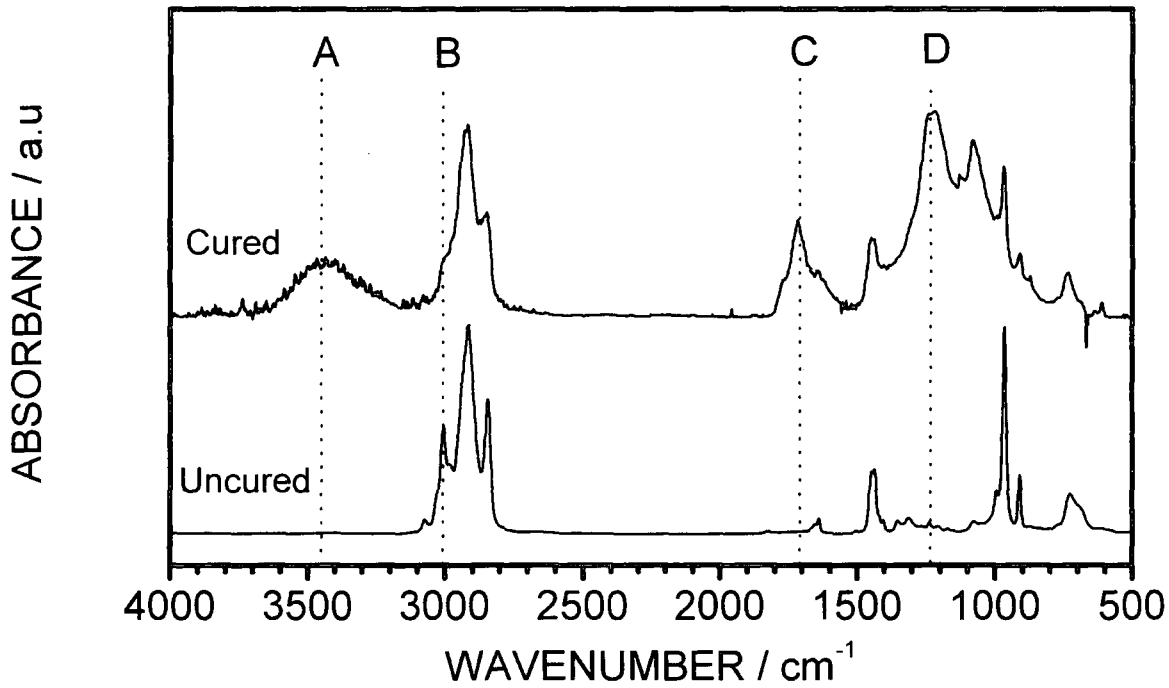

Figure 3.3 IR spectra of cured (165°C, 3 hours) and uncured polybutadiene films.

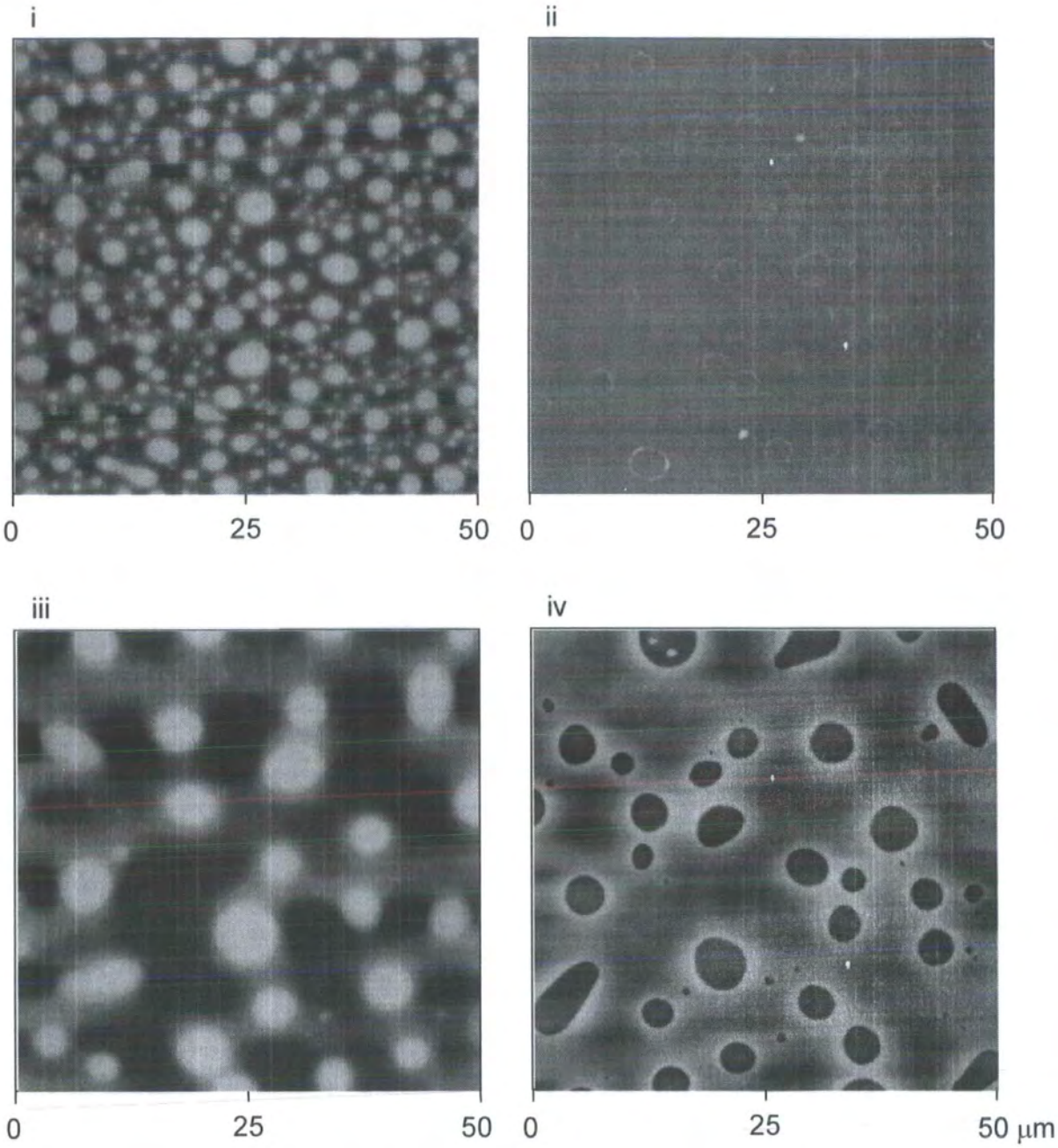

Figure 3.4 AFM height images (x=y=50μm, z=300nm) of cyclohexane washed PS/PBD blend systems: (i) Pre-Curing; (ii) Pre-Cured after wash; (iii) Cured (165°C, 3 hours); (iv) Cured (165°C, 3 hours) after wash.

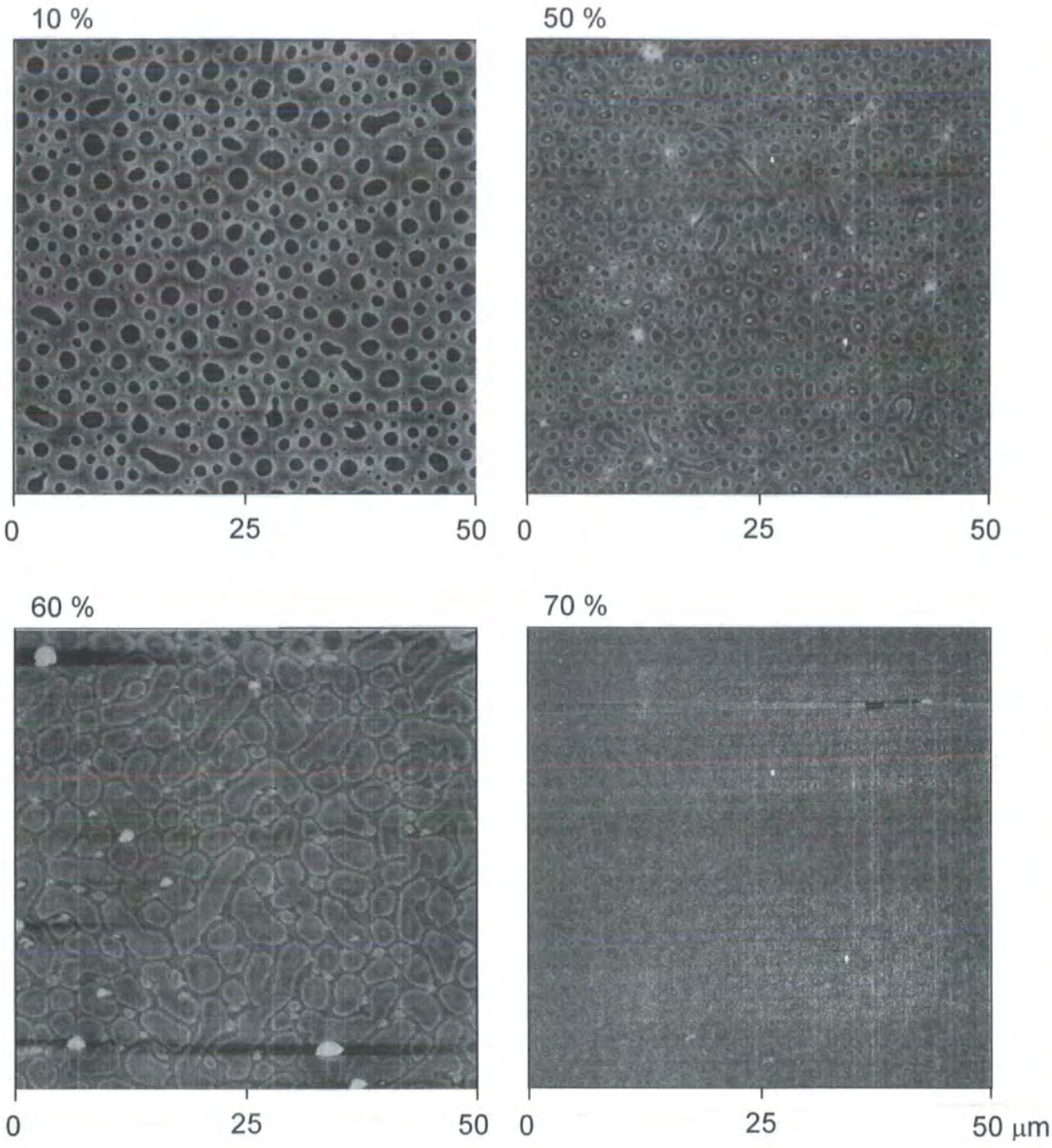

Figure 3.5 AFM height images (x=y=50μm, z=300nm) of cyclohexane washed cured (165°C, 3 hours) PS/PBD as a function of PS content.

3.2.4 Discussion

The immiscibility of polymers can, as has already been mentioned, be calculated using solubility parameters, Equation 3.2. The solubility parameters of polystyrene and polybutadiene are ~14-17 $Mpa^{1/2}$ and ~17.5-19 $Mpa^{1/2}$.[2] Inserting these values in to equation 3.2 will provide a positive value for χ_{AB}, proving the polymers to be immiscible.

The morphology formed by immiscible polymer films is a complex interplay of many factors, including film thickness and polymer composition.[10,11] The morphological variations observed here for systematic increases in polystyrene composition can be attributed not only to the increased volume fraction of polystyrene but also to the effect this has on film thickness.

The presence of height differences between the two polymer domains after solvent evaporation and annealing has been observed elsewhere in the literature and attributed to the system's efforts to achieve thermal equilibrium by the minimization of the surface energies of both polymer components.[13]

The phase difference observed between the polystyrene and polybutadiene regions of the film may potentially be explained in terms of both visco-elastic properties of the polymers and also adhesion between the tip and the polymers. A similar study in the literature reports the storage moduli of polystyrene and polybutadiene to be 1.3 GPa and 1.5 Mpa, respectively. The same study also presents force distance curves showing considerably greater adhesion of the tip to the polybutadiene than to the polystyrene. Both the elasticity and the adhesive differences are responsible for the dramatic phase change.

The reduction in phase difference seen between the polymer domains after annealing in air, is accountable for by the increased hardness of the

polybutadiene due to curing as seen in chapter 2 and also in the literature.[13] This hardening is reported in the literature to increase the storage modulus of the polybutadiene to 1.55 Gpa, i.e similar to that of polystyrene. Force distance curves are again presented by Raghaven *et al*, and these demonstrate a reduction in adhesive interaction for polybutadiene as well as reflecting the increased elastic modulus. Both of these changes may be held responsible for the reduction in phase contrast. The increase in oxygen content in the film suggests that curing occurs via an oxidative cross-linking mechanism as is consistent with results presented in chapter 2.[13,26]

As most common solvents for polystyrene also dissolve polybutadiene, selective removal of one polymer component by solvent washing alone is not easily achievable. Thermal curing of the polybutadiene cross-links the polymer highly rendering it insoluble in solvents capable of dissolving the polystyrene, thus the polystyrene can now be selectively removed by washing with a variety of solvents including cyclohexane and toluene.

The holes remaining in the films after polystyrene removal are of comparable shape and size to the polystyrene domains, suggesting little or no dissolution of the PBD regions. The depth of the holes is also comparable to the thickness of the film as measured by reflectometry, suggesting that the holes penetrate to the substrate. Although previous studies have reported that polystyrene wets both interfaces in polystyrene / polybutadiene blends,[27] the molecular weights were significantly different, with that of polystyrene being several orders of magnitude smaller than that of the polybutadiene. The films analysed also contained significantly greater polystyrene volume fraction. Complete wetting of the interfaces by polystyrene in the aforementioned system is in accordance with the 'plating transition' (of kinetic origin) proposed by

Marko.[28] A further consideration in Geohegan's work is the influence of deuterating some of the polystyrene samples, this leads to an increased molecular weight which can be related to the surface energy by equation 3.3[27], where *A* and *k* are constants relating to a given polymer.

Equation 3.3 $$E = A - \frac{k}{M_W^{2/3}}$$

For the molecular weights and volume fractions it is predicted that both polymers will wet both interfaces.[27] This is consistent with the results presented which suggest that indeed both polymers partially wet both interfaces. Should one of the polymers fully wet the air interface no phase difference would be evident between the regions, the presence of such a phase difference negates complete surface coverage of one component. Considering the polymer / substrate interface, should PBD wet the interface fully, then no phase difference would be observed between the holes and the cured PBD matrix after solvent removal of the PS. Conversely if PS wetted the interface fully, the film would be expected to delaminate under solvent washing conditions. As a distinct phase difference is evident between the holes and the matrix, and the films show no sign of delaminating, both polymer must wet both interfaces. This is confirmed by XPS results presented later in this chapter.

3.3 Plasma Fluorination

3.3.1 Introduction

We have already shown the susceptibility of polybutadiene to CF_4 plasma treatment, providing chemically inert surfaces with very high water contact angles (Chapter 2, Part A). With the aim of selectively fluorinating the polybutadiene regions in the segregated film, we took two approaches: fluorination of both polymer blocks followed by removal of the polystyrene component before and after curing; and removal of the polystyrene followed by fluorination of the remaining polybutadiene.

3.3.2 Experimental

All films used in this section were spun from a 1% w/v solution containing 10% PS and 90% PBD, at a speed of 2000 rpm. These films were subsequently annealed under vacuum, at 120°C for 1 hour to remove entrapped solvent. Curing of the films was performed in an oven open to atmosphere at 165°C for 3 hours.

Plasma treatments were carried out in a cylindrical glass reactor (5 cm diameter, 470 cm^3 volume) with a base pressure of 4×10^{-3} mbar, and a leak rate of better than 6×10^{-9} mol s^{-1}. The system was connected to a two stage rotary pump via a liquid nitrogen cold trap, and the pressure was monitored with a thermocouple pressure gauge. An L-C matching unit was used to minimise the standing wave ratio (SWR) of the power transmitted from a 13.56 MHz R.F. generator to a copper coil wound around the reactor walls. Prior to each plasma treatment, the chamber was scrubbed with detergent, rinsed in propan-2-ol and then further cleaned using a 50 W air plasma for 30 min. Leak rates were calculated as described in chapter 2 and were better than 3×10^{-10}

Mols s^{-1}. A piece of polymer coated silicon wafer was then placed into the centre of the reactor, followed by pumping down to the base pressure. Next CF_4 gas (99.7% purity, Air Products) was admitted into the system via a needle valve at a pressure of 2×10^{-1} mbar, and after 5 minutes of gas purge the plasma was ignited. Upon completion of the treatment, the chamber was evacuated, followed by venting to atmosphere.

Sessile drop contact angle measurements were undertaken at 20°C using a video capture apparatus (A.S.T. Products VCA2500XE). The chosen probe liquid was ultrapurified water (BS 3978 Grade 1).

Toluene rinsing involved pipetting 20 ml toluene <BDH 99.5%> evenly over the surface of the polymer film. The film was then allowed to dry under atmospheric conditions, before proceeding to any further step. After washing the films were allowed to stand for 24 hours prior to analysis to reduce solvent swelling effects.

3.3.3 Results

XPS analysis of plasma fluorinated polybutadiene homopolymer films before and after curing demonstrated extensive fluorination of both films, but greater fluorine content in the uncured film, Table 3.2. CF_4 plasma fluorination of the uncured film did not alter the morphology of the thin films as seen by AFM. However subsequent curing or cyclohexane washing of the uncured segregated film after CF_4 plasma treatment severely distorted the original morphology, Figure 3.6. Fluorination after curing and removal of the polystyrene, however, leaves only the fluorinated polybutadiene matrix, with no significant changes in morphology after plasma treatment Figure 3.7

Toluene rinsing of films after any stage of curing, cyclohexane washing, and CF_4 plasma fluorination, does not alter the morphology, save for removal of the polystyrene regions in cured pre-cyclohexane washed films, Figure 3.7.

	Uncured	Cured
% Carbon	39 ± 2	36 ± 2
% Oxygen	1 ± 2	13 ± 2
% Fluorine	60 ± 2	51 ± 2

Table 3.2 XPS elemental composition of CF_4 plasma treated (20 W, 20 s), cured and uncured poybutadiene films.

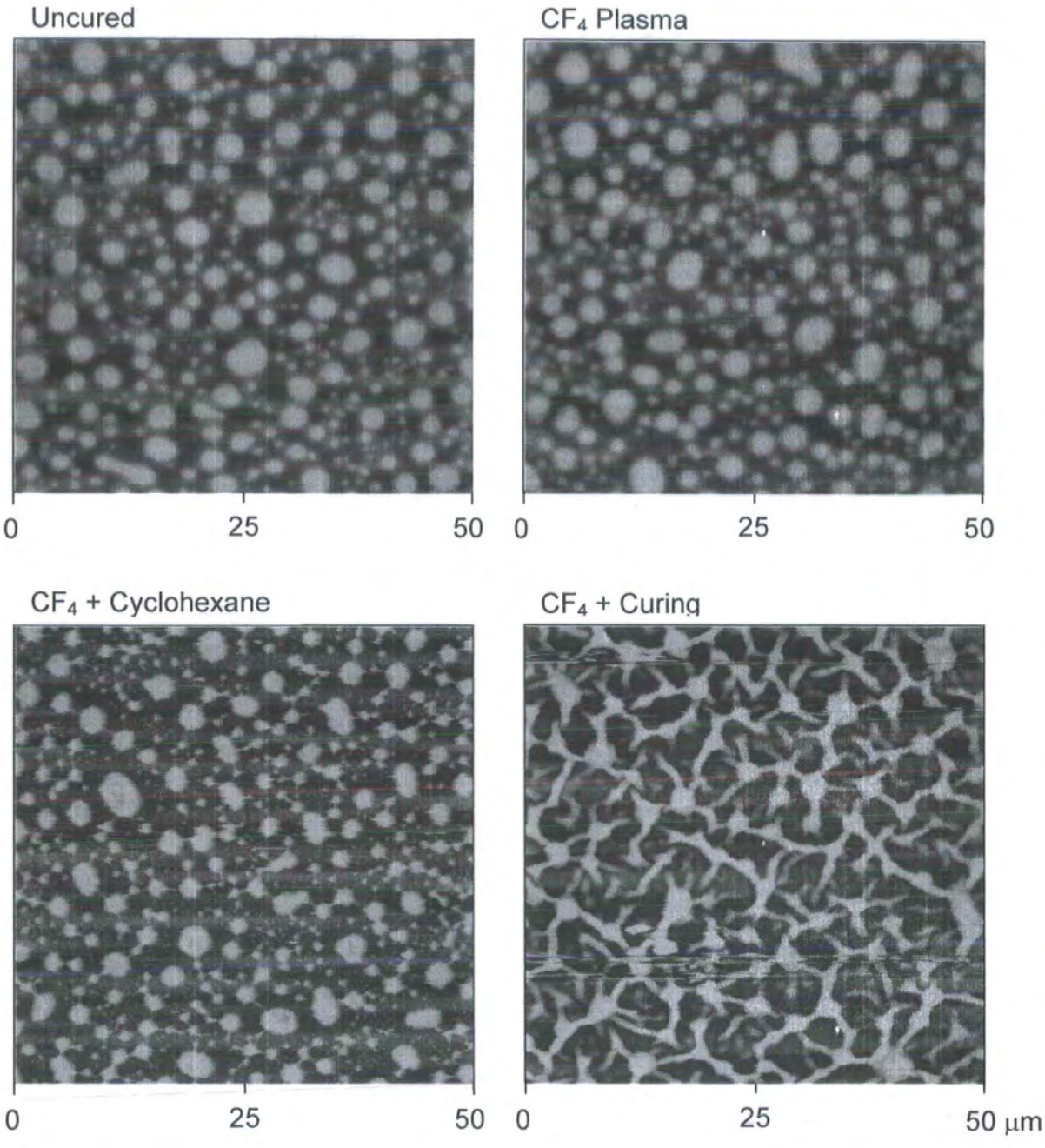

Figure 3.6 AFM height images (x=y=50 μm, z=600 nm) of uncured polymer blend films (10 % PS) and subsequent CF_4 plasma (20 W, 20 s), cyclohexane washing, and curing (165°C, 3 hours) treatments.

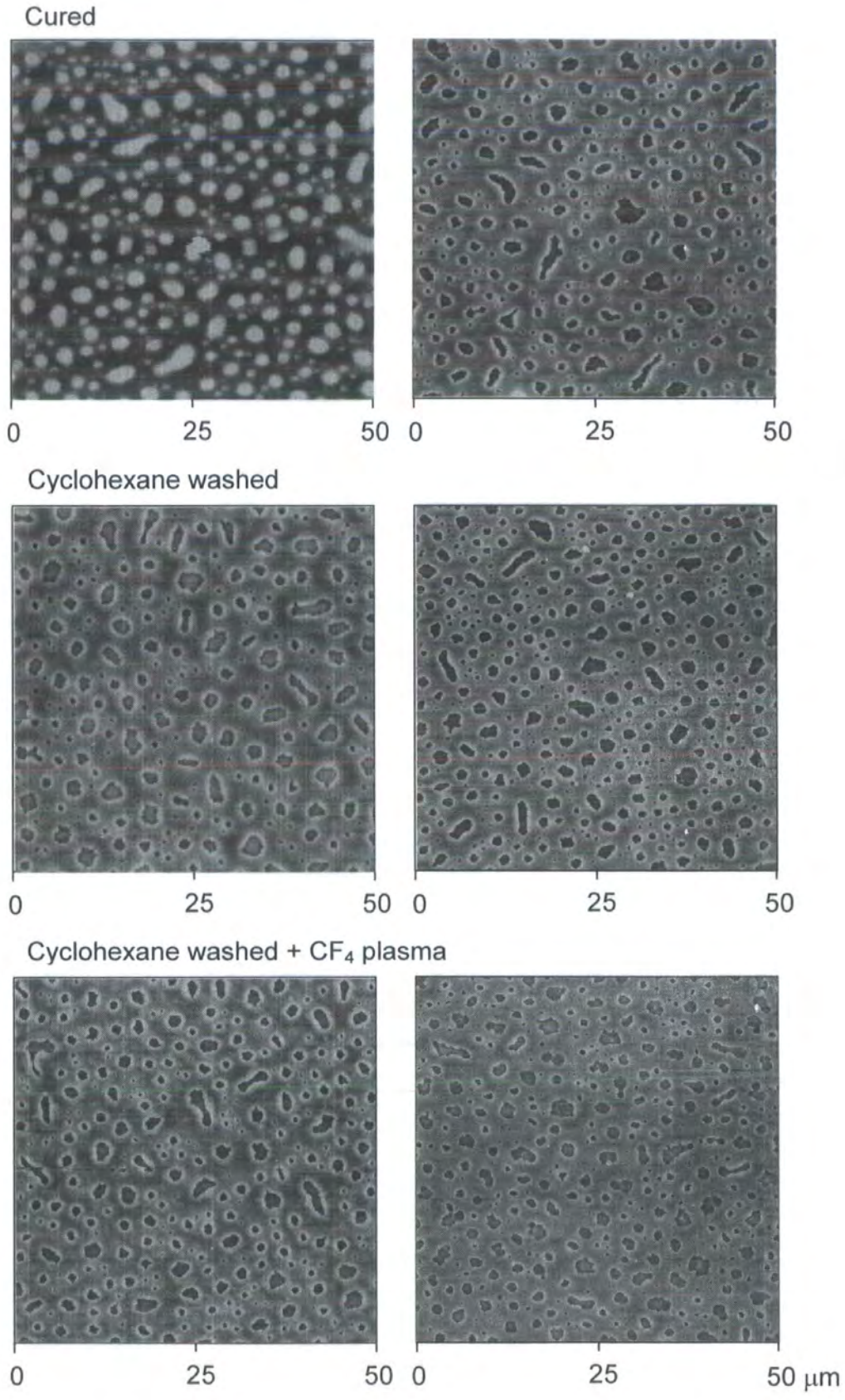

Figure 3.7 AFM height images (x=y=50 μm, z=300 nm) of treated, cured (165°C, 3 hours) polymer blend films (10% PS) as a function of treatment (Left side) and associated toluene washed film at each stage (Right side).

3.3.4 Discussion

CF_4 plasma treatment of polymers has been reported in this thesis and else where in the literature to cause cross-linking at the surface.[29] The results here suggest this to be the case for both PS and PBD as neither is found to be soluble in cyclohexane (a solvent for both[2]) after CF_4 plasma treatment. It is of further interest to note that although there is direct evidence for surface cross-linking of the PBD no roughening is observed. As the film is of the order of 50 nm thick, this is consistent with earlier results demonstrating thickness dependency of this surface roughening by the plasma.

Although the surface cross-linking does prevent removal of the underlying polymer, it appears that solvent can still permeate the cross-linked membrane, and to a degree swell or dissolve the underlying polymers, thus causing the disruption seen in the film morphology. Also the presence of a cross-linked membrane at the surface is most likely responsible for the disruption of the morphology upon annealing. This could either be attributed to a change in thermal equilibrium morphology with the presence of the cross-linked surface, or alternatively due to the restricted mobility of the underlying polymers. With the consideration of polymer mobility during annealing, it has been observed that the frequency and size of the polymer domains can vary somewhat from film to film. This may potentially be due to the differences in thickness of films which may constrain the dimensions of the domains formed.[10]

From these results it is clear that to attain our desired morphology we must remove the PS before CF_4 plasma treatment. By first thermally curing the PBD, then removing the polystyrene by cyclohexane washing, and finally plasma fluorinating we are left with the desired composite surface comprising exposed substrate and highly fluorinated polybutadiene. The reduced degree of

fluorination observed for cured polybutadiene in comparison to that of uncured PBD is in accordance with the reduction in unsaturated carbon centers available for fluorination at the surface,[30] due to the oxidative cross-linking mechanism. The cyclohexane washed morphology is found to be unaltered by plasma fluorination. This is as expected for a pure CF_4 plasma as little or no etching is reported for such plasmas.[31,32,33,34]

Toluene washing again demonstrates the resistance of the cross-linked network to solvents at each stage of the process.

3.4 Bifunctionalisation

3.4.1 Introduction

As we have now produced a composite surface comprising chemically inert fluoropolymer regions and regions of potentially reactive exposed substrate, we attempt to selectively functionalise the exposed substrate. Silicon with surface SiO_2 groups is well known to undergo reaction with silane coupling agents,[36] likewise gold is well known for surface reactions with molecules containing a thiol group.[35] Further to these functionalisations, we attempt to selectively deposit metal salts into the higher surface energy pits, in a similar manner to that presented in chapter 2.

3.4.2 Experimental

Siloxane coupling agent reactions were carried out in the liquid phase by rinsing of the samples in 3-aminopropyltrimethoxy silane (Fluorochem 97%), followed by methanol (Merck 98.5%) washing to remove extraneous coupling agent. All reactions were carried out under a dry nitrogen atmosphere in a glove box.

Surface functionalisation using thiols was carried out by rinsing in 1,2-ethanedithiol (Fluka 98%), and subsequent washing in methanol to remove extraneous thiol.

Salt crystal deposition work was performed by submergence of the film sample into a 0.5 molar $CuSO_4$ solution. The films were removed carefully at perpendicular to the solution surface so as to prevent large droplets remaining anywhere on the sample surface.

3.4.3 Results

3.4.3.1 Bifunctionalisation using 3-Aminoproplytrimethoxysilane

Exposure of a sample with a surface comprising fluoropolymer and exposed silicon to the 3-aminopropyl trimethoxysilane resulted in reaction with only the exposed silicon regions. This is supported by the functionalisation of clean silicon, and lack of chemical change in fluorinated polybutadiene after exposure to the silane, Table 3.3. AFM demonstrates no topographic changes after treatment with the silane, Figure 3.8.

	Silicon wafer		Polybutadiene		Cyclohexane washed cured mixed phase	
	Before silane	After silane	Before silane	After silane	Before silane	After silane
% C	1 ± 2	39 ± 2	35 ± 2	36 ± 2	35 ± 2	40 ± 2
% O	52 ± 2	43 ± 2	13 ± 2	12 ± 2	15 ± 2	14 ± 2
% F	29 ± 2	6 ± 2	52 ± 2	52 ± 2	48 ± 2	44 ± 2
% Si	18 ± 2	14 ± 2	0	0	2 ± 2	1 ± 2
% N	0	4 ± 2	0	0	0	1 ± 2

Table 3.3 XPS elemental composition of CF_4 plasma treated (20 W, 20 s) samples before and after rinsing in 3-aminopropyltrimethoxysilane.

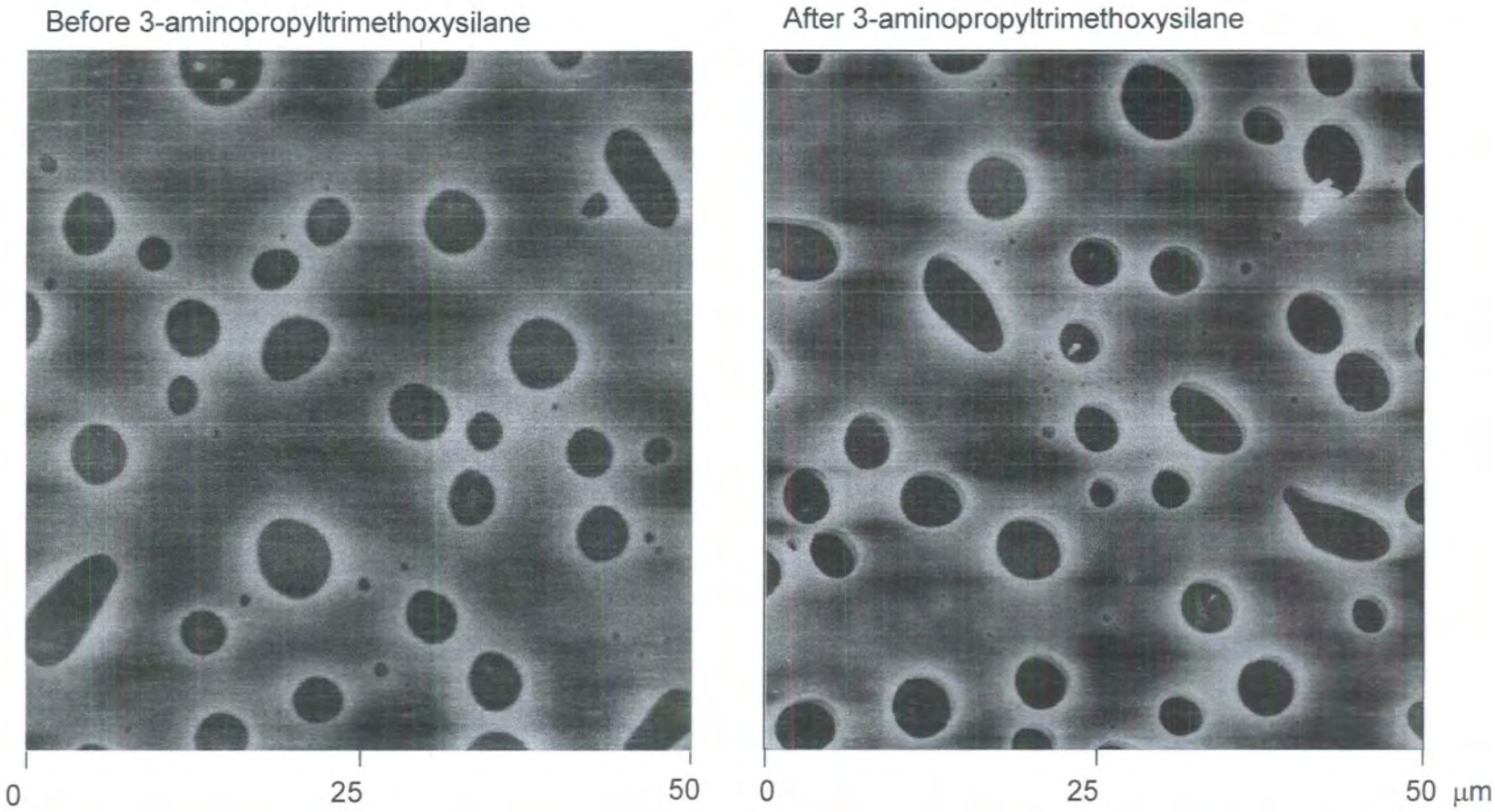

Figure 3.8 AFM height images (x=y=50 μm, z=300 nm) of cured phase separated polymer blend films following cyclohexane washing and CF_4 plasma treatment (20 W, 20 s).

3.4.3.2 Bifunctionalisation using 1,2-Ethanedithiol

XPS analysis showed that exposure of the tailored sample to 1,2-ethanedithiol resulted in thiol functionalisation of only the exposed gold regions. This is supported by exposure of gold and fluorinated polybutadiene to the thiol, which demonstrates thiol functionalisation on only the gold sample, Table 3.4. AFM demonstrated that the film morphology was unaltered by the 1,2-ethanedithiol immersion, and that no morphological changes resulted from use of a gold substrate, Figure 3.9.

	Gold		Polybutadiene		Cyclohexane washed cured mixed phase	
	Before thiol	**After thiol**	**Before thiol**	**After thiol**	**Before thiol**	**After thiol**
% C	22 ± 2	34 ± 2	36 ± 2	37 ± 2	40 ± 2	45 ± 2
% O	4 ± 2	2 ± 2	13 ± 2	12 ± 2	11 ± 2	10 ± 2
% F	19 ± 2	15 ± 2	51 ± 2	51 ± 2	47 ± 2	42 ± 2
% Au	55 ± 2	41 ± 2	0	0	2 ± 2	1 ± 2
% S	0	8 ± 2	0	0	0	2 ± 2

Table 3.4 XPS elemental composition of CF_4 plasma treated (20 W, 20 s) films, before and after immersion in 1,2-ethanedithiol.

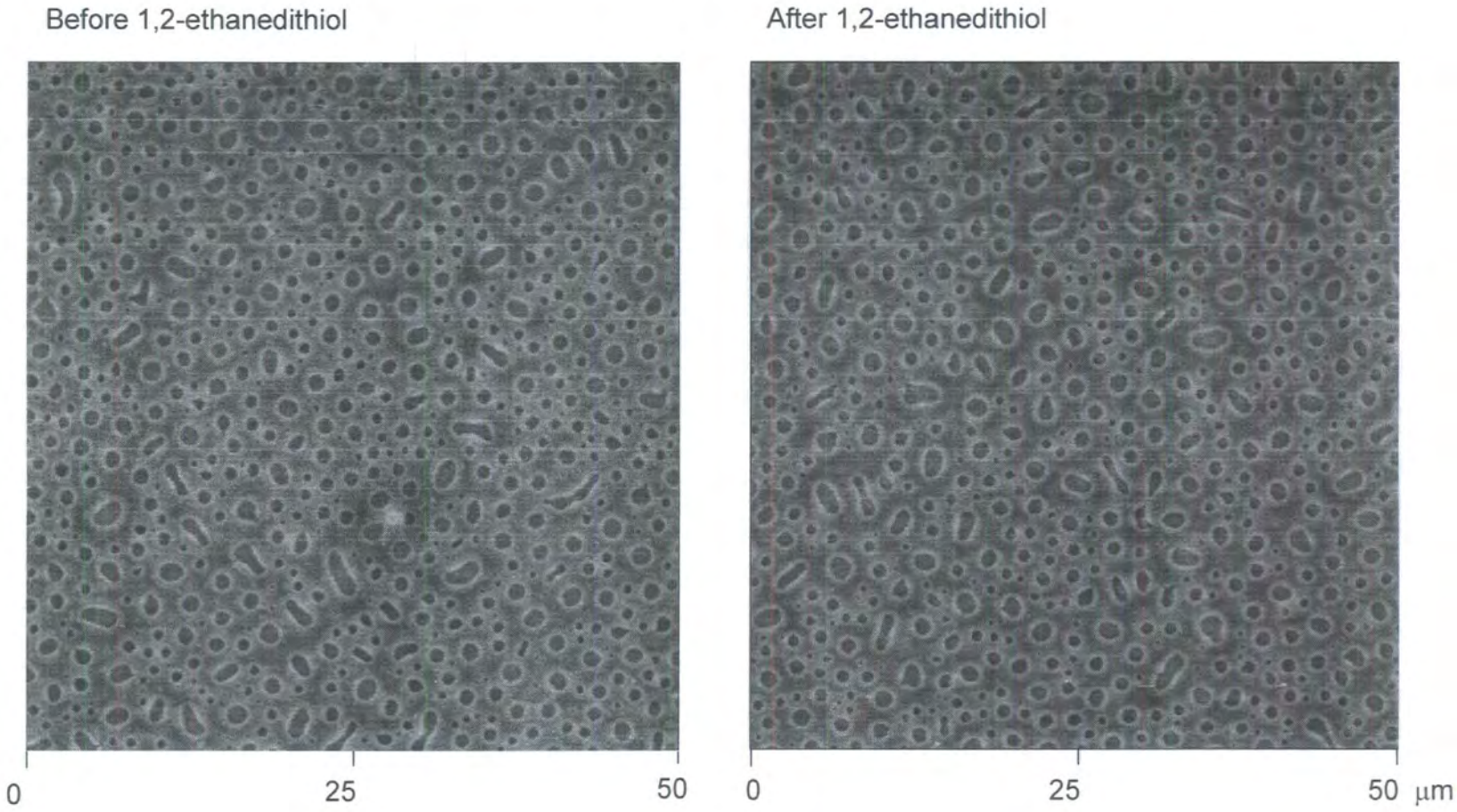

Figure 3.9 AFM height images x=y=50 μm, z=300 nm) of cured phase separated polymer blend films on a gold substrate following cyclohexane washing and CF_4 plasma treatment (20 W, 20 s).

3.4.3.3 Selective $CuSO_4$ deposition

Contact angle analysis using water as a probe liquid on both fluorinated polybutadiene and silicon, showed a contact angle difference of around 59°, with the fluorine-rich polymer surface exhibiting a contact angle of around 107°. Dipping of the tailored films into a $CuSO_4$ solution and subsequent drying produces small crystals in the exposed silicon regions, as shown by AFM, Figure 3.10. These are shown to be $CuSO_4$ by XPS, Table 3.5.

	Before $CuSO_4$	After $CuSO_4$
% C	35 ± 2	34 ± 2
% O	15 ± 2	15 ± 2
% F	48 ± 2	46 ± 2
% Si	2 ± 2	1 ± 2
% S	0	2 ± 2
% Cu	0	2 ± 2

Table 3.5 XPS elemental composition of cyclohexane washed cured segregated films before and after immersion 0.5 molar $CuSO_4$ aqueous solution.

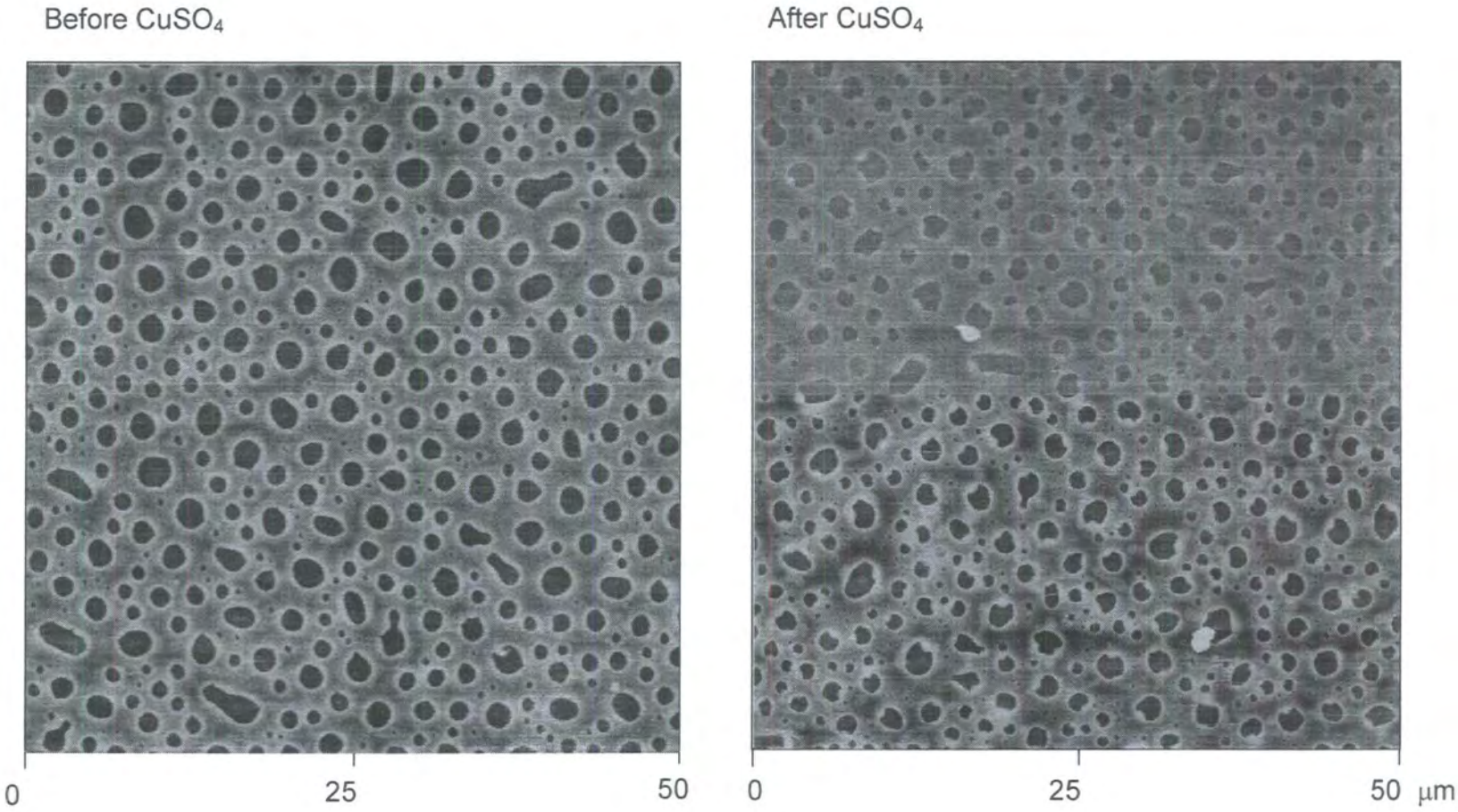

Figure 3.10 AFM height images (x=y=50 μm, z=300 nm) of cured phase separated polymer blend films following cyclohexane washing and CF_4 plasma treatment (20 W, 20 s).

3.4.4 Discussion

Self assembling systems have found application to the formation of patterned surfaces expressing bi-functionality. Many of these are formed by the selective wetting of a patterned region with a functionalised alkanethiol, followed by subsequent wetting of unfunctionalised regions of the substrate with a second functionalised alkanethiol.[40] Here although patterns are random, the formation of surface morphologies is entirely through self assembly.

3.4.4.1 Bifunctionalisation using 3-Aminopropyltrimethoxy silane

The selective reaction of silicon only, upon exposure to 3-aminopropyl trimethoxysilane is consistent with reactions of silanes with surface SiO_2 groups in the literature,[36] and the chemical inertness of the fluoropolymer. The drop in surface oxygen content is consistent with the reaction of surface SiO_2 reaction with the coupling agent. The high degree of fluorination on the silicon surface after CF_4 plasma exposure is consistent with formation of SiF_x (x = 1,2,3,4) groups at the surface.[37] These are reported chemically stable except under severe conditions.[38] Reduction in fluorination after silane exposure may account for the increased hydrocarbon coverage of the surface after treatment due to contamination, as is reflected by the large increase in carbon at the surface.

The degree of exposed silicon is clearly lower than would be expected given the area of the surface removed during cyclohexane washing. This is accountable for by hydrocarbon contamination during the washing process. This contaminant layer is then fluorinated during the CF_4 plasma treatment of the film. This fluorinated hydrocarbon coverage is believed to be loosely bound to the substrate, as the degree of silane functionalisation measured is

somewhat greater than expected for the exposed silicon (as measured by XPS). This is supported by the drop in fluorine content at the surface after functionalisation and washing, suggesting removal of some of the fluorinated contaminant. Therefore it is believed that the loosely bound contaminant layer is perturbed by the liquid phase silane reaction. The lack of change seen by AFM is consistent with the small increases in silane functionalisation and the lack of reaction with the fluorinated polybutadiene.

3.4.4.2 Bifunctionalisation using 1,2-Ethanedithiol

A similar explanation as for the selective silane functionalisation can be applied here. Again the selective reaction of the thiol with the substrate is as expected given the reactivity of thiols to gold[39] and the inert nature of the fluoropolymer. The low percentage of exposed gold is again attributed to a loosely-bound fluorinated hydrocarbon coverage. The greater degree of thiol functionalisation than would be expected, given the degree of exposed gold, again suggests that the thiol also perturbs the contaminant layer to gain access to the underlying substrate.

The consistent morphology of the film with that seen for films supported on silicon is as expected, as, although there are changes in the polar nature of the substrate, neither polymer component is polar.[2]

3.4.4.3 Selective $CuSO_4$ deposition

The location of the $CuSO_4$ crystals in the lower height and higher surface energy regions of the polymer film is consistent with results elsewhere in this thesis and the literature[40]. Both the surface energy and height differences present a driving force for selective location of water droplets in the holes, and

correspondingly the selective deposition of $CuSO_4$, after evaporation. Although it is difficult to evaluate precisely the surface energy in the holes due to the fluorinated hydrocarbon contaminant layer, the contact angle will certainly be lower than that presented by the fluorinated PBD. Again it is plausible that $CuSO_4$ immersion would perturb any fluorinated contaminant layer thus exposing the wettable silicon substrate.

3.5 Conclusions

It is possible to generate a surface comprising both polybutadiene and underlying substrate through de-mixing of a polystyrene / polybutadiene thin film, thermal curing of the polybutadiene, and subsequent solvent washing. Through successive plasma and wet chemical processes these surfaces can be used to produce a templated bifunctional surface. Following plasma fluorination, local differences in surface energy can be used to selectively deposit salt crystals.

Potentially the functionalisation of the exposed substrate could be significantly improved by the incorporation of a cleaning step prior to exposure to either the silane coupling agent or thiol. Given the inert nature of the cross-linked fluorinated polybutadiene it may prove interesting to investigate not only further solvent washing, but more corrosive cleaning means such as air or oxygen plasmas.

3.6 References

1 Krausch, G. *Materials Science and Engineering*, **1995**, R14, 1.

2 Polymer Handbook Fourth Edition, Eds., Brandrup, J., Inmmergut, E. H., Grulke, E. A. John Wiley & sons Inc., New York, **1999**.

3 Akpalu, Y.A., Karim, A., Satija, S.K., Balsara, N.P. *Macromolecules,* **2001**, 34, 1720.

4 Zhu, S., Liu, Y., Rafailovich, M.H., Sokolov, J., Gersappe, D., Winesett, D.A., Ade, H. *Nature*, **1999**, 400, 49.

5 Hashimoto, T. *Materials Science and Technology*, Thomas. E.L., Ed.; VCH: Weinham, **1993**: Vol. 12, p251.

6 Balsara, N.P.: Jonnalagadda,S. V.; Lin, C. C.; Han. C. C.; Krishnamoorti, R. *J. Chem. Phys.* **1993**, 99, 10011-10020.

7 Lin, C. C.; Jeon, H. S.; Balsara, N. P.; Hammouda, B. *J. Chem. Phys.* **1995**, 103, 1957-1971.

8 Sung, L.; Nakatani, A. I.; Han, C. C.; Karim, A.; Douglas, J. F.; Satija, S. K. *Physica B*, **1998**, 241-243, 1013-1015.

9 Boltau, M., Walheim, S., Mlynek, J., Krausch, G., Steiner, U. *Nature*, **1998**, 391, 877.

10 Walheim, S., Boltau, M., Mlynek, J., Krausch, G., Steiner, U. *Macromolecules*, **1997**, 30, 4995.

11 Walheim, S., Ramstein, M., Steiner, U. *Langmuir*, **1999**, 15, 4828.

12 Straub, W., Bruder, F., Brenn, R., Krausch, G., Bielefeldt, H., Kirsch, A., Marti, O., Mlynek, J., Marko, J.F. *Europhys. Lett.*, **1995**, 29, 353.

13 Raghavan, D., Gu, X., Nguyen, T., Vanlandingham, M., Karim, A. *Macromolecules*, **2000**, 33, 2573.

14 Jones, R. A., Norton, L. J., Kramer, E. J., Bates, F. S., Wiltzius, P. *Phys. Rev. Lett.*, **1991**, 66, 1326.

15 Bruder, F., Brenn, R. *Phys. Rev. Lett.*, **1992**, 69, 624.

16 Krausch, G., Kramer, Rafailovich, M. H., Sokolov, J. *Appl. Phys. Lett.*. **1994**, 64, 2665.

17 Bar, G.; Thomann, Y.; Brandsch, R.; Cantow, H. J.; Whangbo, M. –H. *Langmuir* **1997**, *13*, 3807.

18 Brandsch, R.; Bar, G. *Langmuir* **1997**, *13*, 6349.

19 Refier, D.; Windeit, R.; Kumpf. R. J.; Karbach, A.; Fuchs, H. *Thin Solid Films* **1995,** *264,* 148.

20 Chen, X.; Davies, M. C.; Roberts, C. J.; Tendler, S. J. B; Williams, P. M.; Davies, J.; Dawkes, A. C.; Edwards, J. C. *Ultramicroscopy* **1998**, *75*, 171.

21 Finot, M. O.; McDermott, M. T. *J. Am. Chem. Soc.* **1997**, *119*, 8564.

22 Pickering, J. P., Vancso, G. J. *Polymer Bulletin*, **1998**, 40, 549.

23 Frank C. W., Rao, V., Despotopoulou, M. M., Pease, R. F. W., Hinsberg, W. D., Miller, R. D., Rabolt, J. F. *Science*, **1996**, 273, 912.

24 Zhong, Q., Innis, D., Hjoller, K., Elings, V. B. *Surf. Sci.*, **1993**, 14, 3045.

25 Lovering, D. INKD-6000 Technical Manual. Aquila Instruments, Cambridge, UK, **1999**.

26 Dickie, R. A., Carter, R. O., Hammond, J. S., Parsons, J. L., Holubka, J. W. *Ind. Eng. Chem. Prod. Res. Dev.*, **1984**, 23, 297.

27 Geoghegan, M., Jones, R. A. L., Payne, R. S., Sakellariou, P., Clough, A. S., Penfold, J. *Polymer*, **1994**, 35, 2019.

28 Marko, J.F. *Phys. Rev.*, **1993**, 48, 2861

29 Inagaki, N., Kobayashi, N., Matsushima, M. *J. Membr. Sci.*, **1998**, 38, 85.

30 Hopkins, J., Badyal, J. P. S. *J Phys. Chem.*, **1995**, 99, 4261.

31 Wang J.; Feng D.; Wang H.; Rembold M.; Thommen F. *J. Appl. Polym Sci.*, **1993**, 50, 585.

32 Egitto, F. D. *Pure Appl. Chem.*, **1990**, 62, 9, 1699

33 Truesdale, E. A.; Smolinksky, G. *J. Appl. Phys.*, **1979**, 50, 11, 6594.

34 Klausner, M.; Loh, I. H.; Baddour, R. F.; Cohen, R. E. *Polym. Mater. Sci. Eng.*, **1987**, 56, 227.

35 Xia, Y., Whitesides, G. M. *Angew Chem. Int. Ed.*, **1998**, 37, 550.

36 Wirth, M. J., Fairbank, R. W. P., Fatunmbi, H. O. *Science*, **1997**, 275, 44.

37 Shirafuji, T., Stoffels, W. W., Moriguchi, H., Tachibana, K. *J. Vac. Sci. Technol., A*, **1997**, 15, 209.

38 Xia, Q. H., Hidajat, K., Kawi, S. *Stud. Surf. Sci. Catal.*, **2000**, 129, 49.

39 Nuzzo, R.G., Allara D. L. *J. Am. Chem. Soc.*, **1983**, 105, 4481.

40 Qin, D., Xia, Y., Xu, B., Yang, H., Zhu, C., Whitesides, G. M. *Advanced Materials*, **1999**, 11, 1433.

Chapter 4

Selective Plasma Functionalisation of a Segregated Block Copolymer

4.1 Introduction

Phase segregation of block copolymers has been widely reported in the literature,[1,2,4] and is the subject of much interest due to the insight provided into macromolecular self assembly,[3] and potential applications in sub micron lithography.[4,5]

The segregation of the polymer blocks occurs as a result of incompatibility of the component polymers. As described previously immiscibility of polymers can be predicted using the Flory-Huggins parameter, which can in turn be calculated using solubility parameters.

Morphological evolution in block copolymers can be controlled by variation of the Flory-Huggins parameter, which may in turn be controlled by variation of the monomers used, the molecular weight, and by varying the monomer ratio of one or more blocks.[6,7,8,9,10]

Surface segregation of one component of a block copolymer may also occur and has been widely observed for a range of polymer systems in the literature.[11,12,13]

Here we have characterised the surface of a phase segregated block copolymer using XPS, AFM and force volume imaging, to determine the respective surface components. Through the production of a surface comprising two chemically different polymer components, we aim to tailor the surface energies of each component independently, through exposure to successive CF_4 and DBD plasma treatments. In doing this we then hope to use the surface as a template for surface-energy-guided selective salt deposition.[14]

Plasma treatment of polymers using CF_4 has been widely reported in the literature to introduce CF, CF_2 and CF_3 groups at the polymer surface.[15,16,17]

The introduction of these fluorinated groups has been shown to increase the hydrophobic character of the polymer.[18,19]

Dielectric barrier air discharge treatment of polymers is reported to markedly increase the level of surface oxygenation.[20] Through the incorporation of polar oxygen containing groups these treatments increase the wettability of the treated polymers.

4.2 Experimental

A 11 % w/v solution of Kraton D1101c (Shell chemical company), a block copolymer containing 31% polystyrene by mass, dissolved in toluene (BDH, 99.5%) was deposited onto silicon wafers using a spin coater (Cammax Precima) operating at a speed of 2000rpm. Annealing was carried out at 120°C for 1 hour in order to cause phase separation and remove solvent entrapped in the films. Un-annealed Kraton films were pumped down to 4 x 10^{-3} mbar overnight to remove entrapped solvent.

Films of pure polystyrene and polybutadiene were spin coated from 10% w/v solutions at a speed of 2000 rpm onto silicon substrates, and subsequently annealed at 120°C for 1 hour.

Plasma treatments were carried out in a cylindrical glass reactor (5 cm diameter, 470 cm^3 volume) with a base pressure of 4 $\times$ 10^{-3} mbar, and a leak rate of better than 6 $\times$ 10^{-9} mol s^{-1}. The system was connected to a two stage rotary pump via a liquid nitrogen cold trap, and the pressure was monitored with a thermocouple pressure gauge. An L-C matching unit was used to minimise the standing wave ratio (SWR) of the power transmitted from a 13.56 MHz R.F. generator to a copper coil wound around the reactor walls. Prior to each plasma treatment, the chamber was scrubbed with detergent, rinsed in

propan-2-ol and then further cleaned using a 50 W air plasma for 30 min. A piece of Kraton-coated silicon wafer was then placed into the centre of the reactor, followed by pumping down to base pressure. Next CF_4 gas (99.7% purity, Air Products) was admitted into the system via a needle valve at a pressure of 2×10^{-1} mbar, and after 5 minutes of gas perge the plasma was ignited. Upon completion of the treatment, the chamber was evacuated, followed by venting to atmosphere.

Dielectric barrier discharge treatments were carried out in a home-made parallel plate silent discharge apparatus. A pulsed discharge voltage of 11kV was applied to the electrodes with a frequency of 244 Hz. The aluminium electrodes were chemically polished and degreased with isopropyl alcohol. The lower electrode was covered with a polyethylene dielectric, on which the samples were placed.

Salt crystal deposition work was performed by submergence of the film sample into a 0.5 molar $CuSO_4$ solution. The films were removed carefully at perpendicular to the solution surface so as to prevent large droplets remaining anywhere on the sample surface.

XPS spectra were recorded on a VG escalab MkII spectrometer equipped with an unmonochromated Mg K_α X-ray source (1253.6 eV) and a hemispherical analyser. Photoemitted core level electrons were collected at a fixed take-off angle (75° away form the sample surface) with electron detection in constant analyser energy (CAE) mode operating at 20 eV pass energy. Instrument calibration was performed using the $Au(4f_{7/2})$ reference peak at 83.8 eV with a full-width-at-half-maximum (fwhm) of 1.2 eV. No spectral deterioration due to radiation damage was observed during the time scale required for data accumulation. Elemental sensitivity factors were taken as

being C(1s) : F(1s) : O(1s) : Si(2p) : Cu ($2p_{3/2}$) equals 1.00 : 0.35 : 0.45 : 0.9 : 0.26.

Sessile drop contact angle measurements were undertaken at 20°C using a video capture apparatus (A.S.T. Products VCA2500XE). The chosen probe liquid was ultrapurified water.

AFM micrographs, force distance curves and force volume images were acquired with a Digital Instruments Nanoscope III. Damage to the tip and sample surface during images was minimised by using Tapping Mode AFM.[21] Force curves and force volume images were obtained using a tip with an experimentally determined spring constant of 0.412nN. Tip deflections were calibrated against a hard metallic substrate. Force volume images are comprised of an array of force curves over a predetermined area, collected automatically by the AFM. The intensity of the pixels reflects the degree of displacement of the retract curve of an individual force curve, at a chosen z-scanner displacement, with dark pixels representing adhesive interactions, and bright pixels representing a repulsive interaction. A corresponding height image is simultaneously generated and used to equilibrate the tip sample separation for each force curve acquisition. From the data collected force volume images can then be presented for a given scanner displacement, and individual force curves can be extracted for any pixel in the array.

Force distance curves provide detailed localised information about the interaction between the tip and the sample, and allow probing of information such as elasticity, hydrophobicity, and adhesion. Each force curve is a plot of the tip deflection as a function of z-scanner displacement. A typical force curve is shown in Figure 4.1. As the tip approaches the sample (A) longer range forces such as electrostatics may be experienced causing either an attractive

(as shown) or repulsive force to deflect the cantilever (B). After contact with the surface (B) the deflection of the cantilever will increase (C) to a predetermined maximum, where the z-scanner displacement is reversed. As the probe withdraws the tip may experience adhesive interaction with the surface (D). Further retraction breaks this adhesive interaction and the cantilever snaps back to a zero displacement position (E).

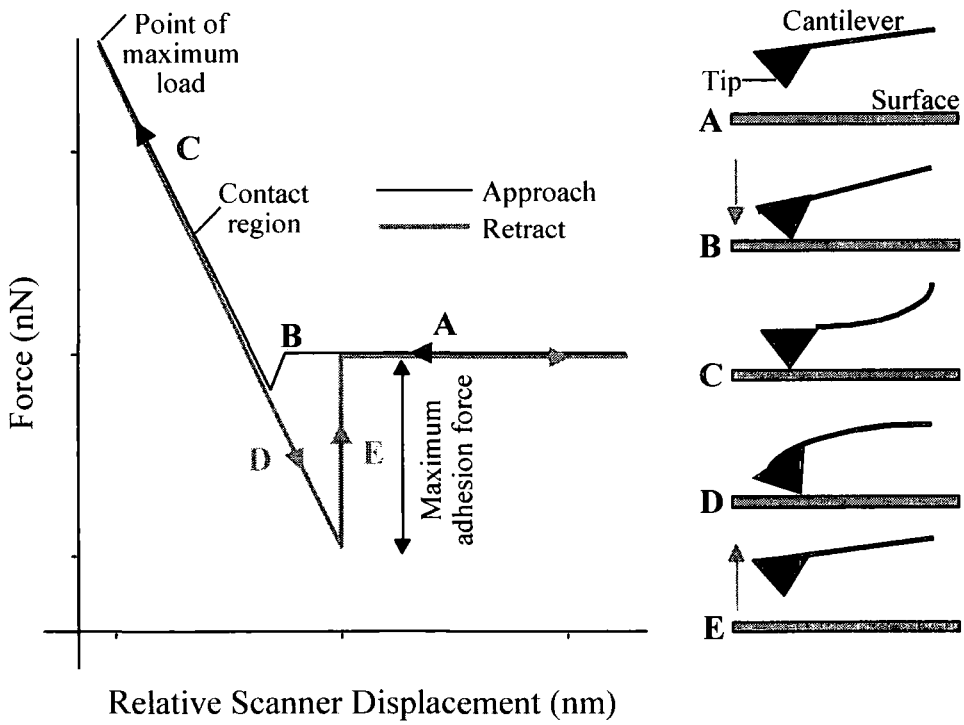

Figure 4.1 Diagram of an idealized force distance curve.

4.3 Results

4.3.1 Segregation

Prior to annealing, the Kraton films have a homogenous surface exhibiting no heterogeneity in both topographic and phase images, as shown by AFM. After annealing, domains, exhibiting a different AFM phase shift from that of the bulk matrix, form at the surface (hereafter these regions are termed 'gaskets'). The films still however exhibits little height variance, Figure 4.2.

Analysis of the π-π^* (291.7 eV)[33] shake up peak in the XPS carbon envelope of annealed and un-annealed Kraton with respect to the homopolymer films, demonstrates surfaces composed of 40% and 12.8% polystyrene respectively, Table 4.1. Force volume imaging of the annealed films, reveals distinct differences between the segregated materials, Figure 4.3. Force curves extracted from the gasket regions show considerably reduced adhesive interaction with respect to curves taken from the surrounding matrix, Figure 4.4.

XPS analysis of the three films reveals high levels of oxygenation in the annealed Kraton, polystyrene and polybutadiene, and a small degree of oxygenation in the un-annealed Kraton, Table 4.2.

	Total Area of Carbon Envelope	**Area of π-π^* Shakeup Peak.**	**Calculated PS Surface Coverage (%)**
PS	8661	368	100
PBD	8614	0	0
Un-annealed Kraton	8950	47	12.8
Annealed Kraton	8478	141	40.1

Table 4.1 Surface composition of polymer films calculated from π-π^* shakeup peaks in XPS carbon envelopes.

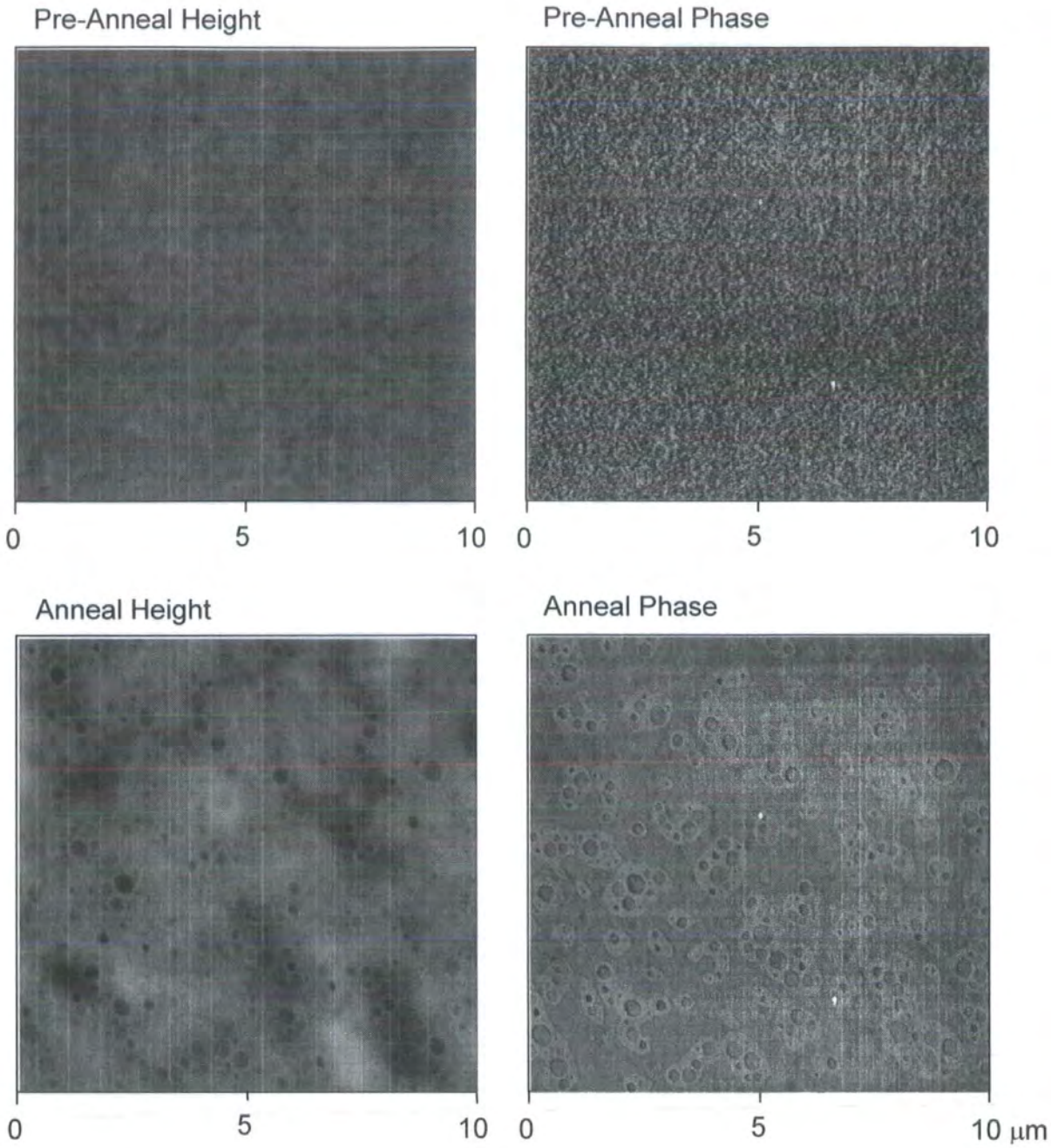

Figure 4.2 AFM height images (x=y=10 μm, z=50 nm) of kraton films before and after annealing (120 °C, 40 min)

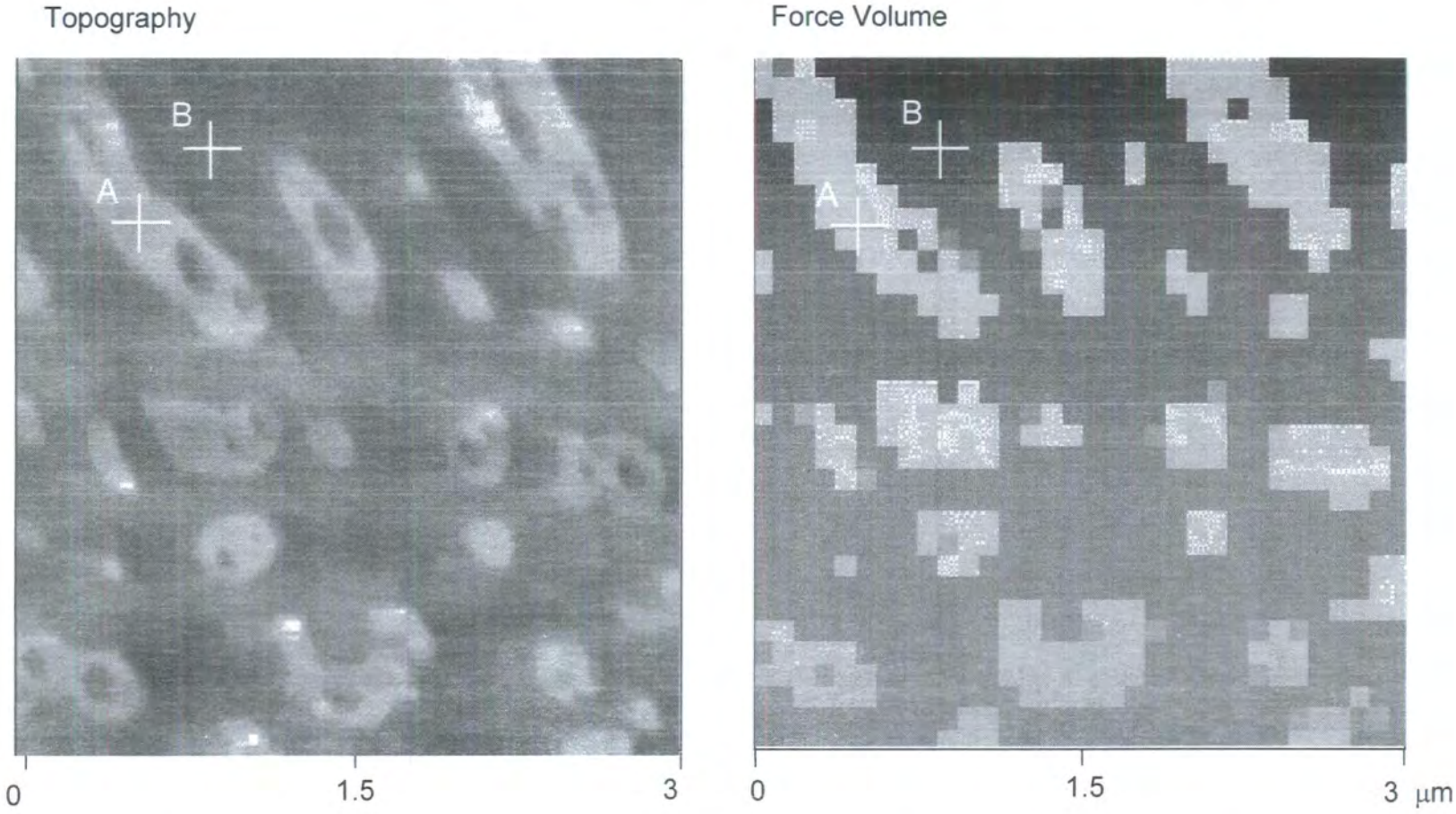

Figure 4.3 Topographic and force volume image (scanner displacement of 760 nm) of an annealed Kraton surface, z range = 100 nm and 150 nm respecively. Points A and B refer to locations of force curve extraction.

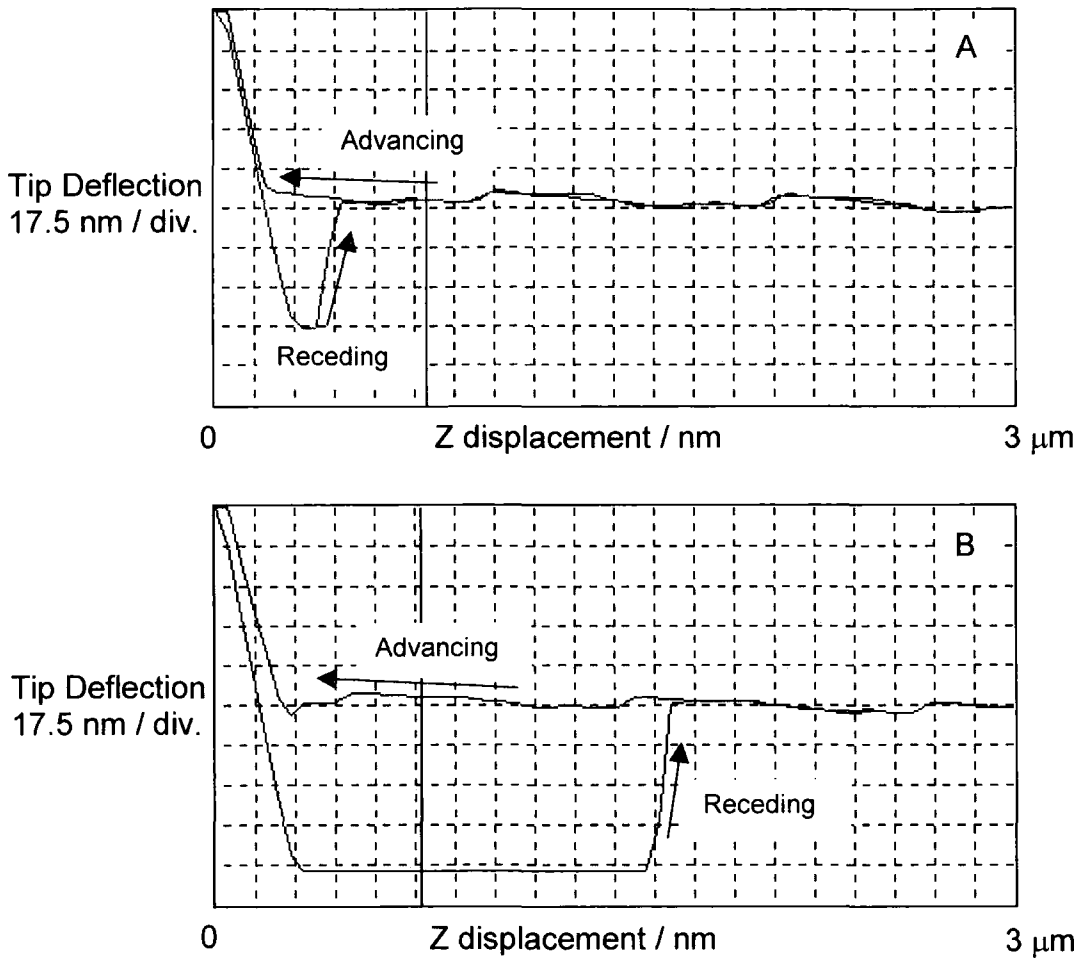

Figure 4.4 Force distance curves extracted from the force volume image of annealed Kraton.

4.3.2 Plasma Treatments

4.3.2.1 Individual Plasma Treatment

AFM shows that CF_4 plasma treatment of polystyrene and annealed Kraton does not alter the surface morphology. However the polybutadiene films undergo considerable roughening as do the un-annealed Kraton film, although on a finer scale than the polybutadiene, Figure 4.5. XPS reveals that all four polymer films are fluorinated to a similar degree, with corresponding drops in surface oxygen content for the polystyrene, polybutadiene and annealed Kraton films. Water contact angles reflect both the extent of surface roughening and surface fluorination, Table 4.3.

DBD treatment of the polystyrene film was shown to produce considerable debris on the surface by AFM. Exposure of the annealed Kraton to the discharge caused a reduction in the height of the gaskets, and no alteration of the surrounding matrix, Figure 4.5. Little change was observed on the surface of the polybutadiene and un-annealed Kraton films after exposure to the discharge. XPS analysis of the polymer films showed high levels of oxidation on the surface of the polybutadiene, and somewhat lower degrees of oxygenation on the polystyrene surface. Both annealed and un-annealed Kraton demonstrated similar degrees of surface oxygenation, intermediate to the polystyrene and polybutadiene, Table 4.2. Water contact angle analysis reveals that all the polymers are more wettable after DBD treatment. Of particular interest are the dramatic reductions in contact angles for both polystyrene and the annealed Kraton surface, Table 4.3.

4.3.2.2 Successive Plasma Treatments

CF_4 plasma treatment prior to DBD exposure did not significantly affect the morphology of the films after exposure to the dielectric barrier discharge, with respect to results for the un-fluorinated films, Figure 4.5. AFM analysis showed the reduction in height of the gasket regions on the segregated Kraton surface to be dependent upon DBD exposure time, Figure 4.6. The reduction in height of the gaskets appears fast initially, then reduces significantly after an exposure time of one minute.

XPS analysis of the fluorinated polystyrene film shows a rapid rise in oxygenation at the film surface with exposure to the DBD discharge up to one minute, and a corresponding decrease in surface fluorination. A more moderate increase in oxygenation is observed for further exposure times, up to eight minutes. A similar trend is observed for fluorinated annealed Kraton films, however the degree of oxygenation is somewhat larger than for the polystyrene, for DBD exposures in excess of 30 seconds. It is interesting to note, that although around half of the surface of the Kraton films has been etched to a depth in excess of 25nm the extent of fluorination is not dramatically reduced, Figure 4.7.

DBD exposure of the fluorinated polybutadiene results in a slight increase in the oxygen content over the DBD exposure times investigated. Fluorinated un-annealed Kraton demonstrates a similar trend reflecting the high surface concentration of polybutadiene, Figure 4.7.

Water contact angle analysis reveals a reduction in the contact angle of the fluorinated polystyrene, mirroring the increases in surface oxygenation as a function of DBD exposure. Interestingly the increased oxygenation at the

surface of the fluorinated annealed Kraton films is not reflected in the water contact angles, Figure 4.8.

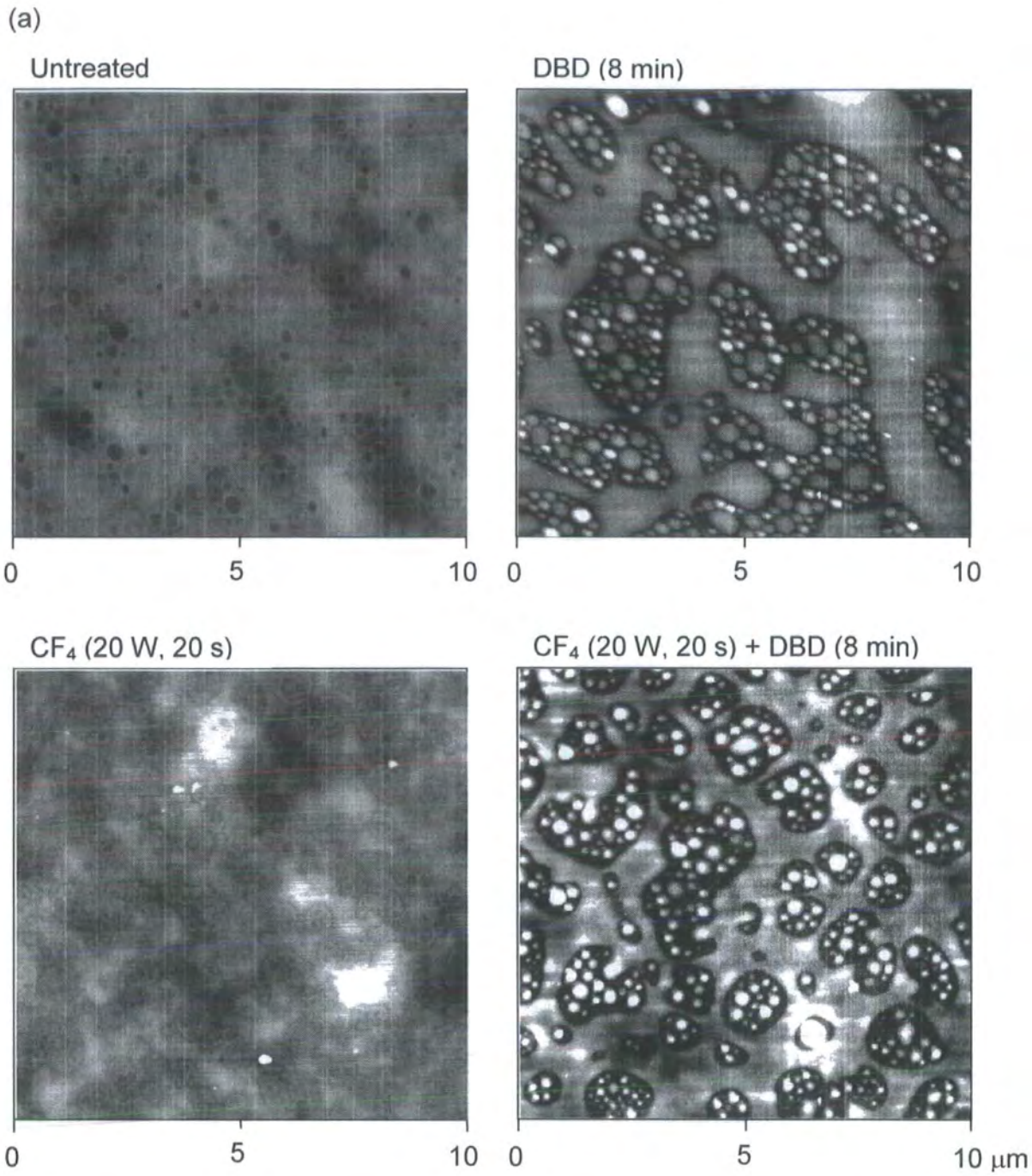

Figure 4.5 AFM height images (x=y=10 μm, z=50 nm) of polymer films, as a function of plasma treatments: (a) annealed Kraton; (b) polystyrene; (c) polybutadiene; (d) Un-annealed Kraton.

(b)

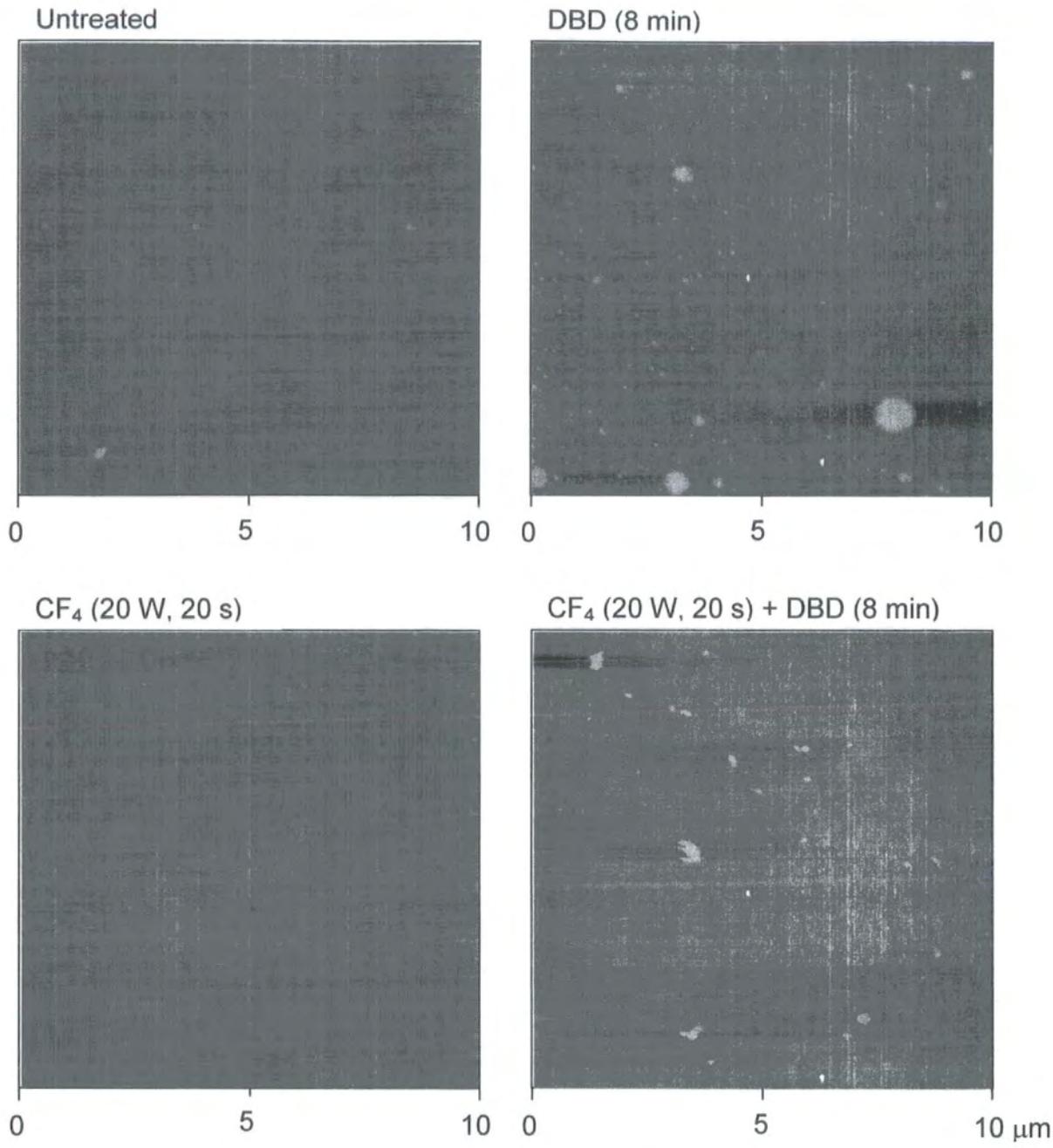
Untreated
DBD (8 min)
CF4 (20 W, 20 s)
CF4 (20 W, 20 s) + DBD (8 min)
0
5
10
0
5
10
0
5
10
0
5
10 μm

(c)

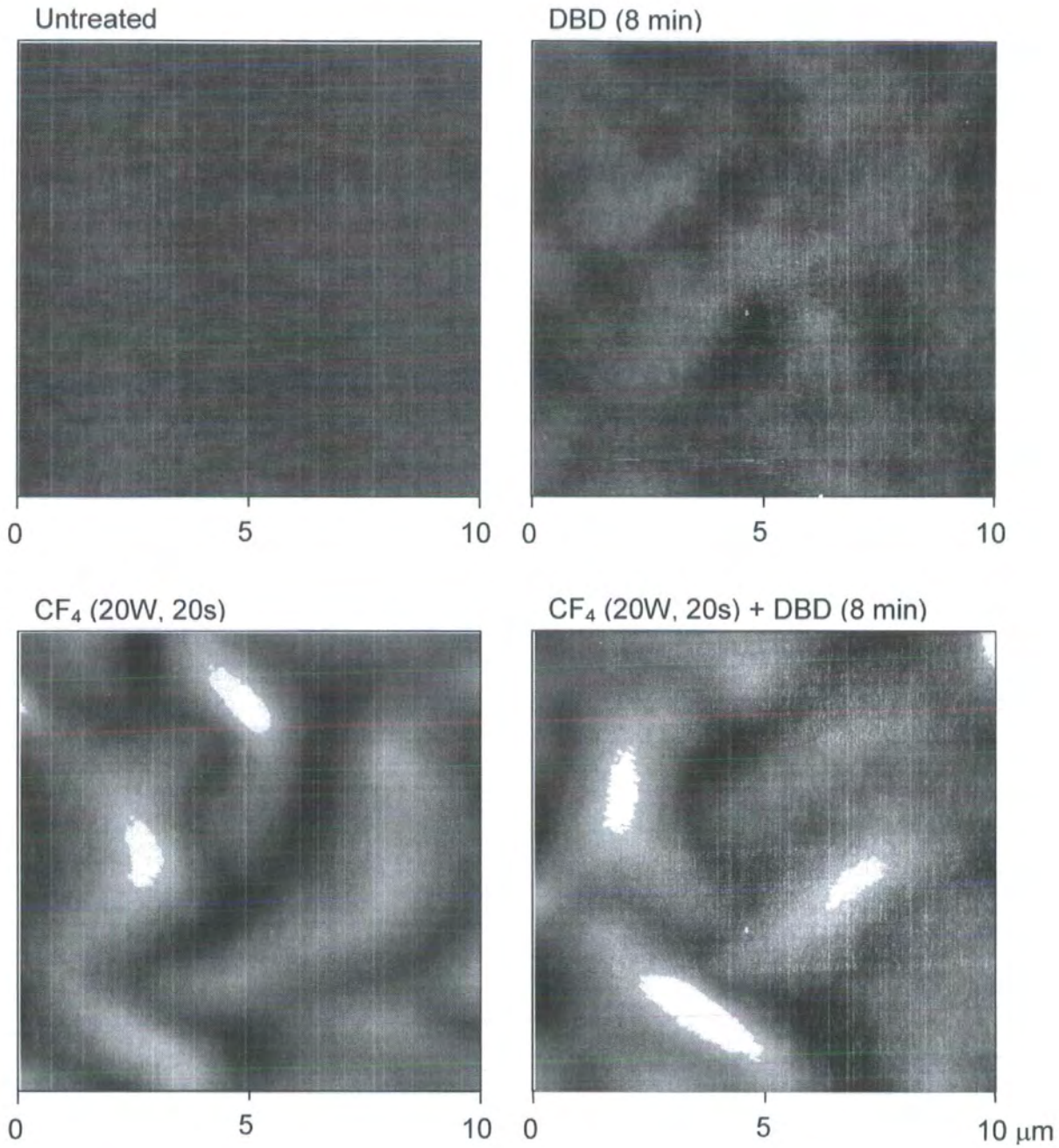
Untreated
DBD (8 min)
0
5
10
0
5
10
CF_4 (20W, 20s)
CF_4 (20W, 20s) + DBD (8 min)
0
5
10
0
5
10 μm

(d)

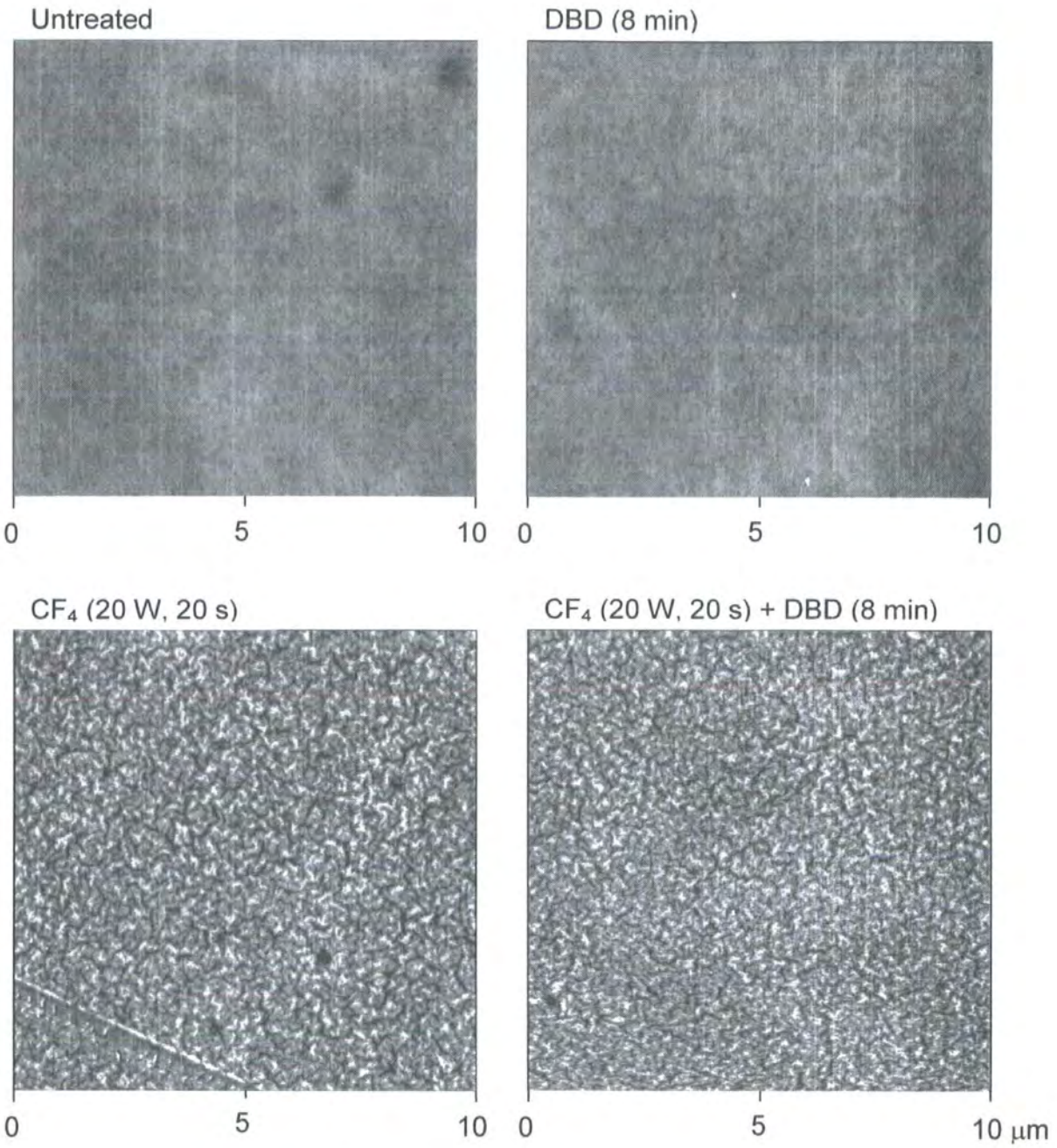
Untreated
DBD (8 min)
0
5
10
0
5
10
CF_4 (20 W, 20 s)
CF_4 (20 W, 20 s) + DBD (8 min)
0
5
10
0
5
10 μm

(a)

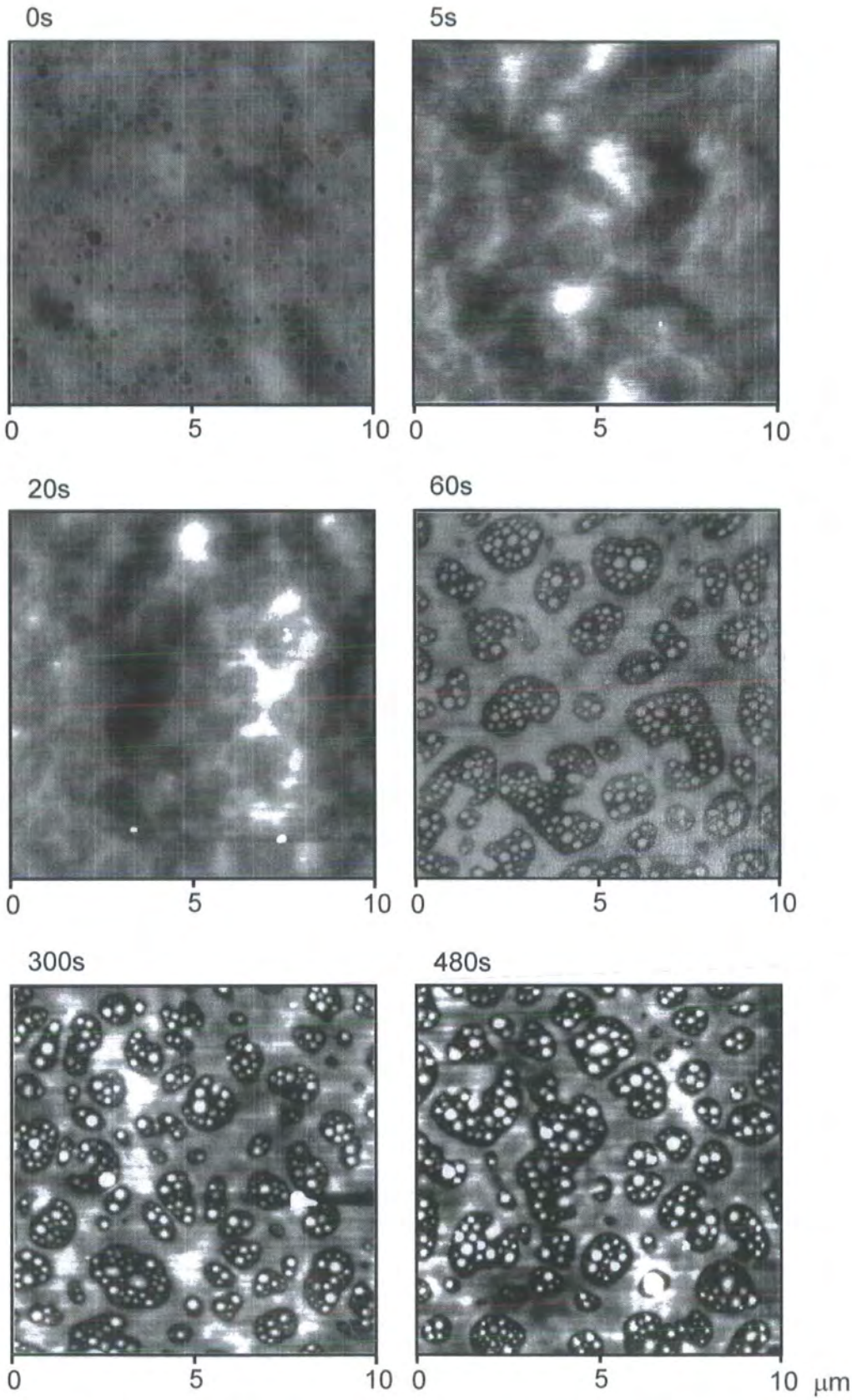

Figure 4.6 CF_4 plasma treated (20 W, 20 s) annealed Kraton as a function of DBD exposure time: (a) AFM height images (x=y=10 μm, z=50 nm); (b) AFM height difference measurement.

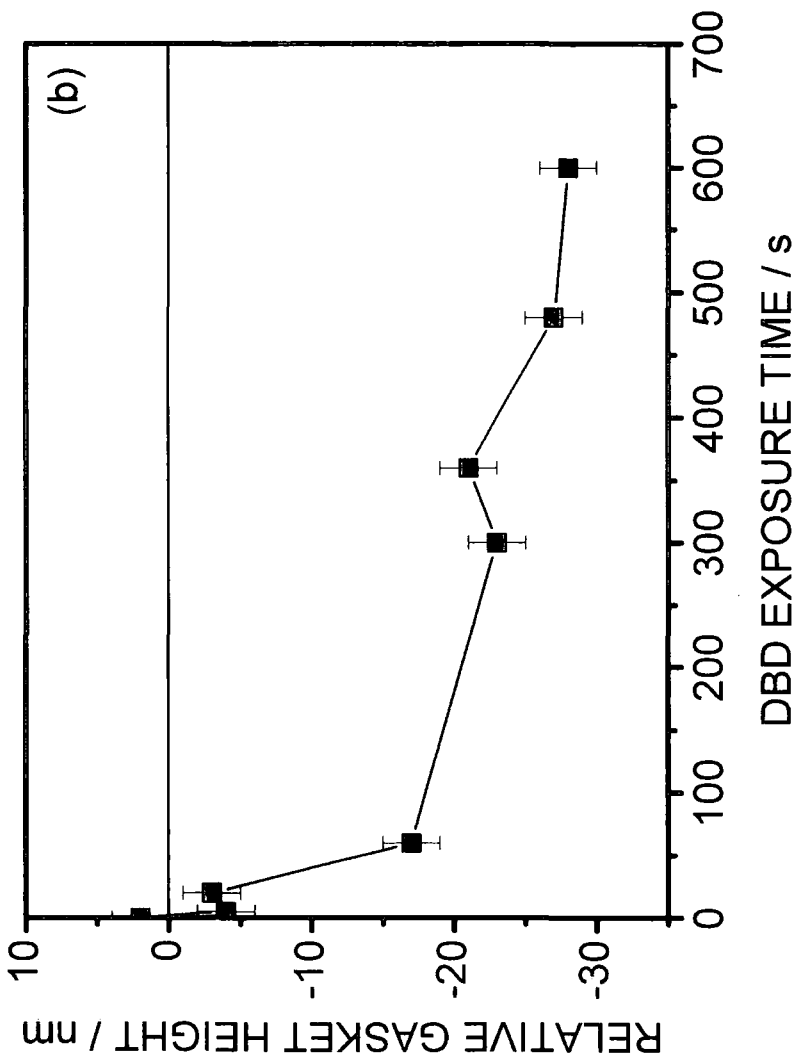
(b)
RELATIVE GASKET HEIGHT / nm
10
0
-10
-20
-30
0
100
200
300
400
500
600
700
DBD EXPOSURE TIME / s

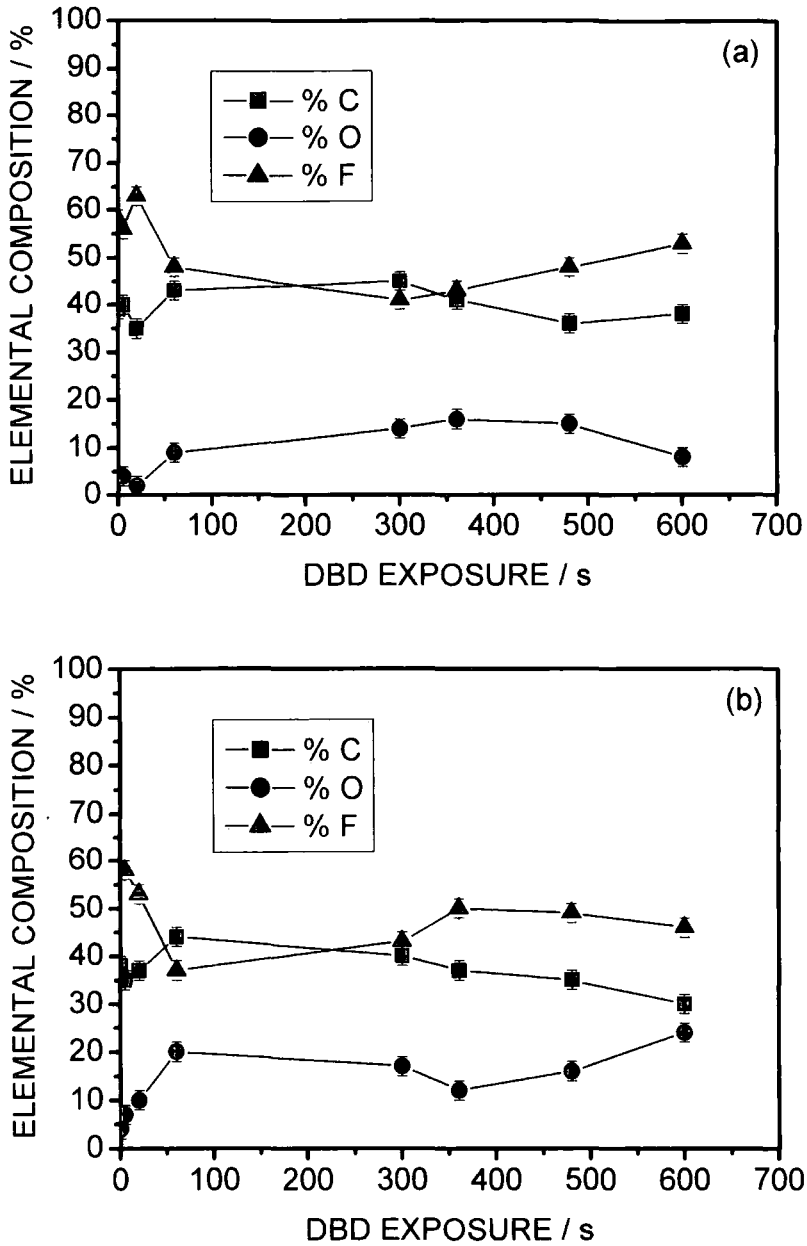

Figure 4.7 XPS elemental composition of CF_4 plasma treated (20 W, 20 s) polymer films as a function of DBD exposure: (a) polystyrene; (b) annealed Kraton; (c) polybutadiene; (d) Kraton.

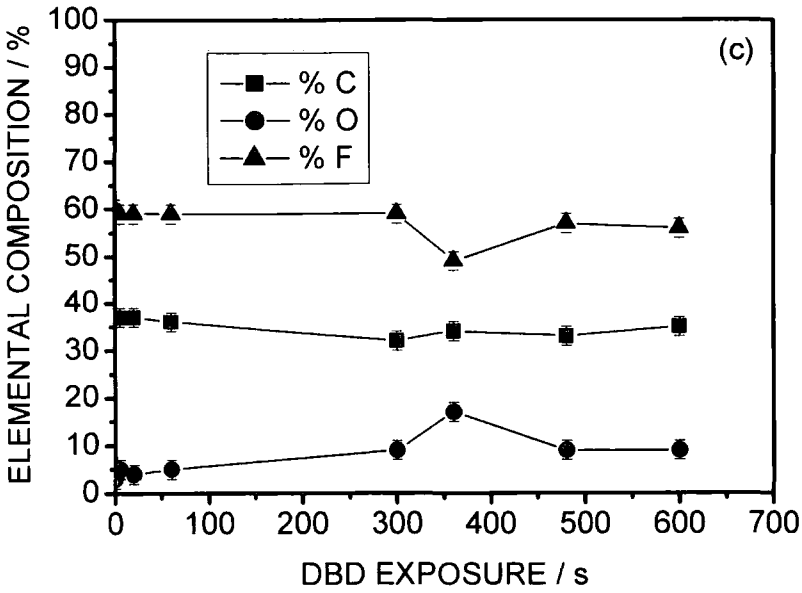
(c)
% C
% O
% F
ELEMENTAL COMPOSITION / %
DBD EXPOSURE / s
0
10
20
30
40
50
60
70
80
90
100
0
100
200
300
400
500
600
700

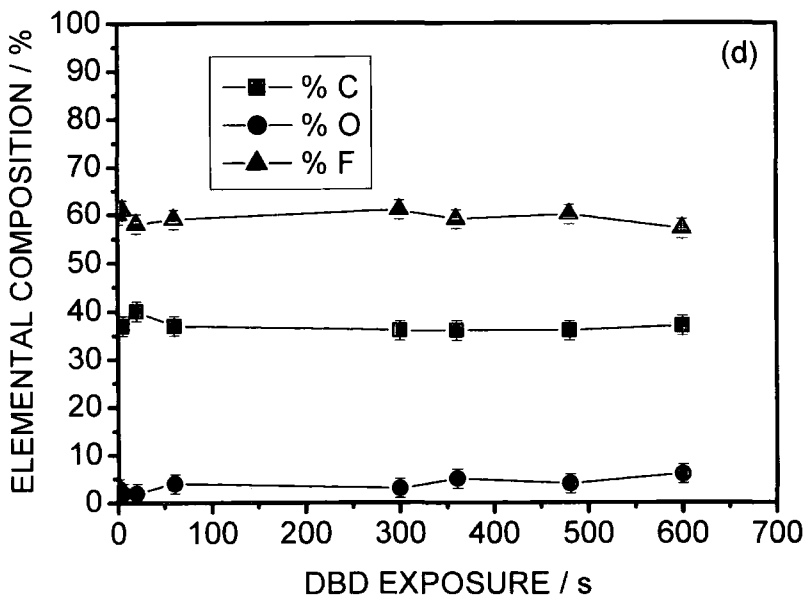
(d)
% C
% O
% F
ELEMENTAL COMPOSITION / %
DBD EXPOSURE / s
0
10
20
30
40
50
60
70
80
90
100
0
100
200
300
400
500
600
700

	Untreated				DBD (8 min)				CF4 (20 W, 20 s)				CF4 (20 W, 20 s) + DBD (8 min)			
	K	AK	PS	PBD	K	AK	PS	PBD	K	AK	PS	PBD	K	AK	PS	PBD
% C	96±2	80±2	86±2	83±2	61±2	58±2	74±2	54±2	37±2	38±2	39±2	37±2	36±2	35±2	36±2	33±2
% O	4±2	20±2	14±2	17±2	39±2	42±2	26±2	46±2	3±2	4±2	3±2	3±2	7±2	16±2	15±2	9±2
% F	0	0	0	0	0	0	0	0	60±2	58±2	58±2	60±2	57±2	49±2	53±2	57±2

(K = Kraton, AK = Annealed Kraton, PS = Polystyrene, PBD = Polybutadiene)

Table 4.2 XPS elemental composition of polymer films as a function of plasma treatment.

	Untreated	DBD	CF_4	CF_4 + DBD
Kraton	92 ± 1	60 ± 2	120 ± 2	122 ± 2
Annealed Kraton	86 ± 2	27 ± 2	113 ± 2	108 ± 2
Polystyrene	98 ± 2	0	111 ± 2	70 ± 2
Polybutadiene	103 ± 2	59 ± 1	136 ± 1	132 ± 1

CF_4 plasma: 20 W, 20 s
DBD: 8 min

Table 4.3 H_2O contact angle measurement of polymer films as a function of plasma treatment.

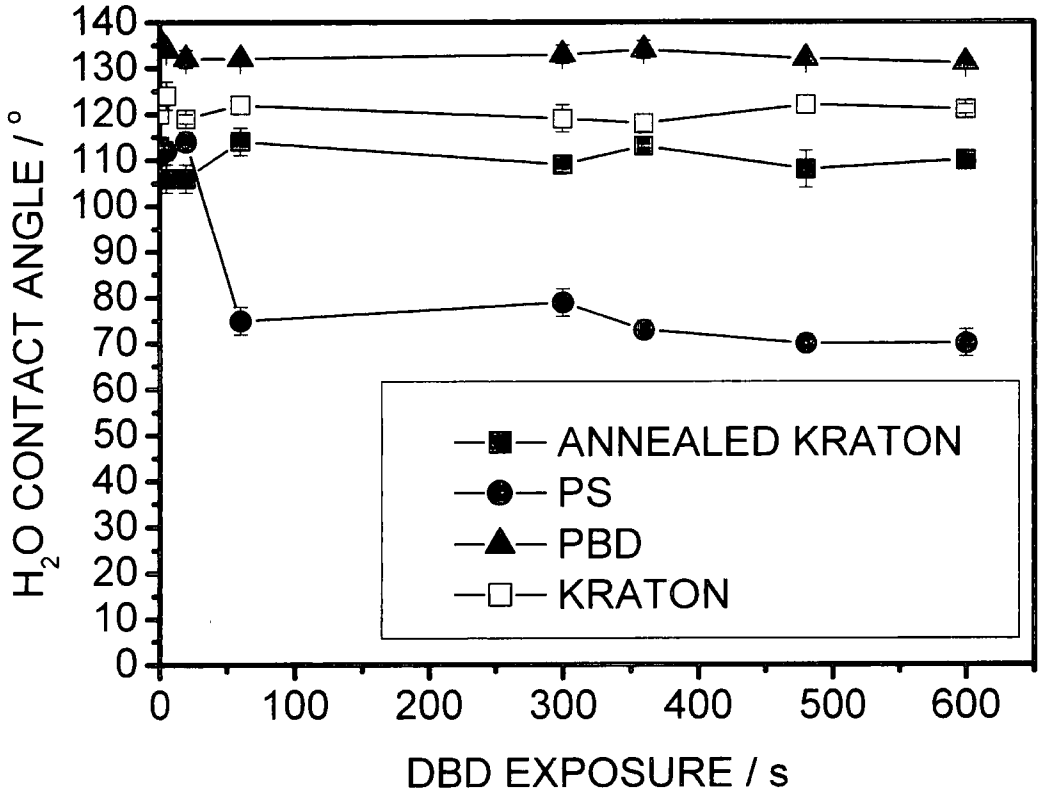

Figure 4.8 H_2O contact angle analysis of CF_4 plasma treated (20 W, 20 s) polymer films as a function of DBD exposure time.

4.3.3 Selective Salt Deposition

Immersion of a fluorinated annealed Kraton film, before and after DBD exposure into copper sulfate solution, resulted in the presence of $CuSO_4$ on the surfaces of both films, as revealed by XPS, Table 4.4. Prior to the DBD exposure the crystals were shown to be distributed randomly on only the polybutadiene regions of the surface using AFM, Figure 4.9. After etching of the gaskets by DBD exposure for 8 minutes, the selectivity of the salt deposition reversed, and crystals were found only in the gasket regions, Figure 4.10.

	Before Etching		**After Etching**	
	Pre $CuSO_4$	**After $CuSO_4$**	**Pre $CuSO_4$**	**After $CuSO_4$**
% C	38 ± 2	35 ± 2	35 ± 2	32 ± 2
% O	4 ± 2	7 ± 2	16 ± 2	15 ± 2
% F	58 ± 2	54 ± 2	49 ± 2	47 ± 2
% S	0 ± 2	2 ± 2	0 ± 2	3 ± 2
% Cu	0 ± 2	2 ± 2	0 ± 2	3 ± 2

Table 4.4 XPS elemental composition of fluorinated annealed Kraton as a function of $CuSO_4$ immersion, before and after DBD etching.

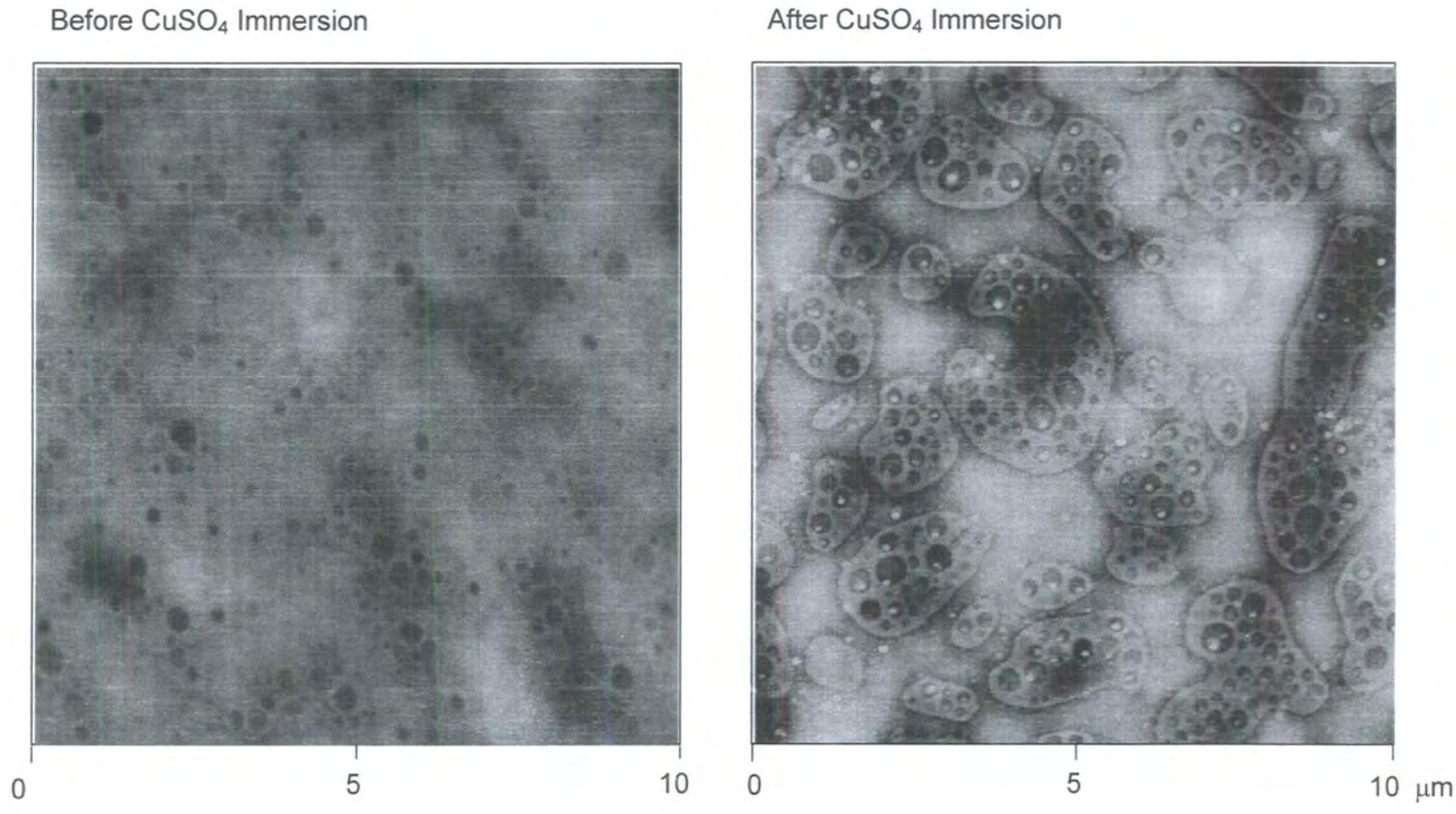

Figure 4.9 AFM height images (x=y=10 μm, z=50 nm) of plasma fluorinated Kraton films, as a function of $CuSO_4$ immersion.

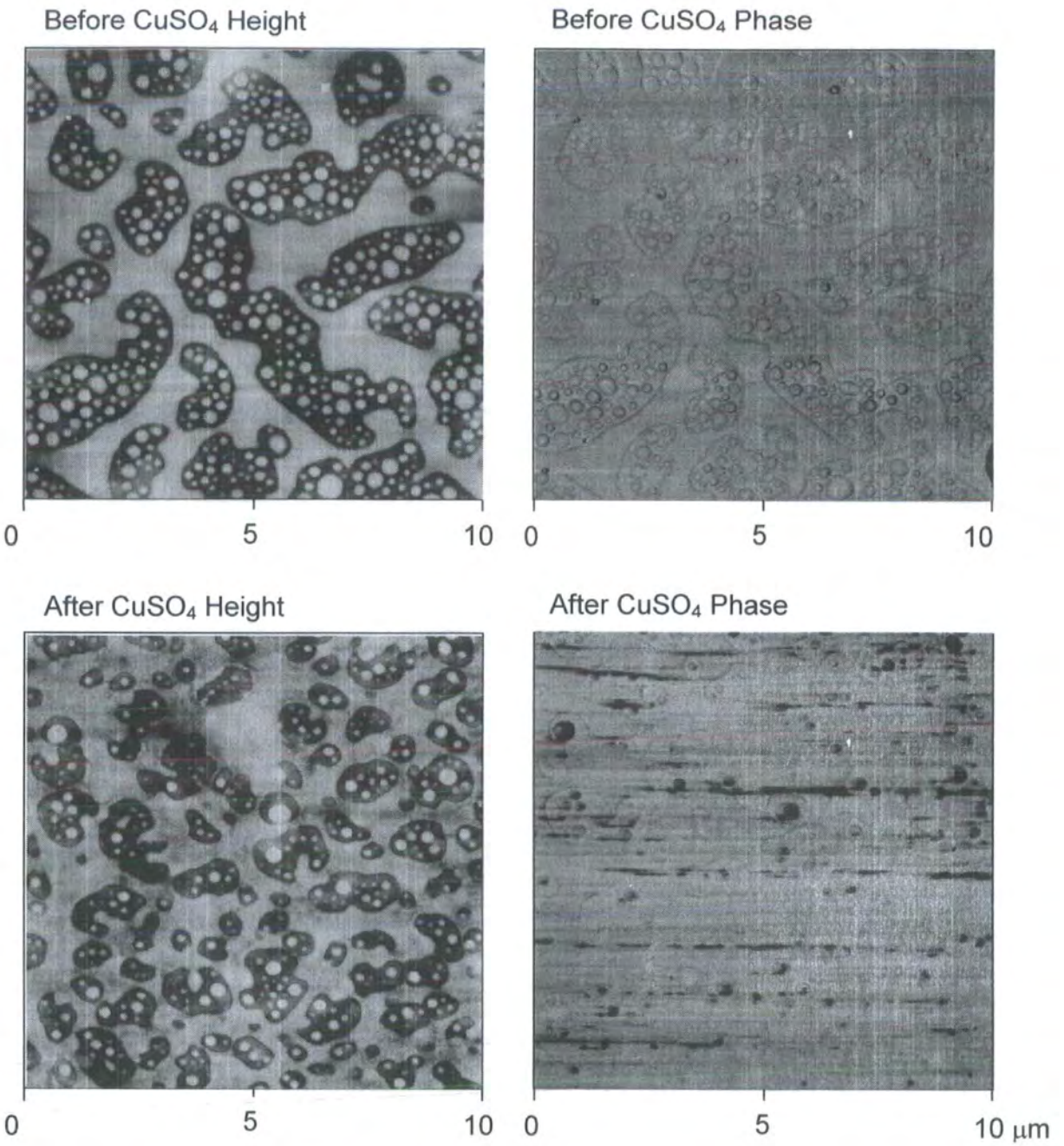

Figure 4.10 AFM height and phase images (x=y=10 μm, z=100 nm) of etched, fluorinated annealed Kraton films before and after immersion in 0.5 molar $CuSO_4$ solution.

4.4 Discussion

4.4.2 Segregation

It has been shown earlier in this thesis that polystyrene and polybutadiene are immiscible, and as such it is expected that phase segregation will occur between these two polymers in the Kraton. Indeed such phase segregation is well reported for styrene butadiene block copolymers in the literature.[1,2] It is this phase segregation that leads to the formation of pseudo crosslinks, in the form of crystalline polystyrene regions, within the amorphous polybutadiene, yielding similar properties to that of vulcanised rubber.[22]

The surface segregation of polymer components in block copolymers is driven by several factors, including segment flexibility,[11] length[11] and surface energy.[12] As polybutadiene is both the lowest surface energy and most flexible block it may be expected to fully wet the air / polymer interface. However as both components partially wet the surface other factors must play a role. Annealing at a temperature in excess of the glass transition temperature for polystyrene (80-100°C)[23] is necessary to achieve segregation within the film as has been observed in the literature.[1]

The differences in adhesive interaction between the polymers and a silicon tip are similar to those seen in the literature for polystyrene and polybutadiene,[29] with the latter giving the greater adhesion. In combination with the increased polystyrene content as measured by XPS the gasket regions can be identified as polystyrene and the surrounding matrix as polybutadiene. Although individual force curves have been used in the literature to identify regions of specific polymer composition,[29] force volume images have up until now not found application in this area.

Phase imaging also facilitates imaging which differentiates between regions of physically different materials,[29,24] further confirming the presence of a heterogeneous polymer surface. The AFM phase difference is as expected for two physically different polymers, and may be attributed to several factors including: elasticity,[25] hydrophobicity,[26,27] adhesion[28] and energy dissipation.[29] The degree of phase change measured may depend upon the imaging conditions chosen, and shows variance and even reversal, according to imaging parameters.[29,24]

It has been reported in the literature that if one component of a block copolymer surface segregates, this may lead to compositional waves which extend perpendicular to the surface into the bulk of the polymer.[12] For the surface presented here this would result in a layer of polystyrene backing the surface polybutadiene region, and a butadiene layer behind the polystyrene surface regions.

4.4.3 Plasma Fluorination

The high degrees of fluorination seen here after CF_4 plasma treatment of all the films are consistent with values predicted from the literature.[15] Given that both polymers exhibit many unsaturated carbon centres the principal method of fluorination is probably attack of atomic fluorine,[15] this being the primary species present in a CF_4 plasma.[30]

Water contact angle measurements reflect both the level of fluorination[17] and surface roughness,[16,31,32] as discussed in chapter 2. It is this surface roughness which is responsible for the increased contact angles of Kraton and polybutadiene compared to the equally fluorinated polystyrene and annealed Kraton films. Both increases in roughening can be attributed to contortions

during surface cross-linking in the plasma treatment (as already discussed in chapter 2). The finer scale roughness seen in Kraton compared to that in polybutadiene is attributable to constraints on the mobility of the polybutadiene due to the polystyrene pseudo-cross-links. Similarly the lack of roughening in the polybutadiene regions of the annealed Kraton film would support the presence of a rigid polystyrene region behind, effectively reducing the film thickness, and thus preventing roughening (as observed in chapter 2). The lack of roughening seen for CF_4 plasma treatment of the polystyrene is consistent with previous results reported in the literature.[16]

4.4.4 DBD Exposure

The degree of oxidation of polymer surfaces in dielectric barrier discharges has been shown to be dependant upon the degree of saturation in the polymer, with unsaturated polymers more susceptible to oxidation. This has been accounted for in the high concentrations of ozone within the discharge,[36] and close correlation has been found to oxidation via ozone exposure.[20] The mechanism however is more complex in the discharge due to the presence of other excited species and the UV component. Oxidation rates considerably in excess of those reported for ozone treatment have been reported for dielectric barrier discharges.[20]

DBD treatment of the polystyrene results in similar degrees of oxidation to that reported in the literature. [33] Similarly the greater degree of oxidation in the polybutadiene is consistent with that expected for ozonation of the double bond, [34,35] given the high concentrations of ozone in the discharge[36] and reports presented for polyisoprene.[20]

The degree of oxidation on the un-annealed Kraton is consistent with a surface comprising 12.8% polystyrene, however the degree of oxidation on the annealed Kraton surface is somewhat greater than would be expected for a surface initially containing 40% polystyrene. The etching of the polstyrene in the discharge may explain this, as removal of surface polystyrene will result in the exposure of polybutadiene, which can then undergo greater oxidation.[20]

The presence of much randomly dispersed material on the surface of the polystyrene after DBD treatment may be a factor of surface etching and degradation.

As the DBD treatment imposes oxygenated functionality on the surface the corresponding drops in water contact angle are as expected. The fully wetting nature of the water on the polystyrene, and drastically reduced contact angle of annealed Kraton may reflect the presence of highly oxidised low molecular weight material (due to etching) on these surfaces, effectively increasing the roughness.

4.4.5 Successive Plasma Treatment

The reduction in oxidation, and constant levels of fluorine seen at the surfaces of fluorinated polybutadiene films after DBD exposure can be explained by the presence of a highly fluorinated cross-linked surface. This reduces the number of double bonds present at the surface due to addition of atomic fluorine[37] and cross-linking in the CF_4 plasma.[38,39] The close correlation of the un-annealed Kraton reflects the high concentration of polybutadiene at the surface of the copolymer.

The consistent presence of fluorine on the polystyrene surface after etching depths in excess of 20 nm is something of a mystery, given that the

fluorination depth of polystyrene in a CF_4 plasma is no greater than 100 Angstoms.[16] A potential explanation of this is that etched fluorinated moieties remain within the discharge, where they can react again with the exposed polymer surface.

The presence of greater oxygenation on the surface of the annealed Kraton than expected for the surface composition is similar to that seen for DBD treatment of the unfluorinated film, and may be attributed to the etching of the polystyrene revealing underlying polybutadiene. The corresponding reduction in the rate of etching of the polystyrene domains after an exposure time of 1 minute further supports this.

Water contact angles in general reflect the degrees of oxygen incorporation into the surface, with the exception of the annealed Kraton. This is a consequence of the reduced height of the oxidised gasket regions with respect to the highly fluorinated polybutadiene regions, and the corresponding formation of a composite interface, similar to that presented in chapter 2.

4.4.6 Selective Salt Deposition

As has already been observed in this thesis and elsewhere[14,40,41] the presentation of a surface with regions of differing surface energy can be used to cause selective wetting, and provide the potential to selectively deposit $CuSO_4$. Gravity has also been shown to play a role in the precise location of the salt crystals, guiding the water droplets responsible for deposition to the lowest points within the restraints imposed by surface energy.[14]

The selective deposition of the metal salt onto the fluorinated polybutadiene regions of the Kraton film prior to DBD etching, is consistent with gravity driven selectivity, as the crystals locate in the lower height regions.

In the case of the DBD etched film, both surface energy and gravity assisted arguments may be used to explain the selective salt deposition into the gasket regions. Although the precise nature of the surface in the base of the gaskets is not known, the results show it to be considerably oxidised, at the extent of fluorine content, and therefore almost certainly more wettable.

.

4.5 Conclusions

It has been shown that annealed Kraton surfaces can through successive plasma treatment yield differing surface properties. These chemical and morphological differences have been used to template the deposition of aqueous salt solution. Selective deposition has been shown to be sensitive to small height changes across the films surface, as well as surface energy differences.

4.6 References

1 Kim, G., Libera, M. *Macromolecules*, **1998**, 31, 2569.

2 Van Dijk, M. A., Van den Berg, R., *Macromolecules* **1995**, 28, 6773.

3 Laurer, J. H., Ashraf, A., Smith, S. D., Spontak, R. J. *Langmuir*, **1997**, 13, 2250.

4 Moeller, M., Spatz, J. P., Moeessmer, S., Eibeck, P., Ziemann P., Kabius, B. *Polym. Mater. Sci. Eng.*, **1999**, 80, 3.

5 Park, M., Harrison, C., Chaikin, P. M., Register, R. A., Adamson, D. H. *Science*, **1997**, 276, 1401.

6 Annighofer, F., Gronski, W. *Colloid Polym. Sci.*, **1983**, 261, 15.

7 Hashimoto, T., Tsukahara, Y., Tachi, K., Kawai, H. *Macromolecules*, **1983**, 16, 648.

8 Buhler, F., Gronski, W. *Makromol. Chem.*, **1986**, 187, 2019.

9 Buhler, F., Gronski, W. *Makromol. Chem.*, **1988**, 188, 2995.

10 Zielinski, J. M., Spontak, R. J. *Macromolecules*, **1992**, 25, 5957.

11 Carignano, M. A., Szleifer, I. *Europhys. Lett.*, **1995**, 30, 525

12 Sikka, M., Sing, N., Karim, A., Bates, F. S., Satija, S. K., Majkrzak, X. F. *Physical Review Letters*, **1993**, 70, 307.

13 Steiner, U., Klein, J., Eiser, E., Budowski, A., Fetters, L. J. *Science*, **1992**, 258, 1126.

14 Qin, D., Xia, Y., Xu, B., Yang, H., Zhu, C., Whitesides, G. M. *Advanced Materials*, **1999**, 11, 1433.

15 Hopkins, J., Badyal, J. P. S. *J. Phys. Chem.*, **1995**, 99, 4261.

16 Strobel, M., Thomas, P. A., Lyons, C. S. *J. Polym. Sci.: Part A: Polym. Chem.*, **1987**, 25, 3343.

17 Strobel, M., Corn, S., Lyons, C. S., Korba, G. A. *J. Polym. Sci.: Part A: Polym. Chem.*, **1987**, 25, 1295.

18. Kissa, E. In *Handbook of Fibre Science and Technology*, Vol II, Part B, Lewin, M.; Sello, S. B., Eds.; Marcel Dekker Inc: New York, **1984**

19 Brady, R. F. Jr. In *Encyclopaedia of Polymer Science and Technology*, Mark, H.; Bikales, N. M.; Overberger, C. G.; Menges, G., Eds.; John Wiley & Sons: Chichester, 1986

20 Greenwood, O. D., Tasker, S., Badyal, J. P. S. *J. Polym. Sci.: Part A: Polym Chem.*, **1994**, 32, 2479.

21 Zhong, Q., Innis, D., Hjoller, K., Elings, V. B. *Surf. Sci.*, **1993**, 14, 3045.

22 Decker, C., Nguyen Thi Vet, T. *Journal of Applied Polymer Science*, **2000**, 77, 1902.

23 Polymer Handbook, Fourth Eddition, Eds., Brandrup, J., Immergut, E. H., Grulke, E. A. John Wiley & Sons Inc., New York,

24 Pickering, J. P., Vancso, G. J. *Polymer Bulletin*, **1998**, 40, 549.

25 Brandsch, R.; Bar, G. *Langmuir* **1997**, *13*, 6349.

26 Refier, D.; Windeit, R.; Kumpf. R. J.; Karbach, A.; Fuchs, H. *Thin Solid Films* **1995,** *264,* 148.

27 Chen, X.; Davies, M. C.; Roberts, C. J.; Tendler, S. J. B; Williams, P. M.; Davies, J.; Dawkes, A. C.; Edwards, J. C. *Ultramicroscopy* **1998**, *75*, 171.

28 Finot, M. O.; McDermott, M. T. *J. Am. Chem. Soc.* **1997**, *119*, 8564.

29 Raghavan, D., Gu, X., Nguyen, T., Vanlandingham, M., Karim, A. *Macromolecules*, **2000**, 33, 2573.

30 Kay, E., *Proc. Int. Ion. Eng. Cong.*, **1983**, 1657.

31 Wenzel, R. N. *Ind. Eng. Chem.*, **1936**, 28, 988.

32 Hazlett, R. D. *J. Colloid and Interface Science*, **1990**, 137, 527.

33 Greenwood, O. D., Boyd, R. D., Hopkins, J., Badyal, J. P. S. *J. Adhes. Sci. Technol.*, **1995**, 9, 311.

34 Criegee, R. *Adv. Chem. Ser.*, **21**, 79, 1992.

35 Bailey, P. S. *Ozonation in Organic Chemistry*, **1978** ,Vol. 1, Academic, New York.

36 Eliasson, B., Hirth, M., Kogelschatz, U. *J. Phys. D: Appl. Phys.*, **1987**, 20, 1421.

37 Hopkins, J., Badyal, J. P. S. *J. Phys. Chem.* **1995**, *99*, 4261

38 Inagaki, N., Kobayashi, N., Matsushima, M. J., *Membr. Sci.*, **1988**, *38*, 85.

39 Kerle, T., Yerushalmi-Rozen, R.; Klein, J., *Europhys. Lett.*, **1997**, *38*, 207.

40 Kumar, A., Whitesides, G. M. *Science*, **1994**, 263, 60.

41 Tadanaga, K., Morinaga, J., Matsuda, A., Minami, T. *Chem. Mater.*, **2000**, 12, 590.

Chapter 5

Selective Charge Deposition on Phase Segregated Polymer Surfaces Using the Electric Force Microscope

5.1 Introduction

Charged surfaces are of importance in many fields of research, these include: optical display devices,[1] biomedical systems,[2] electrostatic filter media,[3] and through the deposition of small localised charge patches; memory storage devices,[4] and templates for micron scale self assembled structures.[5]

Surface charge variations have been mapped previously using electrostatic probes[6] and also with the electric force microscope, the later offering considerably increased spatial resolution.[7,8,9,10]

The Electric Force Microscope (EFM) also offers the possibility of spatially controlled charge deposition. Studies have involved the application of high voltages to a static AFM tip held, both above[7,8] and in contact[4] with the surface. It has also been shown that charge patches may be deposited on polymer films from an EFM tip scanning a controlled distance above the surface.[5]

Kraton polymer films have been shown to phase segregate into regions of polystyrene (termed gaskets) in a styrene / butadiene copolymer matrix. Here we investigate the effect of localised surface charging on this phase segregated system.

5.2 Theory

5.2.1 The Effect of Forces on Phase Shift

An oscillating cantilever has associated with it a phase of oscillation. This phase demonstrates a difference from the phase of the driving oscillation, termed the phase lag. In the case of a freely oscillating cantilever at resonance (maximum amplitude) the phase lag is 90°.[11] AFM phase images measure the change in the phase lag from that of the freely oscillating cantilever to that

perturbed by interactions with the surface (the phase shift).[12,13] The effect of surface interactions is to shift the resonant frequency of the cantilever, from the driven frequency.[14] Correspondingly the phase lag will change according to these interactions. If the cantilever experiences a repulsive force gradient then the resonant frequency will increase and correspondingly the phase lag will drop below 90°, thus the phase shift becomes positive proportionately to the degree of repulsion. Conversely attractive force gradients reduce the resonant frequency, increase the phase lag above 90°, and therefore produce a negative phase shift, Figure 5.1, and Table 5.1.

Interaction Force Gradient	**Resonant Frequency**	**Phase shift** $\Delta\phi$
Repulsive	Increases	Positive
Attractive	Decreases	Negative

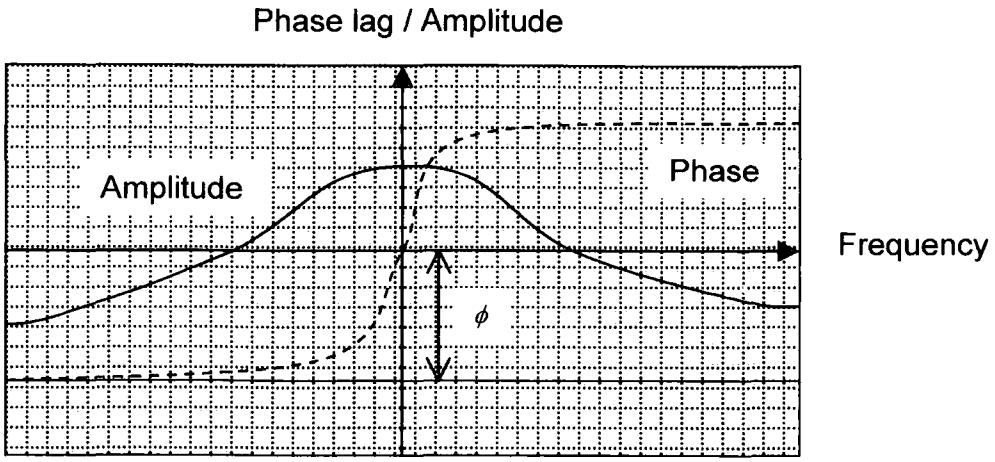

Free Oscillation

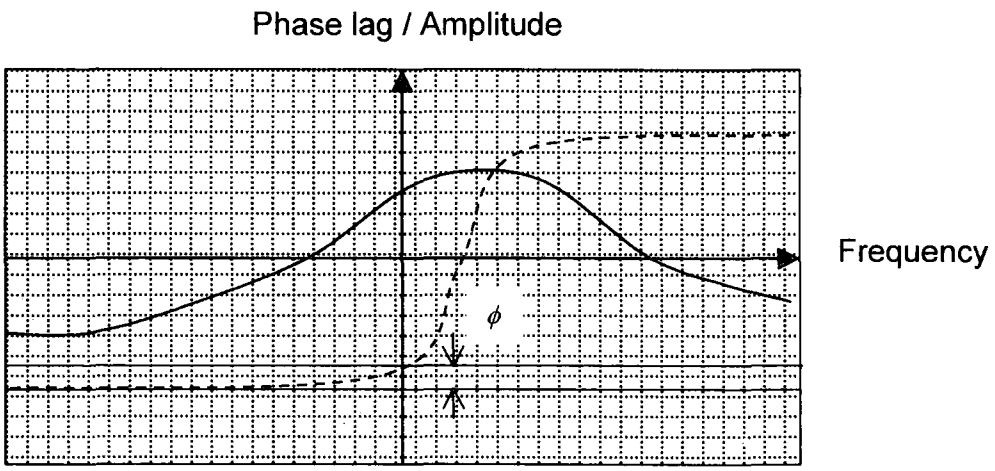

Repulsive Interaction

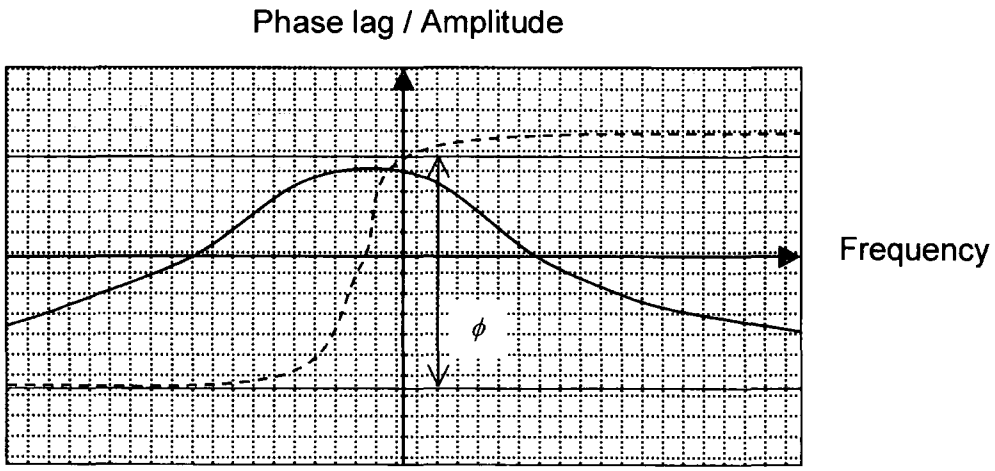

Attractive Interaction

Figure 5.1 The effect of interaction force gradient on oscillation amplitude and phase.

5.2.2 Mapping Electrostatic Forces

Electric force microscopy shares much in common with non-contact AFM, where the cantilever is oscillated at its resonant frequency (just as in TMAFM), however rather than operating in intermittent contact, the tip is oscillated a short distance from the surface[15]. This tip sample separation allows for detection of longer range forces such as van der Waals' forces or electrostatic forces. EFM relies upon a lift mode scan line accompanying each ordinary tapping mode scan line. This entails capturing a height scan line, then retracing this line maintaining a constant user defined tip-sample separation, so as to minimise topographical artifacts.

Phase shifts detected are dependant upon the electrostatic interactions of the surface potential, $V_{surface}$, and the tip potential V_{tip}. V_{tip} is a function of both the mirror charge induced by the surface charge,$-V_{surface}$, and also any externally applied voltage to the tip, $V_{applied}$, Equation 5.1.

Equation 5.1 $$V_{tip} = V_{applied} - V_{surface}$$

When V_{tip} and $V_{surface}$ have the same polarity a repulsive force gradient is experienced and thus a positive phase shift is evident, conversely if they have opposite polarity an attractive force gradient is experienced and the phase shift is negative. The magnitude of this phase shift corresponds to the product of V_{tip} and $V_{surface}$.

From this we can evaluate both the polarity and magnitude of surface charge regions. For example a positive charge patch will yield a bright phase shift when a positive charge is applied to the tip, and a dark phase shift for a

negative applied voltage. A neutral phase shift can be found for a positive applied voltage equal to the surface potential, as this will cancel out the mirrored charge induced in the tip from the surface, Table 5.2. It is expected that an uncharged surface will give a neutral phase shift regardless of tip potential.

Surface Charge	Tip Charge			Force Gradient	Phase Contrast
	Induced	Applied	Total		
+ + +	- - -	+ + + + + +	+ + +	↑	Brighter ↑
+ + +	- - -	+ + + +	+	Repulsive	
+ + +	- - -	+ + +	0	Neutral	Neutral
+ + +	- - -	0	- - -	Attractive	
+ + +	- - -	- -	- - - - -	↓	
+ + +	- - -	- - -	- - - - - -		Darker ↓
0	0	- - - - - -	- - - - - -		
0	0	0	0	Neutral	Neutral
0	0	+ + + + + +	+ + + + + +		
- - -	+ + +	+ + +	+ + + + + +	↑	Darker ↑
- - -	+ + +	+ +	+ + + + +		
- - -	+ + +	0	+ + +	Attractive	
- - -	+ + +	- - -	0	Neutral	Neutral
- - -	+ + +	- - - -	-	Repulsive	
- - -	+ + +	- - - - - -	- - -	↓	Brighter ↓

Table 5.2 Representation of phase contrast during EFM lift-mode Imaging of +ve and –ve charge patches, as a function of voltage applied to the tip.

5.2.3 Deposition of Charge Patches

It has been shown that the electric force microscope can also be used to deposit regions of charge onto polymer surfaces.[5,7,8] This involves the application of a high voltage to the tip during the lift-mode scan. If this voltage overcomes a threshold voltage a corona discharge is established around the tip.[16] Voltages applied to cause such a discharge may be lower than those necessary for bulk treatments due to the low radius of curvature of the tip (circa 13 nm)[17]. It has been shown that both positive and negative charge patches can be selectively deposited, by this mechanism[5].

5.3 Experimental

Polymer films were prepared on clean polished silicon substrates by spin coating as described below.

Polystyrene and polybutadiene films were spun from 10 % w/v solutions at 2000 rpm and subsequently annealed under vacuum for 1 hour at 120°C to remove any entrapped solvent.

Kraton films were spun from 11 % w/v solutions at 2000 rpm. Un-annealed films were pumped down to 4 x 10^{-3} mbar for 24 hours to remove any solvent. Annealed films were placed in an oven open to air for 1 hour at 120°C, leading to the formation of a surface comprising regions of polystyrene and polybutadiene as seen in chapter 4.

Mixed phase polystyrene/polybutadiene films were produced by spinning a 1 % w/v solution (10 % polystyrene) at 2000 rpm. The films were subsequently annealed under vacuum for 1 hour at 120°C, so as to remove any entrapped solvent, and then further annealed to cure at 165°C for 3 hours.

Image acquisition and charge deposition was performed using a Digital instruments Nanoscope III AFM, equipped with an extender module and signal access module. Metalized (~10 nm of Cr by sputter deposition) Olympus tips were used for imaging and deposition of charge. Height and phase images were collected using TMAFM (intermittent contact). Charge mapping and deposition were performed during interleve scans (non-contact), at constant tip-sample separation. The height data obtained in intermittent contact is used to pilot the constant tip-sample separation. In each experiment parameters were set to ensure good mapping of the surface topography and lift heights were sufficiently high as to avoid contact with the surface. All experiments were

performed at a set point ratio of 0.5, and a free amplitude of 100 nm, a constant scan speed of 1 Hz and lift heights of 30 and 60 nm for deposition and imaging respectively. D.C voltage was applied to the tip for deposition and imaging using an external voltage supply for voltages greater than 12 V and the AFM's internal supply for voltages below 12 V. This internal voltage signal was used as a trigger for the external source, so as to apply voltage to the tip only during interleve scans.

For charge deposition experiments the voltage was applied to the tip for one complete scan of the image area.

All depositions were carried out at either ±80 V, with the exception of depositions on annealed Kraton which also included deposition using a tip potential of +140 V. The size and voltages used during charge patch depositon are summarised in table 5.3. Images were taken at +25 V, +17 V, +12 V, 0 V, -12 V and –17 V for positive charge patches, and –25 V, -17 V, -12 V, 0 V, +12 V, and + 17 V for negative charge patches. The polarity of the ±25 V imaging potential was varied according to the charge patch deposited to compensate for the induced charge on the tip from that on the surface. Annealed Kraton films were only imaged using ±17 V.

Substrate	Tip Potential (V)	Area (μm^2)
Polystyrene	± 80	5
Polybutadiene	± 80	5
Polystyrene/Polybutadiene mixed phase	+ 80	10
Kraton	± 80	5
Annealed Kraton	+ 80, + 140	5

Table 5.3 Summary of charging conditions potentials and areas used for each polymer film.

5.4 Results

5.4.1 Charge Deposition onto Polystyrene and Polybutadiene Homopolymer Films.

Electric force microscopy images of the polystyrene surface after –80 V charge deposition experiments show a clear square of the same dimensions and location as the charging scan region, however no height or phase changes are evident in either the height or phase images, Figure 5.1a. The charged square is most clearly visible using a tip potential of +17 V for imaging, and the dark phase contrast of this patch represents an attractive tip / surface interaction. Reducing the imaging potential to +12 V reduces the intensity of the dark patch indicating lower attractive forces. Conversely for tip potentials of –25 V, –17 V and –12 V, a square of brighter phase contrast is present. The brighter contrast of these squares represents a repulsive interaction between the tip and the surface. The phase reversal occurs between imaging potentials of 0 V and –12 V, Figure 5.2a. Using the degree of brightness / darkness of the square patches it is clear that the greater the negative potential applied to the tip during imaging, the greater the degree of repulsion, and the greater the positive potential the greater the tip / sample attraction. As images were taken sequentially the order of imaging is also of importance when considering the degree of phase contrast, and will be further discussed later in this chapter. In this case the order of imaging potentials was: +17 V, +12 V, -17 V, -12 V, 0 V and –25 V.

EFM images of regions exposed to a potential of +80 V demonstrate a similar trend to that for –80 V deposition. However in this instance imaging with tip potentials greater than +12 V provides a square of bright phase contrast, and

correspondingly images taken with a tip potential of below + 12 V yield dark phase contrast, Figure 5.2b. Interestingly there is a reduction in the expected phase contrast for the extreme imaging potentials (+25 V, -17 V), with comparison to images taken with other tip potentials. The order of the image acquisition was in this case: +17 V, +12 V, -12 V, -17 V, 0 V, +25 V.

Charge deposition at ±80 V on the polybutadiene, produced changes in topographic, phase or EFM images, for any of the tip potentials used during imaging, Figure 5.3 and 5.4.

5.4.2 Charge Deposition on Phase Segregated Polystyrene / Polybutadiene Films

Charge deposition was carried out on a mixed phase polystyrene polybutadiene film, which as already discussed produces a surface comprising both polystyrene and polybutadiene regions, Chapter 3. In this instance the charge patch deposited was 10 μm square so as to cover several of the polystyrene regions. Comparison of the electric force image with the height and phase images shows clearly that only the polystyrene regions exhibit phase contrast in the electric force images, and also that no changes occur in the height or phase image as a result of deposition, Figure 5.5a. Images taken for the range of tip imaging potentials used produces dark phase contrast on the polystyrene regions, and no discernable phase contrast on the polybutadiene regions exposed to charging, Figure 5.5b. Again the order of imaging potentials is of importance to understanding the degree of phase shift observed and the order of imaging was: -17 V, +17 V, +25 V, +12 V, -12 V, 0V. An important difference between the mixed phase films and the homopolymer counterparts is the sample topography. The protrusion of the polystyrene from the surface is

exemplified by taking a pseudo-cross section of the film, Figure 5.5C. The markers correspond to a lateral difference of 1.1 μm and a vertical displacement of 224 nm.

5.4.3 Charge deposition on Kraton polymer films

EFM images of a region of un-annealed Kraton exposed to deposition of charge at –80V produced a square exhibiting EFM phase contrast for all the imaging potential used and little change in height or phase images, Figures 5.6a and 5.7a. Again use of a range of imaging potentials reveals a reversal from attractive to repulsive tip / sample interaction between –12 V and –17 V respectively. Interestingly a reduction in phase contrast was observed when the imaging potential was decreased from –17 V to –25 V, and no phase contrast was observed for the 0 V imaging potential. The order in which the images were collected was: -17 V, +17 V, -12 V, +12 V, -25 V, 0V.

Charging using +80 V again provides a square exhibiting phase contrast in EFM images, but here the contrast exhibited by the patch is considerably greater than that for the corresponding negative charge deposition, Figures 5.6b and 7b. The direction of the phase shift reverses from dark to bright between –12 V and + 12V tip voltages respectively. Also the respective bright / dark contrast is seen to increase with an increase in applied tip voltage, with the exception of + 25 V. Again there is no evidence of any phase contrast for a 0 V tip potential. The order of image acquisition was: +17 V, -17 V, +25 V, +12 V, -12 V, 0 V.

EFM images of the phase segregated copolymer surface after exposure to potentials of +80 V and +140 V demonstrated charge retention only on the polystyrene 'gasket' regions, Figure 5.8. Again no changes are observed in

either the height or phase images, Figure 5.8. EFM images using +17 V and –17 V tip potentials produced regions of dark and bright phase contrast respectively for both charging potentials, Figure 5.9.

Interestingly increasing the deposition potential to +140 V produces regions exhibiting charge retention outside the area scanned, whereas a potential of +80 V only charges regions within the rectangle scanned.

(a)

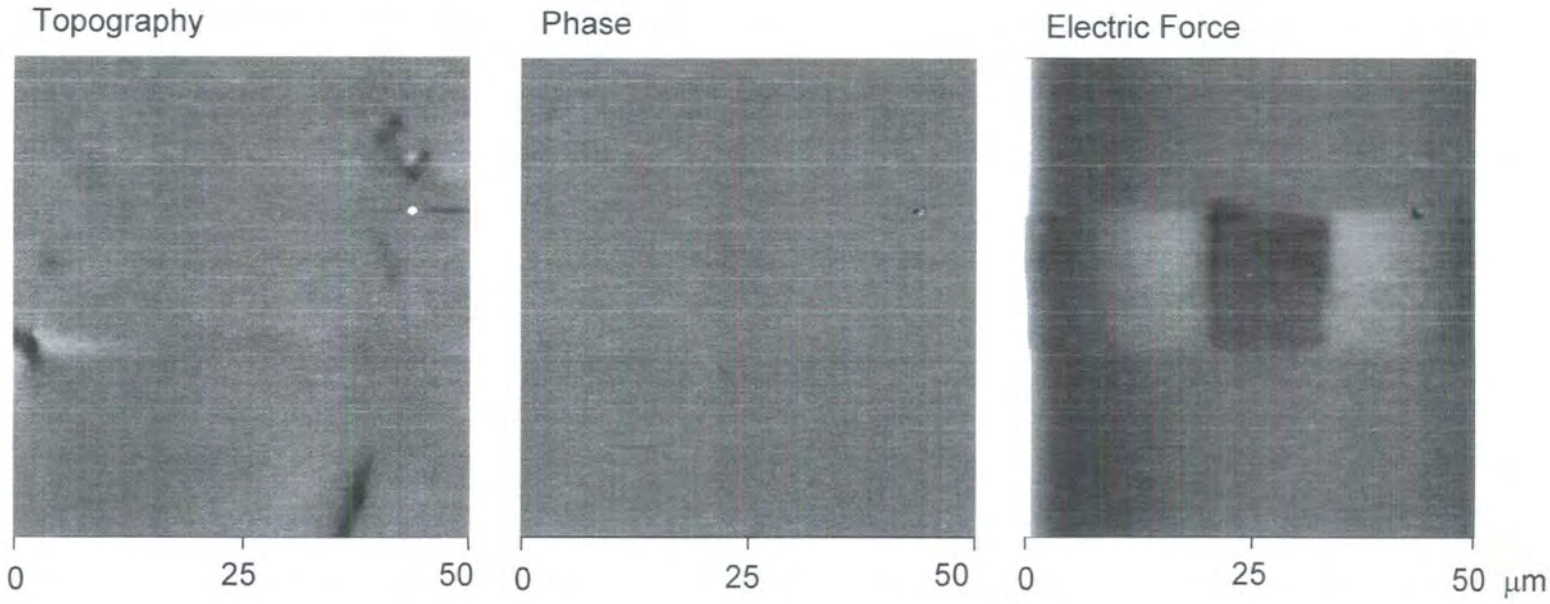

Figure 5.1 Height, phase and electric force images (x = y = 50 μm, z = 50 nm, 45°, and 10° respectively) of polystyrene as a function of corona discharge exposure: (a) –80 V corona, imaged using a tip potential of +17 V; (b) +80 V corona, imaged using a tip potential of –12 V.

(b)

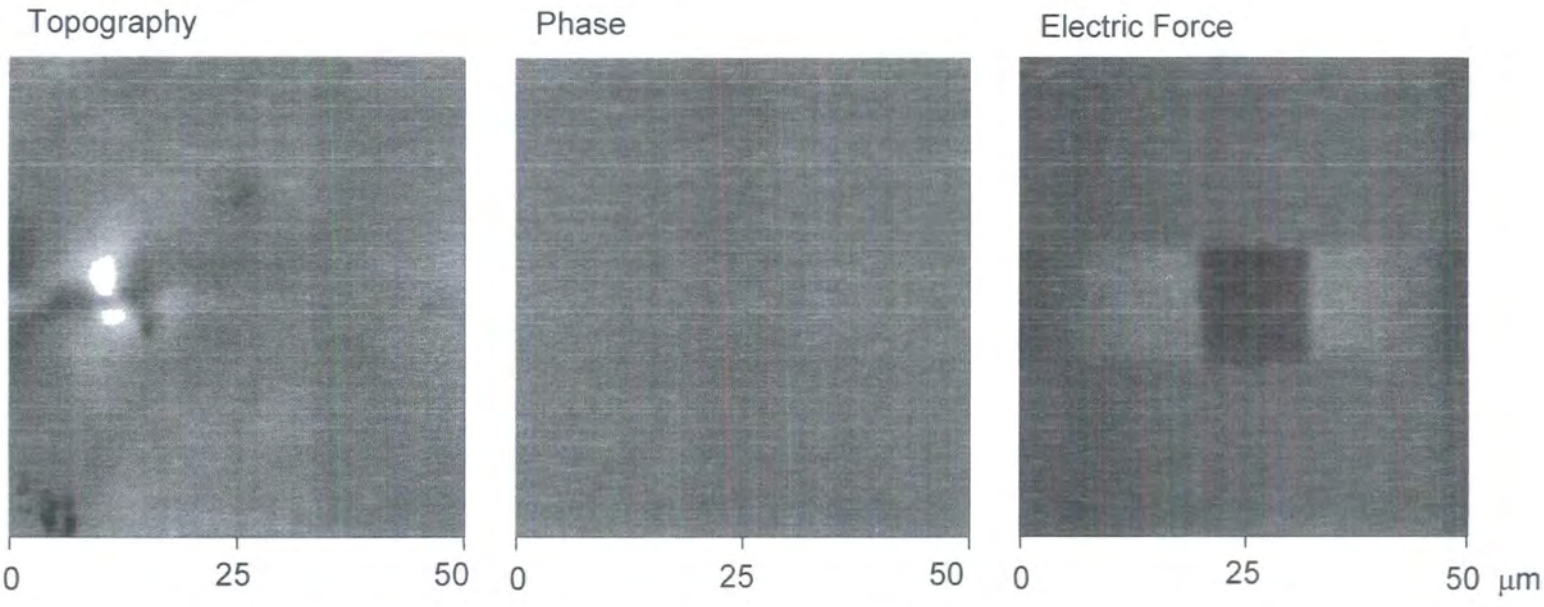

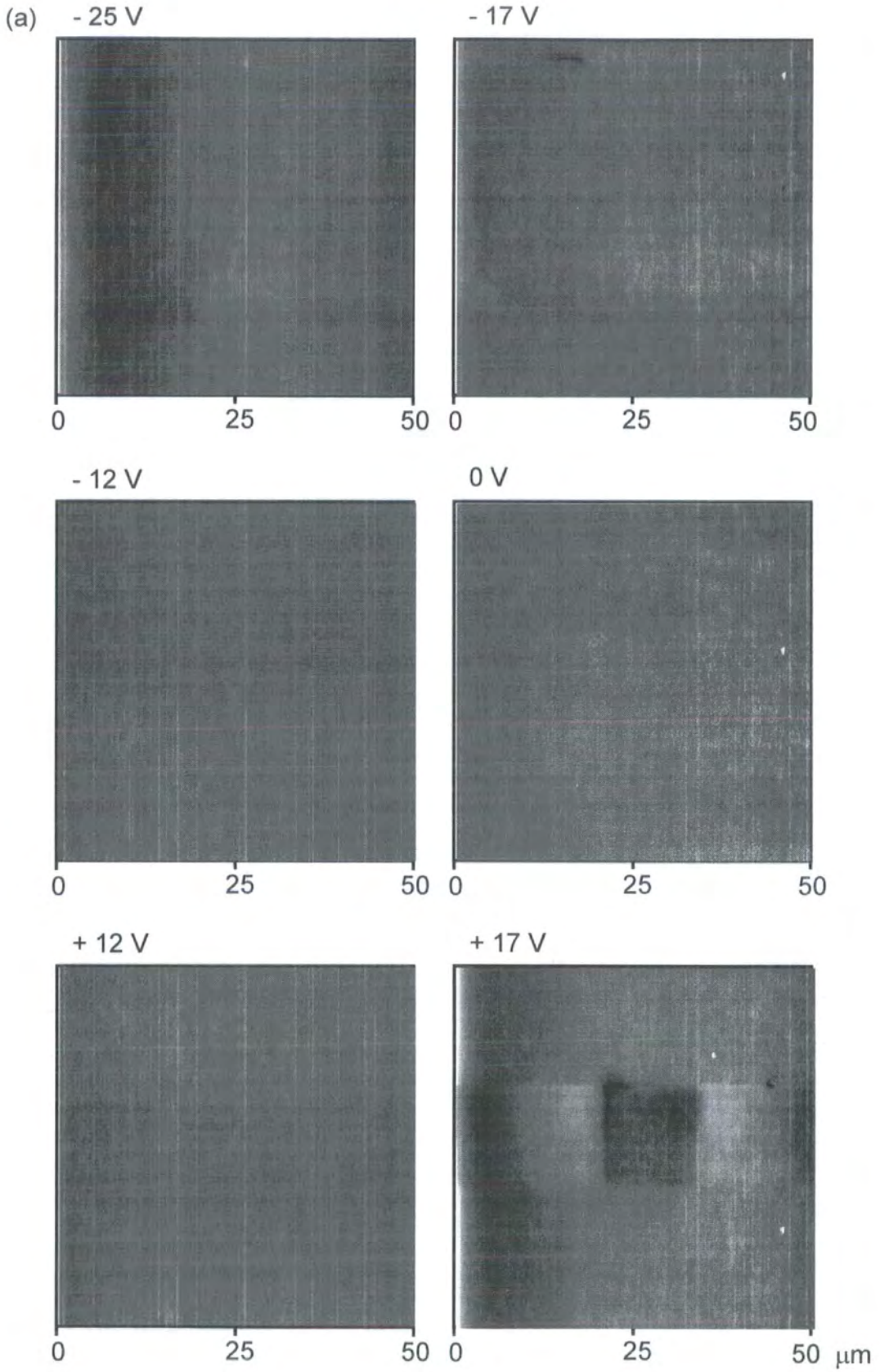

Figure 5.2 EFM images (x = y = 50 μm, z = 10°) taken using indicated potentials, of charge patch deposited on a spin cast polystyrene film: (a) - 80 V deposition potential; (b) + 80 V deposition potential.

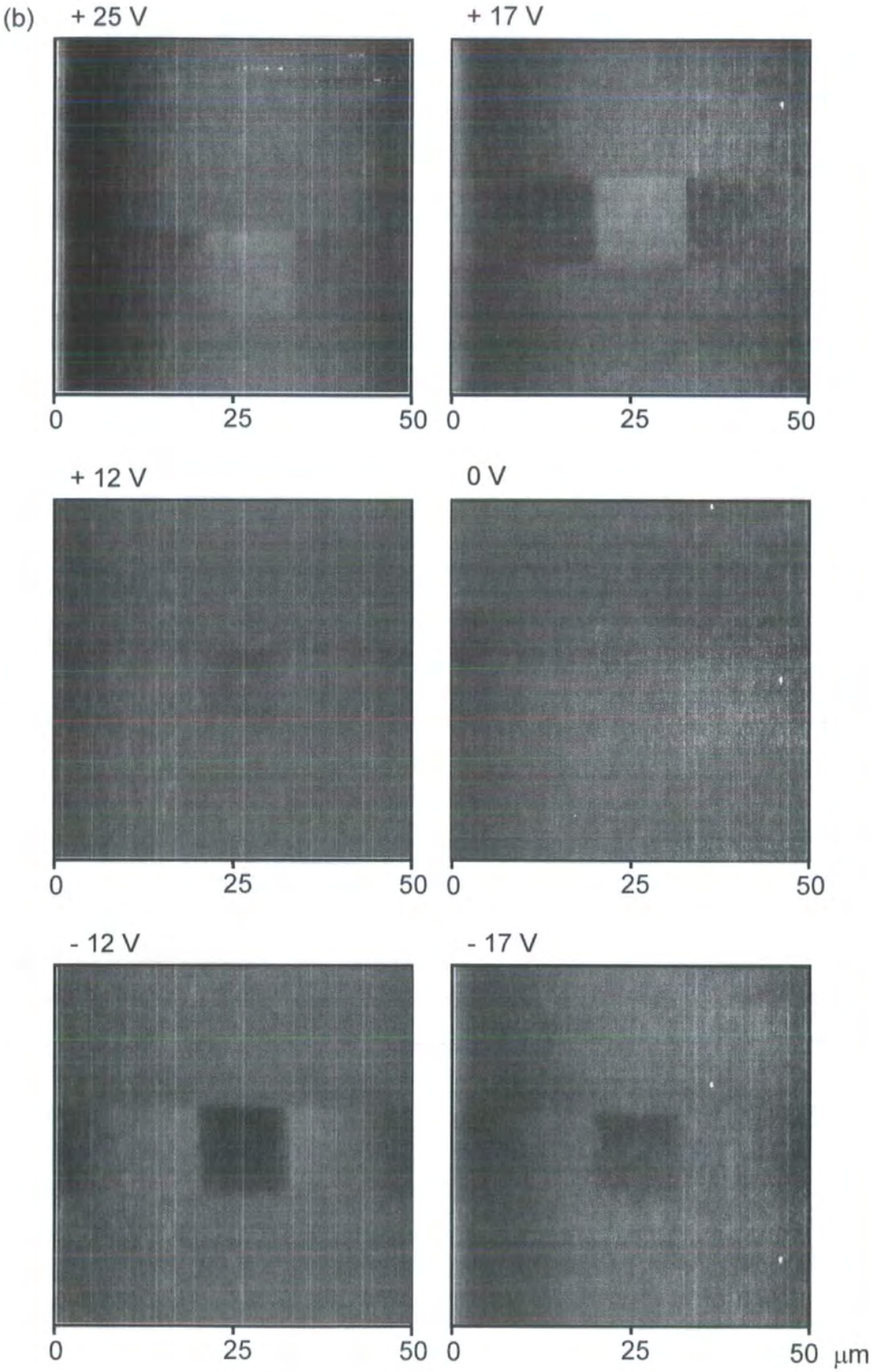
(b)
+ 25 V
+ 17 V
0
25
50
+ 12 V
0 V
- 12 V
- 17 V
μm

(a)

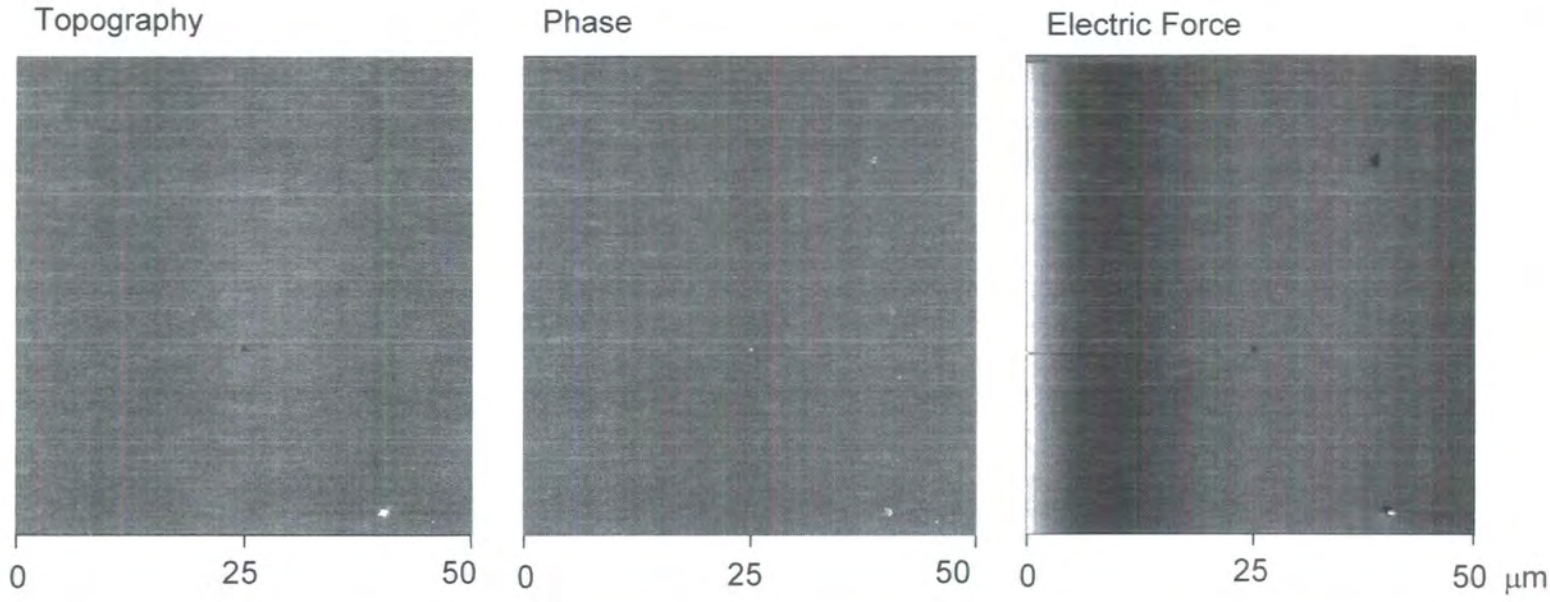

Figure 5.3 Height, phase and electric force images (x = y = 50 μm, z = 50 nm, 45°, and 10° respectively) of polybutadiene as a function of corona discharge exposure: (a) –80 V corona, imaged using a tip potential of +17 V; (b) +80 V corona, imaged using a tip potential of –12 V.

(b)

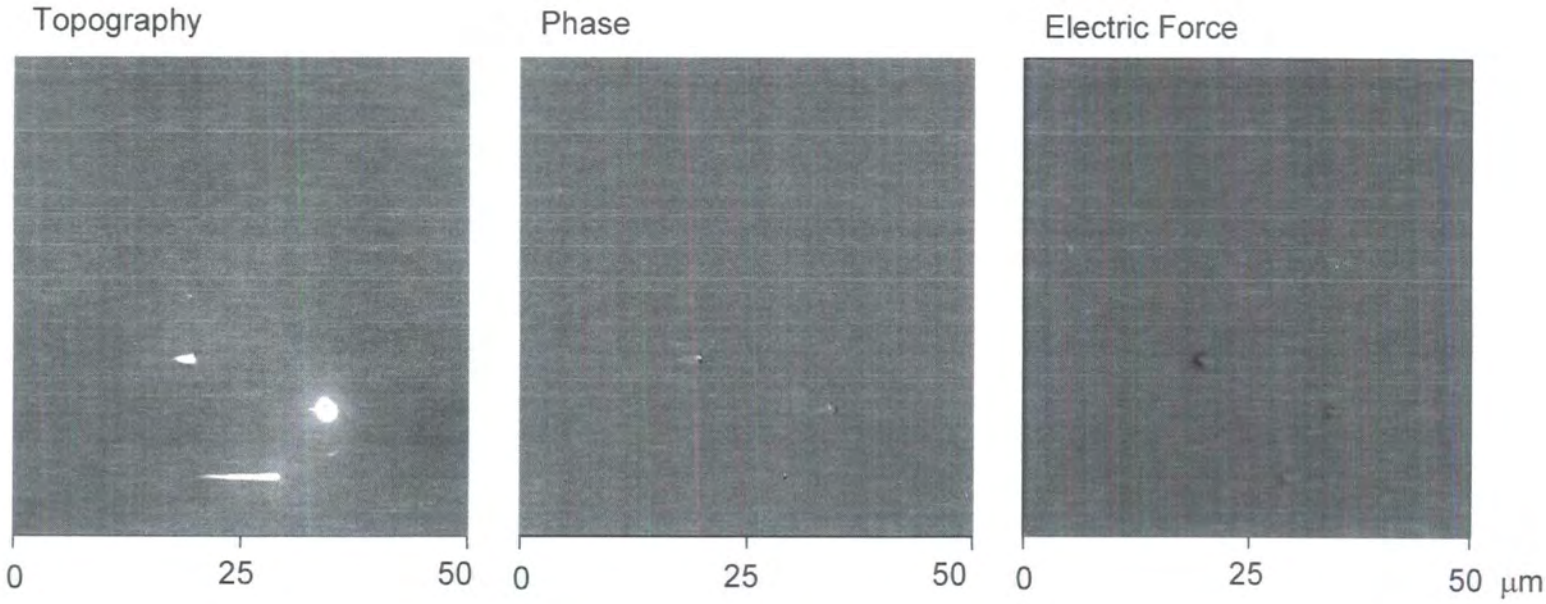

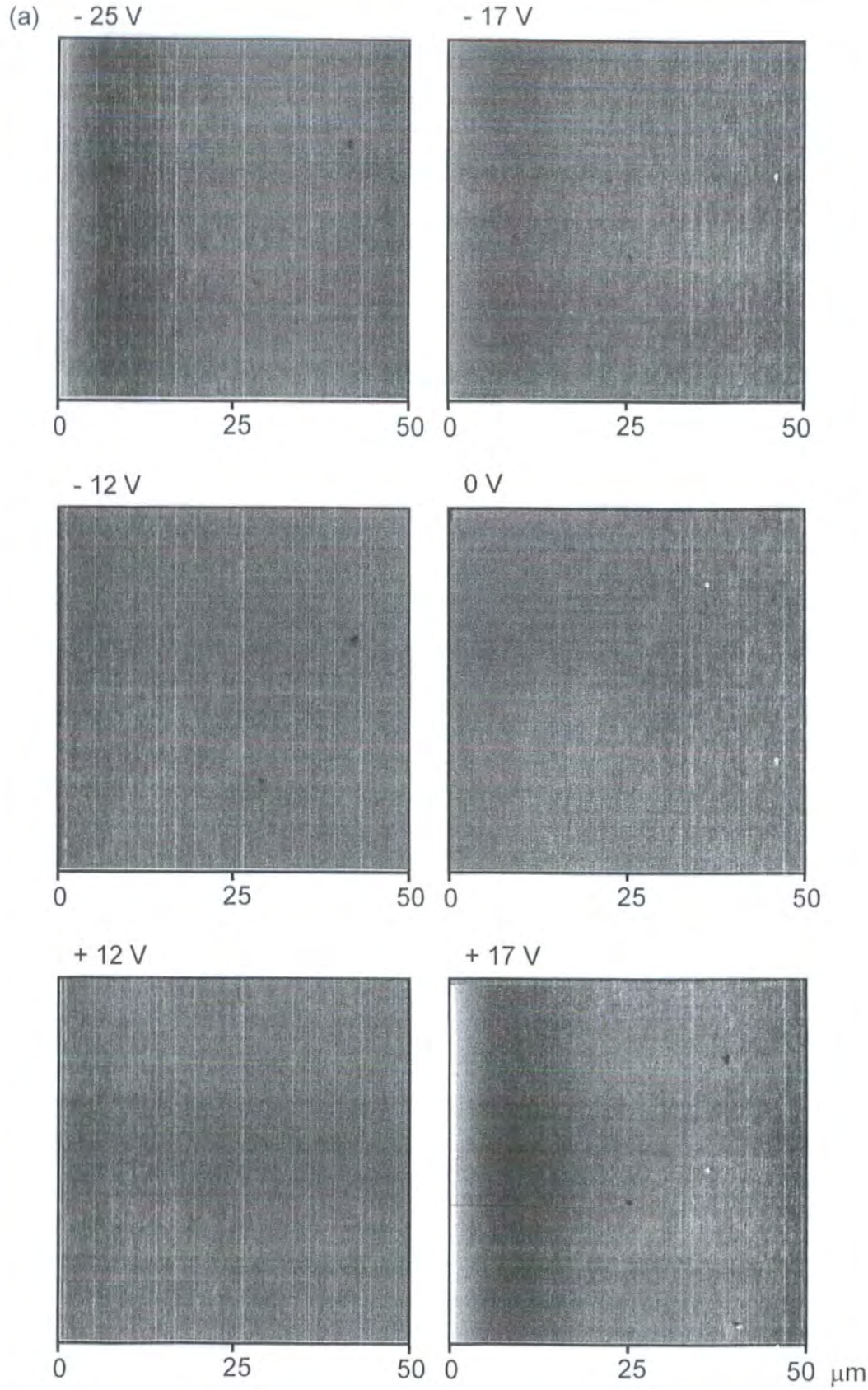

Figure 5.4 EFM images (x = y = 50 μm, z = 10°) taken using indicated potentials, of charge patch deposited on a spin cast polybutadiene film: (a) - 80 V deposition potential; (b) + 80 V deposition potential.

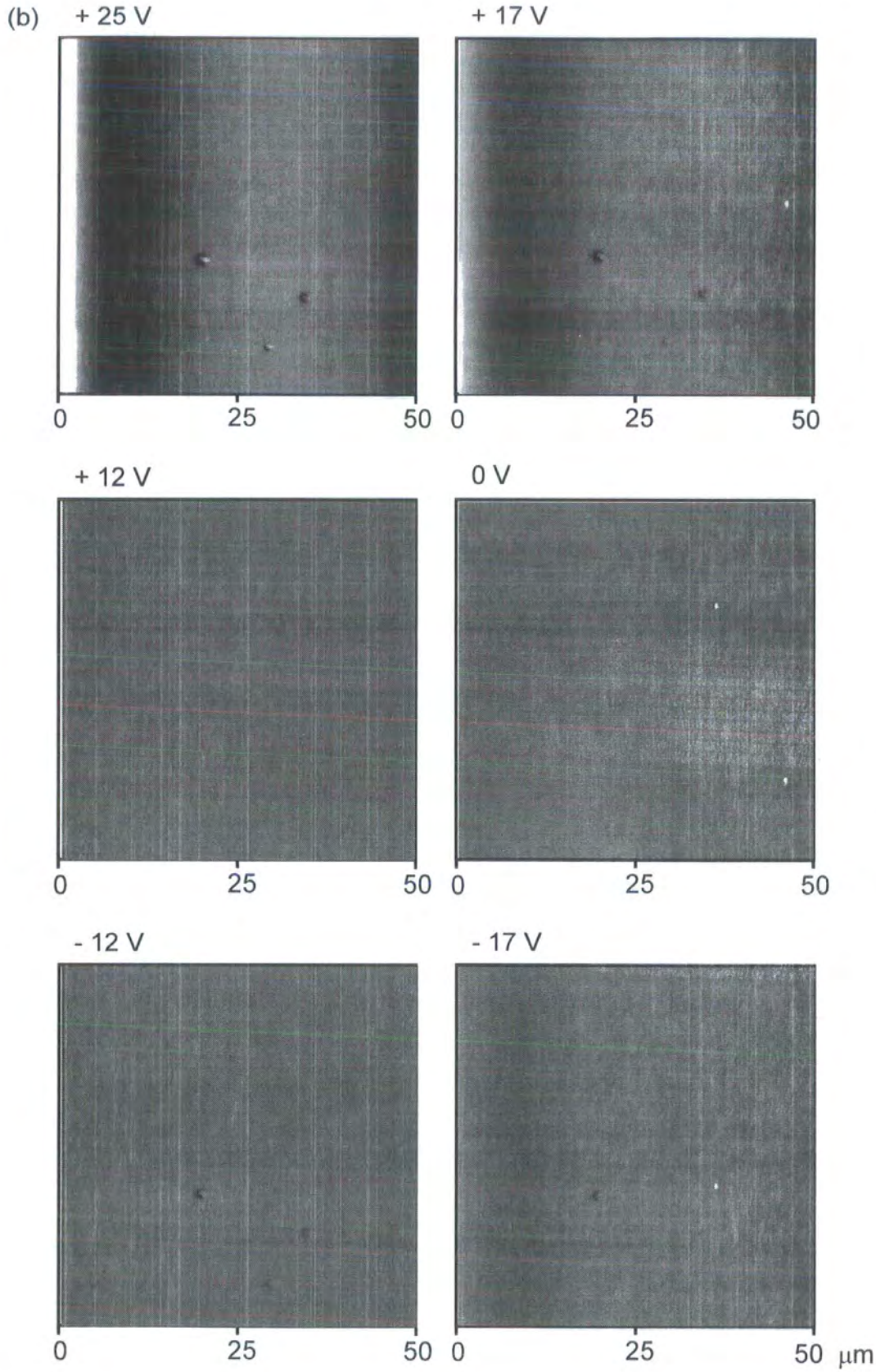
(b)
+ 25 V
+ 17 V
+ 12 V
0 V
- 12 V
- 17 V
0
25
50
μm

(a)

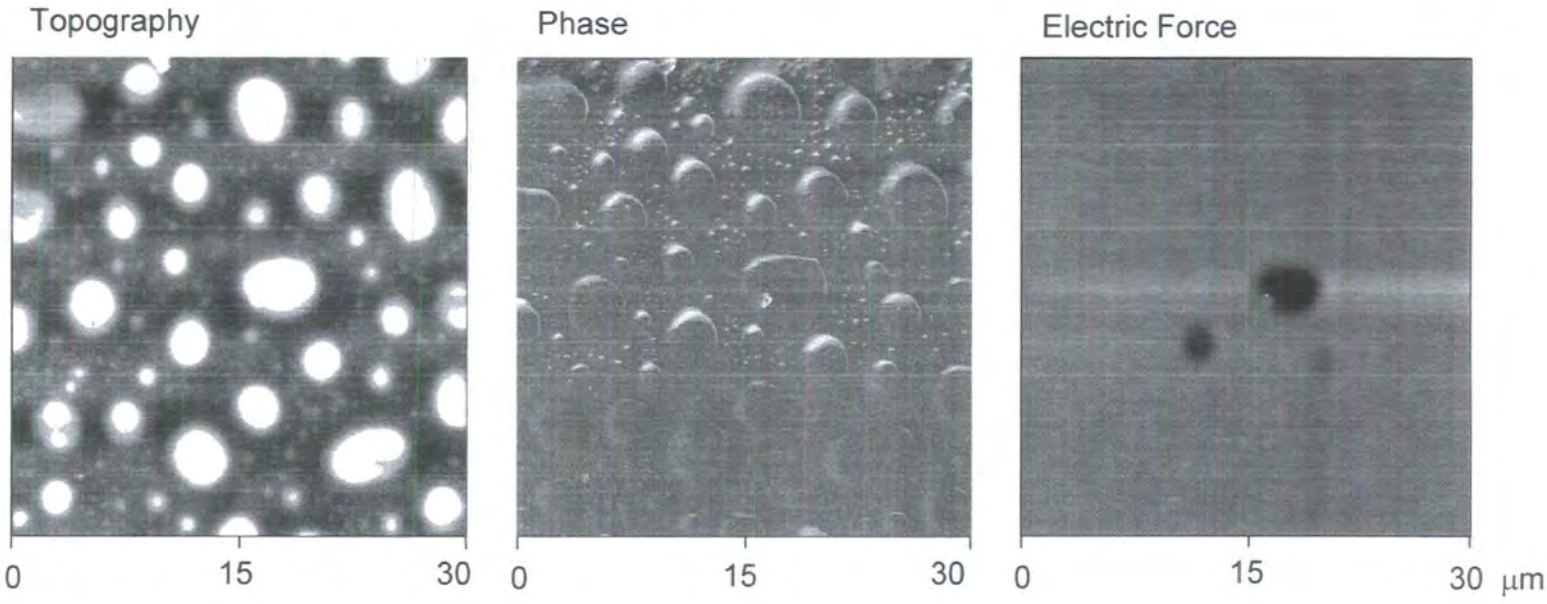

Figure 5.5 AFM and EFM images of phase segregated polystyrene / polybutadiene film after charge deposition (+80 V): (a) height, phase and electric force (+17 V tip potential) images (x = y = 30 μm, z = 350 nm; 90°; 10° respectively); (b) lift mode EFM images (x = y = 50 μm, z= 10°) as a function of imaging tip potential; (c) psudo cross section.

(b)

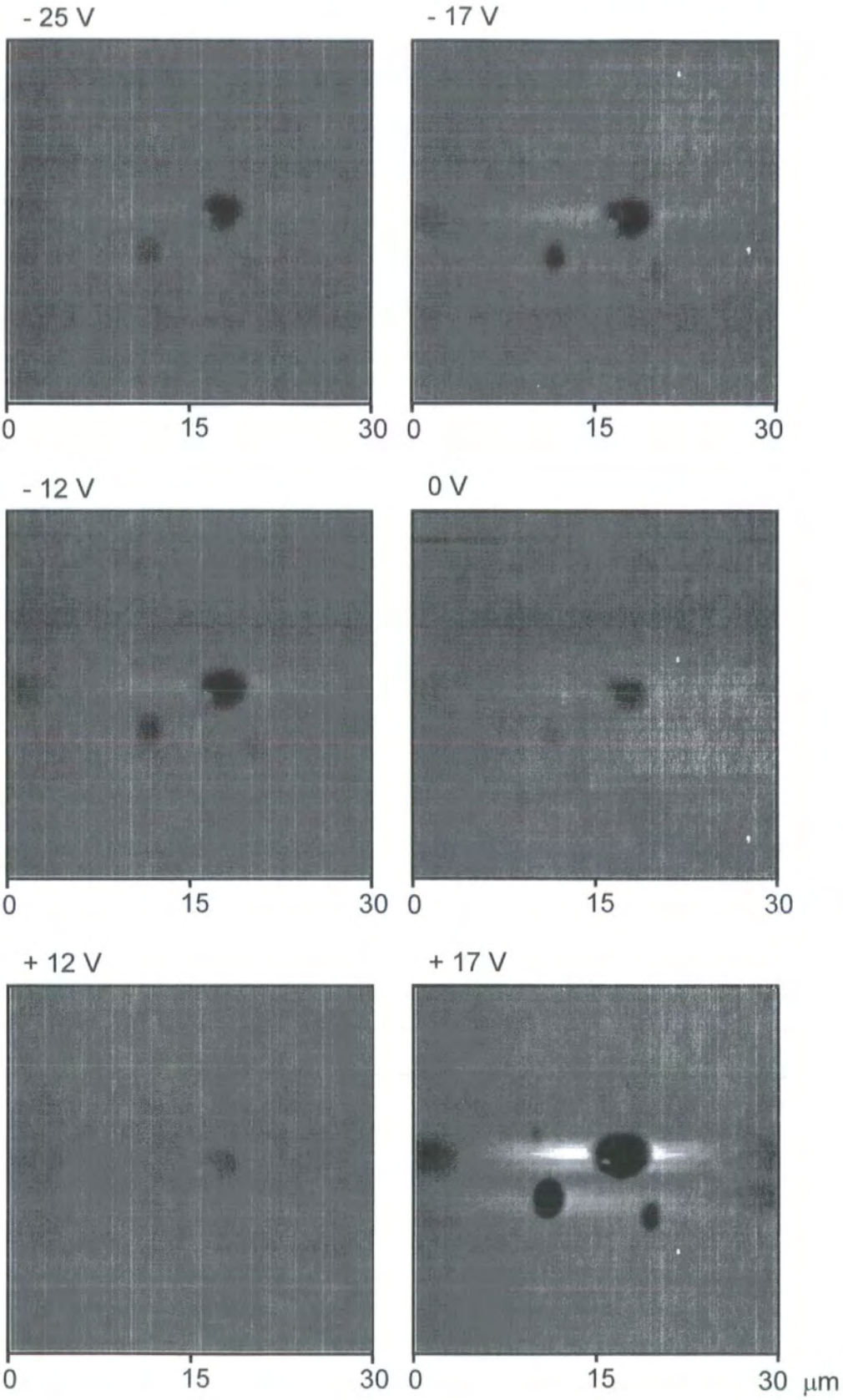

(c)

Topography

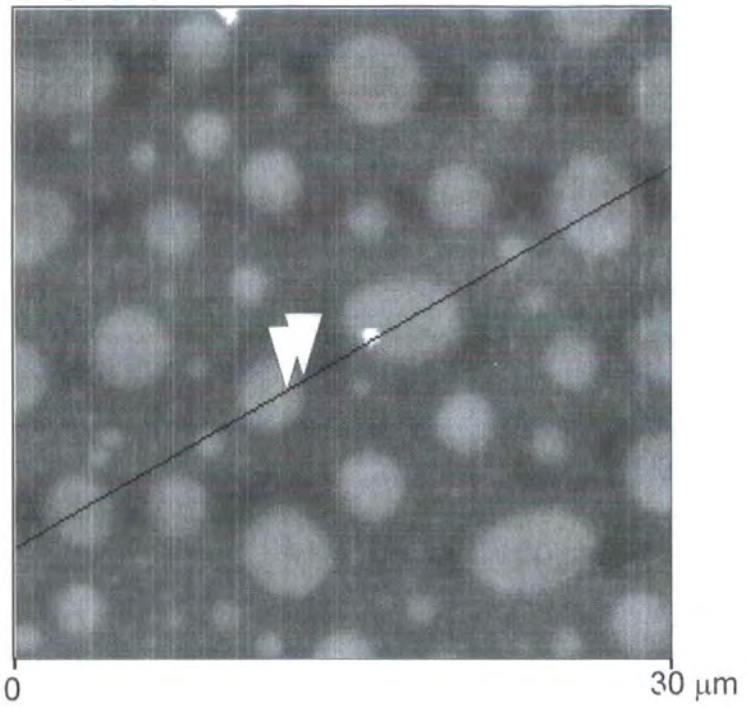

Pseudo cross section

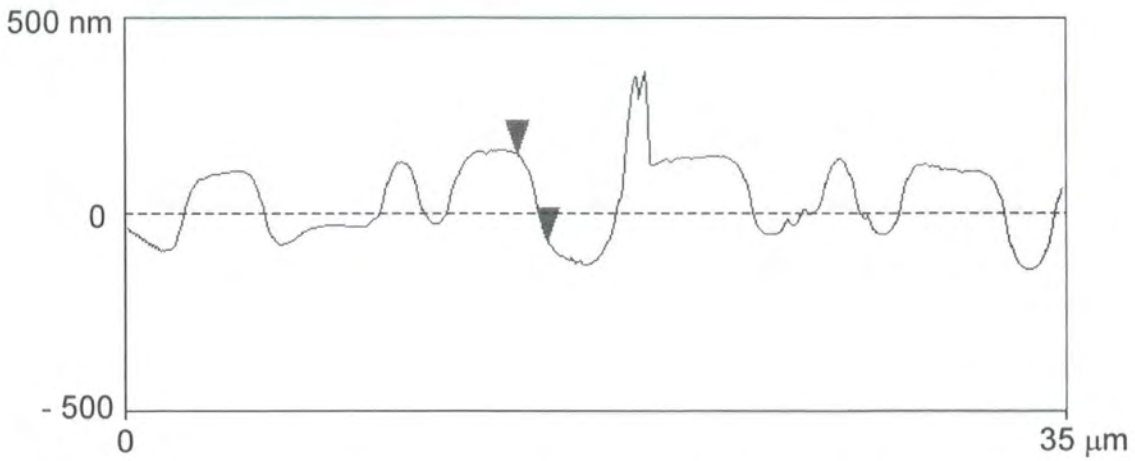

Triangular markers on topography image correspond to those on pseudo cross section.

(a)

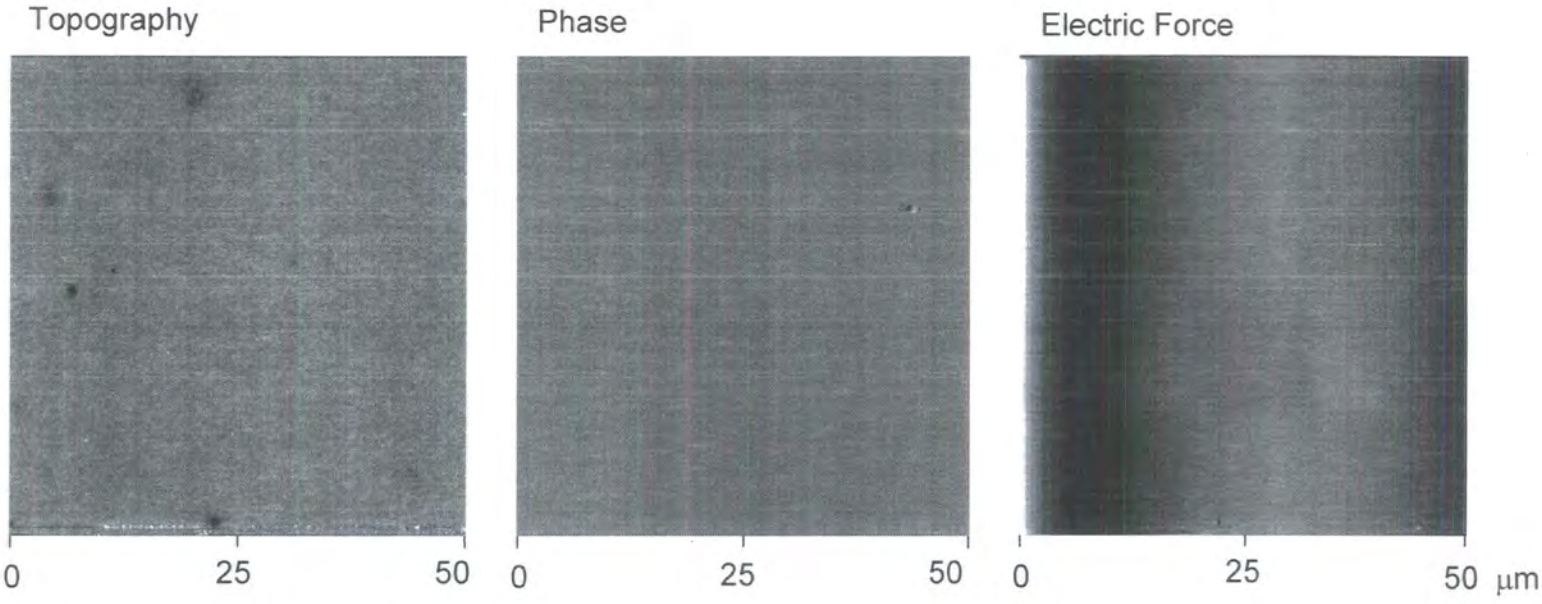

Figure 5.6 Height, phase and electric force images (x = y = 50 μm, z = 50 nm, 45°, and 10° respectively) of Kraton as a function of corona discharge exposure: (a) –80 V corona, imaged using a tip potential of +17 V; (b) +80 V corona, imaged using a tip potential of + 12 V.

(b)

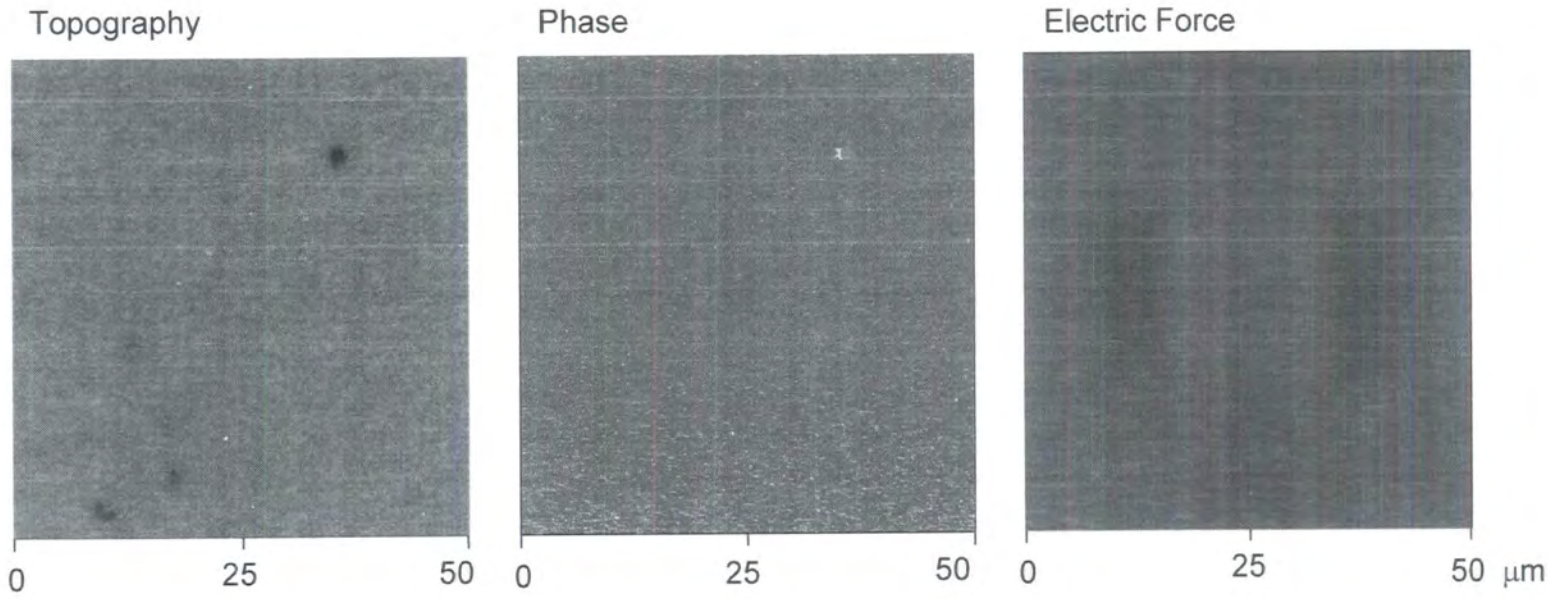

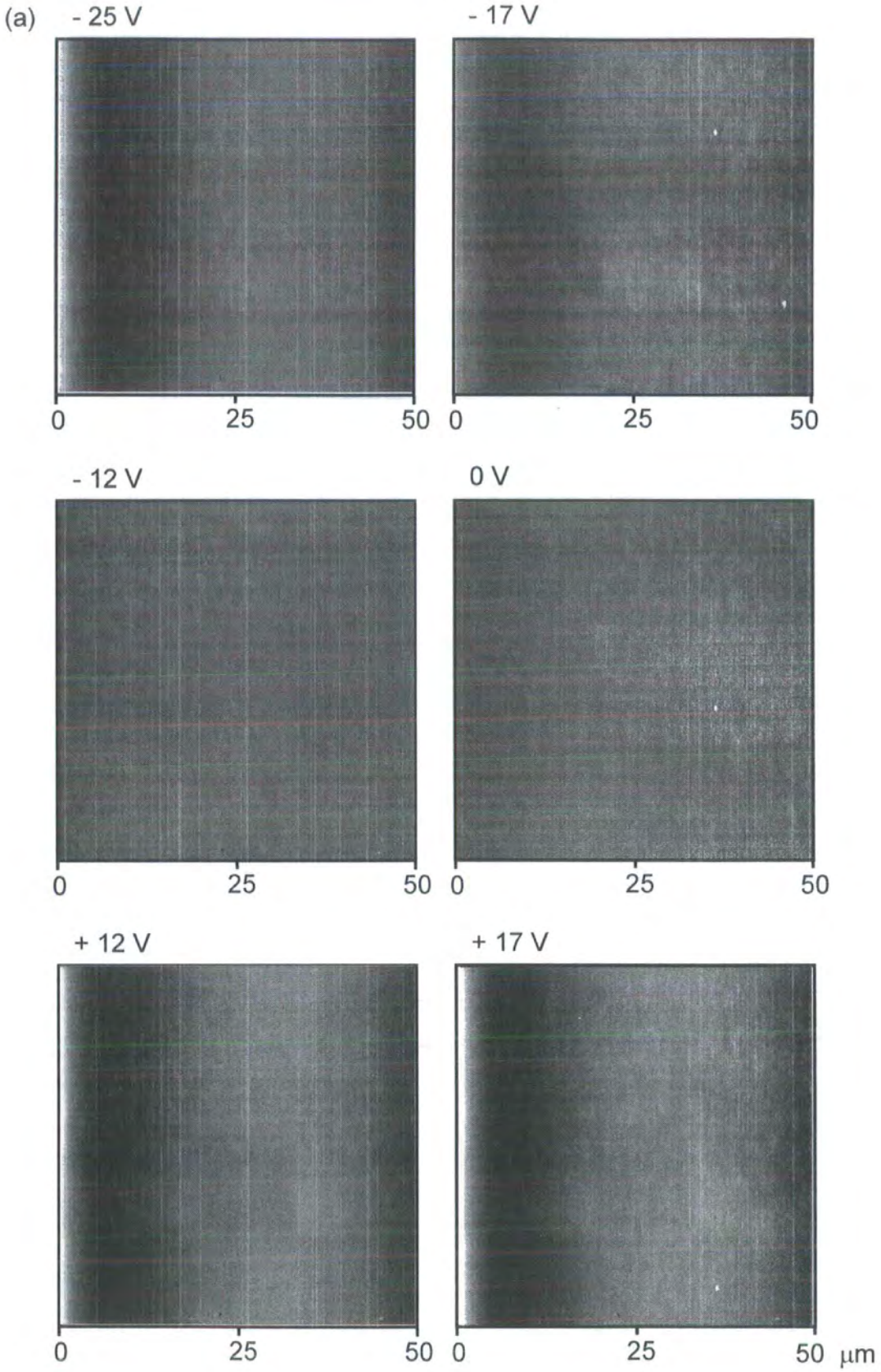

Figure 5.7 EFM images (x = y = 50 μm, z = 10°) taken using indicated potentials, of charge patch deposited on a spin cast pre-annealed Kraton film: (a) - 80 V deposition potential; (b) + 80 V deposition potential.

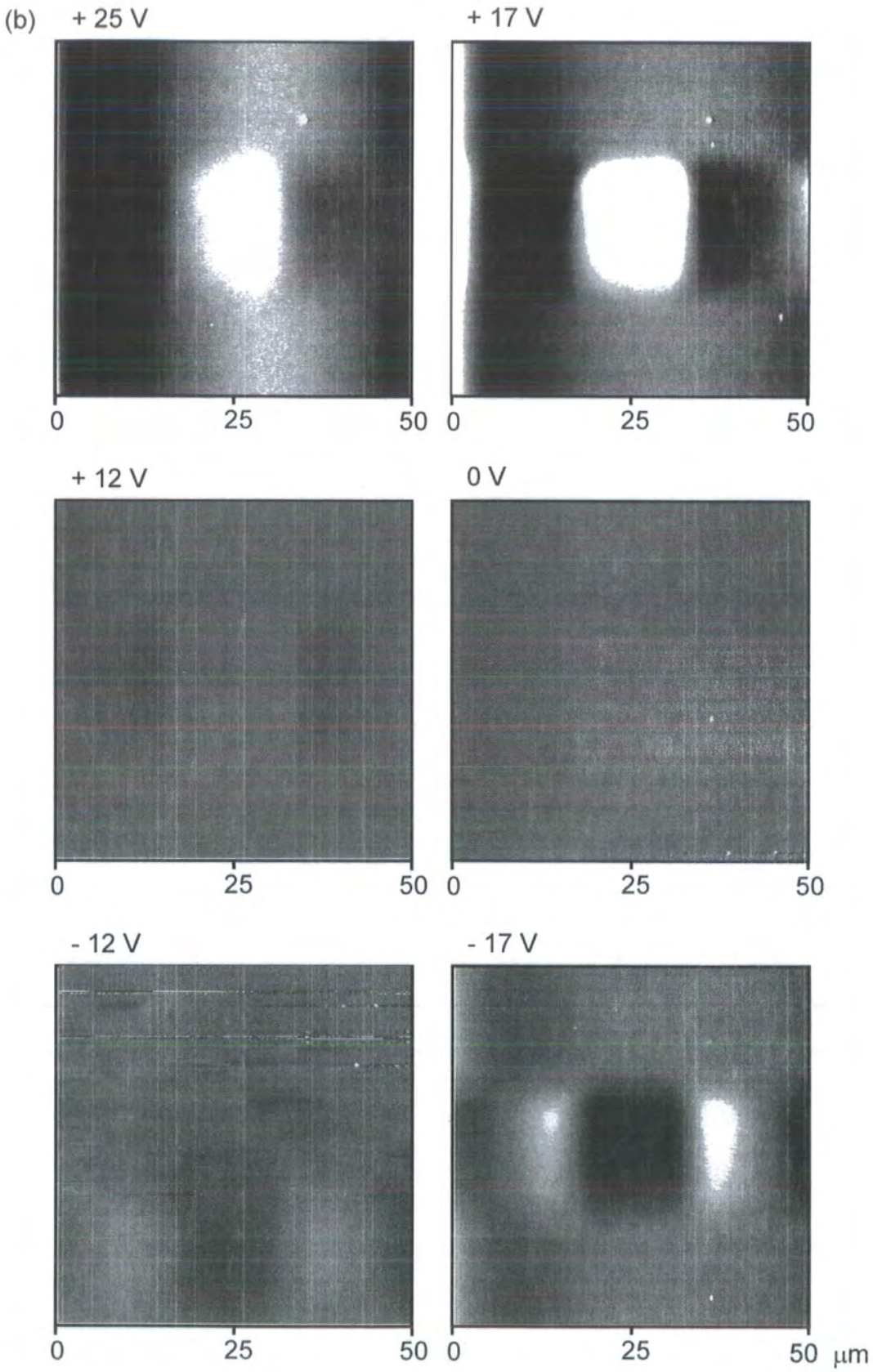
(b)
+ 25 V
+ 17 V
+ 12 V
0 V
- 12 V
- 17 V
0
25
50
μm

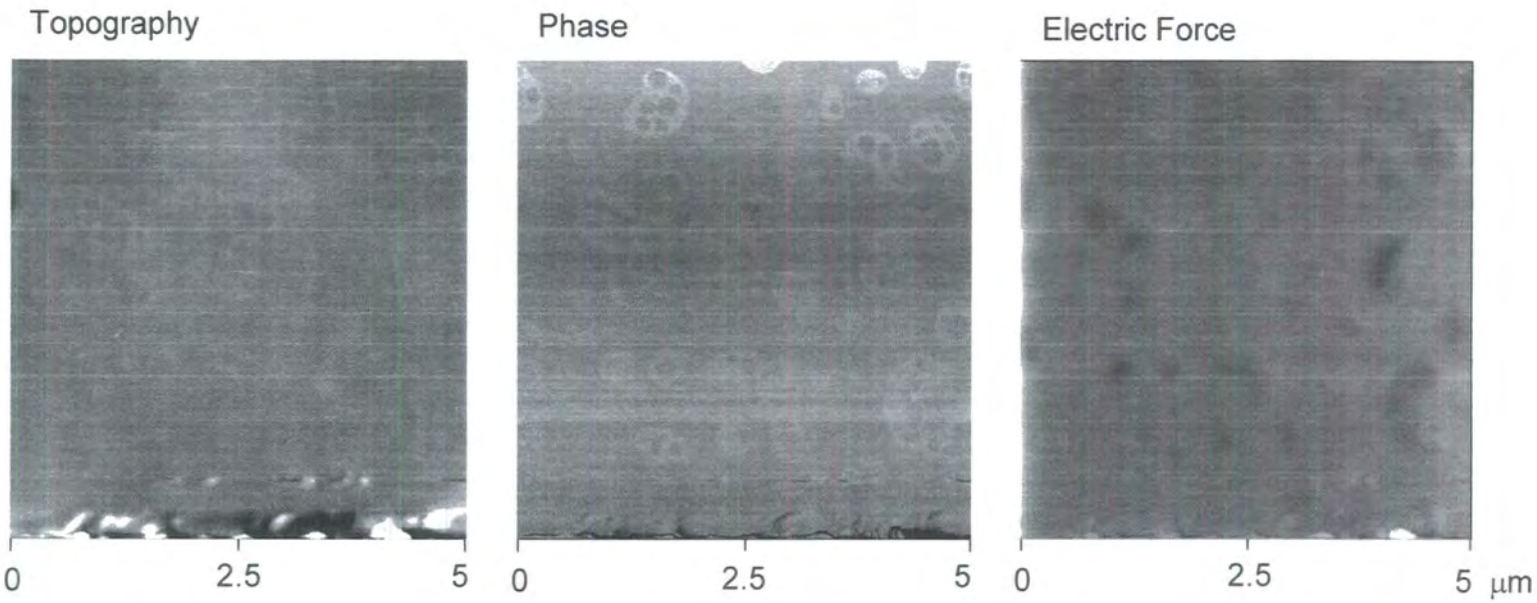

Figure 5.8 Height, phase and electric force (-17 V tip potential) images (x = y = 5 μm, z = 350 nm: 70°; 10° respectively) of annealed Kraton after charge deposition (+140 V tip potential).

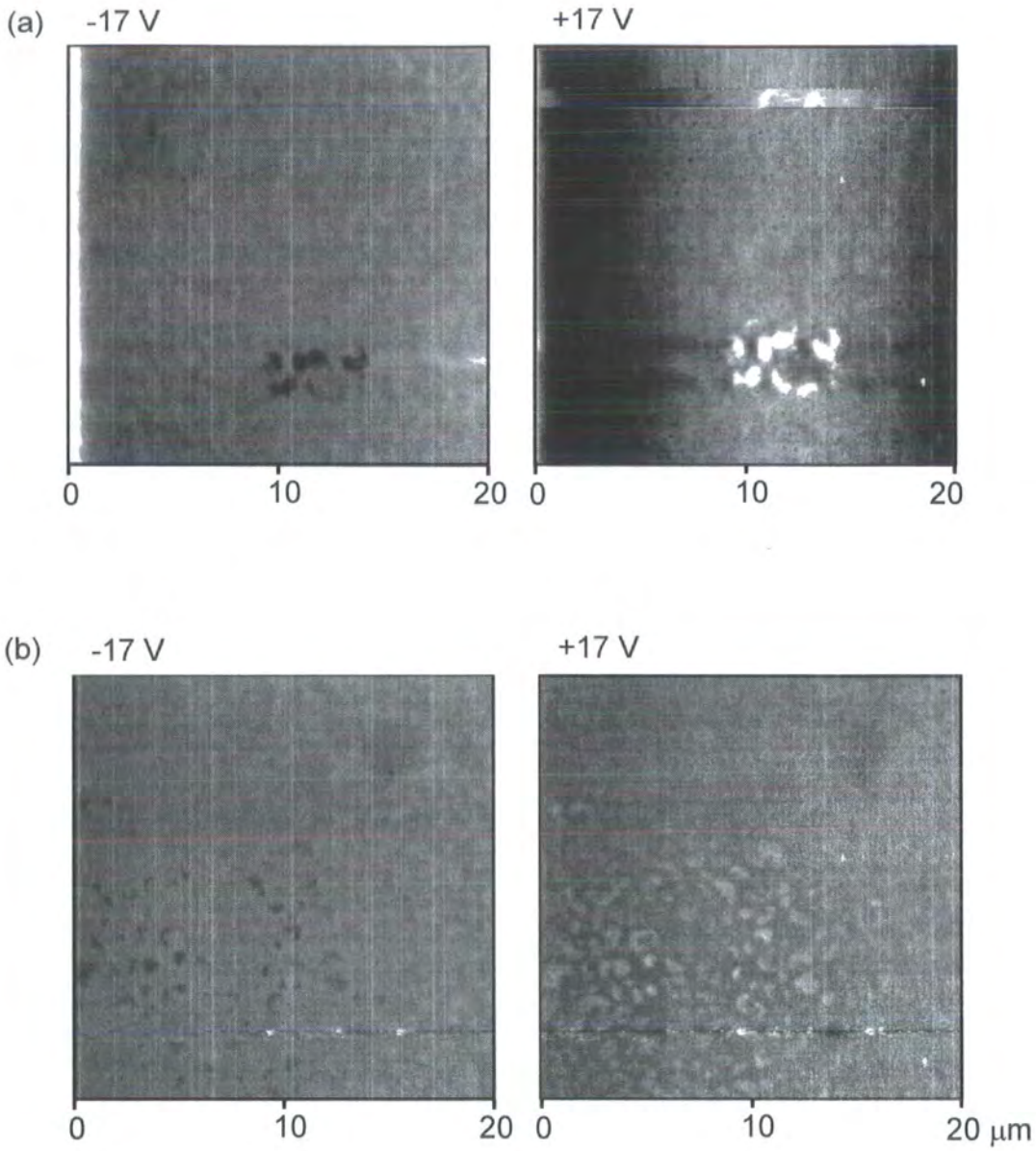

Figure 5.9 EFM images (x = y = 20 μm, z = 10°) taken using indicated potentials, of charge patch deposited on Annealed Kraton: (a) +80 V deposition potential; (b) +140 V deposition potential.

5.5 Discussion

Corona discharges are well known to impart surface charge to insulating polymeric materials. Such discharges are generally carried out on the macroscale using an arrangement similar to that depicted in figure 5.10. A large potential (typically 10 kV)[22] is applied to the needle, causing ionisation of the air surrounding the needle. Charge of like polarity to that applied to the needle is imparted to the surface by the repulsion of like charged species from the needle. These then travel along the electric field gradient to earth, and are intercepted by the surface of the insulating polymer, which gradually accumulates a net charge. Physiochemical changes, such as oxidation may also occur at the surface of polymers as a result of corona treatment.[18]

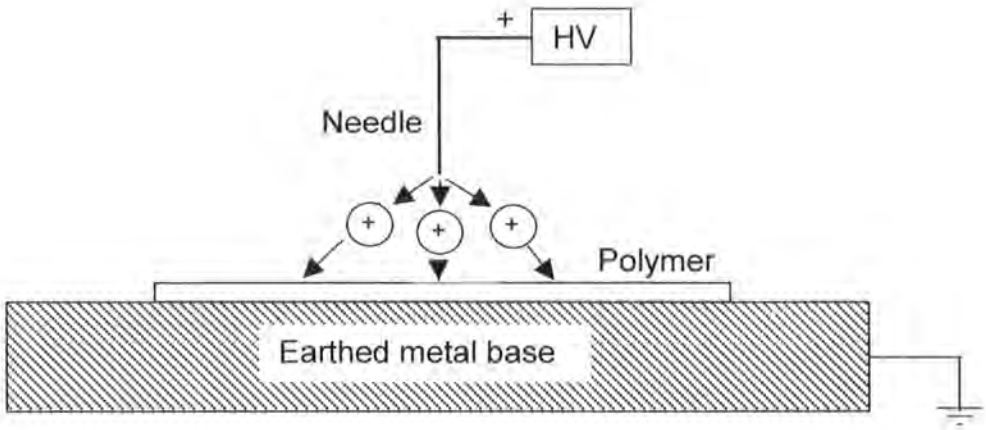

Figure 5.10 Diagramatic representation of corona discharge treatment of a polymer.

Application potentials, of only -50 V to a metalized AFM tip has previously been shown to form a corona discharge around the tip.[5] This dramatic reduction in potential necessary to establish the discharge, with comparison to potentials used for bulk treatments occur as a direct result of the size and curvature of the

tip (radius 13 nm[19]), thereby increasing the density of the field current.[20] Scanning the tip above the polymer surfaces results in exposure to the charged species present in the corona. Charged species of the same polarity as the tip potential then drift down the electric field gradient to the polymer surface in the same was as described above. This process has previously been shown to deposit charged regions on polypropylene surfaces.[5]

Investigation of physiochemical changes on all the polymer surfaces used here, by topographic and phase imaging, demonstrated no change in the exposed regions, as is consistent with previous results on polypropylene.[5]

Scanning of the corona generated by a tip potential of +80 V over the surface of polystyrene produces a positive charge patch on the surface, as is illustrated by systematic variation of the tip potential during EFM imaging. The off setting of the phase reversal point to between +12 V and +17 V is a direct consequence of the mirror charge on the tip, and can be used to gain a crude estimate to the potential on the surface. Also of interest in the positive charge deposition on polystyrene is the depletion in phase contrast from +17 V and –12 V to +25 V and-17 V respectively. As the electrostatic repulsion / attraction should increase for greater potentials, we must also consider the sequence in which the images were collected. In this instance the final three images collected were, in order –17 V, 0 V and +25 V respectively. The reduction in expected contrast in these images suggests that the charge dissipates over time.

Similar sequential variation of tip voltage, during imaging of the charge patch produced by negative corona exposure, proves the surface charge to be negative and between 0 V and –12 V. In this instance the order in which

images were acquired is not contuitive to making obvious reductions in phase intensity due to charge dissipation.

Interestingly EFM imaging of a polybutadiene film exposed to the same charging conditions, produced no evidence of charge retention, for either positive or negative deposition. This difference may be explained in terms of the conductivity of the two polymers. Polystyrene has been well reported to undergo charging by corona treatment in the literature,[21] and is an excellent insulator.[22] Conversely some conduction has been reported in polybutadiene.[23] Although the methods of conduction in the polybutadiene are not fully understood it would seem likely that the extent of electron delocalisation in the chain would play an important role. Alternatively ionic conduction from species remaining from polymer production may play a part.[22]

These results were further reinforced by EFM mapping of positive corona treated phase segregated polymer films. The only differences between the two surfaces was that the polybutadiene was cured in the mixed phase system. The independence of curing upon the conduction of charge in the polybutadiene, may reflect the remaining olefinic character after curing as demonstrated by IR in Chapter 3. Further ionic conduction may still also occur.

The lack of phase inversion for the EFM imaging potentials used implies a surface charge in excess of +25 V, as little evidence of a reduction in intensity is seen for a –25 V imaging potential. The reason for such a high charge retention in this system is not certain. However the sample topography may have an effect. Considering the profile the tip will follow when raised to a constant lift height of 30nm (Figure 5.11), the tip sample separation on the curved polystyrene regions adjacent to tip, will be less than the separation of the film directly under the tip. This may cause greater dosing of these regions

with charged species. This reduced tip / sample separation will also have implication during electric force imaging.

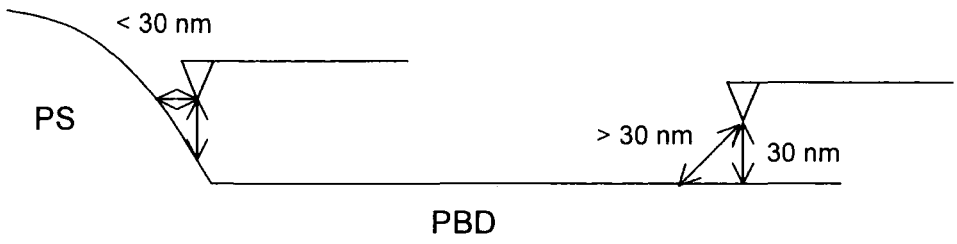

Figure 5.11 Schematic representation of reduced tip sample separation during interleve scanning, as a result of sample topography.

As has been previously described in this thesis, Kraton is a block copolymer comprising segments of polybutadiene and polystyrene, Chapter 4.

Exposure of these Kraton films prior to annealing has been shown to result in charge deposition, with no topographic or material changes. This is consistent with the results earlier in this study for both polystyrene and polybutadiene.

Sequential variation of the charge deposition on Kraton films prior to annealing reveals a similar trend to that seen for the polystyrene film. Exposure of the Kraton to the positive corona produces a surface charge of between 0V and + 12 V. Considering the dramatic phase contrast obtained for the initial image (+17 V) several of the other images, most notably the +25 V and +12 V images demonstrate lower than expected phase contrast. This is again consistent with the order of imaging, as has been previously seen for charge patches on polystyrene and polystyrene / polybutadiene mixed phase films.

Exposure to the negative corona produces a charge patch, exhibiting phase inversion between 0 V and +12 V suggesting the potential on the surface lies between 0V and –12 V. Again images taken later in the series demonstrate lower phase contrast than might be expected for the potentials used, suggesting charge depletion also occurs in this system.

It has been shown in chapter 4 that annealing of Kraton films, results in phase segregation of the polystyrene and polybutadiene at the surface. The selective deposition of charge patches (<+17 V for both depositions) only into the polystyrene regions of the surface is consistent with previous results for both the homopolymer and mixed phase polymer films. The diffuse nature of the charge using a deposition potential of +140 V is consistent with charging from a corona discharge.[5]

5.6 Conclusions

The potential of the electric force microscope to deposit spatially confined charge on the surface of polystyrene has been demonstrated. Conversely the lack of charge retention at the surface of polybutadiene has been demonstrated. The differing charge retention characters of the two polymers has been exploited to produce surfaces where charge deposition is confined by polymer segregation.

5.7 References

1 Bruneel, J. L., Micheron, F. *Congr. Int. Electrost* **1977**, Paper No. 38.

2 Takamatsu, T., Okada, K. K., F. *Jpn. Kokai Tokkyo Koho* 19850925, 1985.

3 Yamazaki, K., Shingagawa, T., Watanabe, T., Takahira, T. *Jpn. Kokai Tokkyo Koho* 19881110, 1988.

4 Barrett, R. C., Quate, C. F. *J. Appl. Phys.* **1991**, *70*, 2725.

5 Ebbens, S. J. Ph.D. Thesis, *Chemical and Electrical Modification of Polypropylene Surfaces*, University of Durham, **2000**.

6 Sessler, G. M., West, J. E. *Phot. Sci. Eng.* **1974**, *18*, 162.

7 Schönenberger, C. *Phys. Rev. B.* **1992**, *45*, 45.

8 Stern, J. E., Terris, B. D., Mamin, H. J., Rugar, D. *Appl. Phys. Lett.* **1988**, *53*, 2717.

9 Nelson, M. W., Schroeder, P. G., Schlaf, R., Parkinson, B. A. *Electrochemical Solid State Lett.* **1999**, *2*, 475.

10 Nelson, M. W., Schroeder, P. G., Schlaf, R., Parkinson, B. A., Almgren, C. W., Erikson, A. N. *Appl. Phys. Lett.* **1999**, *74*, 1421.

11 Whelan, P. M., Hodgson, M. J. *Essential Principles of Physics*, John Murray: London, 1978.

12 Magonov, S. N., Elings, V. B., Whangbo, M. H. *Surf. Sci.* **1997**, *375*, L385.

13 Whangbo, M.-H., Bar, G., Brandsch, R. *Surf. Sci.* **1998**, *411*, L749.

14 Martin, Y., Williams, C. C., Wickramasinghe, H. K. *J. Appl. Phys.* **1987**, *61*, 4423.

15 Stern, J.E., Terris, B.D., Mamin, H.J., Rugar, D. *Appl. Phys. Lett.* **1988**, *53*, 2717.

16 Giacometti, J. A., Oliveria Jr., O. O. *IEEE Trans. Elect. Insul.* **1992**, *27*, 924.

17 Ramirez-Aguilar, K. A., Rowlen, K. L. *Langmuir* **1998**, *14*, 2562.

18 Steinhauser, H, Ellinghorst, G. *Angew. Makromol. Chem.*, **1984**, 120, 177.

19 Ramirez-Aguilar, K. A., Rowlen, K. L. *Langmuir*, **1998**, 14, 2562

20 Tipler, P. A. *Physics for Scientists and Engineers*, Worth, New York, **1991**.

21 Cheung, W. L., Bailey, A. G. *Electrostatics 1995*, Institute of Physics Conference Series, **1995**, 143, 373.

22 Blythe, A. R. in Electrical Properties of Polymers, Cambridge University Press, Cambridge, **1979**.

23 Tkacyzk, S. W., Swiatek, J. *Synethetic Metals*, **2000**, 109, 255.

Chapter 6

Plasma Enhanced Adhesion of Polymer Reinforcing Cord for Tyres

6.1 Aim and Introduction

Rubber goods such as tires and conveyor belts are composite items formed of rubber and reinforcing cords. In tires these reinforcing cords give shape, size stability, bruise resistance and load carrying capacity.[1] Reinforcing cords are typically made from either polymer or steel, both materials needing treatment to improve their adhesion to the rubber matrix.[2,3] The most significant method of improving this adhesion is through the formation of a primary covalent bond.[4] Ideal conditions are provided for such bond formation during the reactive vulcanisation step.[2,3] In the case of steel cords adhesion is improved by a brass coating applied to the cords, that facilitates adhesion through the formation of a complex inter-phase of metal oxides and sulfides during vulcanization.[2] Adhesion improvement of polymer cords such as rayon, nylon and polyester to rubber is of economical and environmental interest. The most common and widely reported method of increasing the adhesion of polymeric cords to rubber is through the use of resorcinol formaldehyde latex (RFL).

The success of RFL lies in its ability to bond well to both the polymer cord and the rubber. Numerous mechanisms have been proposed for adhesion to the rubber including the co-vulcanisation of double bonds in the latex with those in the rubber,[5] and ionic or chemical reaction between the RF resin and the rubber.[6] The internal cohesion of the RFL is reliant upon good interaction of the resin and the latex, and several mechanisms have been proposed for bonding, including the formation of chromanes by reaction of the phenol ring in resorcinol with the double bond in the isoprene, Reaction 6.1.[7,8]

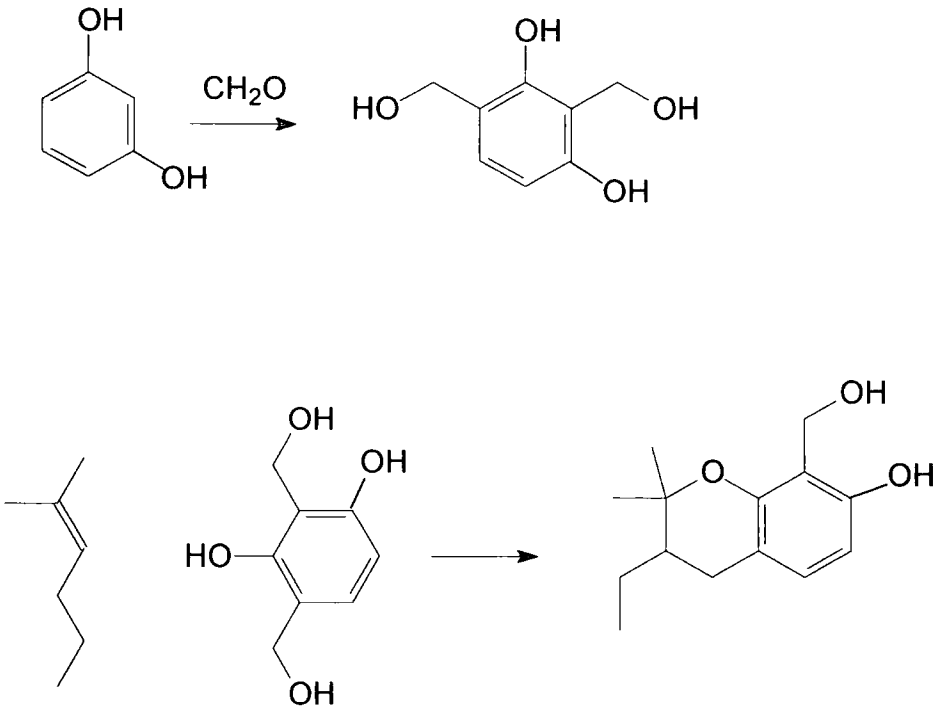

Reaction 6.1: Reaction of resorcinol with isoprene.

RFL was found to adhere well to rayon and nylon, but not to polyester. This is attributed to the presence of hydroxyl and amide groups in the rayon and nylon, allowing condensation reactions with the methylol group in the resin, Reaction 6.2.[6,9]

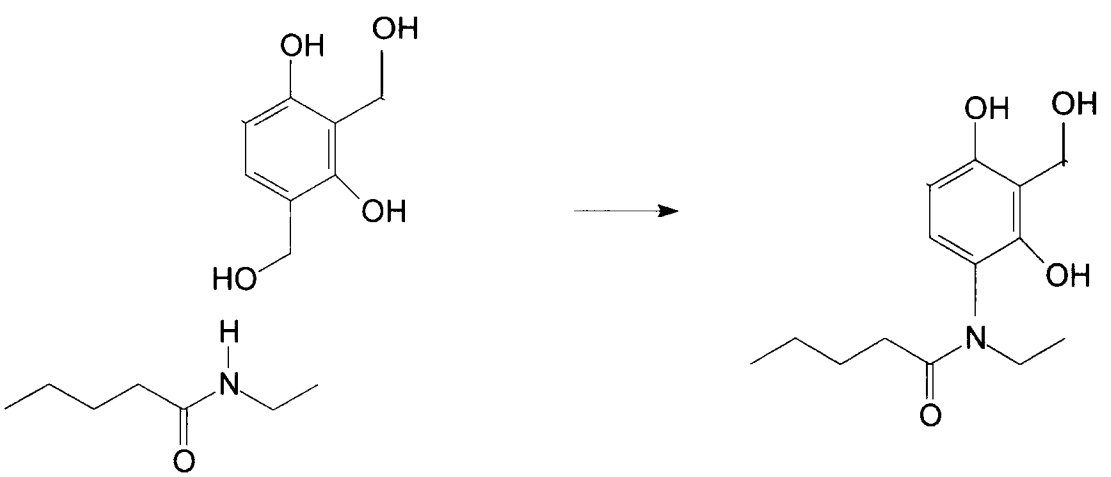

Reaction 6.2: Reaction of Resocinol with Nylon.

Numerous methods have since been proposed to increase the adhesion between polyester and RFL. Several of these methodologies involve the formation of hydroxyl and carboxyl functionality on the polymer surface, thus providing a reactive hydrogen for condensation reactions. The adhesion of polyester to RFL has been improved by these means, by both wet chemical means[10] and plasma treatments.[4,11,12,13]

A few isolated studies have also investigated the potential of plasma based processing to increase the adhesion between polyester and rubber without the need for wet dip processing.[3,14,15] Much scope still exists for gaining an understanding into the potential of differing plasma treatments in the improvement of this direct adhesion.

Several important factors to consider in the improvement of adhesion of polyester have been identified from the literature, these including: the polar component of surface energy,[4] surface roughness,[4] surface mobility,[4] surface degredation,[16,17] and failure in the rubber.[3]

We investigate here several dry plasma methods of increasing the adhesion of the cord directly into rubber without any wet-dip processing.

6.2 Microwave Plasma Treatment

6.2.1 Introduction

Here the effect of microwave oxygen plasma treatment on the adhesion of both polyaramid and polyester cords to rubber was investigated. The time of treatment is considered, and the resulting changes in elemental surface composition, surface energy and adhesion compared and related.

6.2.2 Experimental

Polyester and polyaramid cords were microwave plasma treated at 300 W, in an oxygen atmosphere at a pressure off 53 Pa, by Plasma Finish and were analysed as supplied.

XPS spectra were recorded on a VG escalab MkII spectrometer equipped with an unmonochromated Mg K_α X-ray source (1253.6 eV) and a hemispherical analyser. Photoemitted core level electrons were collected at a fixed take-off angle (75° away from the sample surface) with electron detection in constant analyser energy (CAE) mode operating at 20 eV pass energy. Instrument calibration was performed using the Au($4f_{7/2}$) reference peak at 83.8 eV with a full-width-at-half-maximum (fwhm) of 1.2 eV. No spectral deterioration due to radiation damage was observed during the time scale required for data accumulation. Elemental sensitivity factors were taken as being C(1s) : N(1s) : O(1s) : Si(2p) equals 1.00 : 0.95 : 0.45 : 0.9.

Dynamic contact angle analysis was performed using a Cahn Microbalance, (Model DCA322). For testing single 8 mm long filaments were taken from the cord and glued to the end of 50 mm long lengths of fuse wire. This wire was then bent into a hook at the opposite end to the filament and hung over the B loop of the microbalance. A motorised stage was used to

move a beaker containing the probe liquid upwards over the substrate at a speed of 20 μm s^{-1}, to an immersion depth of 4mm, before returning at the same speed. The advancing contact angle, θ, corresponds to the tangent at the three phase solid / liquid / vapour interface formed during the initial immersion of the fibre. This was calculated by applying the modified Young's equation Equation 6.1.[18]

Equation 6.1

$$\cos\theta = \frac{F}{\gamma \times p}$$

Where F is the wetting force at the meniscus measured by the microbalance, γ is the surface tension of the probe liquid, and p is the perimiter of the meniscus formed at the three-phase interface. The obtained value of θ was used to calculate the surface energy using the combined geometric mean-Young's equation, Equation 6.2.[18]

Equation 6.2

$$(1+\cos\theta)\gamma_l = 2\left[\left(\gamma_l^d \gamma_s^d\right)^{1/2} + \left(\gamma_l^p \gamma_s^p\right)^{1/2}\right]$$

Where γ_l is the surface tension of the probe liquid, and γ_l^d and γ_l^p are the respective dispersive and polar components.[19] The dispersive (γ_s^d) and polar (γ_s^p) surface energy components for the treatments could be calculated by substituting values for water (representing a polar liquid, γ_l^d = 22.1 mN m^{-1} and γ_l^p = 50.7 mN m^{-1})[19] and di-iodomethane (represents non-polar liquid, γ_l^d = 50.8mN m^{-1} and γ_l^p = 0.0 mN m^{-1})[20] into the equation, and solving the

corresponding set of simultaneous equations. Summation of γ_s^d and γ_s^p equates to the total surface energy γ.

Adhesion tests for the polyester cords were performed by Pirelli, using an identical mould and procedure to that described in section 6.3.2.

6.2.3 Results

XPS reveals an increase in the degree of oxygenation at the polyester surface after microwave oxygen plasma treatment of up to 5 minutes. Longer treatment times result in a reduction in oxygen content. A small amount of silicon was also found on the surface irrespective of treatment time, Figure 6.1a. Surface energy measurements showed an increase in the polar component and a reduction in the dispersive component of the surface energy accompanied increased treatment time, Figure 6.1b. Pull-out force measurements demonstrated an increase in adhesion after plasma treatment, and significant reduction for longer plasma exposure times, Figure 6.1c.

Microwave oxygen plasma treatments of the polyaramid cord yielded increases in both oxygen and nitrogen content at the cord surface with increased treatment time, as measured by XPS, Figure 6.2a. Surface energy measurements demonstrated decreases in both the dispersive and polar component after a 1 minute treatment. The polar component then recovering with longer treatment times, Figure 6.2b. Adhesion measurements showed a large increase for a 1 minute treatment, then a reduction in adhesion for longer treatment times, Figure 6.2c.

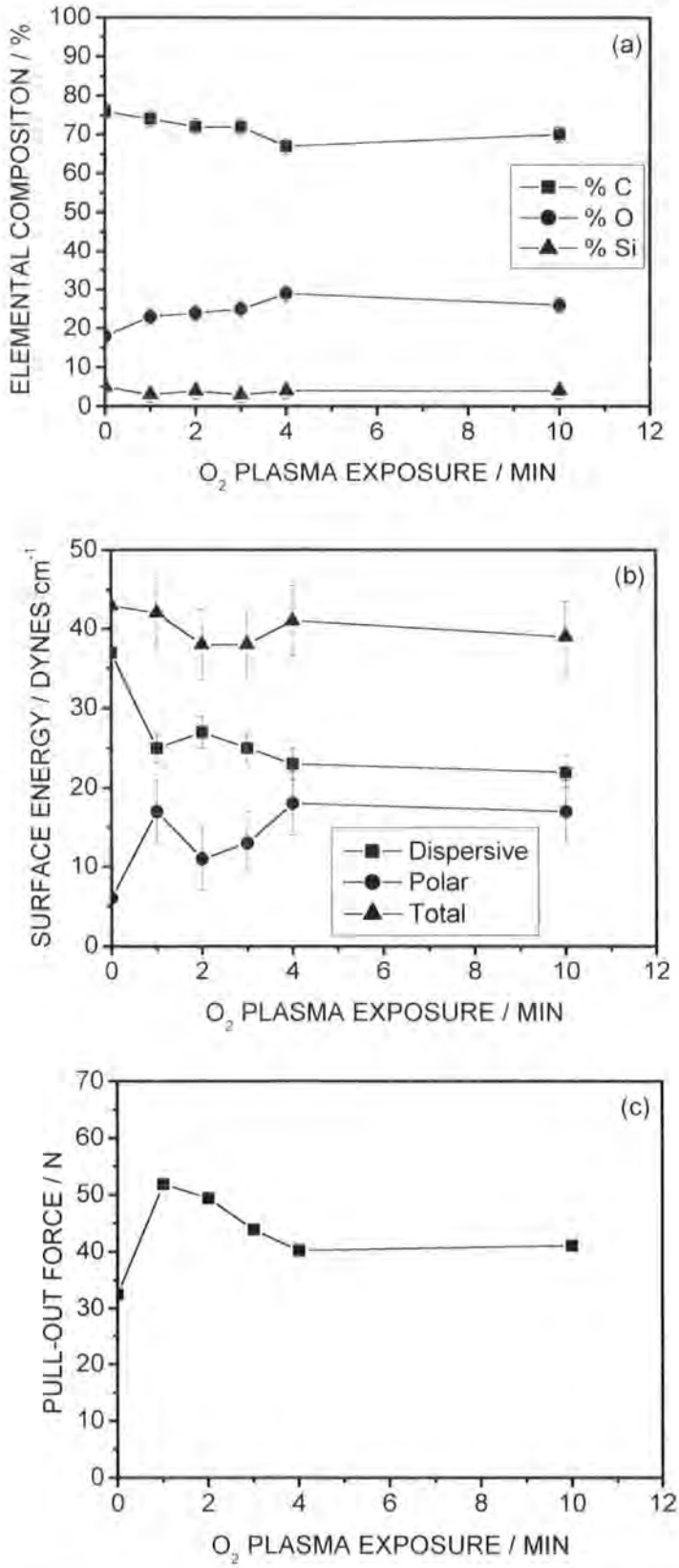

Figure 6.1 300W microwave O_2 plasma modification of polyester cord as a function of treatment time: (a) XPS elemental composition; (b) surface energy; and (c) adhesion.

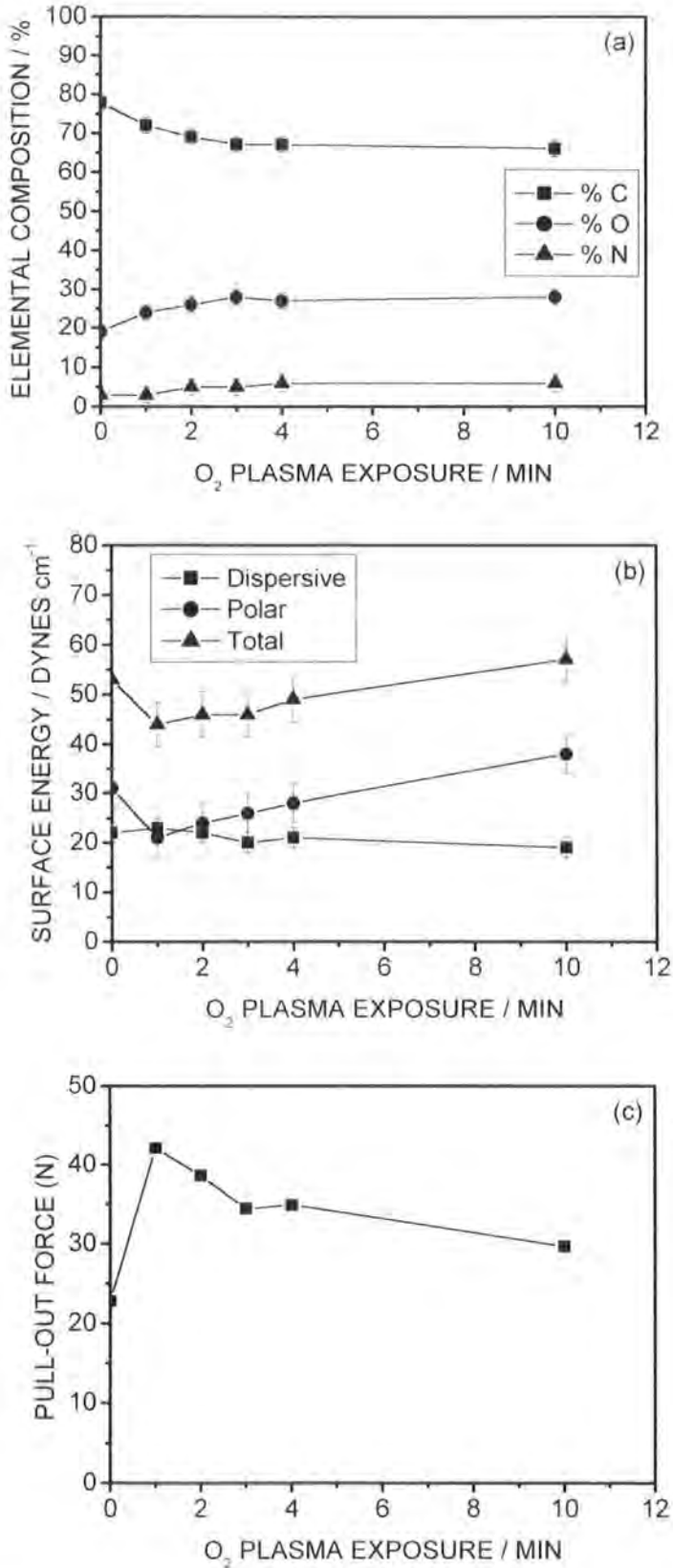

Figure 6.2 300W microwave O_2 plasma modification of polyaramid cord as a function of treatment time: (a) XPS elemental composition; (b) surface energy; (c) adhesion

6.2.4 Discussion

When considering the adhesive interaction between two polymers the two principal factors governing adhesion are the surface energy and macromolecular mobility.[4] The mechanism of adhesion can be broken down into three parts: diffusion, adsorption and interlocking.[4] Firstly considering the diffusion of polymers it is clear that restrictions imparted on molecular mobility within the polymer, such as in glassy or cross-linked polymers will reduce the ability of the polymer to diffuse. If diffusion does occur the compatibility of the polymers is of importance, and thus increases in wetting of the polymers results in increased van-der-waals, acid base and hydrogen bonding interaction. The wetability of the polymer is governed by both the surface chemistry and the roughness.[21]

The initial rise in oxygen content on the surface of the polyester with plasma treatment, is as expected from reports in the literature.[22] The subsequent decrease with prolonged exposure to the plasma is also consistent with the cracking of the polyester by the plasma.[4,22] The polar surface energy contribution to the surface energy reflects the degree of polar interaction between a polar solvent such as ultrapure water, and polar groups on the surface. The close correlation between the polar surface energy and the degree of oxygenation (within experimental error), as a function of plasma exposure, is consistent with the formation of polar functionalities such as carboxyl and hydroxyl groups on the surface of the polyester during plasma treatment, as has been reported in the literature.[17]

From comparisons between elemental composition / surface energy measurement with adhesion values as a function of plasma exposure, it is clear

that factors other than these are responsible for adhesion between the polyester and the rubber.

The similar adhesive response of the polyaramid to oxygen plasma exposure, and corresponding lack of correlation between this and the degree of oxygen incorporation and polar surface energy, again suggest further factors have bearing on the adhesion.

The initial reduction in the polar component of the surface energy for plasma treatment of the polyaramid is likely due to destruction of surface amine and carbonyl groups. The recovery of polar energy thereafter correlates with increased oxygen incorporation, suggesting increases may be due to incorporation of oxygenated functionalities.[23,24]

It is likely that the reduced adhesion for both cords for plasma treatments of longer than 1 minute is due to the degradation of the polymer surface, causing reduced cohesion, [25] possibly due to the UV and VUV components of the plasma.[17,26,27]

6.3 Gas Screening and Dual Plasma Treatments

6.3.1 Introduction

Here we investigate the effectiveness of different gases on the adhesion of both polyester and polyaramid cords to rubber. As well as individual gas plasma treatments, dual treatments involving noble gas pretreatment were investigated. Similar dual plasma treatments have previously been shown to improve both surface functionalisation and roughening[4]. Similar gas screening studies have been investigated in the literature for the increased adhesion of polyester cords to RFL.[4,11] Here we investigate the effect on adhesion directly to the rubber, and consider changes in surface elemental composition and surface energy, as a function of succesive Argon / Oxygen plasma treatments.

6.3.2 Experimental

Plasma treatments were carried out in a cylindrical glass reactor (5 cm diameter, 470 cm^3 volume) with a base pressure of 4×10^{-3} mbar, and a leak rate of better than 6×10^{-9} mol s^{-1}. The system was connected to a two stage rotary pump via a liquid nitrogen cold trap, and the pressure was monitored with a thermocouple pressure gauge. An L-C matching unit was used to minimise the standing wave ratio (SWR) of the power transmitted from a 13.56 MHz R.F. generator to a copper coil wound around the reactor walls. Prior to each plasma treatment, the chamber was scrubbed with detergent, rinsed in propan-2-ol and then further cleaned using a 50 W air plasma for 30 min. Leak rates calculated as described in chapter 2 and found to be better than 3×10^{-10} mols s^{-1}. Polyester (Pirelli) and polyaramid (Pirelli) cord samples (1 meter in length) wound on a custom made glass mount were placed in the centre of the reactor, followed by pumping down to base pressure. Gas was then admitted to

the system via a leak valve at a pressure of 2×10^{-1} mbar, and after 5 minutes of gas purge the plasma was ignited. A further 5 minutes gas purge was carried out after turning the plasma off. Upon completion of the treatment, the chamber was evacuated, followed by venting to atmosphere for single gas treatments, or repetition of the procedure using the second gas, for the dual treatments. The gases used were Ar (BOC 99.99%), He (BOC 99.99%), O_2 (BOC 99.99%), Air, N_2 (BOC 99.99%), CO_2 (BOC 99.99%).

Test specimens for adhesion measurement were produced according to ASTM D4776.[28] This entailed the vulcanization of lengths of cord into rubber strips (Pirelli, standard tyre compound) in a steel mould, using a heated hydraulic press (George Moore) at a temperature of 151°C for 40 minutes at a pressure of 17 tonnes. From the mat of rubber strips and cord extracted from the mould 'H-block' test specimens were cut, these entailed lengths of cord with both ends embedded in the rubber.

Adhesion measurement was performed using a tensileometer (Instron 5543), fitted with grips custom designed to hold the H block test specimens. Samples were pulled apart at a rate of 100mm min^{-1}, and force readings taken every 10 ms. The force at which the fibre loses adhesion to the rubber was measured and termed the pull-out force.

6.3.3 Results

6.3.3.1 Screening of Gas Plasma Treatments

Pull-out force measurement of low pressure plasma treated polyester and polyaramid cord shows a significant increase in adhesion for all plasma treatments. We observe that for polyester cords introducing an argon plasma pretreatment improves the adhesion attained for subsequent N_2, O_2 and air plasma treatments, with only CO_2 demonstrating a reduction. However a helium pretreatment reduces the adhesion of all four subsequent gas plasma treatments, Figure 6.3. The polyaramid cord demonstrates little or no improvement for argon plasma pre-treatment, and a reduction for helium pre-treatments, Figure 6.4.

The greatest adhesion measured was for a dual plasma treatment of the polyester cord using argon followed by oxygen, Figure 6.3.

6.3.3.2 Ar/O_2 Dual Plasma Treatment

XPS demonstrated that, for dual Ar/O_2 plasma treatments varying the Ar plasma power gave rise to an increase in oxygenation at the surface for powers up to 30 W, and a reduction for higher power treatments, Figure 6.5a. Surface energy determination demonstrated an overall increase in the polar component and little change in the dispersive component for increased Ar plasma power, Figure 6.5b, (untreated polyester cord: γ^d: 33mN m^{-1}; γ^p: 13 mN m^{-1} and γ: 47 mn m^{-1}). Pull-out force measurements showed little change in adhesion with increasing Ar plasma power, Figure 6.5c. Similar changes in surface chemistry were observed with increased oxygen plasma power.

XPS analysis of the polyaramid cord as a function of Ar plasma power showed an increase in the degree of surface oxygenation for powers up to 30 W

and a subsequent reduction for powers above 30 W, Figure 6.7a. Surface energy determination showed an initial increase in the polar component of the surface energy up to powers of 20 W then a reduction for treatment at greater power, but little change in the dispersive component, Figure 6.7b, (untreated polyaramid cord: γ^d : 16 mN m^{-1}; γ^p : 32 mN m^{-1} and γ : 48 mN m^{-1}). Pull out force measurements showed an initial increase in adhesion for a 10 W plasma then decreases for powers thereafter, Figure 6.7c. Varying the oxygen plasma power provided little change chemically in the polyaramid cord, Figure 6.8a. Surface energy determinations showed an overall increase in the polar component and a slight decrease in the dispersive component for increasing plasma power, Figure 6.8b. Pull-out force measurements showed a decrease in adhesion for oxygen plasma powers up to 30 W, and an increase for powers greater than 30 W, Figure 6.8c.

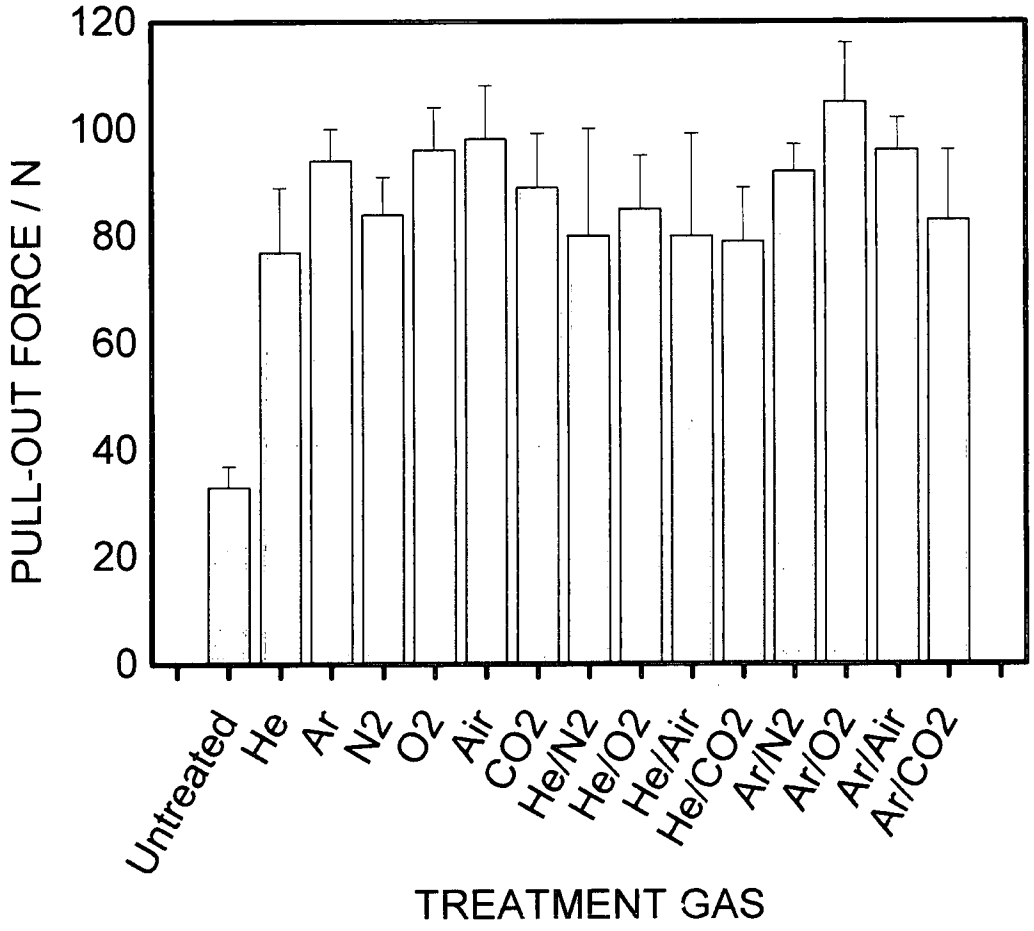

Figure 6.3 Pull-out force measurement of polyester cord as a function of plasma treatment gas; individual treatments (50 W, 5 min); double treatments (50/50 W, 5/5 min)

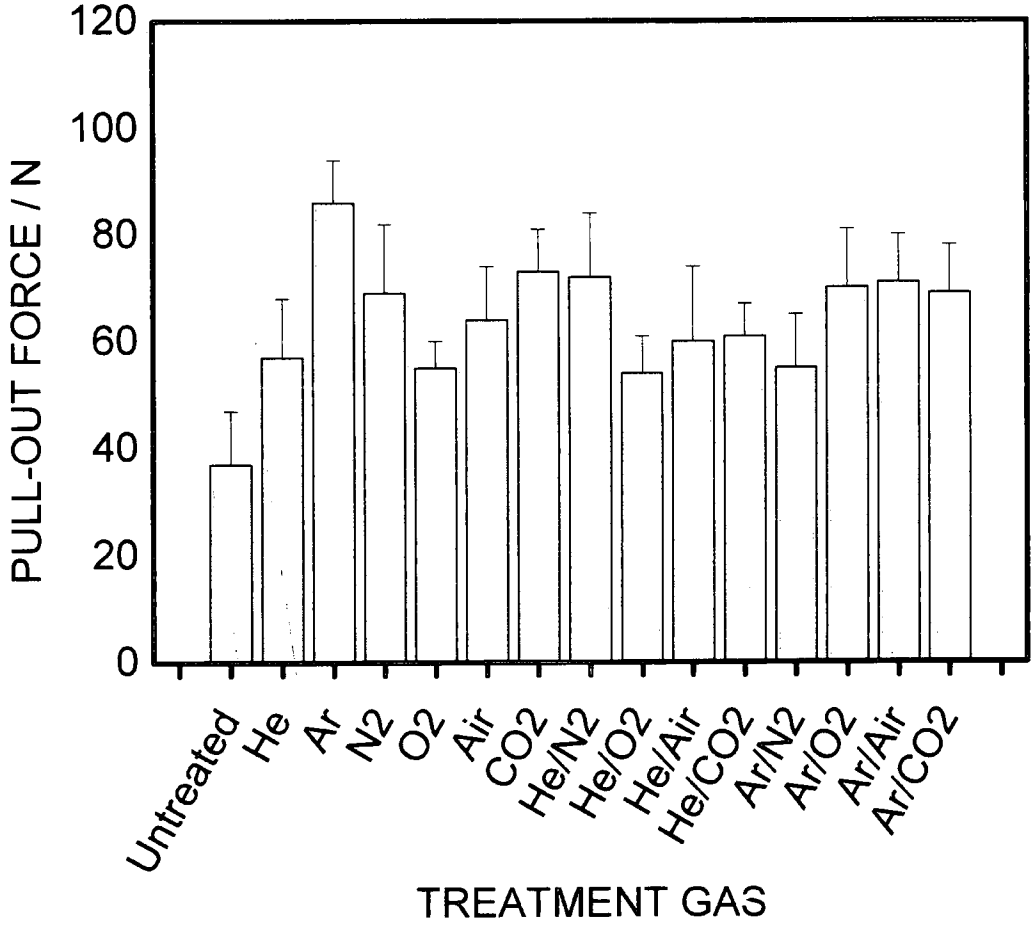

Figure 6.4 Pull-out force measurement of polyaramid cord as a function of plasma treatment gas; individual treatments (50 W, 5 min); double treatments (50/50 W, 5/5 min)

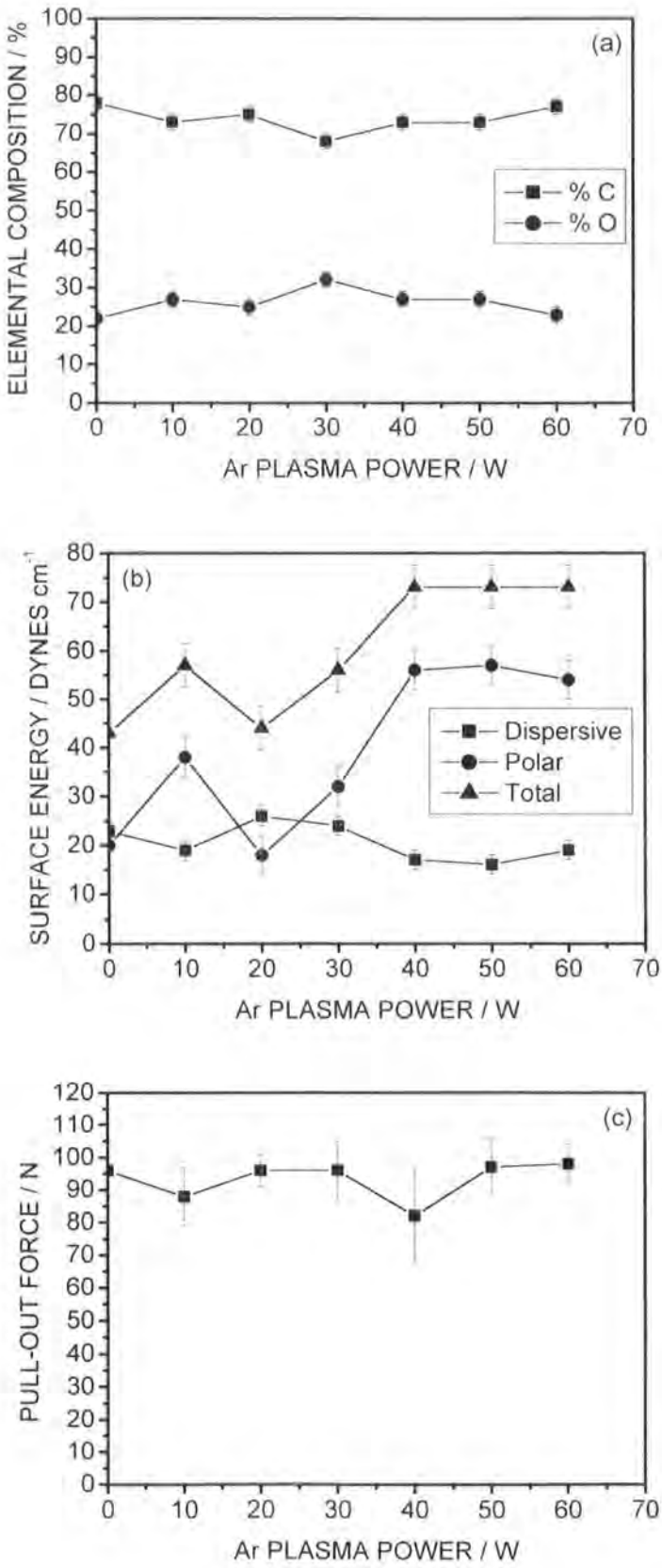

Figure 6.5 5 min Ar plasma treatment followed by O_2 plasma treatment (5 min, 50 W) of polyester cord as a function of Ar plasma power: (a) XPS elemental composition; (b) surface energy; (c) adhesion.

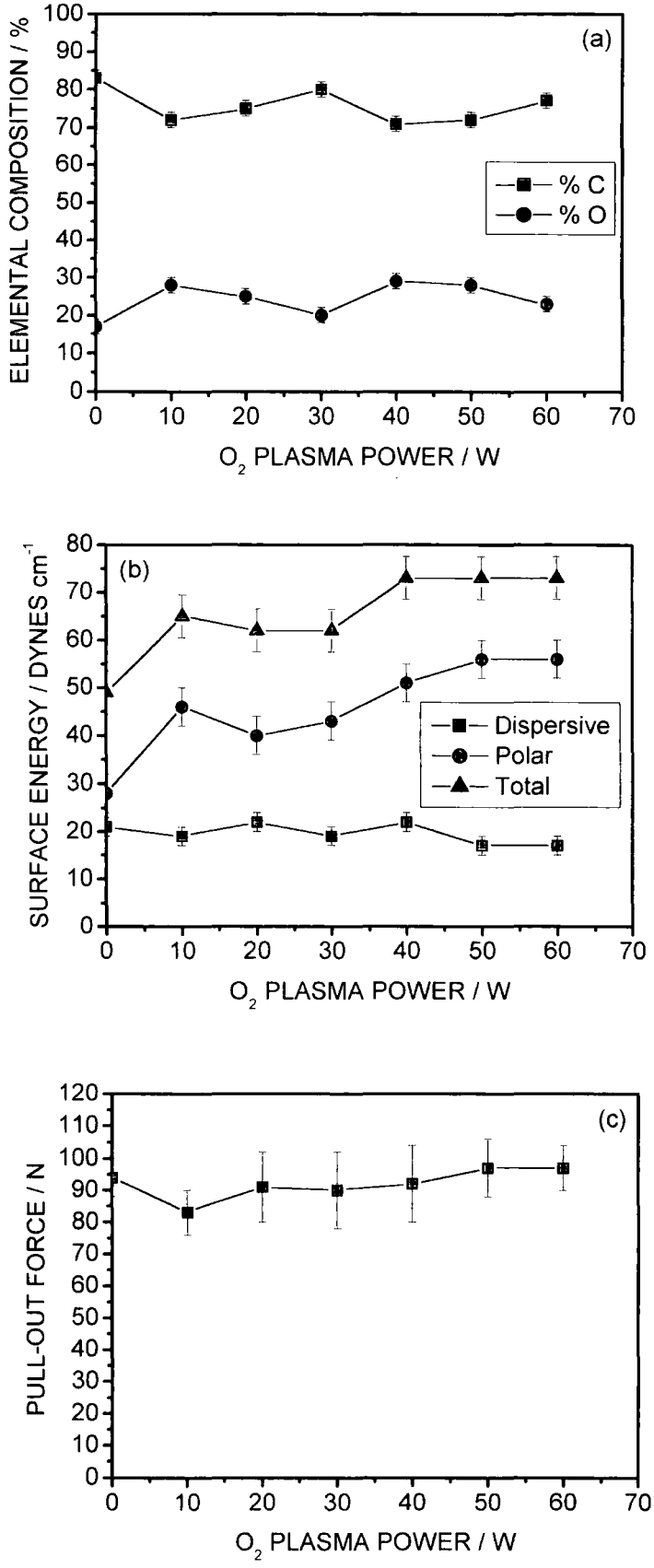

Figure 6.6 5 min O_2 plasma treatment preceded by Ar plasma treatment (5 min, 50 W) of polyester cord as a function of O_2 plasma power: (a) XPS elemental composition; (b) surface energy; (c) adhesion.

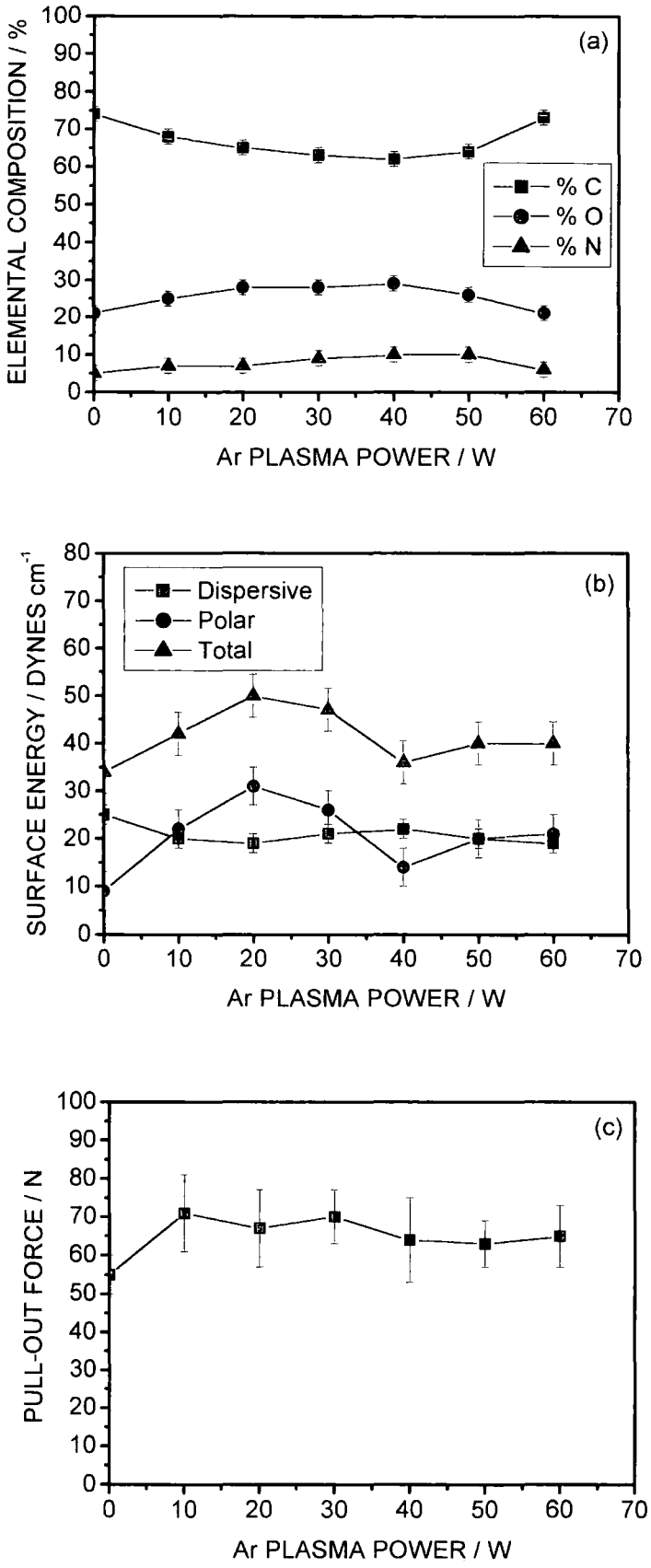

Figure 6.7 5 min Ar plasma treatment followed by O_2 plasma treatment (5 min, 50 W) of polyaramid cord as a function of Ar plasma power: (a) XPS elemental composition; (b) surface energy; (c) adhesion.

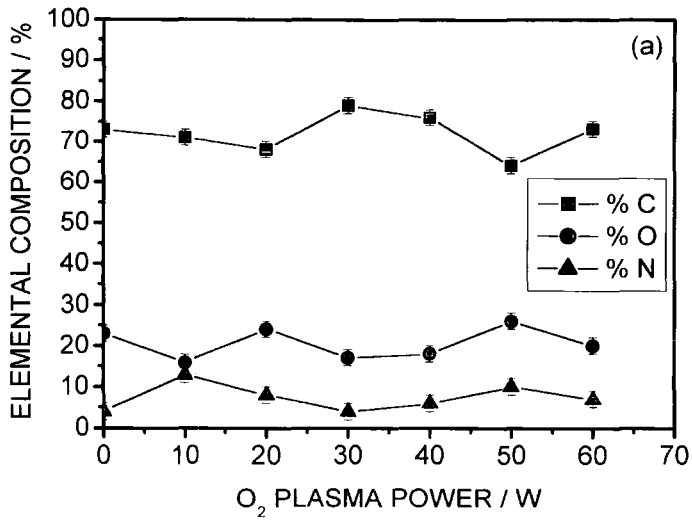

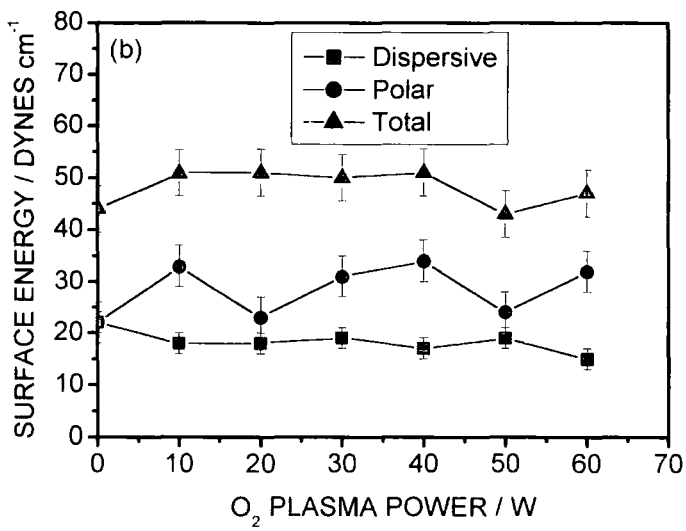

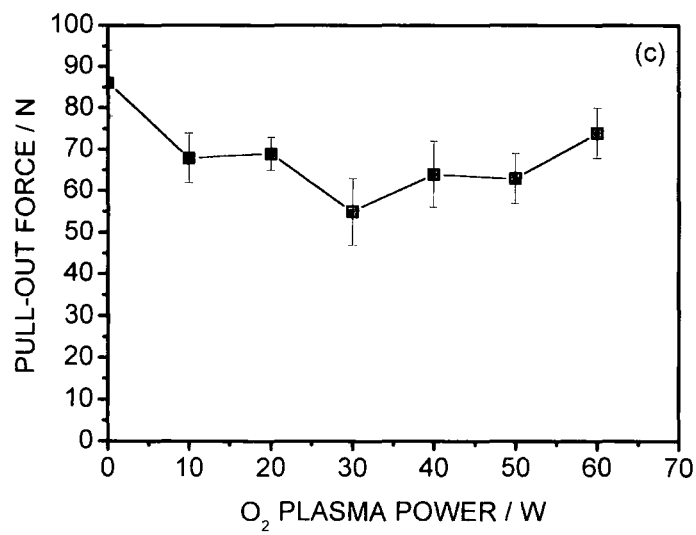

Figure 6.8 5 min O_2 plasma treatment preceded by Ar plasma treatment (5 min, 50 W) of polyaramid cord as a function of O_2 plasma power: (a) XPS elemental composition; (b) surface energy; (c) adhesion.

6.3.4 Discussion

6.3.4.1 Screening of Gas Plasma Treatments

The increase seen in adhesion for all the plasma treatments of both cords over that of the untreated cord may potentially be attributed to increases in surface energy, roughness and surface mobility.[4] Increases in adhesion seen for argon pre-treatments of polyester cord before O_2, N_2 and air plasmas may possibly be explained by either greater degrees of functionalisation, due to cross-linking during the argon plasma treatment,[29] or increased roughening due to the Ar plasma.[4] The reductions in adhesion seen with helium plasma pretreatment, may be attributed to greater damage to the fibre due to either higher energy species of increased UV components in the plasma. The lack of increased adhesion in the polyaramid cord after noble gas plasma pretreatment, may be explained by the greater sensitivity of polyaramid to UV damage in comparison to the polyester,[30] UV and VUV being components of the plasma treatments used[17]

6.3.4.2 Ar/O_2 Dual Plasma Treatment

As increasing either the argon or oxygen plasma power yields little change in adhesion for the polyester cord it would seem that either a 50 W, 5 minute plasma treatment of either oxygen or argon saturates the properties responsible for adhesion increases.

Differences between the extent of oxygenation and the polar surface energy may be accounted for in the potential removal of highly oxidised low molecular weight material in the vacuum associated with XPS analysis.

These results again show that the adhesion directly to rubber is dependant on factors other than the polar surface energy of the cords.

The lack of change in oxygenation, surface energy and adhesion seen for increased exposure of the polyaramid to either plasma suggest that for all treatments, changes are taken to saturation. This is reinforced by adhesion reduction with increased oxygen plasma exposure, which is likely to be a consequence of fibre degradation in the plasma, possibly due to the UV and VUV components. [17]

6.4 Pulsed Plasma Deposition

6.4.1 Introduction

Previous attempts have been made to improve on polymer cord adhesion to rubber by plasma assisted polymerisation.[3,31] Only one of these studies bypassed the RFL coating[3]. This entailed plasma polymerisation of CS_2 onto polyester and polyaramid cords, using a microwave continuous plasma treatment. Passage of pure organic vapours into this type of medium may yield a polymer coating, however structural rearrangements may be a limitation.[32] Pulsing the electrical discharge on the μs-ms time scale overcomes this drawback by minimising damage to the growing polymer layer, and allowing free-radical polymerisation reactions during the duty cycle off-time.[33] Using pulsed plasmas we impart specifically chosen functionalities to the polymer cord.[34,35,36]

In the formation of an adhesive bond using plasma polymers, failure has been reported at both the plasma polymer / fiber interface and also in the rubber[3]. Therefore it is important to consider both adhesion of our coatings to the fiber as well as to the rubber.

6.4.2 Experimental

For pulsed plasma deposition experiments a signal generator was used to trigger the R.F. source, and an oscilloscope used to monitor the pulse width and amplitude. The average power $\langle P \rangle$ delivered to the system was calculated using equation 6.3.[37]

Equation 6.3

$$< P >= P_p \left[\frac{T_{on}}{T_{on} + T_{off}} \right]$$

Where P_p is the continuous wave power and $T_{on} / (T_{on} + T_{off})$ is defined as the duty cycle. Prior to plasma treatments all monomers underwent freeze thaw cycles sufficient to remove all dissolved gaseous impurities. Monomer vapour: 2-hydroxyethyl methacrylate (Aldrich >99%), 2-cyanoethyl acrylate (Aldrich 99%), glycidyl methacrylate (Aldrich 97%), maleic anydride (Aldrich 99%), furfuryl methacrylate (Aldrich 97%), butyl acrylate (Aldrich >99%),and 1,2-ethaneditiol (Fluka >98%), was then admitted into the chamber at a pressure of 2×10^{-1} mbar, and after 5 minutes of purging the plasma was ignited. A further 5 minutes purge was carried out after turning the plasma off. Upon completion of the treatment, the chamber was evacuated, followed by venting to atmosphere.

6.4.3 Results

Pull-out force measurement of polyester and polyaramid cords coated in plasma polymers (parameters in Table 6.1), demonstrated an increase in adhesion for all monomers used, Table 6.2. It is interesting to note that monomers containing acrylate groups gave greater adhesion than monomers without an acrylate group.

With the exception of 2-hydroxyethylmethacrylate and glycidylmethacrylate, little difference was observed between the adhesion of treated polyester and polyaramid cords.

Monomer	Pressure (mTorr)	Time (min)	Peak Power (W)	Time on (μs)	Time off (ms)	Average power (W)
2-Hydroxyethyl methacrylate	100	10	40	20	20	0.04
2-Cyanoethyl acrylate	200	5	40	20	20	0.04
Glycidyl methacrylate	200	15	40	20	30	0.03
Maleic Anhydride	90	20	5	20	1.2	0.08
Furfuryl methacrylate	200	30	40	20	20	0.04
Butyl acrylate	150	10	40	20	20	0.04
1,2-EthaneDithiol	200	10	20	NA	NA	20

Table 6.1 Plasma polymerisation parameters for the monomers.

Monomer	Pull Out Force (N)	
	Polyester	Polyaramid
Untreated	33 ± 4	37 ± 10
2-Hydroxyethyl methacrylate	94 ± 9	55 ± 7
2-Cyanoethyl acrylate	59 ± 16	75 ± 9
Glycidyl methacrylate	100 ± 15	72 ± 12
Maleic anydride	46 ± 6	44 ± 9
Furfuryl methacrylate	60 ± 11	58 ± 6
Butyl acrylate	56 ± 6	67 ± 11
1,2-Ethanedithiol	42 ± 6	45 ± 7

Table 6.2 Pull out force adhesion measurement of cords treated by plasma polymerisation as a function of monomer.

6.4.4 Discussion

Plasma polymerisation of all the monomers investigated here, using the parameters listed has been shown to yield films exhibiting good functional group retention at the surface, Table 6.3. Polymerisation of the acrylate containing monomers occurs via the activated double bond in the acrylate group. A similar method of polymerisation occurs in the plasma deposition of maleic anydride through the double bond in the ring.

The functionalities presented at the surface of the plasma polymer films are summarised in table 6.3.

Monomer	Surface Functionalities
2-Hydroxyethyl methacrylate	-OH[38]
2-Cyanoethyl acrylate	-CN[34]
Glycidyl methacrylate	Epoxy[36]
Maleic anydride	Anhydride[33]
Furfuryl methacrylate	Furan[38]
Butyl acrylate	Butyl[39]
1,2-Ethanedithiol	-SH[40]

Table 6.3 Functionalities present at the surface of plasma polymer films.

When considering the adhesion of the plasma polymer films to rubber, several possible reactions may occur, including attack of sulfur during the vulcanisation process, and also reaction of the polymer functionality with the double bonds in the rubber. Of the functionalities imparted during plasma polymerisation the epoxide ring is likely to undergo ring opening under nucleophilic attack by sulfur, possibly explaining the high levels of adhesion observed for this coating. Correspondingly the thiol, hydroxy, cyano and anhydride functionalities may be expected to react with the double bonds in the rubber, in the presence of radical initiators,[41] which are commonly added to rubber.[42]

From the differences in adhesion seen between groups expected to present similar chemistries, such as 1.2-ethanedithiol and 2-hydroxyethyl methacrylate it is clear that other factors are important.

Potentially the cohesion of the plasma polymer is likely to be of importance. Correspondingly the clear increases in adhesion for plasma polymer containing the acrylate group may suggest this to form films exhibiting greater cohesion. Also of importance is the adhesion of the plasma polymer to the fibre. However the similar trends in adhesion improvement, for both polymer cords may suggests good adhesion between the cord and plasma polymer, as is expected for plasma polymer coatings.[33] The inability of the polyaramid to attain adhesion greater than ~70N is in accordance with other results in this chapter.

To further elucidate where adhesion failure is occurring would require more adhesion measurements with a range of fibres offering differing mechanical and surface chemical properties, and further analysis of cords after adhesion failure to elucidate the point of failure.

6.5 Conclusions

Adhesion of the polymer cords directly to rubber, can be attributed to a complex interplay of surface functionality, surface polarity, surface roughness and surface degradation. Individual gas plasma treatments were not sufficient to rival the adhesion provided by conventional wet dip processing. Adhesion improvement through plasma polymerisation is perhaps a more promising area of research, and is worthy of further investigation.

6.6 References

1 Kovac, F. J., *Science and Technology of Rubber*, Academic Press, Ed. Eirich, F. R., **1990**, 575.

2 Hammer, G. E., *Metallurgy, Processing and Applications of Metal Wires*, Ed Paris, H. G., Kim, D. K., **1996**, 155.

3 Shuttleworth, D., Mowood, S. K., Waddell, W. H., Richards, J. L., Ofstead, E. A., Brenner, J. L., *US. Patent 5,283,119*, **1994**.

4 Carlotti, S., Mas, A., *J. Appl. Polym. Sci.*, **1998**, 69, 2321.

5 Dietrick, M. I., *Rubber World*, **1957**, 136, 847.

6 Moult, H. in *Handbook of Adhesives*, ed, Skeist, I. Reinhold Publishing Corp., New York, **1962**, 495.

7 Greth, A. *Angew. Chem.*, **1938**, 51, 719.

8 Hultzsch, K. *kunstst.*, **1947**, 37, 43.

9 Miller, A. L., Robinson, S. B. *Rubber World*, **1957**, 137, 397.

10 Ludwig, H. *Polyesterfasern, chemie und Technologie*, Akademie-Verlag, Berlin, **1965**, Chapter 11.

11 Lawton, E. L., *J. Appl. Polym. Sci.*, **1974**, 18, 1557.

12 Manenq, F., Carlotti, S., Mas, A., *Die Angew. Makromol. Chemie*, **1999**, 271, 11.

13 Lawton, E. L., *US Patent 3,853,657*, **1974**.

14 Yang, W., Sung, N., *Abstracts of Papers of the American Chemical Society*, **1990**, 1991H, 99PSM.

15 Ahlblad, G., Kron, A., Stenberg, B., *Polymer International*, **1994**, 33, 103.

16 Lawton, E. L. *J. Appl. Polym Sci.*, **1974**, 15, 1557.

17 Petasch, W., Rauchle, E., Walker, M., Elsner, P., *Surface and Coatings Technology*, **1995**, 74-75, 682

18 Mittal, K. L., *Contact Angle, Wettability and Adhesion* VSP BV, Netherlands, **1993**.

19 Jasper, J. J., *J. Phys. Chem. Ref. Data*, **1972**, 1, 841.

20 Kaye, G. W. C., Laby, T. H., (Eds.), *Table of Physical and Chemical Constants*, 15th edn., Longman Scientific and Technical, Harlow, **1992**.

21 reference cassie baxter or wenzel, the roughness one.

22 Friedrich, J., Loeschcke, I., Frommelt, H., Reiner, H. D., Zimmermann, H., Lutgen, P. *Polymer Degradation and Stability*, **1991**, 31, 97.

23 Groning, P., Collaud, M., Dietler, G., Schlapbach, L., *J. Appl. Phys.*, **1994**, 76, 887.

24 Beake, B. D., Ling, J. S. G., Leggett, G. J., *J. mater. Chem.*, **1998**, 8, 2845.

25 Greenwood, O. D., Hopkins, J., Badyal, J. P. S., *Macromolecules*, **1997**, 30, 1091.

26 Hudis, m., *J. Appl. Polym Sci.*, **1972**, 16, 2397.

27 Jentschke, H., *Diplomarbeit*, Institut fur Plasmaforschung der Universitat Stuttgart, **1989**.

28 Book of Standards, Volume 07.02.

29 Stoller, H. M., *Int. Sampe. Tech. Conf.*, **1986**, 18, 993.

30 Goodfellows Catalogue **2000**.

31 Manenq, F., Carlotti, S., Mas, A. *Die Angew. Makromol. Chemie.*, **1999**, 271, 11.

32 Yasuda, H., *Plasma Polymerisation*, Academic Press, Orlando, **1985**.

33 Ryan. M. E., Hynes, A. M., Badyal, J. P. S., *Chem. Mater.*, **1996**, 8, 37.

34 Tarducci, C., Schofield, W. C. E., Badyal, J. P. S., Brewer, S. A., Willis, C., *Chem. Mater.*, **2001**, 13, 1800.

35 Evenson, S. A., Fail, C. A., Badyal, J. P. S., *Chem. Mater.*, **2000**, 12, 3038.

36 Tarducci, C., Kinmond, E. J., Badyal, J. P. S., Brewer, S. A., Willis, C., *Chem. Mater.*, **2000**, 12, 1884.

37 Nakajima, A., Bell, A. T., Shen, M., *J. Appl. Polym. Sci.*, **1979**, 23, 2627.

38 Tarducci, C. Ph.D. Thesis, University of Durham, **2001**.

39 butyl acrylate ref

40 Evenson, S. A. Ph.D. Thesis, University of Durham, **1998**.

41 March, J. Advanced Organic Chemistry (Fourth Edition), John Wiley & Sons, New York, **1992**.

42 Coran, A. Y. in Science and Technology of Rubber, Ed. Eirich, F. R., Academic Press, New York, **1978**.

Appendix A

Colloquia, Seminars, Presentations and Lecture Courses

University of Durham
Board of Studies in Chemistry

Colloquia and Seminars from Invited Speakers.

1998

October 21	Professor P. Unwin, Warwick University. Dynamic Electrochemistry: Small is Beautiful
October 27	Professor A. Unsworth, University of Durham What's a Joint Like This Doing in a Nice Girl Like You?
October 28	Professor J.P.S. Badyal, University of Durham Tailoring Solid Surfaces, Inaugural Lecture
November 3	Dr. C. J. Ludman, University of Durham Bonfire Night Lecture
November 18	Dr. R. Cameron, Cambridge University Biodegradable Polymers

1999

January 27	Professor K. Wade, University of Durham Foresight or Hindsight? Some Borane Lessons and Loose Ends
October 27	Dr. C. Braddock, Imperial College Novel Catalysts for Atom Economic Transformations

November 10 — Dr. I. Samuel, University of Durham
Improving Organic Light Emmitting Diodes by Molecular, Optical Device Design

November 16 — Professor A. Holms
Conjugated Polymers for the Market Place

2000

January 19 — Dr. P. R. Fielden, UMIST
Minaturised Chemical Analysis (Lab on a Chip): Functional or Merely Fashionable?

March 1 — Professor D. Tidsley, Unilever (Head of Research)
Computer Simulation of Interfaces: Fact and Friction

March 20 — Professor S. Marder, University of Arizona
Design of Molecules for Two-Photon Absorption and their Application to 3D Polymerisation and Imaging

October 25 — Dr. S. F. Campbell, Former Senior Vice President of Pfizer
Science, art and Drug Discovery, A Personal Perspective

November 8 — J. P. L. Cox, Bath University
Cosmic: a Universal, DNA-Based Language for Communicating with Aliens and Other Intelligent Life forms

November 22 — Dr. W. Hayes, University of Reading
Synthesis of Novel Dendimers and Hyperbranched Polymers

December 6 — Professor R. Compton, University of Oxford
Dual Activation Approaches to Electroanalysis: Ultrasound, Microwaves, and Laser Activation.

2001

January 24	Dr. A. deMello, Imperial College Chemical Integrated Circuits: Organic Synthesis and analysis on a small scale
February 28	Professor A. Balazs, University of Pittsburgh Modeling Meso- and Molecular Scale Interactions in Polymeric Systems

Presentations Attended

August 2001 University of Durham Ph.D. Presentations

"Microfluidic Patterning of Solid Surfaces"

Examined Lecture Courses

Spectroscopies (Dr. Halliday)

Experimental Design (Prof. Badyal)

Numerical Methods (Dr Wilson)